



**From Textile Waste to Carbon Nanomaterials for Offshore Wind
Turbine Blades**

being a thesis submitted in fulfilment of the
requirements for the degree of

Doctor of

Chemical Engineering

in the University of Hull

by

Hannah Marsden, MChem, PGDip

July 2023

Faculty of Science and Engineering

Acknowledgements

I would like to thank my supervisory team, Dr Dmitriy Kuvshinov and Dr Grazia Francesconi, I could not have completed the PhD without your assistance. Thank you Grazia for helping with the use of the XRD, and getting as excited as I was about the results. I would also like to thank the Aura CDT team especially Dr Danielle Smith, Joanna Arnett and Joanne Dewey for their support over the years, and always having a smile on their faces. Further thanks to Tim Dunstan for his expertise using the SEM, and Dean Moore, for his assistance with all the University of Hull analytical equipment. Both provided invaluable support for characterisation. I acknowledge the Henry Royce Foundation for providing funding to cover transmission electron microscopy expertise. I also acknowledge my funding from Grant Number EP/S023763/1.

I would also like to thank the students of the Aura CDT for their camaraderie and moral support and my colleagues in the office for the copious cups of coffee and all the laughs that came along the journey. To my friends, who supported me through the hard times and celebrated my joy, I appreciate all the support you have provided and the happiness you have brought me. Finally, I wish to thank my parents and sister, thank you for your unwavering belief in me over all the years.

Abstract

The aim of this research was to determine the feasibility of carbon production from the pyrolysis of textile waste, seeking a way of increasing the sustainability of “fast fashion” and recycling the 92 million tonnes of textile waste entering landfill globally each year. Pyrolysis is an untapped method for the recovery of gases, oils and chars from textile waste. In this research, 91 % polyester 9 % lycra and 100 % cotton textile waste samples were pyrolysed individually with both fixed temperatures (heating rate 49.5 °C/min) and slow pyrolysis (heating rate 2.5 °C/min). The heating rates were selected due to instrumental limitations, and to cover both fast and slow pyrolysis. Different pyrolysis temperatures yielded different proportions of non-condensable gases, with both textile waste samples producing a maximum methane yield of 20 %. Chemical vapour deposition of the gas yield from the pyrolysis over a 90 % nickel catalyst was used to explore the opportunity of producing carbon nanomaterials sustainably. It was found that the 91 % polyester 9 % lycra sample gave the highest yield of carbon nanomaterials. The research then explored if these could be used to manufacture offshore wind turbine blades. The carbon nanomaterials produced were mixed with an epoxy matrix to create carbon fibre composites. Mechanical testing of composites with different carbon weight loadings (0.5, 2 and 3.5 wt. % in a bisphenol A diglycidyl ether) showed a decrease in both Young’s Modulus and flexural modulus but an improvement in the composite’s resistance to weathering. The synthesised carbon nanofibers produced may be used as a reinforcing agent to protect the leading edge of a wind turbine blade to improve weathering and attrition resistance. The research found that waste textile pyrolysis is a feasible approach to improve the sustainability of both fast fashion but also offshore wind industry. This could be used to strengthen the circular economy and contribute to meeting the UN’s Sustainable Development Goals. This research is innovative because it considers how waste materials can be used to produce nanomaterials which have a wide range of applications.

Table of Contents

Acknowledgements	ii
Abstract	iii
Table of Contents.....	iv
List of Figures.....	ix
List of Tables.....	xiv
Abbreviations list.....	xvi
Chapter 1 - Literature review	1
1.1. Green energy	2
1.2. Wind turbine blades.....	3
1.3. Carbon nanomaterials; background, types and synthesis	10
1.3.1. Fullerenes.....	10
1.3.2. Carbon Nanotubes (CNTs).....	12
1.3.3. Graphene	14
1.3.4. Application of carbon nanoparticles.....	18
1.4. Chemical vapour deposition process	19
1.4.1. Chemical vapour deposition for the formation of carbon nanoparticles	19
1.4.1.1. Graphene	20
1.4.1.2. Carbon nanotube synthesis through chemical vapour deposition	22
1.4.1.3. Carbon nanofibers.....	24
1.4.1.4. Fullerenes.....	26
1.5. Background and environmental issues caused by textile waste	28
1.5.1. The environmental impact of textile waste	34
1.5.1.1. Solid waste	34
1.5.1.2. Liquid waste	34
1.5.1.3. Gas waste	35
1.5.2. Current approaches for textile waste disposal	35
1.5.2.1. Landfill.....	35
1.5.2.2. Recycling natural and synthetic fibres	36
1.5.2.3. Incineration	36

1.6.	Pyrolysis process	36
1.6.1.	Types of pyrolysis.....	36
1.6.2.	Pyrolysis of textiles and biomass	36
1.7.	Catalysts; synthesis, uses and supports	37
1.7.1.	Common active metals for catalysis	39
1.7.2.	Catalyst support structures.....	39
1.7.3.	Traditional heterogenous catalyst synthesis	40
1.7.3.1.	Co-precipitation	40
1.7.3.2.	Sol-Gel.....	41
1.7.3.3.	Deposition precipitation	42
1.7.3.4.	Impregnation.....	42
1.7.4.	Deactivation mechanisms of catalysts	43
1.7.5.	Catalyst selection	43
1.8.	Thesis aims and objectives.....	43

Chapter 2 - Experimental methodologies 44

2.1	Catalyst Preparation.....	44
2.2	Pyrolysis	45
2.3	Chemical Vapour Deposition	45
2.4	Carbon composite	46
2.5	Characterisation.....	48
2.5.1	Activity of catalyst.....	48
2.5.2	Gas Chromatography with thermal conductivity detector.....	48
2.5.3	Gas chromatography-Mass spectroscopy.....	48
2.5.4	Scanning Electron Microscopy	48
2.5.5	Energy dispersive X-ray spectroscopy.....	48
2.5.6	Transmission Electron Microscopy	48
2.5.7	Thermogravimetric analysis (TGA).....	49
2.5.8	Porosity and surface area (BET analysis)	49
2.5.9	Fourier transform infrared spectroscopy (FTIR)	50
2.5.10	Powder X-ray Diffraction.....	51
2.5.11	Dry ashing of the sample for trace analysis	52
2.5.12	Inductively coupled plasma mass spectrometry (ICP-MS).....	52
2.5.13	Elemental analysis (CHN)	53
2.6	Composite testing to determine mechanical properties	54
2.6.1	Tensile strength.....	54

2.6.2	3-point bending.....	56
2.6.3	Accelerated weathering.....	56

Chapter 3 - Pyrolysis, and characterisation, of textile waste 58

3.1	Background to the textile waste and characterisation approaches	59
3.2	Thermogravimetric analysis, and resultant kinetics, for different textile waste samples....	60
3.2.1	TGA analysis of 100 % Cotton textile waste.....	60
3.2.2	TGA analysis of 91 % Polyester 9 % lycra textile waste	64
3.3	Gas chromatography to determine the concentration of gas products following pyrolysis of textile waste samples.....	67
3.3.1	Different sampling approaches for determining the gas concentration in a pyrolysis sample	67
3.3.2	Gas products of pyrolysis of 100 % Cotton textile waste at different temperatures ...	70
3.3.3	Gas products of pyrolysis of 91 % polyester 9 % lycra textile waste at different temperatures	76
3.4	GC-MS of textile waste samples	84
3.4.1	Pyrolysis oils produced from the pyrolysis of 100 % cotton.....	84
3.4.2	Oil analysis of pyrolysis oils produced from pyrolysis of 91 % polyester 9 % lycra mix	86
3.5	SEM to determine the structure of textile waste and the influence of temperature on the structures and defects seen.....	89
3.5.1	Pyrolysis char produced from of 100 % Cotton textile waste at various temperatures	89
3.5.2	Pyrolysis char of 91 % Polyester 9 % lycra mix textile waste at various temperatures	91
3.6	Energy dispersive X-ray spectroscopy for inorganic elemental analysis of char produced from textile waste pyrolysis.....	93
3.6.1	Elemental analysis on chars produced from the pyrolysis of 100 % Cotton textile waste using EDS93	
3.6.2	Inorganic elemental analysis on chars produced from the pyrolysis of 91 % Polyester 9 % lycra textile waste using EDS.....	95
3.7	Fourier-transform infrared spectroscopy (FT-IR) for the determination of structural bonds comprising the structure of chars produced from the pyrolysis of textile waste feedstocks.....	96
3.7.1	Structural properties of chars produced through the pyrolysis of 100 % cotton textile waste	96
3.7.2	Structural properties of chars produced through the pyrolysis of 91 % polyester 9 % lycra textile waste	99

3.8	Elemental analysis to determine the CHN and oxygen content of chars produced through the pyrolysis of textile waste at different temperatures.....	103
3.8.1	Elemental analysis of chars produced through the pyrolysis of 100 % cotton textile waste	103
3.8.2	Elemental analysis of chars produced through the pyrolysis of 91 % polyester 9 % lycra textile waste.....	105
3.9	Nitrogen physisorption, porosity and surface area of chars produced through the pyrolysis of textile waste at different temperatures	106
3.9.1	Porosity and surface area of chars produced from pyrolysis of 100 % cotton textile waste	106
3.9.2	Porosity and surface area of chars produced from pyrolysis of 91 % polyester 9 % lycra textile waste.....	110
3.10	Conclusions	112

Chapter 4 - Production, and optimisation, of carbon using catalytic chemical vapour deposition..... 115

4.1	Introduction	116
4.2	Nickel alumina catalysts used for catalytic chemical vapour deposition	117
4.2.1	X-ray diffraction of nickel catalysts	117
4.2.2	Microscopy and elemental analysis of nickel catalysts.....	120
4.2.3	Porosity and surface area of produced catalysts.....	129
4.2.4	Activity of the nickel alumina catalysts.....	131
4.3	Optimisation of the deposition of carbon from a variety of feedstocks over a catalyst	133
4.4	X-ray diffraction of synthesised carbons from pyrolysis-CVD.....	136
4.5	Surface area and physisorption of synthesised carbons.....	138
4.6	Scanning Electron Microscopy of carbon nanofibers	140
4.7	Infrared spectroscopy of the different carbons produced from different feedstocks	146
4.8	Comparison between polyester/lycra carbon and the synthetic gas mix carbon	147
4.9	Conclusion.....	151

Chapter 5 - The mechanical properties of the composite materials 154

5.1	Introduction	155
5.2	Determination of the tensile strength of the composite material	156
5.3	Determination of the flexural strength of the composite material.....	164
5.4	Accelerated weathering and post weathering tensile testing.....	174

5.5	Comparison of mechanical properties between different tests.....	178
5.6	Scanning Electron Microscopy on fractured composite materials	180
5.7	Thermogravimetric analysis of composite materials.....	183
5.8	Infrared spectroscopy for the determination of bonds within the carbon composite material.....	187
5.9	Conclusions	189

Chapter 6 - Conclusions and future work 191

6.1	Conclusions	192
6.1.1	The potential for using pyrolysis techniques for the re-use of polyester/lycra and cotton textile waste.....	192
6.1.2	The production of carbon from pyrolysis of textile waste.....	194
6.1.3	The mechanical properties of the carbon-epoxy composite material	195
6.2	Future work.....	196

List of Figures

Figure 1.1. Sections of an offshore wind turbine blade [17]	4
Figure 1.2. Wind turbine blade set up for load testing [26]	7
Figure 1.3. Wind turbine blade showing the application of torsion, represented by T, adapted from [35].....	9
Figure 1.4. Set up for IZOD test for determination of hardness [36]	10
Figure 1.5. Fullerene structure (drawn on chemdraw)	11
Figure 1.6. Schematic representation of the Arc Discharge method set up [44]	12
Figure 1.7. Comparison of three different configurations of carbon nanotube structures a) armchair b) zigzag c) chiral [48]	13
Figure 1.8. Structure of graphene (drawn on chemdraw).....	15
Figure 1.9. Taxonomy of textile fibres [119].....	29
Figure 1.10. Structure of cellulose	30
Figure 1.11. Schematic representation of cotton fibre [122].....	30
Figure 1.12. Structure of polyethylene terephthalate (PET) (drawn on chemdraw)	31
Figure 1.13. Structure of nylon 6,6 (drawn on chemdraw)	31
Figure 1.14. Structure of acrylonitrile, the monomer used to produce acrylic material (drawn on chemdraw).....	32
Figure 1.15. Structure of polyurethane (drawn on chemdraw)	33
Figure 1.16. Structure of orange Azo dye, used for colouring textiles (drawn on chemdraw)	34
Figure 1.17. Structure of Acid Black 1, for dyeing textiles (drawn on chemdraw).....	35
Figure 1.18. The difference between a heterogeneous (two phase) and homogeneous (one phase) catalyst [204].....	38
Figure 1.19. Schematic representation of the steps of surface adsorption theory [205]	39
Figure 1.20. Difference between microporous, mesoporous and macroporous materials [221].....	40
Figure 1.21. Different precipitation points for metal salts for co-precipitation at room temperature [224]	41
Figure 1.22. The process for creating sol-gel materials and the conditions required for producing a xerogel, aerogel and cryogel formation [226].....	42
Figure 2.1. (a) Reaction set-up for the CVD of carbon from a synthetic gas mix containing carbon monoxide, carbon dioxide, methane and hydrogen (b) schematic for the reaction set up	46
Figure 2.2. 3D printed mould negative showing the dimensions of the composite sample...	47
Figure 2.3. (a) LLOYDS instrument EZ50 with a 50 kN load cell set up for tensile testing (b) schematic view of the LLOYDS EZ50	55
Figure 3.1. Thermogravimetric analysis curve for 100 % cotton sample	61
Figure 3.2. DTG curves for the different heating rates of 100 % cotton textile waste material.	63
Figure 3.3. Kissinger plot for the determination of activation energy for 100 % cotton textile	63
Figure 3.4. Thermogravimetric Analysis curve for 91 % polyester and 9 % lycra.....	64

Figure 3.5. DTG plots for 91 % polyester 9 % lycra at different heating rates	66
Figure 3.6. Kissinger plot for the 91 % polyester 9 % lycra textile waste sample	66
Figure 3.7. The effect on the gas sampling approach on the relative concentration of gases produced where (A) is the evolved gas (B) is the use of a peristaltic pump (C) is using a syringe and (D) is the use of a carrier gas, in this case Ar was used. The gas balance is made of the carrier gas.	68
Figure 3.8. Hydrogen production from the fast pyrolysis of 100 % cotton at different temperatures	70
Figure 3.9. Nitrogen production from the fast pyrolysis of 100 % cotton at different temperatures	71
Figure 3.10. Carbon monoxide production from the fast pyrolysis of 100 % cotton at different temperatures	72
Figure 3.11. Methane production from the fast pyrolysis of 100 % cotton at different temperatures	73
Figure 3.12. Carbon dioxide production from the fast pyrolysis of 100 % cotton at different temperatures	74
Figure 3.13. The gas concentrations produced through the stepped pyrolysis of 100 % cotton textile waste.....	75
Figure 3.14. Hydrogen generation from the fast pyrolysis of 91 % polyester 9 % lycra mix at differing temperatures.....	77
Figure 3.15. Nitrogen generation from the fast pyrolysis of 91 % polyester 9 % lycra mix at different temperatures	78
Figure 3.16. Carbon monoxide generation from the fast pyrolysis of 91 % polyester 9 % lycra mix at different temperatures	79
Figure 3.17. Methane generation from the fast pyrolysis of 91 % polyester 9 % lycra mix at different temperatures	80
Figure 3.18. Carbon dioxide generation from the fast pyrolysis of 91 % polyester 9 % lycra at different pyrolysis temperatures	81
Figure 3.19. The gas production from the stepped pyrolysis of 91 % polyester 9 % lycra textile waste materials.....	82
Figure 3.20. Scanning Electron Microscopy images on the chars produced from pyrolysis of cotton at different temperatures (a) raw cotton (b) 350 °C (c) 500 °C (d) 650 °C (e) 800 °C and (f) stepped pyrolysis char.....	90
Figure 3.21. Scanning Electron Microscopy images of polyester/lycra mix chars produced through pyrolysis at different temperatures (a) raw polyester/lycra mix (b) 400 °C (c) 500 °C (d) 650 °C (e) 800 °C (f) stepped pyrolysis of polyester/lycra mix	91
Figure 3.22. Lower magnification image of unreacted polyester/lycra textile waste feedstock	92
Figure 3.23. Energy Dispersive Spectroscopy data analysis on cotton chars produced at different temperatures during pyrolysis of 49.5 °C/min	94
Figure 3.24. Energy Dispersive Spectroscopy analysis on chars produced from fast pyrolysis of polyester/lycra at different temperatures	95

Figure 3.25. Fourier-Transform Infrared Spectroscopy data carried out on cotton chars produced at different pyrolysis temperatures where the labelled bands relate to O-H bonding (A), C-H bonding (B), C=C bonding (C) and C-O bonds (D).....	98
Figure 3.26. Fourier-transform infrared spectroscopy data for the chars produced at varied temperatures of pyrolysis of polyester/lycra textile waste where the labelled bands relate to O-H bonds (A), C=O bonds (B), C-O bonds (C) and C-H bonds (D).....	102
Figure 3.27. Absorption for the chars produced from pyrolysis of cotton textile waste at different temperatures of fast pyrolysis, from unreacted feedstock to 800 °C as well as the slow pyrolysis sample	107
Figure 3.28. Offset adsorption isotherms for cotton chars produced through high temperature fast pyrolysis, as well as the unreacted feedstock.....	108
Figure 3.29. Adsorption isotherm for polyester textile char samples following pyrolysis at different temperatures	111
Figure 4.1. X-ray diffraction and an example of electron diffraction for different metal loaded catalyst powders, metal loadings were seen to be 70 % Ni, 80 % Ni and 90 % Ni. The hkl peaks were assigned based off the ICDD's PDF-2 2023 database.	119
Figure 4.2. Scanning electron images of the catalyst at different metal loadings (a) 70 % nickel 30 % alumina (b) 80 % nickel 20 % alumina and (c) 90 % nickel 10 % alumina	121
Figure 4.3. Catalyst cluster size distributions, for different metal loading for catalysts (a) 70 % nickel 30 % alumina (b) 80 % nickel 20 % alumina and (c) 90 % nickel 10 % alumina.....	122
Figure 4.4. Transmission electron microscopy image of the (A) 70 % Ni 30 % alumina sample (B) 80 % Ni 20 % alumina and (C) 90 % Ni 10 % alumina sample	123
Figure 4.5. Particle size distribution for nickel and alumina nanoparticles within (A) 70 % nickel 30 % alumina catalyst (B) 80 % nickel 20 % alumina catalyst (C) 90 % nickel 10 % alumina catalyst	124
Figure 4.6. Energy dispersive x-ray spectroscopy elemental analysis on the different metal loadings of the catalysts produced with theoretical yields of 90, 80 and 70 % Nickel. Multiple measurements were taken and presented to show the range of data collected.	126
Figure 4.7. Elemental map of the 90 % Ni 10 % alumina sample	128
Figure 4.8. Adsorption and desorption of nitrogen on the surface of the produced catalyst	130
Figure 4.9. Plots showing the conversion of methane to hydrogen at different catalyst metal loadings as a way to determine the activity of the catalyst	132
Figure 4.10. Powder x-ray diffraction plot showing the components, and relative crystallinity, of the carbons produced through the pyrolysis to chemical vapour deposition of 91 % polyester 9% lycra cotton and methane. The peaks have been assigned hkl values based on the ICDD's PDF-2 2023 database.....	137
Figure 4.11. Nitrogen physisorption for carbon samples produced through chemical vapour deposition of pyrolysis gases	139
Figure 4.12. Scanning electron microscopy images of carbon produced through chemical vapour deposition of carbon containing gases, or a reference gas, over a 90 % nickel 10 % alumina catalyst with (a) polyester/lycra textile waste (b) cotton textile waste and (c) methane gas.....	141

Figure 4.13. Transmission electron microscopy images of carbon nanofibers produced from (A) polyester feedstock (B) methane feedstock and (C) cotton feedstock. All were deposited on a 90 % Ni catalyst.	144
Figure 4.14. Distributions of the width of different carbon fibres produced through the chemical vapour deposition of (a) methane (b) cotton pyrolysis gases (c) polyester/lycra pyrolysis gases over a 90 % nickel 10 % alumina catalyst	145
Figure 4.15. Fourier-Transform infrared spectroscopy of carbons produced from different feedstocks showing (A) C≡C stretching.....	146
Figure 4.16. Scanning electron microscopy images of carbon produced through chemical vapour deposition over 90 % nickel 10 % alumina catalyst of (a) a synthetic gas mix to mimic that of the polyester/lycra textile waste gas phase and (b) pyrolysis of polyester/lycra textile waste.....	147
Figure 4.17. Distribution of the widths of nanoparticles seen in the carbon produced through the chemical vapour deposition of a synthetic gas mix to mimic that of the polyester/lycra textile waste gas phase over a 90 % nickel 10 % alumina catalyst at 600 °C	148
Figure 4.18. Transmission electron microscopy of carbon nanofibers produced from a synthetic gas mix.....	149
Figure 4.19. Powder x-ray diffraction of the carbon produced from the synthetic gas mix designed to mimic the gases produced through the pyrolysis of 91 % polyester and 9 % lycra textile waste with hkl values assigned based on the ICDD's PDF-2 2023 database.....	150
Figure 4.20. Electron diffraction pattern for the synthetic carbon with labels showing the identified hkl values	151
Figure 5.1. Plots to show the maximum tensile loading (stress) before failure for composite materials at different carbon loadings (a) pure epoxy sample (b) 0.5 wt.% carbon in the epoxy sample (c) 2 wt.% carbon in the epoxy sample and (d) 3.5 wt.% carbon in the epoxy sample (e) 0.5 wt.% synthetic carbon (f) 2 wt.% synthetic carbon (g) 3.5 wt.% synthetic carbon	158
Figure 5.2. Results of 3-point bending tests to determine the flexural strength of a composite material made of (a) pure epoxy and composite materials of pure epoxy and (b) 0.5 wt.% methane carbon (c) 2 wt.% methane carbon (d) 3.5 wt.% methane carbon (e) 0.5 wt.% synthetic carbon (f) 2 wt.% synthetic carbon and (g) 3.5 wt.% synthetic carbon	166
Figure 5.3. Images of epoxy samples before and after accelerated weathering, the individual samples are labelled in the image, where the type of carbon is not specified it is methane produced carbon.....	176
Figure 5.4. Comparison of different test parameters (A) Compression (B) Pre-weathering (C) Post-weathering on the Young's Modulus and Maximal Stress of composite materials.....	179
Figure 5.5. SEM images showing the tensile fracture sites of (A) 0.5 wt.% methane carbon loaded into epoxy (B) 2 wt.% methane carbon loaded into epoxy and (C) 3.5 wt.% methane carbon loaded into epoxy	181
Figure 5.6. TGA and DTG curves for different composite materials where (A) pure epoxy (B) 0.5 wt.% methane carbon (C) 2 wt.% methane carbon (D) 3.5 wt.% methane carbon (E) 0.5 wt.% synthetic carbon (F) 2 wt.% synthetic carbon and (G) 3.5 wt.% synthetic carbon.....	185

Figure 5.7. Fourier-Transform infrared spectroscopy for different carbon composite materials where (A) is CH stretching (B) is CH stretching (C) is HCH, CCH and CC stretching (D) is CCH and out of ring CC stretching (E) is CC stretching in-ring (F) is CO and CC stretching in rings and (G) is torsions in the rings and CC out of plane bending.....188

List of Tables

Table 1.1 Parts of the wind turbine blade and their function [19].....	5
Table 1.2. Different synthesis parameters to produce carbon nanofibers	25
Table 1.3. Different parameters for the synthesis of fullerenes	27
Table 1.4. Bond enthalpy for different bonds seen in the chemical structures of textile fibres [138 – 139]	34
Table 1.5. Tonnes of textile waste sent to landfill per country per year.....	35
Table 1.6. Parameters for the pyrolysis of cotton textile waste	37
Table 2.1. Mass of nickel metal salt needed for the preparation of catalysts	44
Table 2.2. Required masses of carbon for different epoxy composite compositions.....	47
Table 3.1. Thermogravimetric Analysis results of 100 % cotton	61
Table 3.2. Thermogravimetric Analysis temperature results for 91 wt.% polyester and 9 wt.% lycra.....	65
Table 3.3. Gas Chromatography-Mass Spectrometry data for pyrolysis oils produced through the pyrolysis of cotton textile waste at different temperatures	84
Table 3.4. Classification of classes of compounds seen following gas chromatography-mass spectrometry analysis of pyrolysis oils produced from polyester/lycra mix.....	87
Table 3.5. Table showing the expected peaks from cotton char Fourier-transform infrared spectroscopy [269].....	97
Table 3.6. Expected peaks for the Fourier-transform infrared spectroscopy of polyester/lycra chars produced at different temperatures [269].	100
Table 3.7. CHN analysis of 100 % cotton chars produced at different pyrolysis temperatures	104
Table 3.8. Elemental analysis of polyester/lycra mix chars produced at different pyrolysis temperatures	105
Table 3.9. Surface area, pore size and pore volume calculated from the physisorption of nitrogen at different temperatures on chars produced through the pyrolysis of cotton at different temperatures	109
Table 3.10. Surface area, pore volume and size for the physisorption of nitrogen at different temperatures on chars produced through the pyrolysis of polyester at different temperatures	112
Table 4.1. Table showing the elemental composition of different catalyst materials	129
Table 4.2. Surface area, pore volume and pore size for the produced catalysts	131
Table 4.3. The optimisation parameters and results for the production of carbon from the pyrolysis to chemical vapour deposition of textile waste feedstocks	135
Table 4.4. Surface area, pore volume and size measurements for the produced carbon from CVD.....	140
Table 5.1. Stress, strain and Young's Modulus for composite samples that contain either no carbon, 0.5 wt.% carbon, 2 wt.% carbon or 3.5 wt.% carbon from different feedstocks	161
Table 5.2. Calculation of the maximal flexural stress, strain and flexural modulus from different composite materials composed of epoxy and varying loadings of carbon nanomaterials	168

Table 5.3. Stress and Young's Modulus for different carbon composite materials following accelerated weathering	176
Table 5.4. Thermogravimetric Analysis temperature results for different carbon composite materials	186

Abbreviations list

BET – Braunauer-Emmett-Teller

BOD – Biological Oxygen Demand

CHN – Carbon Hydrogen Nitrogen

CNTs – Carbon Nanotubes

COD – Chemical Oxygen Demand

CVD – Chemical Vapour Deposition

EDS – Energy Dispersive X-ray Spectroscopy

FTIR – Fourier Transform Infrared Spectroscopy

GC – Gas Chromatography

GC-MS - Gas Chromatography Mass Spectrometry

GC-TCD - Gas Chromatography Thermal Conductivity Detector

HDPE – High Density Polyethylene

ICP-AES – Inductively Coupled Plasma Atomic Emission Spectroscopy

ICP-MS – Inductively Coupled Plasma Mass Spectroscopy

LCoE – Levelised Cost of Energy

LDPE – Low Density Polyethylene

MC – Methane Carbon

MWCNTs – Multiwalled Carbon Nanotubes

NMR – Nuclear Magnetic Resonance

PET – Polyester Terephthalate

PP - Polypropylene

PU – Polyurethane

SC – Synthetic Carbon

SDG – Sustainable Development Goals

SEM – Scanning Electron Microscopy

STEM – Scanning Transmission Electron Microscopy

TEM – Transmission Electron Microscopy

TGA – Thermogravimetric Analysis

UV – Ultraviolet

XRD – X-ray Diffraction

Chapter 1 - Literature review

1.1. Green energy

If temperature increases are not capped at an increase of 1.5 °C, significant changes to the climate will occur [1], ocean acidification has already bleached over half of the shallow water corals in the Great Barrier Reef, whilst in the Arctic the Permafrost has started melting [2]. Temperature increases occur due to the accumulation of gases, such as carbon dioxide, methane and water vapour, which reflects radiation back to Earth causing the surface temperature to rise [3]. Human behaviours are leading to an increase in releases of these gases, through industrial processes, farming, transport and agriculture. Whilst natural sinks do exist, such as trees and algal systems, they are put at risk through human behaviour spanning from deforestation for cattle rearing to ocean acidification leading to a reduction in the population of algae [4]. Whilst carbon dioxide is the best documented greenhouse gas, others are more a cause of concern.

Atmospheric methane concentrations have increased rapidly since the 1980s with more than 50 % of emissions being directly correlated to human activities [5]. Current findings show that this is steadily increasing and has been over the last 20 years [5]. Methane is 25 times more potent than carbon dioxide, whilst nitrous oxide is 298 times more potent. This potency is due to the reactions within the ozone layer, leading to depletion and the origin of holes. The presence of these gases will lead to an increase of reflected radiation, causing a temperature rise [6]. As both methane and nitrous oxide are released through the combustion of fossil fuels as well as agriculture, changing global habits may reduce these emissions [7].

With increasing risks to the environment from global warming, and rising levels of greenhouse gases, 192 countries globally have signed the Kyoto protocol [8] and although not all countries have shown a significant decrease in emissions [9] the UK has. In line with the UK government goal to reach net zero by 2050, there is increased reliance on renewable sources of energy such as offshore wind, solar panels and tidal energy. In the UK the amount of energy produced through renewable sources has increased whilst the dependence on non-renewable sources has decreased, this also leads to an increase of self-sufficient energy production [10]. The levelised cost of energy (LCoE) is a measure of the current price of produced energy, considering the economic costs of maintenance and construction [11]. To further encourage

improvements to both environmental and human sustainability, the UN has produced Sustainable Development Goals (SDGs) [12]. These SDGs show the wide range of issues that need to be addressed, from affordable and clean energy through to clean water and sanitation and gender equality [13]. The research presented in this thesis will consider SDGs 7 and 12; affordable and clean energy, and responsible consumption and production. By utilising waste material to produce new materials to lower the LCoE of a clean energy production method both of these development goals can be furthered.

Due to improvements in the design and efficiencies of offshore wind turbines, the LCoE for offshore wind energy has decreased globally in the last decade by 60 %, whilst in Europe the LCoE decreased by 29 % between 2020 and 2021 [14]. This makes offshore wind energy a much more attractive option for energy generation, especially for the UK with the amount of coastal space available [15].

1.2. Wind turbine blades

Offshore wind turbine blades consist of a blade root, spar cap and shear web, as shown in Figure 1.1. These are all encapsulated within the shell which is the outer layer of the blade. Each section requires different material properties depending on their function, for example, the root requires stability, whilst the tip needs flexibility due to the application of loads [16].

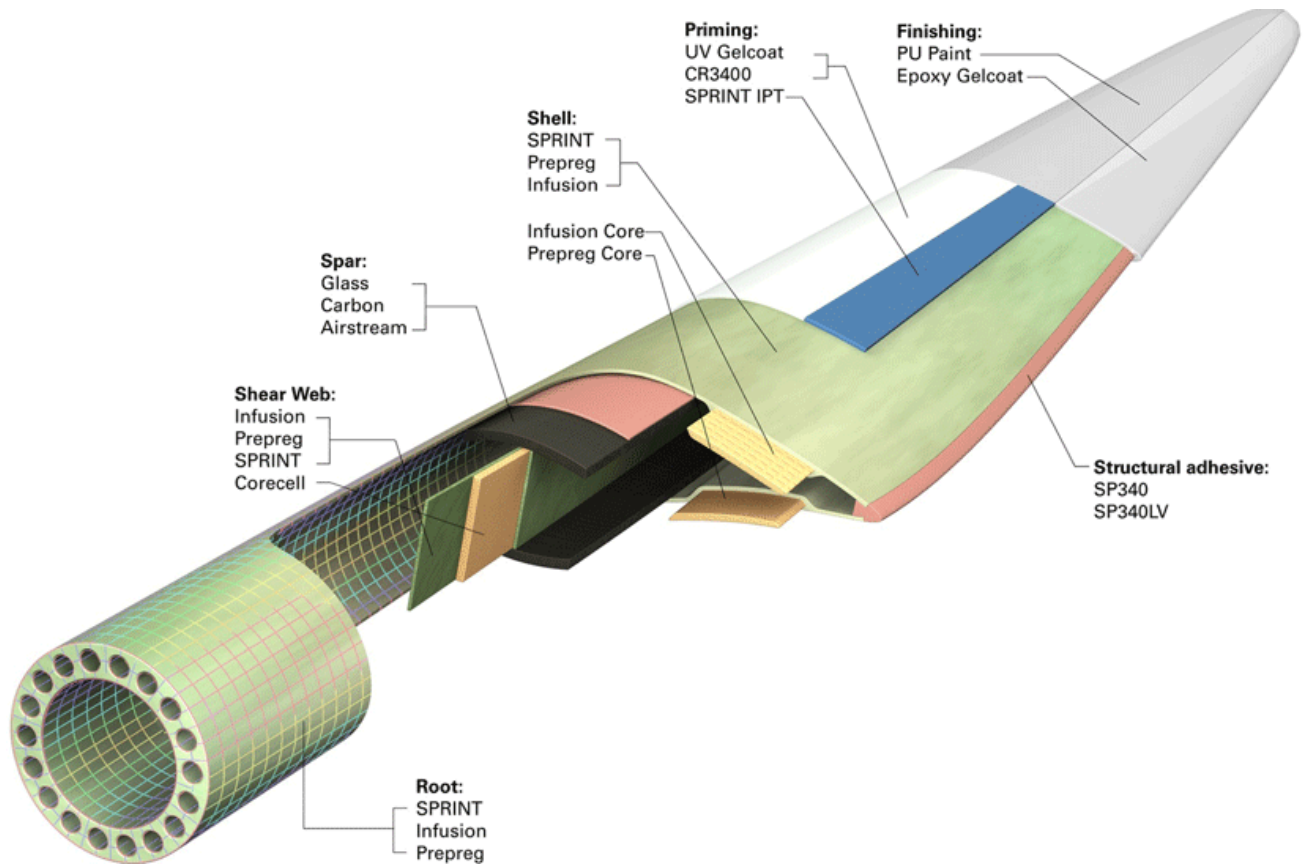


Figure 1.1. Sections of an offshore wind turbine blade [17]

As shown in Table 1.1, different parts of the blade have different functions as well as different drivers for material choice. The root requires a high-performance material, whereas the choice of shell material is driven by cost. A low material cost is beneficial in maximising the levelised cost of energy [18].

Table 1.1 Parts of the wind turbine blade and their function [19]

Blade element	Function	Performance vs Cost
Root	1. Connection of blade to hub. 2. Transference of loading from blade to hub.	Performance
Spar cap	Structural stability of the overall blade	Performance
Shear web	Transference of shear force and loadings between the faces and edges of the blade	Cost
Shell	Efficiency	Cost

Blade manufacture historically has been via a “wet-layup” process, where open moulds are used for the bulk of the blade and the internal webs. The moulds are painted in a gelcoat before fibre mats are placed inside. A resin and hardener are mixed together and manually poured and spread around the mould using rollers to ensure all the fibres are fully wetted [20]. This approach was superseded due to its labour intensity as well as environmental concerns over the release of volatile organic compounds [21]. Resin transfer moulding was the successor to the “wet-layup” process. The initial process is identical, however, instead of using rollers to spread the resin, a vacuum bag covers the blade and the resin and hardener are pumped in. The vacuum allows a uniform wetting of the fibres, allowing a reduction in imperfections, defects and voids [20]. The current approach for manufacturers is the use of prepreg technology. The fibre mats are pre-impregnated with an uncured mixture of resin and hardener. The blade is laid up in the same process as wet-layup and then vacuum bagged. The mould is heated to ensure that the resin hardens. The main disadvantage of this approach is the limited shelf life and the curing temperatures [20].

Siemens Gamesa has developed IntegralBlade, which allows the wind turbine blade to be manufactured in one piece, without the need for bonding the two halves of the blade together. The blade is produced by using fibreglass that is encased in a fixed outer shell with

an expanding internal mould. The resin is applied under vacuum conditions to the shell material and the enclosed blade is hardened at high temperatures. Once hardened, the inner mould is collapsed, leaving a seamless blade [22].

Following the design and optimisation of the blade, a scale model is usually produced, which is tested under conditions resembling those that the blade will be exposed to. The blade is also tested using mechanical tests. Following testing, the sample is analysed to monitor cracks or other defects such as voids. Most cracks remain enclosed within the sample and within the individual layers where they started [23]. Mechanical load testing is used to determine if the blades are suited to use, including monitoring the reaction to dynamic and static loads. This can aid in preventing large-scale failures. Blade testing can be separated into static testing, where the load is applied in one direction, and dynamic testing, which uses cyclic loading. The test-load can be either load-based or strength-based. Load-based tests determine if the blade will withstand operational loads, whilst strength-based tests are carried out to failure [24]. Composite materials are at risk of delamination through instabilities caused by propagation of cracks, or moisture intrusion, making it vital that these are monitored, as if left these can lead to catastrophic failures.

Fagan et al, approached the testing of blades by using load saddles, as seen in Figure 1.2. Wind turbine blade set up for load testing to evenly distribute weight over the blade prototype. It was found that the flap-wise forces were affected by lift and drag, meaning they may compromise the thrust generated. Lead and lag wise forces are also affected by lift and drag, however, they contribute torque which drives the wind turbine [25]. There was no discussion concerning operational loads such as centrifugal forces, which may lead to stretching and compression of the blade causing crack propagation and delamination.



Figure 1.2. Wind turbine blade set up for load testing [26]

Shear tests determine the level of in-plane, parallel force that a material can withstand, as well as how well a composite material can withstand delamination. Within the shear test umbrella term, there are two main approaches; the V-Notched rail and Iosipescu. The main difference between these approaches is the V-Notched rail utilises a larger area, whilst the Iosipescu test is carried out by taking a sample of material that has a notch cut into it and secured in the test machinery. For both approaches one end has downward pressure applied whilst the other end remains static. This can be used to determine the potential for delamination in a composite material as a reduced shear load may indicate a greater risk of delamination [27].

The potential for delamination of the composite blade material has been explored using a specimen made of glass fabric-reinforced polymers layered at 0° and 90° to produce warp and weft. Specimens were cut to 40mm length with 25mm width and 1mm thickness. Impact tests, discussed later in this section, were carried out to generate impact data with delamination modelled using software alongside the impact data to generate cohesive-zone elements. These cohesive-zone elements simulate initiation and progression of lamination in a sample. It was found that the composite blade materials used exhibited permanent deformation rather than brittle behaviours. Based on the experimental work seen, the

perpendicular weave can be assumed to be relatively resistant to impact related delamination [28].

Vibrational testing is important so the blade avoids structural resonance. As the blades rotate, the stiffness changes due to centrifugal inertia forces. This can lead to unforeseen vibrations, which, in turn, may cause failure [29]. Blade vibrations can be grouped based on the excitation force and the way this force affects vibration. The excitation can be electronic or mechanical in nature. If external materials have resonances that are similar to the blade's natural resonance then vibration will increase within the blade [30] leading to potential failures.

One approach to vibrational testing is to use computational modelling to determine the natural frequencies of the blade as it rotates [29]. However, this approach can only be carried out following full-scale modelling. There was no discussion on how this may be scaled up on lab-trials, and the impact that this may have on the performance of blade. Another approach is to use physical laboratory testing comprising static tests, rotational tests and in-service tests. Static tests measure all the natural frequencies and modes of vibrations at laboratory scale, meaning that testing can be carried out using small scale models. The rotational tests measure the natural frequencies under the influence of centrifugal forces. This can also be carried out on small scale models. In-service tests measure the dynamic stresses and natural frequencies seen during operations. In these tests, a pulse hammer was used for the static tests, an air jet for the rotational tests whilst the in-service tests were carried out on site [30]. The results can be monitored using vibration meters attached to the blade.

Torsion testing is carried out by fixing one end of the sample and then introducing a rotational force along the length, as shown in Figure 1.3. It is important to create minimal shear stress so that only torsion is being measured during this test. Torsion is an important consideration for offshore wind turbine blades to prevent flutter [31, 32]. Flutter is the phenomenon where the torsional mode matches a flap-wise bending moment which leads to an amplification of both motions. This can lead to significant fatigue and ultimately failure within the blade [33] [34].

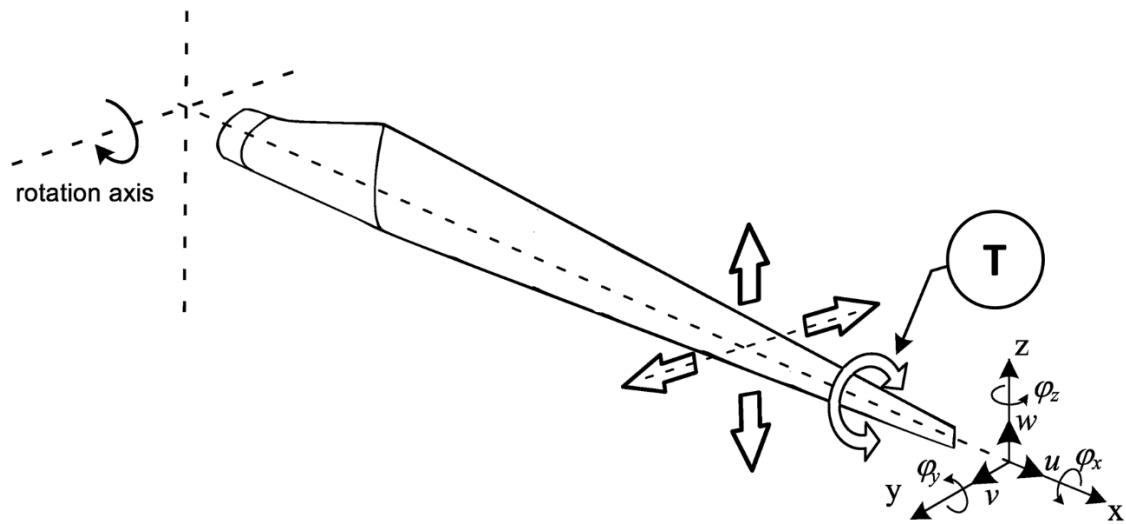


Figure 1.3. Wind turbine blade showing the application of torsion, represented by T, adapted from [35]

Impact testing is used to determine the amount of energy absorbed by a specific material during impact, which relates to the material toughness. Impact testing can be separated into IZOD and Charpy, both of which load a small section of the sample. The Charpy tests are mostly carried out on metals whilst IZOD is mostly performed on plastic samples. The IZOD test is set up using a test sample with a notch cut into one face. One end is fixed in place facing towards a pendulum, as shown in Figure 1.4. The Pendulum is swung, and the force of impact required to break the test sample is recorded. The IZOD test results give information about how resistant the material is to impact, which in turn allows the wind turbine blade to be designed to optimise hardness.

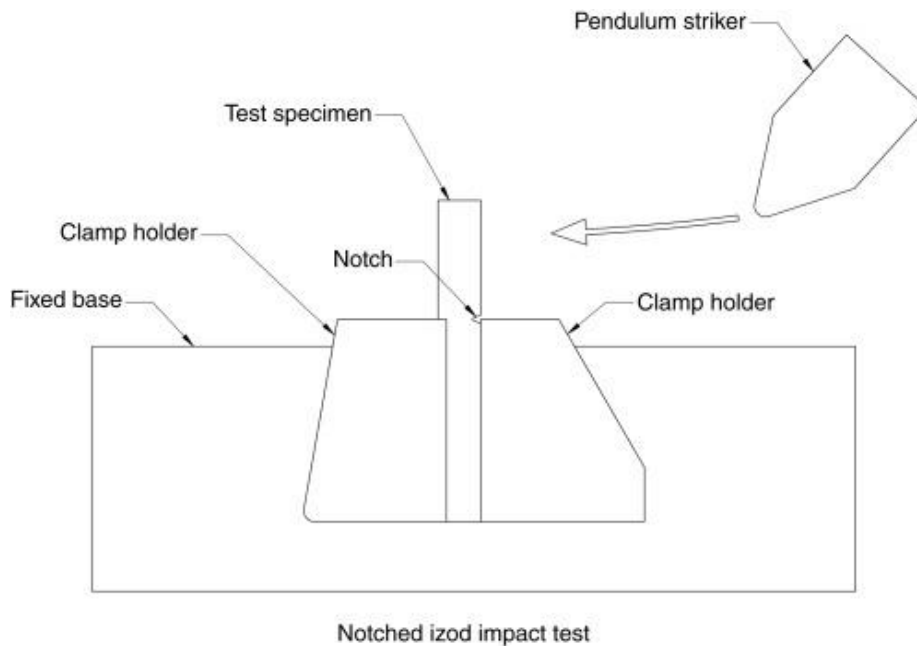


Figure 1.4. Set up for IZOD test for determination of hardness [36]

Testing is crucial on small scale models so that once the full-size blade is constructed, it will be efficient and the loads acting on it will be mitigated. This will diminish maintenance costs and reduce the LCoE. However, impact tests usually show poor reproducibility due to the presence of microfractures within the sample [37].

1.3. Carbon nanomaterials; background, types and synthesis

Carbon materials are one of the most researched areas in material sciences. Fullerenes, Carbon nanotubes (CNTs) and graphene are the main focus of the research. As wind turbines are becoming more multifaceted, the materials they are made from are becoming more complex. There is a demand for lightweight materials that can withstand high loads and environmental conditions [38].

1.3.1. Fullerenes

Fullerenes, also known as buckminsterfullerene, or bucky balls, are a nanostructured allotrope of carbon that was discovered in 1985, by Sir Harry Kroto and his research team [39]. They are in the form of spheres that are made of C_n but the most common is C_{60} , as shown in Figure 1.5 [39]. They have been used to produce membranes, water channels and electrical sensors [40]. Fullerenes have a good range of electrochemical properties due to the highest occupied molecular orbital, and lowest unoccupied molecular orbitals, leading

to negative potentials. This makes them of interest for the energy industry as they can support a range of different applications, such as in photovoltaic cells [41].



Figure 1.5. Fullerene structure (drawn on chemdraw)

Initially, fullerenes, Figure 1.5, were produced using laser evaporation of graphene [39], however, the main approach currently is to produce fullerenes is using the Arc discharge method, Figure 1.6. Dubrovsky et al, used argon gas as the plasma gas as part of the arc discharge to vaporise carbon black in a high temperature environment with a strong gas shield created by the gas stream to prevent the carbon black being vaporised too fast. In a sample of 180 mg/mm of carbon black the yield was 2 % fullerenes. Synthesis occurs in evaporation, enhanced by the inter-electrode gap and during condensation. Limitations occur due to the velocity of the carbon black. There is discussion of the potential re-use of the carbon black. In this study optimisation had not been carried out, meaning a higher yield may be found [42].

The arc discharge method, as shown in Figure 1.6, uses a direct-current arc voltage which is applied across two graphite electrodes, which are the source of the carbon used to form the nanomaterial, surrounded with an inert gas. When pure graphite is used for the electrodes the fullerenes are deposited as soot whilst carbon nanotubes are deposited on the cathode [43].

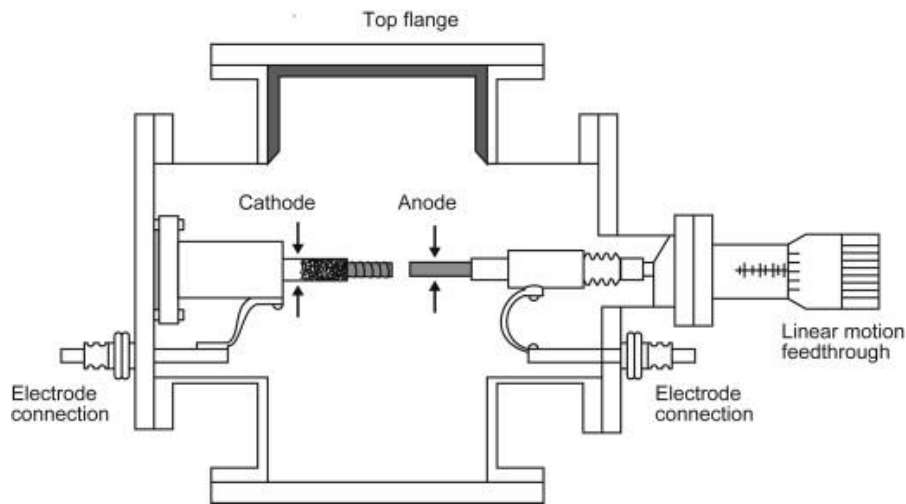


Figure 1.6. Schematic representation of the Arc Discharge method set up [44]

1.3.2. Carbon Nanotubes (CNTs)

Carbon nanotubes (CNTs) can be separated into single-walled or multi-walled depending on the layering visible within the sample. As an allotrope of carbon, they are one dimensional but with a tube like structure [45]. They are envisioned as rolled up sheets of graphene planes and can be capped at one end with a fullerene hemisphere. The physiochemical properties of graphene are similar to those of CNTs, showing high mechanical strength alongside thermal and electric conductivity, they also can absorb light over a wide range of wavelengths. The difference is that carbon nanotubes have a high aspect ratio whilst graphene is layered. CNTs can also be tuned to different pore sizes and roughness requirements [46]. Carbon nanotubes have a reported tensile strength of between 10 to 110 GPa with a Young's Modulus of 0.62 to 1.2 TPa [46]. There has been research into the use of CNTs as nano modifiers helping hardness, wear resistance and crack resistance in the material [47].

As shown in Figure 1.7 [48], there are three main configurations of carbon nanotube. These are achieved by altering the way that the graphene is wrapped into the cylinder. The diameter and twist of the carbon nanotube, which is directed by the configuration, determines if it is metallic or semiconducting. Armchair configurations show electrical properties similar to metals whereas the majority of chiral and zigzag configurations show properties similar to semiconductors. All three configurations show good electrical conductivity as the electrons can travel freely in a delocalised wave, with no resistance [48].

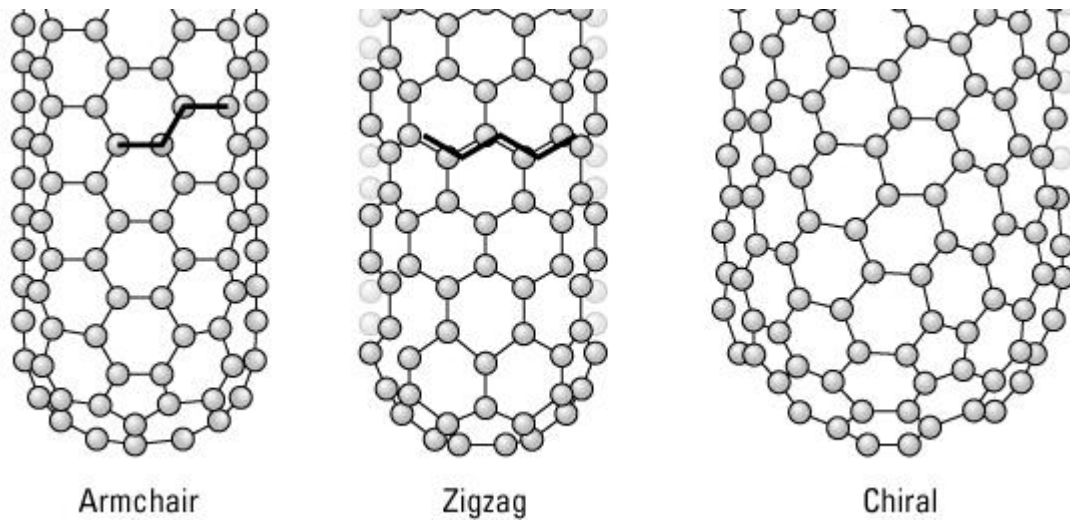


Figure 1.7. Comparison of three different configurations of carbon nanotube structures a) armchair b) zigzag c) chiral [48]

Due to the high reported mechanical strengths CNT polymer, additives can be used to help reduce external loading conditions as well as edgewise and flapwise bending moments. They also help reduce the impacts of cyclic loadings. CNTs can also reduce long cracks and prevent delamination due to their agglomeration properties. They are especially valuable in materials that need to have a high resistance to fatigue, high strength, low weight, high stiffness and high resistance to adverse environmental conditions [45]. Most CNTs have been reported to be synthesised using chemical vapor deposition or arc discharge [47] and can be either grown onto fibre surfaces or added to a polymer resin. A “one-pot” approach can be utilised to produce CNTs from polypropylene (PP) by the combination of activated carbon and Ni_2O_3 . This occurs through the carbenium ion mechanism where carbenium ions promote the degradation of PP to preferentially form carbon that can be catalysed to form CNTs. The carbon source is dissociated and then absorbs within the metal catalyst, once the catalyst is supersaturated, the carbon precipitates to form CNTs. Experimental data showed that different metal catalysts were used with nickel being found to be the most efficient [49].

The growth of CNTs can be controlled through the properties of catalyst, the addition of promoter, metal-support interactions and reaction conditions [50]. The metal-support interactions govern the growth mechanism seen. Tip-growth occurs where there is a weaker metal-support interaction, whilst a base-growth mechanism occurs where stronger interactions were seen [51], although these can only be measured where there is anchoring

of the catalyst to a surface. The choice of catalyst is a crucial decision to be made. Nickel-based catalysts were again found to be the most efficient to produce high quality CNTs. In a study by Wang et al, the majority of CNTs formed using pyrolysis and a nickel catalyst were multiwalled carbon nanotubes (MWCNTs) whilst a strong metal support reaction was seen to occur using a magnesium catalyst, making cleaning the nanotubes a more complex process. However, this also suppressed the growth of CNTs to produce short and irregular nanotubes [52].

Pyrolysis of waste plastics to produce the CNTs is a trending area of research [53]. This approach is economic and eco-friendly, as 50,000,000 tonnes of plastic is produced globally each year [53]. High density (HDPE) and low density (LDPE) polyethylene are some of the most common waste plastics, and it was reported that a specially designed reactor was required. The catalyst chosen in the study carried out by Bajad et al, was $\text{Ni}_4\text{Mo}_{0.2}\text{MgO}$, and was placed on trays within the reactor, the top tray was exposed to more hydrogen and gave a higher level of aligned CNTs than the bottom tray, showing that hydrogen. It was considered a very efficient process for batch synthesis, however, it was unclear how feasible mass production would be [54]. Further research by Bajad et al, showed that recycling the exhaust fumes can increase the conversion rates. It was reported that at a temperature of 700 °C a 5.5 % yield of CNTs was produced. Hydrogen was reported as critical for enhancing the growth of CNTs. NMR and GC were used to analyse the resultant CNTs to determine their structural homogeneity. A higher pyrolysis temperature saw improved yields due to presence of free radicals and cracking of hydrocarbons [53].

Research carried out by Veksha et al, showed that pure PP and PE can produce good gases for nanotube synthesis. However, the landfill plastics are usually a mix of types and quality. polypropylene, polyester, polystyrene and polyethylene terephthalate (PET) account for 80 % of plastic waste, when chemical vapor deposition was carried out in temperatures between 500 to 1000 °C the synthesis of CNTs was seen [55].

1.3.3. Graphene

Graphene is another allotrope of carbon, seen to be chemically inert, friction reducing and with good mechanical properties. Graphene is produced from sp^2 hybridised carbon atoms

packed into a honeycomb lattice with high thermal, mechanical and electrical properties, as shown in Figure 1.8 [56].

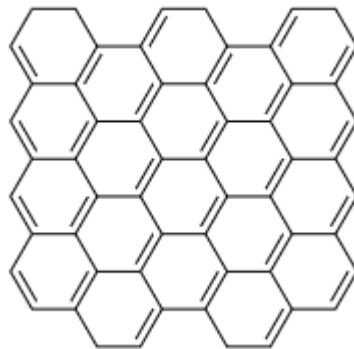


Figure 1.8. Structure of graphene (drawn on chemdraw)

Huang et al [57], showed how a chemical vapour deposition (CVD) approach could be used to produce graphene. The relative merits of the CVD process will be further discussed in Section 4. Copper foil was placed in a tube furnace and the pressure altered to reach 0.5 Pa. Hydrogen was used to purify the area before the chamber was heated to 1060 °C with a 26 °C/min heating rate, and maintained at a stable temperature for 100 minutes. Graphene was grown using 10 sccm hydrogen and 5 sccm methane for 60 min. The resultant graphene was washed with deionised water to remove contaminants [57].

Graphene can also be produced using the arc discharge approach where temperature variations can easily be increased up to 2000 °C and there is a low reported defect density. A fluorine modified graphene can be produced using a graphite rod with a CF_x powder inside as an anode and a pure graphite rod as the cathode. The arc discharge then occurs to produce the graphene. Arc discharge is simple and straightforward as an approach, whereas the CVD approach is time consuming and requires multiple steps as well as high temperatures and pressures. It also requires aggressive reagents and complex equipment [58].

The aim of adding nanomaterials into an epoxy matrix is to combine the properties of epoxy and the nanomaterials being added [59]. Polymer networks can form giant macromolecules with weak cross-links called elastomers. The inclusion of solid particles in this material can tune the properties of materials. Carbon nanomaterials are used for reinforcement fillers due to their structures, morphology and dimensionality [60]. A suggested mechanism is a

formation of filler network which results in a transmission of strength to the network which leads to the improved mechanical properties of the material. In the study dissipative particle dynamic techniques were used to study the stress/relaxation and oscillatory shear [61].

Nanosized reinforcing particles can be generated via a sol-gel mechanism by catalysing hydrolysis of alkoxy derivatives of metals such as Si, Ti or Al. Polymer nanocomposites usually exhibit better mechanical properties than pristine polymers, due to improvements in mechanical properties from the nanocomposite filler. Depending on the shape of the filler such as length to filler ratio, the state of dispersion and the chemical composition the properties of the polymer can be altered. There are difficulties in obtaining homogenous dispersion of CNTs due to the bundling occurring from the van der Waals forces.

Functionalisation of the surfaces is expected to improve interactions with polymer chains to assist in dispersion and optimise physical characteristics. The incorporated CNTs can be used to create a continuous network whilst nano-graphite did not [62].

The sol-gel method is a process that allows the fabrication of a carbon material, working as the solution evolves towards the formation of a gel-like matrix. Following formation, the gel is treated and dried to harvest a solid material. It requires low temperatures to work, 100 to 300 °C, making it an attractive approach for the production of nanoparticles [63].

A study by Bokobza et al, used nitrile rubber with MWCNTs, the CNTs used were produced using CVD and purified to 95 %, mixed with toluene at 11000 rpm to give homogeneity. The rubber was also mixed at 300 rpm for 12 hours. A 200 µm film was produced. It was found that a 3.8 wt. % addition imported a significant increase in Young's Modulus. Due to agglomerate defects, reduction in stress and strain is seen as the CNTs are not fully dispersed. It is important to determine if the dispersion rate can be improved and what processing steps can be used for optimisation. Considerations also need to be made in terms of surface modification which can be used to create interactions with polymer chains and improving reinforcing ability [64].

In a study by Agnelli et al, the relation of different allotropes of carbon and binary fillers were tested in terms of shear stresses. CNT showed positive results. CNT showed increase in relative modulus is brought about by using nanofiller in a pure matrix. Correlation was found between the interactions and the interfacial area [62]. In a study with Boonbumrung

et al, nitrile rubber was reinforced with MWCNT, conductive carbon black, carbon black and precipitated silica. The improvements caused by the filler were monitored using viscoelastic behaviour, bound rubber content, electrical properties, cross-link density and the mechanical properties. The results of testing showed reinforcing fillers were incorporated and yielded high mechanical properties. However, their incorporation caused processability issues due to the viscosity of rubber. The results also showed that a high load of filler may give negative properties, such as compression and heat build-up. The use of MWCNT as a filler showed a positive increase in tensile strength, modulus, hardness and abrasion resistance [65].

Graphene is a highly researched material, and could be used to improve mechanical properties as a filler material. It has high carrier mobility at room temperature meaning that it can easily act as an electrical and thermal conductor. Graphene-polymer composites can be produced using solution mixing and sonication but high speed shearing combined with ice cooling has also been used [57].

CNTs are one of the most researched materials when acting as reinforcing fillers. However, the surfaces need to be treated as they are smooth and devoid of any dangling bonds meaning that strong matrix-filler relationships are hard to form. This can lead to poor load transfer during deformation. Chemical modification is being used to overcome this issue and may cause a compromise in intrinsic properties. There is also an issue with inhomogeneous dispersion of nanomaterials due to van der waals forces. This may be overcome using surface treatments. [60]. The current issues with these materials are:

- The performance of materials is based on the intrinsic properties of the filler,
- Dispersion of a filler and interactions between the filler and epoxy.
- Manufacturing and moulding processes need to be improved
- Environmental issues, such as the release of BPA and other potentially harmful emissions [59].

Further research is required to limit the effects of agglomerations and to improve the interactions between the filler material and the bulk material.

The applications of these materials can be seen in Li ion batteries, supercapacitors, fuel cells and photovoltaic devices [57]. There are also structural applications in terms of materials

with requirements of high strength, stiffness, toughness and lightness as well as materials that require high conductivity and energy transfer materials [60].

1.3.4. Application of carbon nanoparticles

The current applications of carbon nanomaterials are broad and varied. From energy applications, wastewater treatment and concrete reinforcement to biological and medical uses. Research has been carried out into medical applications, such as drug delivery and imaging. Carbon nanotubes can be functionalised with different surface additions, meaning that they can be adapted to the specific needs of the targeted ailment [66]. The shape of carbon nanotubes further promotes cellular uptake which makes them excellent for drug delivery [67]. Gold nanotube caps were researched to trap the drug within the nanotube, so it is released when it is needed. Functionalisation of the nanotubes can also allow tissue engineering and repair to be carried out. Biosensing can also be optimised using carbon nanotubes, due to their shape, and small size [68]. Graphene can be used for drug delivery and bioengineering due to the physiochemical and mechanical properties [69]. Fullerenes have been utilised against HIV, by attaching anti-viral compounds to a fullerene. The unique shape of fullerenes allows an accessible molecule [70].

Energy storage is another area that has seen high levels of research due to the excellent electric conductivity of the nanomaterials. CNTs have been utilised for Li-ion batteries due to their high reversible capacity. This also allows graphene and CNTs to be useful in catalyst applications in respect to their high surface areas and thermal conductivity [71]. They are also applicable for energy storage because of their “tunability” as depending on the chosen configuration of the CNTs, the electronic properties vary [72]. Wastewater treatment utilises CNT composites as filtration systems as does desalination treatment. Due to their ability to be functionalised, they can act as catchment systems for heavy metals.

Functionalisation with sulphuric acid can increase heavy metal capture by 94 % [73]. CNTs can also withstand high acidity, salinity and temperature environments due to their chemical stability [74]. Carbon nanomaterials can also be used to improve corrosion resistance, especially within concrete where CNTs interact with calcium silicate hydrate, which are the binding particles within concrete. The large surface area of CNTs allows a high level of interaction, alongside the shape and flexibility. This means that the CNTs can form bridges and circles that can then cross any microcracks which form, preventing them from

spreading [75]. CNTs have also been observed to be effective as corrosion resistant coatings on structural steel due to their high tensile strength and conductivity. This has also led to their use as sacrificial coatings [76].

1.4. Chemical vapour deposition process

Chemical vapour deposition is the process where a thin film is formed on a heated substrate via a chemical reaction of a gaseous precursor. This deposition can be triggered by a few approaches such as the presence of a catalyst, photo-initiated chemical vapour deposition or the use of vacuum or plasma. The gaseous precursor can be generated in-situ of the reactor or as a product of an external reaction that is passed into the reactor for the chemical vapour deposition [77]. In the typical thermal chemical vapour deposition, the gaseous sample is the precursor gas to be decomposed to the desired coating which leads to the formation of the thin film. The vapour is deposited on the substrate and adsorbed where chemical reactions occur to bind the coating to the substrate. Once this has occurred, the gaseous by-products are separated from the substrate and can exit the reactor, it is essential that the by-products can leave the reactor as otherwise they limit the coating ability.

Chemical vapour deposition allows the full coverage of a substrate, and can be manipulated to a desired shape, meaning that the film can be adjusted to coat any surface shape, although the substrate needs to be thermally stable to ensure reaction will occur. To ensure an even deposition of the coating, contaminants must be removed from the substrate as these will reduce the effectiveness of the coating and lead to improper reactions which can affect the chemical properties of the coating.

Chemical vapour deposition is also used to produce semiconductors, single crystal metal oxides and silicon wafers as well as for the production of coatings [78]. In this section, the literature will only be used to consider the use of chemical vapour deposition for the formation of carbon nanoparticles since, this is the field relevant to this research.

1.4.1. Chemical vapour deposition for the formation of carbon nanoparticles

The use of chemical vapour deposition is reported as an efficient approach for the synthesis of carbon, as discussed in section 1.3.2. It is an ideal approach to synthesise the carbon

nanoparticles due to the ability to tune the shape of the produced film, as well as altering the design of the reactor to maximise the yield.

1.4.1.1. Graphene

For the synthesis of graphene, a carbon containing gas is passed over metal surfaces to trigger the deposition of carbon. This is especially effective on copper surfaces, as this led to a high yield of high-quality graphene, although promising results have also been seen on nickel and platinum. The chemical vapour deposition growth of graphene can be separated into two reaction pathways. The first pathway includes:

1. the adsorption and decomposition of the precursor
2. diffusion and deposition of the carbon species
3. separation of the diffused carbon species and
4. nucleation and growth phase of graphene,

whilst the second only follows steps (1) and (4) [77]. The two pathways are dependent on the selected pre-cursor and the temperature of the reaction.

Monolayer graphene occurs on nickel foil [78] in a self-limiting process, as confirmed through the use of Raman spectroscopy and optical microscopy. The use of a nickel – molybdenum alloy can be used as an effective substrate for a uniform graphene monolayer.

Graphene can also be deposited on copper, in both single and multilayer graphene films. A chemical vapour deposition process was selected to allow the formation of thin films, which can easily be transferred for semiconductors. Chemical vapour deposition also allows the graphene to be doped based on manipulation of the substrate selected for growth, if the template has metal nanoparticles on the surface these will become embedded in the graphene. The reaction of this follows the basic steps of carbon deposition on the substrate, as more carbon is deposited, the carbon nanostructure grows as the deposited carbon layers and the sp bonds connect leading to the formation of nanotubes.

In one study graphene was synthesised using a split-tube furnace and heated to 950 °C with a methane feedstock [79] whilst another study used a mixture of methane and hydrogen and temperatures of 1000 °C [80]. The graphene produced through these methods was seen to be high quality and tuneable, as well as easily transferred to other locations. Due to the

process of deposition, there were concerns that the oxidation products of copper would influence the nucleation density of the produced graphene. The oxidation states were determined to be CuO and Cu₂O depending on the temperature, partial pressure and oxidation times. Annealing the copper in hydrogen limits the formation of CuO allowing the formation of a graphene layer, whilst Cu₂O inhibits the carbon deposition as well as reducing the nucleation density of graphene [81]. Microwave plasma chemical vapour deposition was used as an alternative for the preparation of carbon on a copper substrate using methane as a feedstock. Three stages of development were seen:

1. pre-treatment of the substrate in hydrogen plasma for 30 mins to clean the substrate of any surface oxide
2. introduction of methane for 5 to 10 mins and
3. microwave plasma post-treatment for 5 mins at a lower microwave power.

This graphene was affected by microwave plasma etching due to the top-down growth mechanism seen, showing that this approach can allow for tuning [82]. The thermodynamics of chemical vapour deposition of graphene showed a reaction enthalpy of 91.8 ± 2.4 KJ/mol through the novel use of an independent triple loading reactor allowing the variations of parameters to be considered [83]. Further investigations into the kinetics of the deposition of the graphene layer found that molecular and atomic hydrogen would diffuse in copper with an activation energy of 0.20 ± 0.01 eV. Hydrogen dissociation will compete with methane dissociative dehydrogenation leading to hydrogen being a limiting factor in the kinetics of graphene growth [84]. Sites became blocked on the copper surface from the presence of the hydrogen, leading to inhibited growth and quality of the graphene, especially as point defects caused by hybridized sp³ C-H bonds. It is recommended that alternatives to hydrogen plasma should be investigated for the removal of contaminants on the substrate surface to ensure a high-quality graphene production.

Nickel was also explored as a suitable transition metal substrate using microwave plasma chemical vapour deposition [82]. It was found to be a better substrate due to its atomic arrangement allowing a greater deposition of the carbon layer, as well as fewer defects caused by the microwave plasma etching [82]. The kinetics of graphene deposition on the nickel film has also been investigated, and it was found that, compared to the use of a copper substrate, hydrogen recombined on the surface, preventing the point defects seen

for the copper substrates, reducing the level of defects seen overall [84]. The study concluded that the selection of the transition metal substrate is important to achieve higher quality graphene with reduced point defects. Methods to control the deposition of methane to form carbon were investigated, and promising research was carried out. It was determined that the deposition process and, by extension, the film thickness could be controlled through alteration of the electrical resistance hence affecting the solubility of the nickel surface [85].

1.4.1.2. Carbon nanotube synthesis through chemical vapour deposition

Carbon nanotubes can also be produced through chemical vapour deposition, through a range of feedstock gases, although particular success has been seen through the use of acetylene. Optimisation was carried out so it was fully understood. Again, CVD was selected as the ideal process for the synthesis of carbon nanotubes as it can be easily tuned and adjusted to ensure the correct orientation is achieved.

Camphor was used as a carbon feedstock for the production of carbon nanotubes, with a binary catalyst of Co/Ni supported with a SiO₂ mesh powder with a reaction temperature of 850 °C. The carbon nanotubes decreased in quality with a lower cobalt to nickel ratio and an increased presence of amorphous carbon was seen [86]. The ideal catalyst composition was 1:1 cobalt to nickel for a camphor feedstock. Stainless steel 304 was used for the synthesis of carbon nanotubes, the stainless steel was cleaned using acetone in an ultrasonic bath before etching in 35 to 38 % HCl was carried out and the stainless steel was heated to 850 °C for 30 mins in nitrogen. Once the substrate was prepared carbon nanotube synthesis was carried out at 700 °C with ethane as a feedstock before being held at the same temperature in a nitrogen atmosphere. An increase in the HCl etching time saw an increase in the carbon nanotube coverage from 7 % at 1 minute to 97 % at 10 minutes [87]. As the substrate is fixed, the orientation of the carbon nanotubes can be controlled, and allow an accurate investigation in the growth mechanism. A stainless-steel mesh could therefore be used to produce carbon nanotubes without any additional catalyst, making the process cheaper (although there is no discussion on the removal of the resultant carbon nanotubes from the stainless-steel surface).

Another catalyst free approach was explored using anodized aluminium oxide templates for the production of seamless nanotube pillars through continuous carbon - carbon bonding. This was carried out at a lower temperature for the stainless-steel, only 620 °C, with a carbon gas source of acetylene. The etching for the anodized aluminium oxide template was carried out using NaOH and for 48 hours. These parameters were selected based on previous optimisation experiments. The resultant carbon nanotubes were not as high a quality as those seen on the stainless-steel substrate [88]. Therefore, it can be seen that although non-catalytic approaches can be considered, they are less reliable for the high-quality synthesis of carbon nanotubes.

Traditional catalysts have also been used to produce carbon nanotubes from chemical vapour deposition. Ni and Fe were used at different conditions to determine the effect of the catalyst, temperature and feedstock on the carbon nanotubes produced. Ni and Fe were compared when carbon nanotube synthesis was carried out at 750 °C with an ethylene feedstock. The catalysts were introduced through ion sputtering so a thin layer is achieved, although the thickness of this layer was varied and seen to influence the carbon nanotube composition. It was determined that a metallic underlayer, such as Al was required for the formation of carbon nanotubes, especially for a Ni catalyst layer [89]. There did not seem to be a significant difference in the properties of the carbon nanotubes caused by the metal catalyst used.

Silicon wafers are also used for the preparation of carbon nanotubes, as they allow a cost effective, and easily transferrable, approach for synthesis the nanotubes. Silicon wafers are also an attractive option as they can be patterned to influence the growth of the carbon nanotubes. The silicon wafers were heated to 800 and 900 °C with methane and hydrogen used as the feedstock gases. It was seen that there was less sensitivity to the gas concentrations at 800 °C, whilst at 900 °C the hydrogen influenced the yield of nanotubes. A higher hydrogen concentration led to an increased production [90]. Nickel oxide was seen to produce stronger interactions with the graphitic planes of the carbon nanotubes, especially compared to copper, making it a better option for the synthesis of the CNTs [91]. A spherical NiO/Al₂O₃ catalyst was used for this with the parameters identified as (a) reaction temperature (b) flow rate of the carbon source gas and (c) the process and reaction time. Initial findings showed that, at reaction temperatures below 700 °C, there were fewer active

sites on the surface area of the catalyst, leading to less deposition, whilst a reaction temperature over 1000 °C led to the increased deposition of amorphous carbons. This is due to self-diffusion of acetylene, and is similar to the process seen during the synthesis of graphene in [77]. The effect of the precursor gas flow rate is associated with the morphology. When the flow rate was lower than 100 mL/min there was insufficient diffusion of the carbon to the catalyst particles, limiting the tubularity of the carbon nanotubes. If the flow rate was set too high then there was an increase in the amorphous carbon, although this produced the greatest yield of carbon nanotubes [91-93].

Based on these studies, it can be seen that the process of synthesising carbon nanotubes is reliant on the reaction temperature. There is a directly proportional relationship between the reaction temperature and the mean diameter of the carbon nanotubes. The precursor flow rate is also proportional to the mean diameter. However, at higher flow rates a greater yield of amorphous carbon is also seen [91, 93]. Carbon nanotubes can be synthesised without a catalyst present [87, 88] although they are of higher quality, and of a more controllable size through the use of catalysts [89, 92, 94]. The temperatures seen for the production of carbon nanotubes are seen to be lower than for graphene, showing the effect of temperature on the synthesis of the carbon nanoparticles.

1.4.1.3. Carbon nanofibers

Carbon nanofibers have also been successfully synthesised using CVD. Carbon nanofiber synthesis requires the use of a transition metal catalyst and a carbon source [95]. The catalyst particle size determines the size and graphitic structure of the nanofibers with similar growth types to carbon nanotubes, as discussed in section 1.3.2, which alters the deposition growth seen. Due to the chemical vapour deposition process, the resultant nanofiber can be doped with other metals to improve the properties, and applicability of the nanofiber [96]. Different parameters will lead to differences within the structure of carbon nanofibers, some of these are seen in Table 1.2.

Table 1.2. Different synthesis parameters to produce carbon nanofibers

Feedstock	Catalyst	Temperature (°C)	Reference
Acetylene	Cobalt on alumina	700	[97]
Hexane	Ni ₃ C	350	[98]
Acetylene	Nickel on alumina	550 - 700	[99]
Acetylene	SnO ₂ /Fe ₂ O ₃ /SnO ₂ Fe/Sn ratio of 1:2.6	700	[100]

It was found that the differences in chemical states, as well as the shape of the catalyst particle would influence the morphology and structure of the carbon nanofiber. This shows the catalyst nanoparticle influences the carbon nanofiber, and therefore, the conformation and orientation of the desired carbon nanofibers can be controlled. The temperature of the reaction also influences the structure of the carbon nanofibers, at 550 °C they were seen to be spirals, whereas at 700 °C they became thicker yet more uniform.

An alternative approach of chemical vapour deposition is the use of inductively coupled plasma-enhanced chemical vapour deposition, where an argon plasma is used to create an inert atmosphere for the deposition process. In this study, two types of catalyst were used; a ferrocene dissolved in carbon precursor and a nickel film on the substrate, which varied from silicon, glass and Pyrex. Toluene solvent was used as a source of carbon with a reaction temperature of 650 °C. The resultant carbon nanofibers were well-aligned, with the growth time seen varying depending on the catalyst and substrate [101]. The ferrocene catalyst saw a growth time of 15 mins at any substrate whilst the nickel catalyst saw a greater variance, showing that the catalyst substrate interactions can affect the synthesis of the carbon nanofibers.

Stainless-steel was used as for a catalyst free approach. A stainless-steel reactor was cleaned and then etched with 10 mL concentrated hydrochloric acid for 5 minutes before rinsing to remove the acid. A reaction temperature of 700 °C was reached with a heating rate of 20 °C/min. To provide the carbon a sample of ethanol was boiled on a hot plate, with the vapour introduced into the reactor using a carrier gas of 40 L/h nitrogen for 20 mins.

The reactor was allowed to cool to room temperature and the soot generated collected [102]. This shows a similar process to the stainless-steel reactor used for the synthesis of carbon nanotubes, as seen in [87], which, due to the similarities in chemical and physical properties, is expected. Carbon nanofibers form from sheets of angled graphene, which are caused through the use of a faceted catalyst, whereas the carbon nanotubes will grow from a more uniform surface. The etching carried out for the synthesis of carbon nanotubes was done with a stronger concentration of HCl, meaning that a smoother surface would have been attained. Therefore, the carbon nanofibers are produced from the faceted surface produced from the etching. It also reported that hydrogen in a system leads to changes in the formation of nanoparticles, due to the termination of dangling bonds at the edges of stacked graphite sheets, leading to a conversion from graphite to carbon nanofibers [103]. The nanofibers produced from the stainless-steel substrate have a larger diameter than those seen from the traditional transition metal catalysts, due to the source nanoparticle size, showing that the preparation of the nanofibers can be tuned to suit the required dimensions [101-103]. The size of the catalyst nanoparticle, as well as the orientation of the metal of the catalyst, influenced the carbon nanofiber conformation. There did not seem to be any influence of temperature on the carbon nanofibers produced, and the flow rate and type of the precursor gas appear to have less influence on the overall structure of the carbon nanofiber.

1.4.1.4. Fullerenes

Fullerenes can also be produced through the use of chemical vapour deposition, although where graphene, carbon nanotubes and carbon nanofibers all are all more clearly related to each other; fullerenes, as discussed in section 1.3.1, are a unique form of carbon.

Chemical vapour deposition is the most cost-effective and efficient process for the synthesis of fullerenes. The formation of fullerenes through chemical vapour deposition allows the fullerene to be doped with other metals, enabling tuning of the chemical and physical properties. Fullerene synthesis through the use of chemical vapour deposition requires higher temperatures than those seen for the synthesis of graphene, carbon nanotubes and nanofibers. Different parameters for the synthesis of fullerenes have been summarised in Table 1.3, below.

Table 1.3. Different parameters for the synthesis of fullerenes

Feedstock	Catalyst	Parameters	Type of CVD	Reference
CH ₄ /C ₂ H ₂	(111) faceted platinum	500 °C	Conventional	[104]
H ₂ /CH ₄ 1:0.25 ratio	Silicone substrate	50 – 60 A 2000 – 2200 °C	Hot filament (tungsten)	[105]
Ar/C ₂ H ₂ /H ₂ 2:2:1 ratio	N/A	100 W 2.45 GHz	Microwave enhanced	[105]
C ₂ H ₂ /Ar 1:5 ratio	Ferrocene	800 to 1000 °C	Conventional	[106]

There is evidence that, to promote the formation of fullerenes from this approach, there should be limited carbon containing gas, with higher hydrogen, especially compared to the formation of the carbon nanotubes, nanofibers and graphene. This may be to promote the formation of the structure of the fullerene over the deposition of amorphous carbon at higher carbon concentrations. Higher temperature conventional CVD led to the formation of onion like fullerenes with multiple layers [106]. The multiple layers formed were caused by the differentials of reactions within iron nanoparticles, and increases in deposition on these with time. As the reaction progresses, the increased deposition of graphite layers on the iron nanoparticle core leads to the formation of the “onion” like sample which was produced. To control for this, a templated nanoparticle substrate can be used [104], which will influence the growth and ensure it occurs in the desired way.

There is evidence that multiple carbon nanoparticles can be synthesised at the same time, as both carbon nanofibers and fullerenes were seen to be produced through the use of a Fe/Y catalyst with a mass ratio of 2 : 1 for Fe : Y prepared through dip coating on a copper plate. Once ready the catalyst was positioned in a furnace, for the synthesis of the interspersed fullerene and carbon nanofibers. A temperature of 800 °C was used with a gas mixture of C₂H₂, Ar and H₂ and a reaction time of 10 mins [107]. The carbon nanofibers have a diameter of 60 nm with a mesoporous structure. The pore sizes were seen to range from 2 nm to over 100 nm. The fullerenes produced through this approach are interspersed through the graphitic layers that are deposited on the catalyst, leading to distortion. This distortion continued through to the synthesised fullerenes, as they have an ellipsoidal

structure over a spherical one. The presence of argon and hydrogen has a similar effect to the microwave enhanced chemical vapour deposition, showing that these lead to the deposition of fullerenes on the surface of the catalyst. There was no discussion of the range of fullerene sizes seen. However as the reaction parameters are similar to the microwave enhanced chemical vapour deposition seen it can be assumed that there would be a similar range in the fullerenes seen [105]. It is seen that a different reaction temperature would lead to the change in formation seen with an increased deposition of other carbon nanoparticles seen. Overall production of other nanoparticles occurs, which is to be expected as the mechanism lacks selectivity and fullerenes are usually formed within soot deposited on the reactor sides.

It appears that the formation of fullerenes leads to a reduced purity, and the presence of other carbon nanomaterials are common. The highest purity yield for producing fullerenes used the template made of platinum nanoparticles. However, the highest yield in total was through the hot filament approach.

1.5. Background and environmental issues caused by textile waste

With the rise of social media, fashion trends are becoming more global, leading to increased reliance on “fast fashion” brands to produce a greater volume of textiles. The short life of these trends leads to much of this textile ending up in landfill. The rate of purchasing is predicted to increase by 67 million tonnes over 20 years, which can be used to predict that the volume of textile waste produced will also increase [108].

This rate of increase in production will exacerbate the existing environmental demands of the textile industry, leading to greater emissions of CO₂ and NO_x as well as producing more polluted wastewater. A greater rate of purchasing will lead to a greater volume of discarded textiles needing to be disposed of. Unless textile recycling capabilities improve, the majority of this will be sent to landfill which pollutes the surrounding land. Pyrolysis could be used as an approach that will allow the production of useful products that can be used for financial gain. Global textile production is set to reach 145 million metric tonnes by 2030 [109], was valued at \$1 trillion, and expected to expand at a compound rate of 4.4 % between 2021 to 2028 [110]. These increases can be attributed to changes in trends outpacing the rate of natural consumption, leading to a greater amount of waste being generated. Garment sales

grew by £17 billion in ten years in the UK alone [111], demonstrating the increased consumption and consequent textile waste generation.

In the UK 206,000 tonnes of textile waste was produced in the UK in 2018 [112], with an estimated 92 million tonnes produced globally [113]. This is expected to reach 134 million tonnes by 2030 [114]. Only 12 % of the UK waste is currently recycled [115], which means the disposal of the remainder is mainly split between landfill and incineration, although small proportions are lost during collection, processing and microfibre release into the environment. Even with the textile waste that is recycled, only 1 % of the waste is used to produce new clothes of a similar quality [115], with the rest being used for lower quality items, such as fillers or insulation [115].

Only a small proportion of textiles can be recycled to items of comparable quality due to wear and tear on the fibres and a lack of infrastructure to cope with the volume of waste [116]. Currently most direct quality textile waste recycling plants focus on cotton. However synthetic fibres now comprise 80 % of produced garments [115] so this requires further optimisation of recycling approaches. Fibre blends of three, or more fibre types, are also not suited for direct quality recycling [117]. This limits the amount of fibres that can be used for direct fibre-to-fibre recycling, increasing the demand on alternative disposal techniques. Textile fibres can be separated into two broad classifications; natural and synthetic fibres [118]. As shown in Figure 1.9, natural fibres come from plants or animals, such as cotton or wool [119]. Synthetic fibres are produced from polymer materials such as polyester and nylon [120].

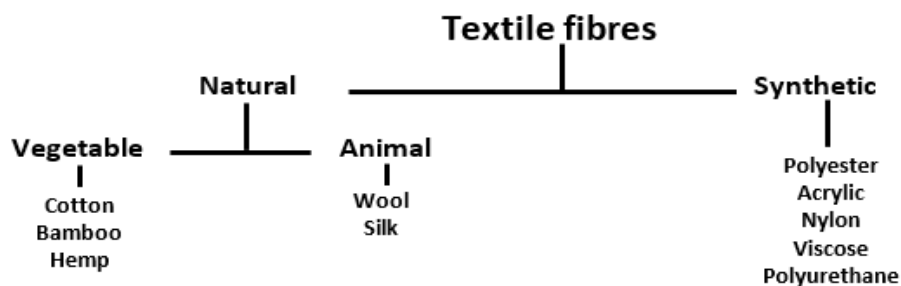


Figure 1.9. Taxonomy of textile fibres [119]

Cotton, after scouring and bleaching, is 99 % cellulose, which is a macromolecule of repeating glucose molecules linked through glycoside bonds, as shown in [121]. Due to the

ring structure within cellulose, they can form a rigid, supportive coating. A primary wall forms with the natural dimensions of the fibre. Helical layers of cellulose form the inner secondary wall with a hollow core through the fibre, as seen in Figure 1.11 **Error! Reference source not found.**[122, 123]. This shows that the fibres are flexible and easy to dye as they are porous.

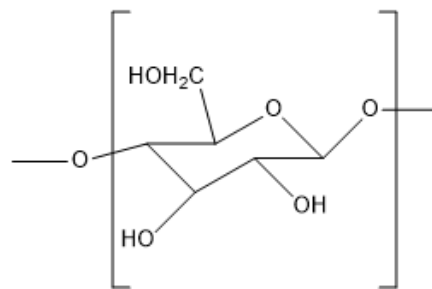


Figure 1.10. Structure of cellulose

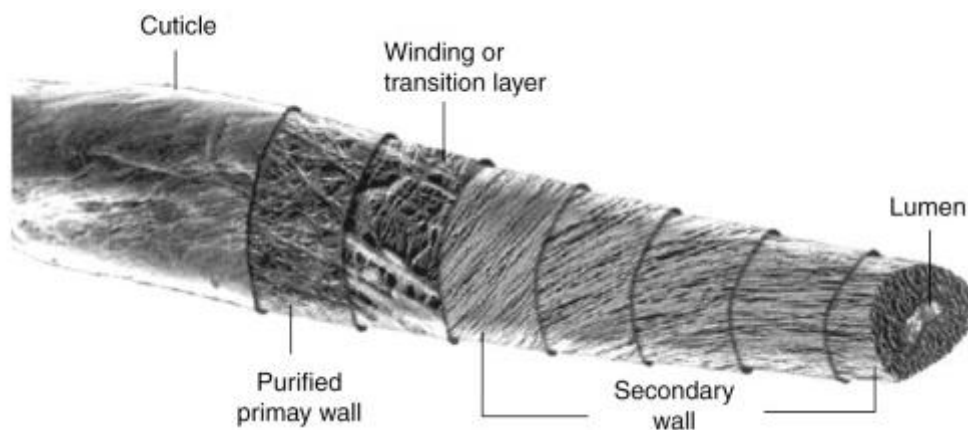


Figure 1.11. Schematic representation of cotton fibre [122]

Cotton forms within the cotton boll, Figure 1.11. When the plant reaches maturity, the boll opens and cotton fibres dry. The cellulose chains within the cotton fibres are held with hydrogen bonds leading to closely packed molecules, shown in Figure 1.10 [124].

Polyester, on the other hand, is one of the most popular textiles for garment use, found in 60 %vol of garments for sale globally [108], as well as accounting for 75 % of synthetic fibres produced world-wide [125]. Polyester can be combined with cotton to form polycotton, with a combination of 65 % cotton 35 % polyester being a common combination. Polyester is normally made by reacting dimethyl terephthalate with ethylene glycol in the presence of an antimony catalyst at temperatures between 150 – 210 °C to form a monomer [123]. This

monomer is combined with terephthalic acid at 280 °C and extruded to form ribbons of material. Once dried, the material is chipped and heated to 265 °C and placed in a spinneret to form polymer fibres [123].

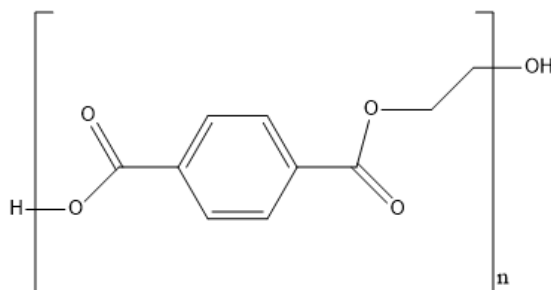


Figure 1.12. Structure of polyethylene terephthalate (PET) (drawn on chemdraw)

One of the most common forms of polyester used in clothing is polyethylene terephthalate (PET) which can easily be recycled into fibres, as the material can be melted and reformed. The presence of a benzene ring, as shown in Figure 1.12, leads to a rigid structure, higher melting points, 250 °C, and a greater strength. During synthesis, water is released as a by-product, similar to all polymerisation reactions. PET can be recovered from plastic water bottles or waste polyester [126]. It was found that recycled-PET fibres had similar properties to virgin-PET [127].

Nylon is another common synthetic material, commonly produced through the condensation of diamines with diacids. The common form, nylon 6,6, is formed from polycondensation of 1,6-diaminohexane and hexandioic acid [128]. The structure of the product is shown in Figure 1.13.

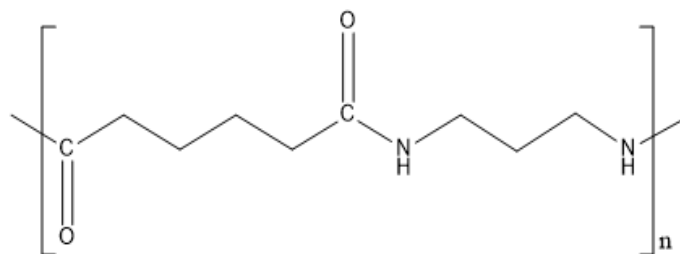


Figure 1.13. Structure of nylon 6,6 (drawn on chemdraw)

Due to the presence of amines, the reaction releases nitrous oxide [129], which is 264 times more potent than carbon dioxide [130] at trapping heat. Although, due to the properties of

the nylon, it can be recycled however [131], reducing the environmental load. Nylon is typically found in yarn materials alongside acrylics.

Acrylic materials, often formed from acrylonitrile, are resistant to mould, mildew and wrinkling, making them a popular choice for clothing [132]. The fibres are comparable to wool, and accounted for 20 % of global fibre production in 2001 [133]. Acrylic fibres are formed by continuously spinning fibre-forming substances, based on the monomer acrylonitrile, shown in Figure 1.14 against a plate. As acrylonitrile contains a cyano group, polymerisation leads to the release of cyanide, which causes health issues and environmental impacts. When the fibres contain more than 85 % acrylonitrile they are referred to as acrylic [134].

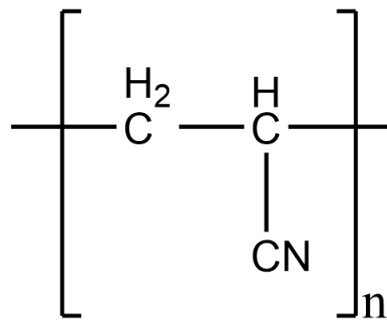


Figure 1.14. Structure of acrylonitrile, the monomer used to produce acrylic material (drawn on chemdraw)

Polyurethane (PU) comes in many classes, such as thermoplastic, flexible, rigid and water-borne, and is usually used in carpets, and other textiles such as insulating materials. PU is formed from isocyanate and a polyol molecule, usually containing two or more isocyanate and hydroxyl groups [135].

The properties of PU depend on the starting molecules, as the amount of cross-linking can alter the properties of the final material [136]. Figure 1.15 shows the structure of polyurethane formed from Di-isocyanate and polyol. During synthesis, CO₂ and urea are produced. PU materials contain high levels of cross-linking, ensuring the majority of PU products do not soften when heated [137]. As the synthesis of polyurethane is exothermic, it can be assumed that more bonds are made during synthesis than are broken. During synthesis, different additives can be added, including catalysts, such as amine catalysts,

crosslinkers, colourants and fillers. The catalysts can deblock isocyanates, decrease the relevant reaction temperature and enhance the efficiency of the reaction [137].

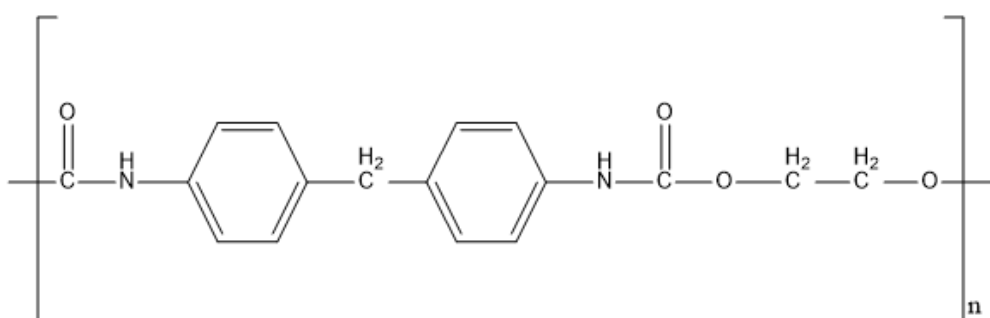


Figure 1.15. Structure of polyurethane (drawn on chemdraw)

As each discussed fibre has distinct properties and is in use for textile production in alternative combinations then different disposal options have to be developed for specific classes of textile materials.

As shown in Figure 1.13 and Figure 1.15, both Nylon and polyurethane will produce nitrogen containing gases when heat treated due to the presence of amine groups. This means that for these two types of textiles, mechanical recycling is a better option than temperature driven approaches.

Figure 1.12 and Figure 1.15 show that both PET and PU contain benzene rings, which increases the energy requirement for bond breaking, meaning pyrolysis at higher temperature will be required to fully utilise the material. Cellulose as shown in Figure 1.10, is comprised of a hexacyclic ring structure which will require less energy to break compared to benzene. This shows that cotton, which is mainly comprised of cellulose as stated earlier, will be able to be utilised at lower temperatures whereas polyester will require higher energies to overcome the benzene ring bonds.

Due to the unbranched, and relatively simple structure of Nylon, it can be assumed that, alongside cellulose, it would require less energy to break the bonds within the molecule. Due to the bond energies seen, simple C-C bonds will break first, before C-O, C=O, C≡N and benzene, these are illustrated in Table 1.4 [138] [139]. This shows that, during heating, intra-chain scissions will occur in the fibres due to the different bond energies.

Table 1.4. Bond enthalpy for different bonds seen in the chemical structures of textile fibres [138 – 139]

Molecule	Bond enthalpy (kJ mol ⁻¹)
C-C	348
C-O	358
N-H	391
O-H	463
Benzene	518
C=O	799
C≡N	891

1.5.1. The environmental impact of textile waste

1.5.1.1. Solid waste

The

1.5.1.2. Liquid waste

Cotton

Textiles

Synthetic dyes can include azo dyes, shown in Figure 1.16, acid dyes, shown in Figure 1.17, base dyes and reactive dyes. These are comprised of functional groups such as carboxylic acid, amine and azo groups [154]. Natural dyes are less desirable as they have poor colour fastness, poor reproducibility and use metal mordants [155].

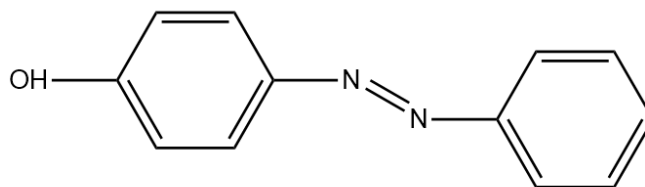


Figure 1.16. Structure of orange Azo dye, used for colouring textiles (drawn on chemdraw)

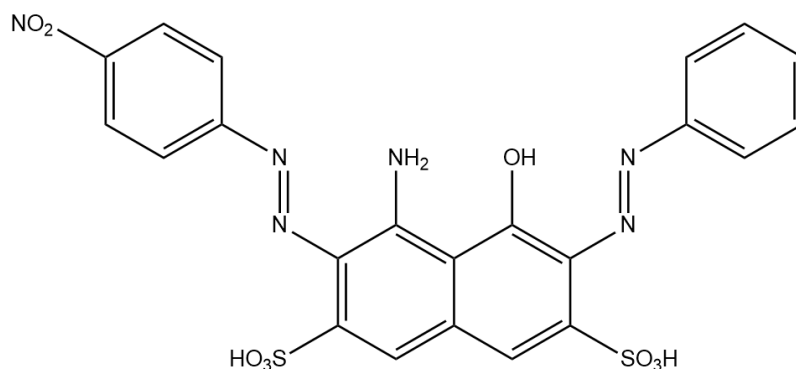


Figure 1.17. Structure of Acid Black 1, for dyeing textiles (drawn on chemdraw)

1.5.1.3. Gas waste

Due

The

Due

1.5.2. Current approaches for textile waste disposal

1.5.2.1. Landfill

In

Table 1.5. Tonnes of textile waste sent to landfill per country per year

Year/Textile	USA	UK	Italy	China	Global
1980	2104669				
1990	3873679				
2000	5697120				
2005	6867388	180000			
2010	8073944				
2012		350000		20000000	
2015	9561727		266948		

2016		300000		
2017	10115110		26000000	92000000
2018	10251188	206000	465925	

1.5.2.2. Recycling natural and synthetic fibres

Polyethylene

The

Recycling

1.5.2.3. Incineration

Incineration

This

1.6. Pyrolysis process

Pyrolysis

Currently,

Pyrolysis

1.6.1. Types of pyrolysis

There

Slow

Fast

Flash

Both

1.6.2. Pyrolysis of textiles and biomass

Textile

Cotton,

Table 1.6. Parameters for the pyrolysis of cotton textile waste

Pyrolysis	Heating	Products	Reference
700	10	74 wt.% oil 13.5 wt.% gas 12.5 wt.% char	[183]
600	5	29.49 % oil	[196]

		54.26 % gas	
		16.25 % char	
500	300	16 % char	[197]

Catalytic
Polyester,
Other
Another
It

1.7. Catalysts; synthesis, uses and supports

All
Catalysts

Catalysts can be classified as either heterogeneous or homogeneous depending on the phase of the reaction. As illustrated by Figure 1.18, heterogeneous catalysts are typically solid and used in a liquid or gas reactions whilst homogeneous catalysts can be liquid or gas and are used in either liquid or gas reactions respectively.

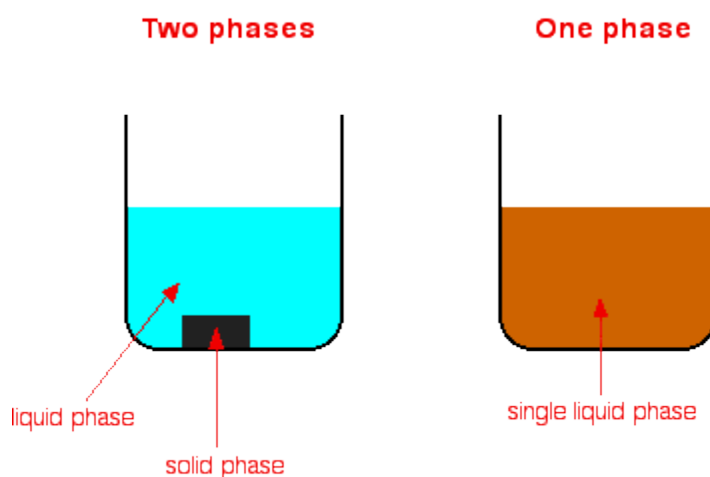


Figure 1.18. The difference between a heterogeneous (two phase) and homogeneous (one phase) catalyst [204]

According to surface adsorption theory, as shown in Figure 1.19, catalysts follow five main stages of reaction:

Stage

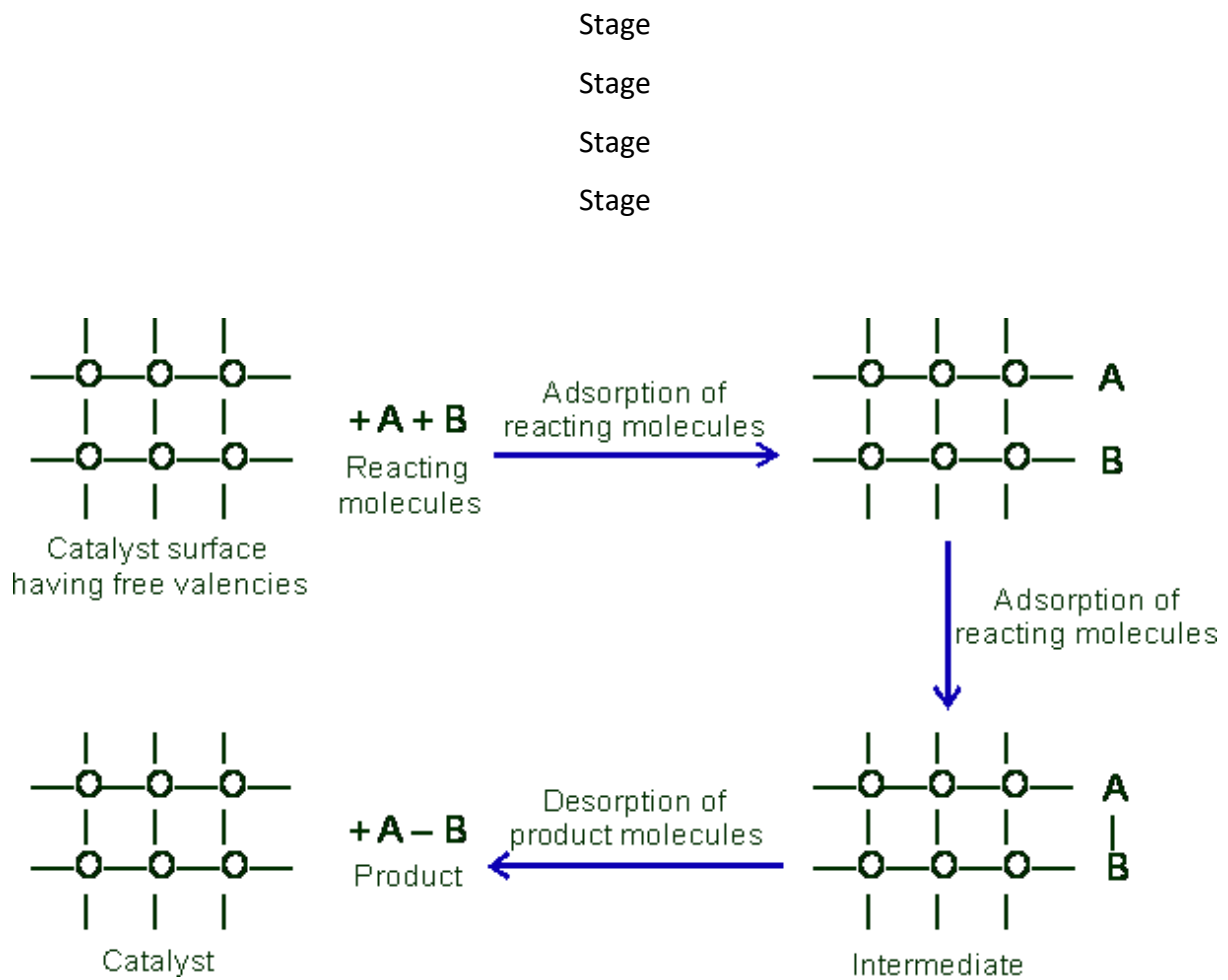


Figure 1.19. Schematic representation of the steps of surface adsorption theory [205]

A

1.7.1. Common active metals for catalysis

The

Group

Nickel

As

Bimetallic

Copper

1.7.2. Catalyst support structures

Catalysts

Zeolites

Cobalt

An

Carbon has been studied as a catalyst support due to the large specific surface area, ease for chemical functionalisation and ability to have metal nanoparticles imparted on the surface. Depending on the pore size of carbon they can be microporous, mesoporous or macroporous, which can be utilised to adapt the material to the correct dimensions. Figure 1.20 shows the difference between microporous, mesoporous and macroporous. Carbons have crystalline structures but this is short-range and lacks stacking direction. Carbon nanotubes are promising options for templates of metallic nanoparticle deposition to form architectures appropriate for supports of heterogeneous catalysts. Carbon aerogels have been developed from the nanostructured carbons from carbonising organic aerogels from the sol-gel method. These have a tunable pore size, pore volume and surface area, depending on the processing and synthesis conditions. Carbon is also cheaper than alumina and silica supports, whilst maintaining tunability [219]. Carbon nitride was specifically studied as a catalyst support, due to its classification of being a wide band semiconductor. It is promising as a photosensitive catalyst material. It is also promising for the manipulation of defects which may act as active sites. However, further research proved the extensive synthesis steps and high processing costs, may prevent this becoming a widespread catalyst until further work can be undertaken [220].

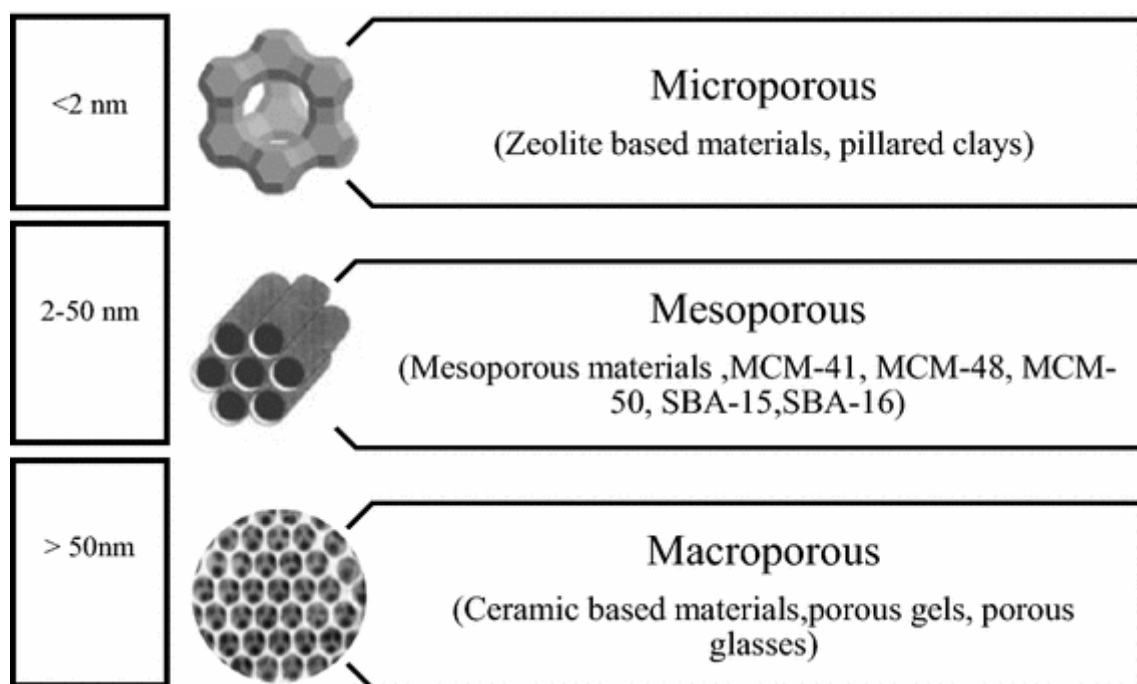


Figure 1.20. Difference between microporous, mesoporous and macroporous materials [221]

Polymer

1.7.3. Traditional heterogenous catalyst synthesis

The

1.7.3.1. Co-precipitation

Co-

- constant pH and
- variable pH

The

Choice of base is important as there may be reactions between the metal cations. For example, Cu^{2+} forms soluble complexes with aqueous ammonia meaning that Na_2CO_3 is more appropriate. The choice of metal salt provides potential poisonous anions. Nitrates are favoured as any nitrate anions are easily decomposed during calcination. Both chlorides and sulphates can cause surface retention on the catalyst. As different cations precipitate at different pHs it is important to ensure that cations are precipitated by the chosen base, as shown in Figure 1.21. This varies on the individual metal and the form of salt used.

Therefore, for Ni it can be seen that for both hydroxides and carbonates a pH of around 8 would be appropriate. Aging occurs where the dissolution and re-precipitation of the cations happens in the reaction. The precipitate is left in contact with the precipitating solution for longer than required. This can affect its crystallinity, performance and particle size. More aging will typically lead to a larger particle size.

The

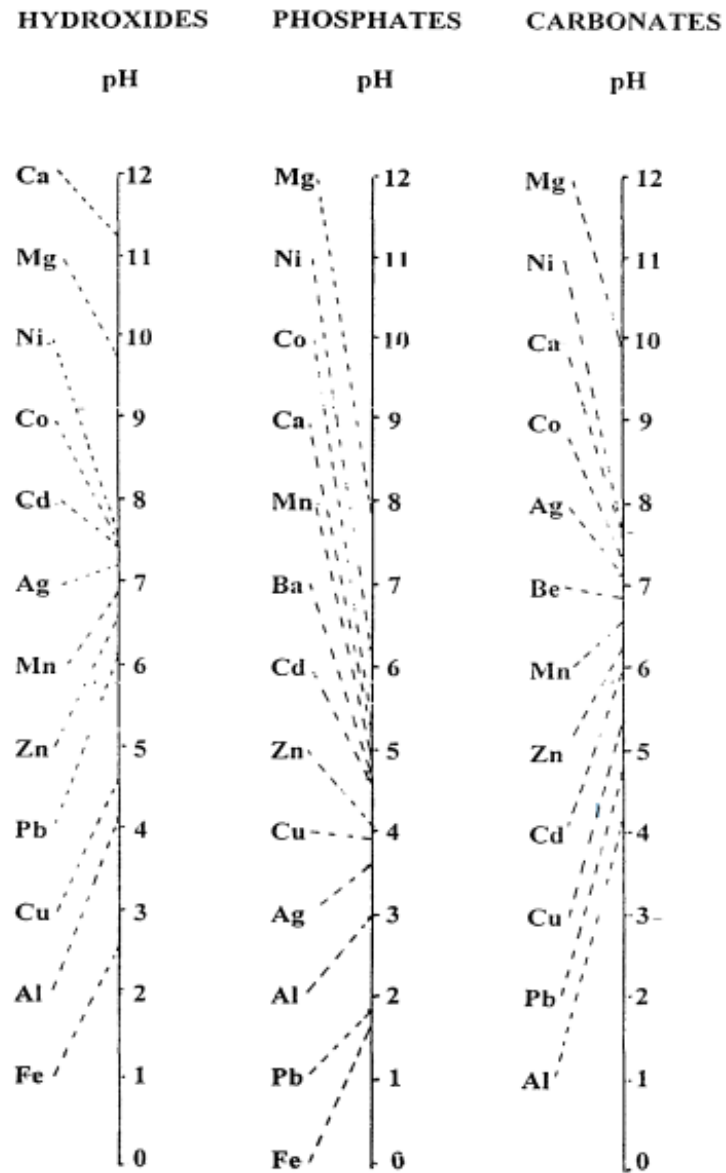


Figure 1.21. Different precipitation points for metal salts for co-precipitation at room temperature [224]

1.7.3.2. Sol-Gel

A

- water to alkoxide ratio
- number and nature of alkyl groups
- size of the cation
- the pH and
- the temperature [224].

As shown in Figure 1.22, different drying conditions lead to different gel formations and each of these will have different properties. During the drying phase, care must be taken to ensure that the pores are not shrunk, which would reduce the surface area. The advantages of sol-gel include low thermal conductivity and good structural and textural stability, even at high temperatures [225]. However, even dispersion of the active material can become difficult.

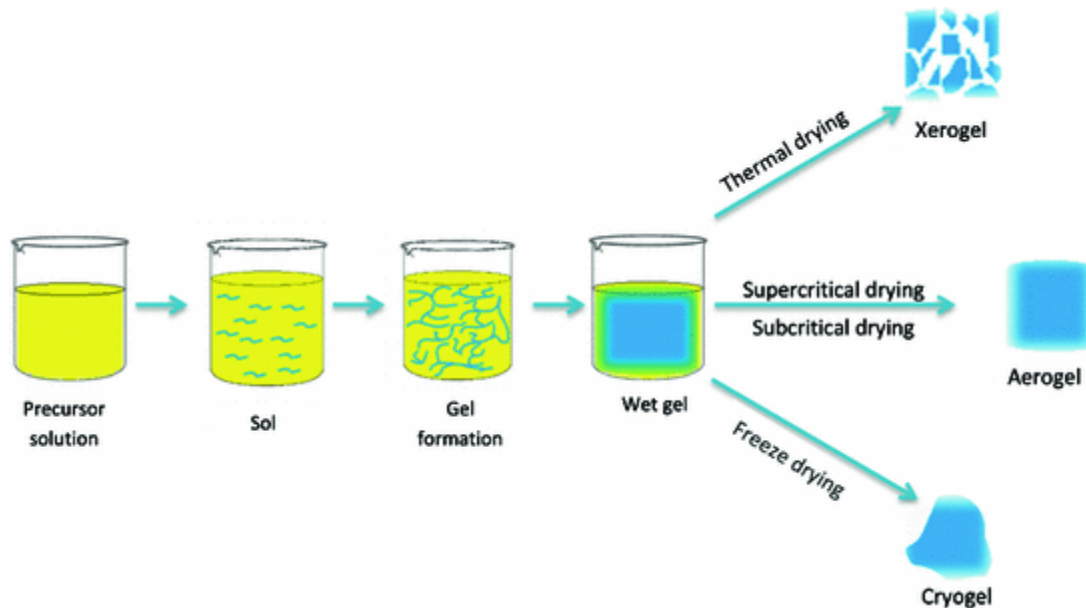


Figure 1.22. The process for creating sol-gel materials and the conditions required for producing a xerogel, aerogel and cryogel formation [226]

Recent

1.7.3.3. Deposition precipitation

Deposition

Deposition

Deposition precipitation can be carried out using one of three procedures;

- A precipitating agent is added to a support suspended in a solution of precursor of an active species
- A solution of precursor is added to a suspension of a support in an alkali solution
- A solution of a precursor is mixed with the alkaline agent to form colloidal compounds which are then brought into contact with the support.

Deposition

Deposition

When

1.7.3.4. Impregnation

Impregnation

1.7.4. Deactivation mechanisms of catalysts

Whilst

Poisoning

Fouling

Sintering

Leaching

Surface

Attrition

1.7.5. Catalyst selection

It

As

Co-

Therefore,

1.8. Thesis aims and objectives

This thesis aims to:

- Study the effects of pyrolysis type, temperature, residence time and carrier gas presence on the products seen from the pyrolysis of different textile waste feedstocks. This will allow an understanding of the effectiveness of the use of pyrolysis to produce carbon containing gases for use in chemical vapour deposition.
- Optimise the chemical vapour deposition process for the carbon containing gases, methane, carbon dioxide and carbon monoxide, produced through pyrolysis of different textile waste samples. This will consider the impact of reaction temperature, flow rate and catalyst type as well as the different textile waste feedstocks, on the rate of carbon deposition.
- Determine the type of carbon deposited on the catalyst through chemical vapour deposition. Identification of the carbon type allows a greater understanding of how

to tailor the composite material to optimise the improved reinforcement seen in the mechanical properties of the carbon-epoxy composite.

- Produce a composite containing a matrix and the produced carbon to determine the impact of increased carbon loading on the mechanical properties of the composite material. This will involve the use of bisphenol A and different wt.% of carbon loading.
- Determine the effectiveness of this approach for the reinforcement of offshore wind turbine blades. Different mechanical testing will be required to determine this, as well as weathering tests so the longevity of the samples can be guaranteed.
- Produce carbon nanomaterials from textile waste materials in order to augment the mechanical and physical properties of a composite material, which could be used to improve the performance of offshore wind turbine blades.

Chapter 2 - Experimental methodologies

2.1 Catalyst Preparation

Depending

Table 2.1. Mass of nickel metal salt needed for the preparation of catalysts

Mass	wt.	Mass	wt.	Mass
0.5g	70 %	1.7326g	30 %	2.0830g
0.5g	80 %	1.9728g	20 %	1.3800g
0.5g	90 %	2.2277g	10 %	0.6940g

Catalysts

The

The

The

2.2 Pyrolysis

Pyrolysis

A

After

The

For

Different

2.3 Chemical Vapour Deposition

Chemical

A

Further

Due

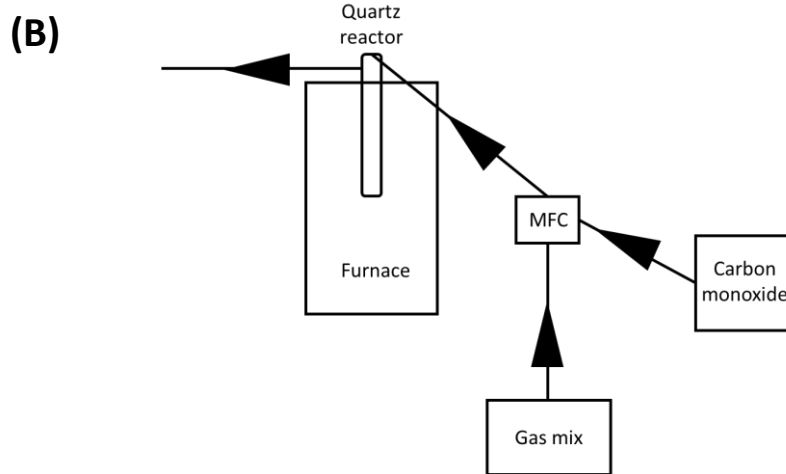
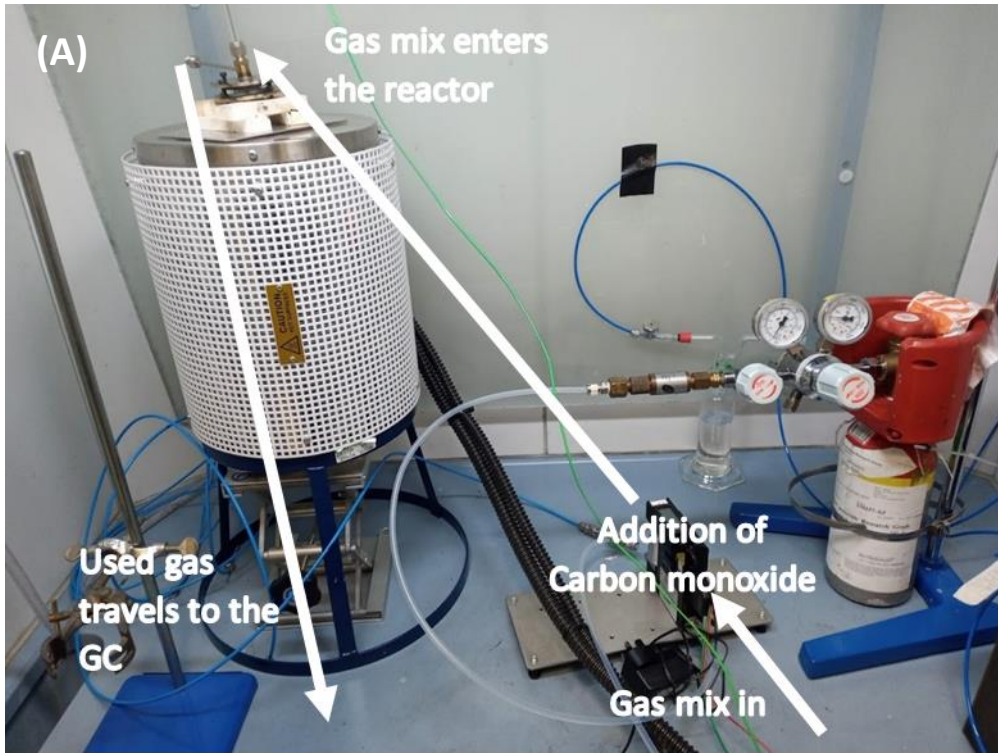


Figure 2.1. (a) Reaction set-up for the CVD of carbon from a synthetic gas mix containing carbon monoxide, carbon dioxide, methane and hydrogen (b) schematic for the reaction set up

2.4 Carbon composite

The

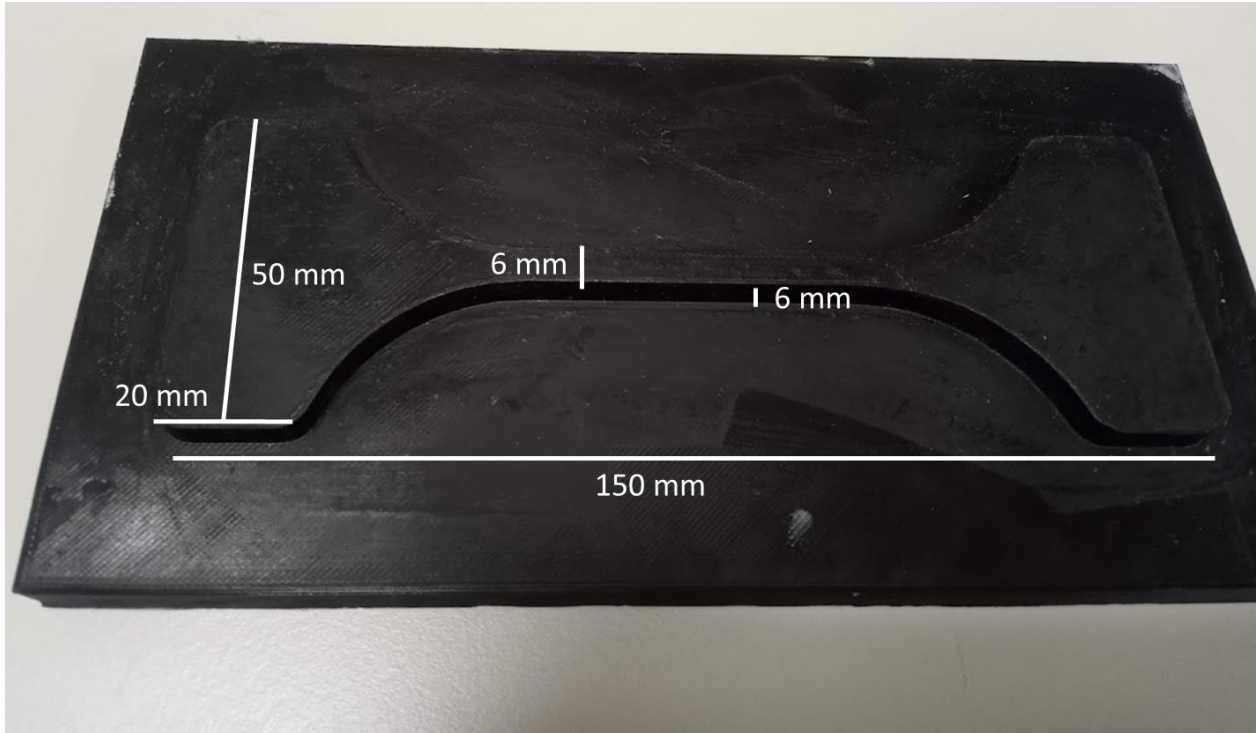


Figure 2.2. 3D printed mould negative showing the dimensions of the composite sample

For

Table 2.2. Required masses of carbon for different epoxy composite compositions

Sample Name	Mass of carbon required (g)
Pure epoxy	0
3.5 wt.% carbon	0.619
2 wt.% carbon	0.354
0.5 wt.% carbon	0.088

Once

For

2.5 Characterisation

Characterisation

2.5.1 Activity of catalyst

The

The

2.5.2 Gas Chromatography with thermal conductivity detector

Gas

A

In

Once

2.5.3 Gas chromatography-Mass spectroscopy

GC-

Gas

Mass

The

2.5.4 Scanning Electron Microscopy

Microscopy

Scanning

Samples

2.5.5 Energy dispersive X-ray spectroscopy

Energy

Energy

2.5.6 Transmission Electron Microscopy

Transmission

Transmission

2.5.7 Thermogravimetric analysis (TGA)

Thermogravimetric

TGA

TGA

Sections

2.5.8 Porosity and surface area (BET analysis)

Porosity

Before

Brunauer-

The isotherm for the surface area can be determined using the BET equation [266], shown

$$\frac{1}{x_m c \left(\frac{p}{p_0} \right) - 1} = \frac{1}{x_m c} + \frac{c-1}{x_m c} \left(\frac{p}{p_0} \right)$$

Equation 1.

$$\frac{1}{x[(p_0/p)-1]} = \frac{1}{x_m c} + \frac{c-1}{x_m c} \left(\frac{p}{p_0} \right)$$

Equation 1.

Where:

- X is the weight of nitrogen adsorbed (mg)
- (p₀/p) is the given relative pressure
- X_m is the monolayer capacity

Monolayer capacity, and BET constant, are calculated from the isotherm plot, as depicted in

$$x_m = \frac{1}{s+i} = \frac{c-1}{c_s}$$

Equation 2

[267]. This defines the amount of adsorbate which is needed to occupy all adsorption sites as determined by both the chemical nature and structure of the adsorbent.

$$x_m = \frac{1}{s+i} = \frac{c-1}{c_s}$$

Equation 2.

Where:

- S is slope
- I is intercept
- C is BET constant

Total surface area, S_t, can be calculated, using $S_t = \frac{x_m L_{av} A_m}{M_v}$

Equation 3 [266].

$$S_t = \frac{x_m L_{av} A_m}{M_v}$$

Equation 3.

Where:

- L_{av} is Avogadro's number
- A_m is the cross-sectional area of the adsorbate (0.162nm² for nitrogen)
- M_v is the molar volume (22414 mL)

Once the total surface area measurements have been calculated, the specific surface area can be calculated. This allows the calculation of the surface area that is related to the mass of the sample. Specific surface area, shown in $S_{BET} = \frac{S_t}{a}$

Equation 4, is a comparable measure and allows samples to be compared in relation to surface area [268].

$$S_{BET} = \frac{S_t}{a} \qquad \text{Equation 4.}$$

Where:

- S_t is the total surface area (m^2)
- A is the mass of the sample (mg)

Surface

2.5.9 Fourier transform infrared spectroscopy (FTIR)

Infrared

Infrared

Each

Infrared

The

Fourier

2.5.10 Powder X-ray Diffraction

Powder

All samples must be in powder form, ideally with a smooth, homogenous surface. Despite the sample appearing to be a uniform powder, there will be small variations in the orientations. A large quantity of crystallites with the desired orientation will allow for constructive interference with incidence rays. Constructive interference will lead to the diffraction pattern of the crystalline or amorphous sample. Bragg's law, $n\lambda = 2d \sin\theta$

$$\text{Equation 5 } n\lambda = 2d \sin\theta$$

Equation 5 explains how refraction angles are only observed when the interplanar distance is equal to an integer multiplied by the x-ray wavelength [271].

$$n\lambda = 2 d \sin \theta$$

Equation 5.

where:

- λ is the wavelength of the x-ray (nm)
- n is the order of reflection
- d is the interplanar distance (nm)
- θ is the diffraction angle for the associated peak ($^{\circ}$)

X-ray diffraction uses an x-ray source, Cu radiation for all samples in this thesis, leading to photoemission to produce vacancies in core electron shells, similar to EDS. Each energy change brought about through outer shell electrons filling these vacancies produces an x-ray. This emitted radiation is angled towards a monochromator, and passed over the powder sample. As the x-ray beam rotates around the sample, all constructive interference is collected. Once the diffractogram has been collected, a miller index can be used to determine the lattice planes, giving useful information on the structure of the crystalline structure. The miller indices will allow the determination of orientation of the crystalline structure, as well as identification of the sample. The crystallinity of a sample can be determined through the width of the observed peaks. A broader peak shows a more amorphous sample, whereas a sharp peak shows high crystallinity. This allows the determination of the structure of the sample, as well as the individual structures for each component.

Once the diffractogram has been created, Miller Indices can be applied to display the atomic arrangements of the resultant materials. These are known as the hkl values, each relating to a different point on the axis of the cubic outline. For example (111) relates to fractional intercepts at 1,1,1 whilst (220) relates to $\frac{1}{2}$, $\frac{1}{2}$, ∞ . The unit cell can be calculated through the addition of the miller indices and then fitted to certain rules. These can be attributed to peaks, allowing the cubic structure of the crystal to be identified. These can be one of seven crystal systems; cubic, tetragonal, orthorhombic, rhombohedral, hexagonal, monoclinic and triclinic, each having different axial lengths and angles. The lattice parameter of the sample, a , can also be calculated, which in turn can be used to calculate the lattice structure of the crystalline sample. This allows the size of the unit cell to be calculated as well as confirming the unit cell identification.

2.5.11 Dry ashing of the sample for trace analysis

Ashing of the sample was carried out in a carbolite oven set to 600 °C with a heating rate of 25 °C/min and a hold time of 3 hours. This was carried out in oxygen to ensure the combustion of all organic components. These conditions were selected based on standard usage, to make sure full combustion of organic components. There were no ashing agents added to the sample ensuring that the ash was available for further analysis without any contamination. Sample sizes of 1.543 g and 1.5943 g of the 91 % polyester 9 % lycra and cotton textile waste were analysed. The sample size selected was based on the size of the crucible used for this analysis. Once the samples had cooled and the ashes were weighed, they were measured again and the inorganic component contribution could be determined. The weight percent contribution can be applied to the elemental analysis to allow the determination of the contribution of oxygen to the sample.

2.5.12 Inductively coupled plasma mass spectrometry (ICP-MS)

Inductively coupled plasma mass spectrometry (ICP-MS) used Agilent 8800 ICP-MS to determine the percentage composition of the catalyst samples. ICP-MS analysis was carried out in both air and hydrogen atmospheres to account for the presence of oxides. Compared to the EDS analysis ICP-MS will determine the elemental composition of the whole sample, and not just the surface level. To digest the metal oxide for testing, a sample was digested in 6 mL of aqua regia (4.5 mL HCl and 1.5 mL HNO₃ (both high purity from Romil)) in CEM XP-1500 plus vessels before being heated to 170 °C in a CEM Mars 5 microwave digester following an alumina process where the samples underwent a 15 min ramp up to 200 °C with a power of 1600 W. Once the peak temperature was reached it was held for 20 min before cooling. The temperature and pressure were constantly monitored.

Once the sample has been digested and is in solution, it is ionised through the plasma source, decomposing to the component elements and then into ions. These ions are skimmed from the plasma through the use of a skimmer, interference cones and extraction lenses. Off-axis ion lens are implemented to remove photons and neutral ions to reduce the background noise of the sample. Kinetic energy discrimination causes larger polyatomic ions to lose energy faster than analyte ions, removing these larger, less useful particles to be removed from the sample beam. The beam of ions travels into the quadrupole of the mass spectrometer and the ions are separated on the mass-to-charge ratio. This ensures that only

the selected ions will travel to the detector for analysis and reporting. Intensities of the detector signals are related to the number of ions formed in the plasma which reach the mass spectrometer detector. To ensure accurate quantification, external calibration using standards of the desired metals is carried out, in this case a nickel and aluminium standard (ROMIL Nickel 1000 ppm PrimAg and ROMIL Aluminium 1000 ppm PrimAg) were used.

2.5.13 Elemental analysis (CHN)

Proximate elemental analysis was carried out using a LECO Truspec CHN Combustion analyser, with a furnace temperature of 950 °C or the FISONs instruments EA 1108 CHN with the same furnace temperature. Sample sizes were between 50.00 and 60.00 mg. A weighed sample is dropped into a heated combustion furnace, combusting the sample. This converts any carbon, hydrogen or nitrogen in the sample to CO₂, H₂O and N₂ respectively. These gases are carried through into the detector systems with an inert carrier gas. Independent IR detectors are used for the simultaneous detection of carbon and hydrogen whilst nitrogen is measured using a thermal conductivity detection system.

Following analysis, the weight percentages of each element are given allowing the accurate comparison of the composition. Due to other contaminants within the sample, the use of filters, scrubbers and other absorbents are required to protect the internal mechanisms from damage.

To determine the oxygen content within the sample, Equation 6 is used.

$$\text{Oxygen (\%)} = \text{C(\%)} + \text{N(\%)} + \text{H(\%)} + \text{Ash(wt)}/10 \quad \text{Equation 6.}$$

Where;

- C is the wt.% carbon
- N is the wt.% nitrogen
- H is the wt.% hydrogen
- Ash is the weight of the ash produced through the combustion of the sample

2.6 Composite testing to determine mechanical properties

2.6.1 Tensile strength

A LLOYDS instrument EZ50 with a 50 kN load cell was used to carry out the tensile tests on samples. Nexygen plus was used to collect data for postprocessing. A load rate of 250 N/min was used. For the samples tested post-accelerated weathering a Testometric M350 10CT tensile tester was used with a rate of 2 mm/min.

The Lloyd instrument EZ50 is a universal material testing machine, shown in Figure 2.3, allowing a range of tests to be carried out on it. A dumbbell shaped sample was inserted into the serrated grips. The sample was lowered into the lower clamp to ensure a secure fit in the machine. Once the sample was set up, a new batch measurement was set up using Nexygen plus software, allowing the required load and machine parameters to be set. The force seen from the machine was tared to allow the accurate measurement of the sample. Once the sample is placed under tensile strain, the machine loads the sample at the set load rate. Each material has a maximum load that it can withstand before failure occurs, and once this point is reached the test will end. This can be used to determine the Young's Modulus of the sample, as well as to calculate the strength of the sample.

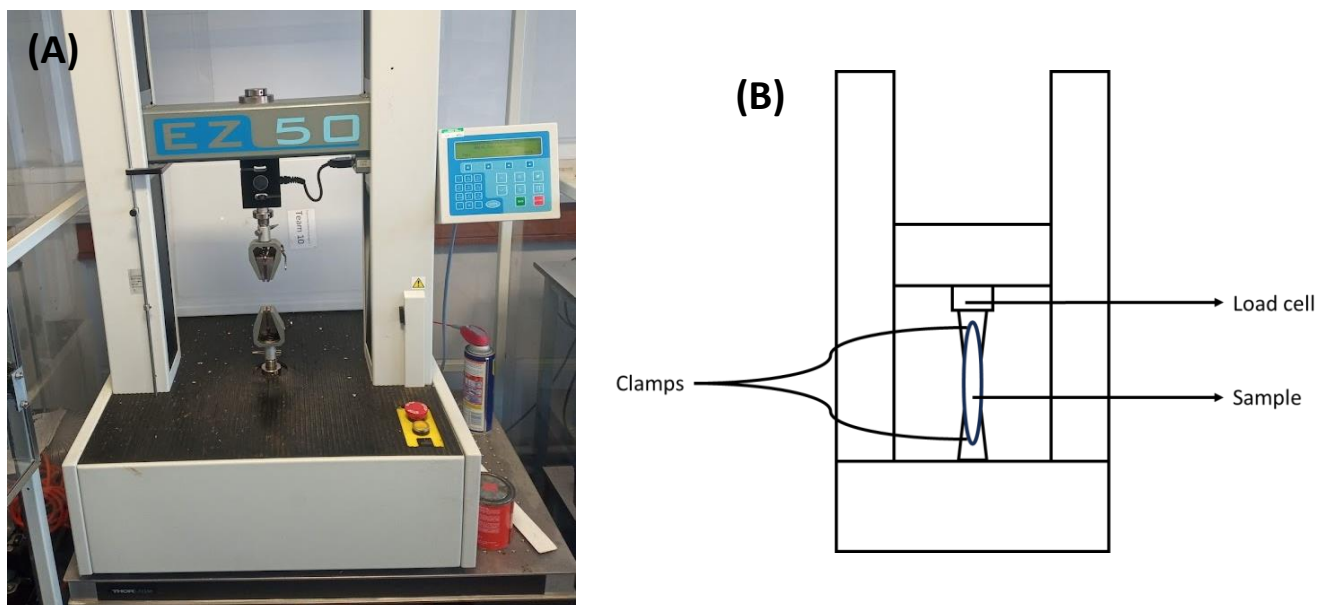


Figure 2.3. (a) LLOYDS instrument EZ50 with a 50 kN load cell set up for tensile testing (b) schematic view of the LLOYDS EZ50

Tensile testing allows the determination of tensile strength, the maximum load a sample can withstand whilst being stretched in plane. When the material is subjected to small stresses,

the atomic bonds are stretched; when the stress is removed, the bonds relax. This elastic deformation is reversible as the material can return to the original shape. At higher loads, the planes of atoms start to slide over each other, leading to permanent deformation, known as plastic deformation [272].

Elastic strain leads to linear portions within the stress strain graph. When the stress increases towards plastic strain the plot will stop being linear and the strain will continue to affect the sample following the removal of the load. At the point between plastic deformation occurring, and the fatigue point being reached, both elastic and plastic strain contributes to the total strain experienced by the sample.

During testing, the gauge of the sample undergoes loading. After the initial maximum is achieved, all deformation will occur in a small region and continual elongation of the sample will be caused by propagation of the deformation region. Different materials will show different deformation patterns following the application of load. A brittle material will not start to deform, and will just shatter, whilst a more ductile material will form a neck.

2.6.2 3-point bending

A LLOYDS instrument EZ50 with a 50 kN load cell was used to carry out the three-point bending tests on samples. Nexygen Plus was used to collect data for postprocessing. A load rate of 100 N/min was used.

The sample was carried out using the same universal material testing machine as described in 2.6.1, although for three-point bending tests the sample is horizontally supported on two points, 6 cm apart, with the load cell applying pressure in the centre of the gauge. By controlling the load rate, the flexural properties of the sample can be determined. The deflection of the sample is measured as the load is applied, which can be used to calculate the flexural modulus. Varying parameters are measured, such as applied load, distance from the load cell and also time, allowing a full understanding of the effect of loading on the sample.

The initial part of the resultant graphs shows the reversible deformation, occurring due to pressure applied, as a linear section. As the load increases, the elastic strain starts to overlap with plastic strain leading to irreversible deformation occurring. Once the plastic strain leads

to material fatigue, the material will fail. A sudden decrease is seen at the point of failure, determining the loading capacity of the sample.

To ensure all results are comparable, the parameters need to be maintained. Therefore, the loading rate, position of the supports, length and width of the sample as well as cross sectional area of the sample all need to be maintained. Any defects within the material, such as air bubbles or micro-cracks, will lead to a reduced flexural strength.

For isotropic, homogenous materials, the flexural modulus of elasticity will be equivalent to the Young's Modulus, whilst inhomogeneous, anisotropic materials will not necessarily be comparable. Composite materials for example, contain combinations of materials which can lead to small variations in the loading strength.

2.6.3 Accelerated weathering

Accelerated weathering was carried out to ISO 12944-9:2018 standards using a QUV SE Spray with solar eye control with a fluorescent tube manufactured by QLab Corporation to determine the ability of a sample to withstand UV and weathering tests, mimicking external conditions [273]. The salt spray chamber used was a Liebisch S400 M-TR 400L with a domestic freezer that was adapted to run at -20 °C .ISO 12944-9:2018 is typically a test used to determine the effectiveness of coatings on a test sample, but can be adapted to test bulk materials, such as the epoxy and composite materials produced throughout this research.

The accelerated weathering test process set was conducted in cycles, each lasting 168 hours. The testing carried out considered four cycles to give a greater chance of degradation, and whilst accelerated weathering cannot be linked to real world applications, a better performance, for a longer time, would indicate a better performance. A UVA 340 lamp used with a spectral wavelength range from 290 to 400 nm was used to apply UV radiation. Condensation was added through a heated water-tray, and condensation is ensured through the use of air cooling at the back of the samples. Cycles of UV exposure and condensation are carried out for three days at 4 hours for each with the UV period being carried out at 60 °C and condensation section being carried out at 50 °C. Following exposure to the UV and condensation cycle, the samples will undergo exposure to salt spray, produced by dissolving sodium chloride in a minimum of grade 3 purity water to produce a concentration of 50 g/L, and the pH of the solution adjusted so it falls between

6.5 and 7.2. This solution was sprayed onto the test samples at a continual rate for a further 72 hours at ambient temperatures. The samples were then rinsed with deionised water before being exposed to low temperatures of -20 °C for 24 hours. For some samples, scratches can be applied to see how the internal structure is affected by the weathering. However, this is usually only done when the surface of the material is covered in a coating, so in the case of the produced samples, this is not necessary.

Accelerated weathering can be used in conjunction with other mechanical tests to determine the effect of weathering, and corrosion on the mechanical properties of the sample selected. This is primarily selected to ensure that the weather resistance of samples can be compared through known parameters. Whilst these known, and controllable parameters can lead to comparable results, they can also be used to alter the atmosphere based on the environment that the sample material will be exposed to. This can involve changing the UV wavelength, increasing the temperature or increasing the low temperature region.

Chapter 3 - Pyrolysis, and characterisation, of textile waste

3.1 Background to the textile waste and characterisation approaches

Alternatives to landfill for the disposal of textile waste have increased in popularity in order to limit the quantity sent to landfill, as well as to recover useful resources. Pyrolysis is an option that is increasing in popularity, with different types of textile giving differing product profiles. Pyrolysis occurs due to the thermal degradation of a feedstock causing bonds to degrade, producing gas, oils and leaving a char behind [186, 193, 194, 197]. By analysing both the unreacted, and reacted chars, the changes caused by pyrolysis can be mapped and the process can be adapted depending on the desired products. The pyrolysis of textile waste will also lead to the production of pyrolysis gas and oils, which can also be captured for further interest [198, 201]. Some lab-scale studies have considered catalytic pyrolysis [158, 201], but in the interest of this experiment only thermal pyrolysis is of interest, as it is a cheaper alternative, and catalytic pyrolysis did not improve the product yields significantly. Thermal pyrolysis is a more financially attractive process as it does not require the use of catalysts.

Analysis was carried out on both the unreacted textile samples, as well as the resultant products. Initially thermogravimetric analysis (TGA) was used to determine the effects of thermal treatment on the textile waste, as well as providing the base temperature to start pyrolysis at. The TGA used a thermal gradient to fully decompose the material. During pyrolysis three main products were seen; chars, oils and gases. Gas chromatography (GC) was used to identify and quantify the gases produced. Whilst gas chromatography-mass spectrometry (GC-MS) was used for determining what liquid constituents were present at differing temperatures. The pyrolysis chars were analysed using scanning electron microscopy (SEM) alongside energy dispersive x-ray spectroscopy (EDS) to show the structures and elemental composition, which was supported by elemental analysis, whilst Fourier-transform infrared spectroscopy (FTIR) was used to identify bonding patterns, and how these change with the changes in pyrolysis temperature. Finally, nitrogen physisorption was used to determine the surface area and pore size and volume of both the chars and the unreacted textile waste.

During pyrolysis, there were three proposed sampling methods; injection, peristaltic pump and carrier gas. Following experimentation, it was seen that both injection and peristaltic pump sampling led to increased nitrogen content in the gas output. It was decided that the

use of argon as a carrier gas, whilst potentially leading to some dilution, would be a more accurate representation of the gas composition, as all components should be reduced by the same amount.

The textile waste samples were determined, based on the attached labels, to be 91 % polyester and 9 % lycra (Sainsburys TU clothing brand, leggings with a purple and grey dye) and 100 % pure cotton (The White Company, white bedsheets). The sampling method consisted of utilising waste clothing from the researchers. Pyrolysis of these textile samples will allow an understanding of the process by which the feedstock will influence both the gaseous products and the components seen within the liquid phase. The choice of feedstock will also influence the char porosity and physical properties, which will be determined through characterisation of each of the products formed through the pyrolysis of these waste textile samples. Two pyrolysis approaches were considered; slow and fast. Slow pyrolysis is also referred to as stepped pyrolysis in this study, where the sample was held at a set temperature for 20 minutes before the temperature was increased by 50 °C, as this gives a heating rate below 20 °C/min it can be referred to as slow pyrolysis [191, 192]. The fast pyrolysis, or as referred to in this research fixed temperature pyrolysis, was carried out at higher initial temperatures, with an increased heating rate of 49.5 °C/min, fast pyrolysis is seen to favour gas and oil formation over char development [182, 185, 187].

3.2 Thermogravimetric analysis, and resultant kinetics, for different textile waste samples

3.2.1 TGA analysis of 100 % Cotton textile waste

The TGA data collected from cotton textile waste showed that the onset temperature was 300 °C, as seen in Figure 3.1, before a steep weight loss section starting at 350 °C cumulating at 400 °C. This shows that there are no volatile materials, and minimal moisture in the sample, as can be seen through the one-step weight loss.

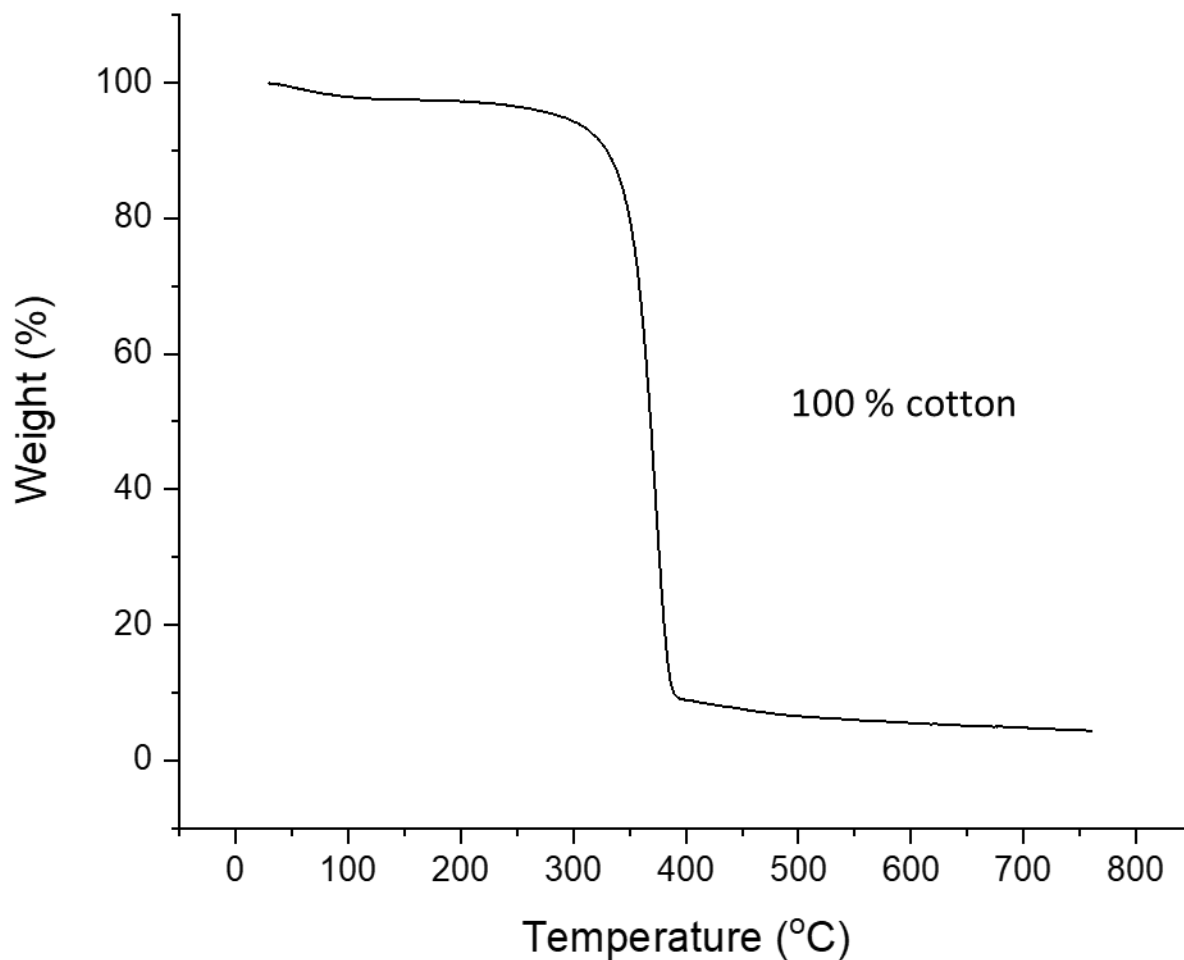


Figure 3.1. Thermogravimetric analysis curve for 100 % cotton sample

The obtained TGA data allowed the calculation of different temperature points, which are calculated from changes in mass, these are presented in Table 3.1. T_{onset} is the point at which weight loss begins, and whereby pyrolysis will start to occur. T_{hl} is the half-life where 50 % of the mass is seen to have been lost, showing the midpoint of the reaction, as seen in Table 3.1, this is at 368.78 °C. The end point temperature, T_{end} , is calculated from the changes in mass, where the mass changes cease. From the mass remaining at T_{end} it can be assumed that the material is predominantly comprised of organic materials.

Table 3.1. Thermogravimetric Analysis results of 100 % cotton

Level	Temperature (°C)	Weight (%)
T_{onset}	300	94.2
T_{hl}	368.9	50.0

T _{end}	693.5	4.8
------------------	-------	-----

This data shows that a preliminary investigation into the effects of pyrolysis should begin at 300 °C, as this is where primary weight loss step begins, although there is an initial weight loss at 100 °C which can be attributed to moisture loss. It would be expected that most activity would be seen in the region of 300 - 400 °C because this is where there is a clear weight loss step.

Experimental data allowed the determination of the activation energy through the Kissinger method, which was found to be 19.18 kJ/mol. A limitation of the Kissinger method is that it assumes that the reaction is zero order, which can apply to this reaction as the rate is independent of the concentration. A greater initial mass of the cotton textile waste will not increase, or decrease, the rate of reaction. The DTG curves of the textile waste samples at different heating rates can be seen in Figure 3.2, there is one weight change step, with the greatest change in mass occurring for the 5 °C/min heating rate, whilst the 10, 15 and 20 °C/min heating rates did not cause significant differences in the weight loss step. This is consistent with Figure 3.1, where there is a single degradation step seen. There is a slight secondary weight loss peak seen at around 440 °C, which as the first peak at 5 °C/min is at a lower temperature than the other three heating rates may show that there are in fact two weight change steps, which become one at the higher heating rates. As the peaks show negative % weight loss with time it can be seen that mass loss occurs with the increasing temperature. The weight loss step seen in Figure 3.2 lines up with the main loss in Figure 3.1 which is expected, although it appears, that for the higher heating rates the mass loss DTG peak appears towards the end of the TGA weight loss step.

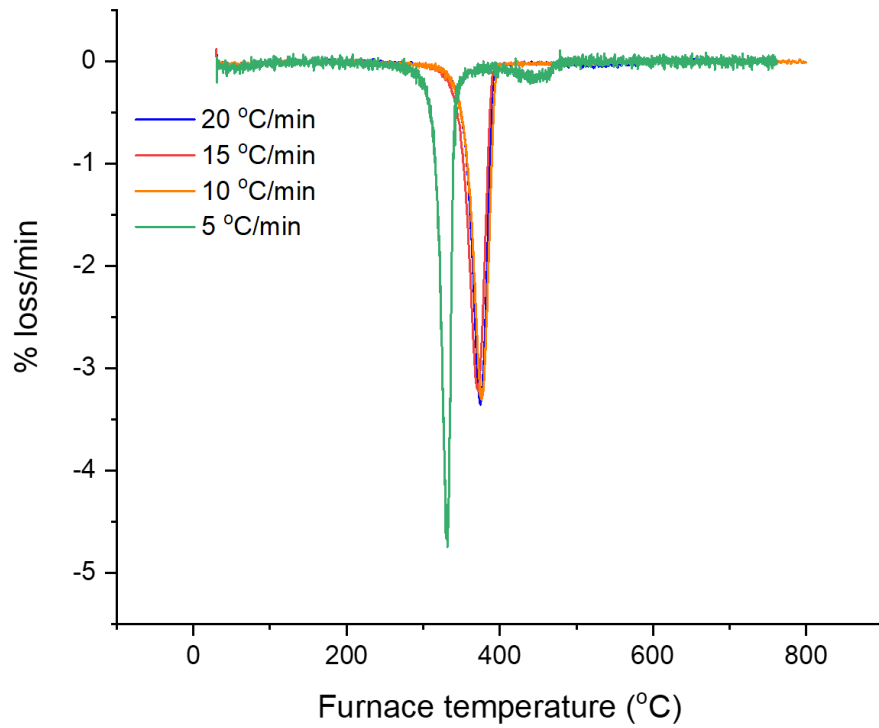


Figure 3.2. DTG curves for the different heating rates of 100 % cotton textile waste material.

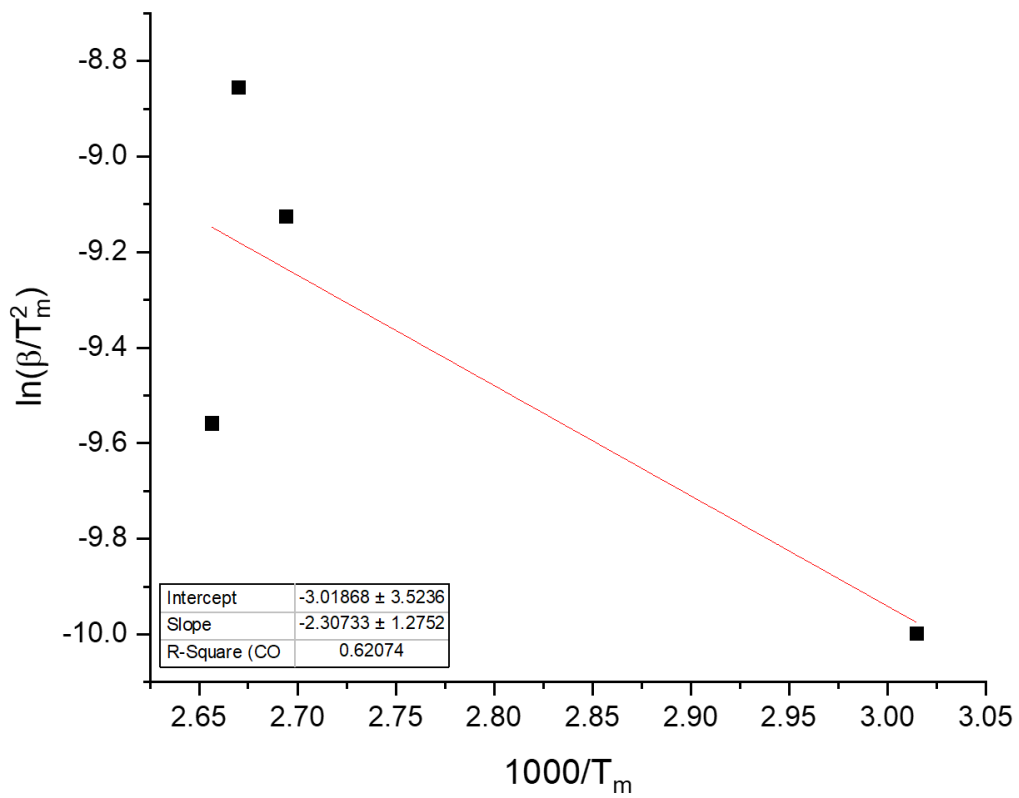


Figure 3.3. Kissinger plot for the determination of activation energy for 100 % cotton textile

The activation energy of the cotton textile waste was calculated using the slope of the Kissinger plot in Figure 3.3. The calculation of these points used the peak temperatures seen in the DTG plots, this further shows that the peak temperature of the 5 °C/min sample was lower than that seen for the other heating rates.

3.2.2 TGA analysis of 91 % Polyester 9 % lycra textile waste

TGA analysis was carried out on the polyester/lycra sample. Weight loss starts to occur at 390 °C and a steep weight loss is seen from this point before termination at 475 °C, as displayed in Figure 3.4, similar to Figure 3.1, there is no evidence of volatiles within the sample.

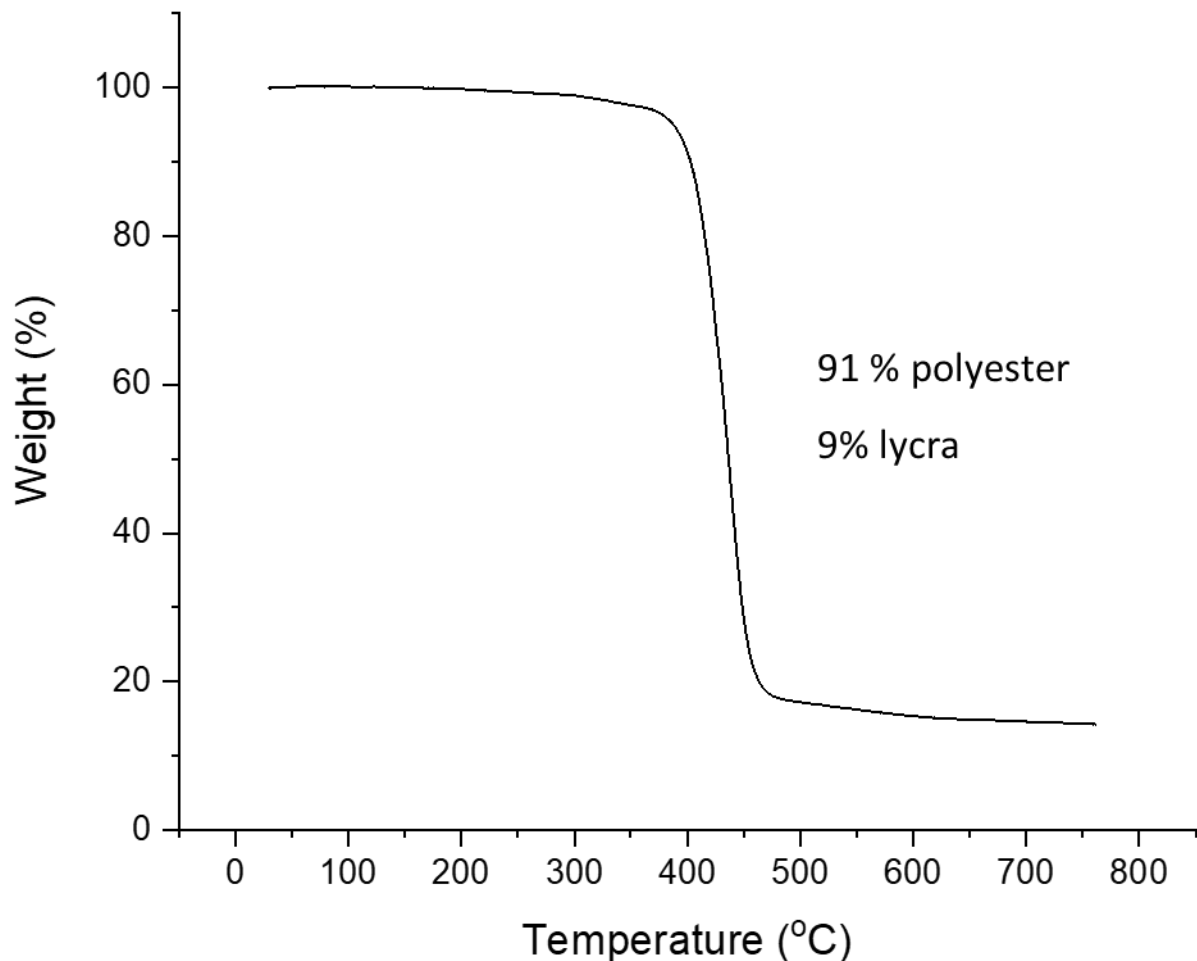


Figure 3.4. Thermogravimetric Analysis curve for 91 % polyester and 9 % lycra

The specific temperature points are seen in Table 3.2. The final weight percentage seen at T_{end} shows a higher mass of ash compared to that seen in Table 2.2. This is attributed to a higher presence of inorganic matter within the sample. The polyester sample was dyed

whilst the cotton sample was not, this may have influenced the inorganic matter remaining after the thermal degradation of the samples. As dyes are predominantly synthesised with inorganic compounds, Section 1.5, they will lead to a greater presence of inorganic materials.

Table 3.2. Thermogravimetric Analysis temperature results for 91 wt.% polyester and 9 wt.% lycra

Level	Temperature (°C)	Weight (%)
T _{onset}	390	94.5
T _{hl}	436.6	50.0
T _{end}	761.5	14.3

Based on the data seen, the initial pyrolysis temperature for pyrolysis exploration should be selected to be 390 °C, with most activity being seen between 390-490 °C. It is expected that the initiation temperatures will be higher for the polyester/lycra mix due to the higher bond enthalpies seen. This means the samples require a higher energy input to overcome these bonds, leading to the release of gases and oils.

The activation energy of the polyester and lycra textile waste sample, 28.68 kJ/mol, was calculated through the same process as for cotton with the Kissinger plot shown in Figure 3.6. DTG curves were plotted for the polyester material and were found to occur in one main weight loss step, although compared to Figure 3.2, there are other features within these, showing a more complex weight loss. These cannot be separated into peaks, even at 5 °C/min and so it must be considered as a singular peak. The weight loss peaks seen in Figure 3.5 match the weight loss step seen in Figure 3.4. The peak temperature of the 5 °C/min heating rate was seen to be 420 °C whilst the other three heating rates show peak temperatures around 440 °C, which similarly to that of cotton occurs nearer the end of the TGA weight loss step.

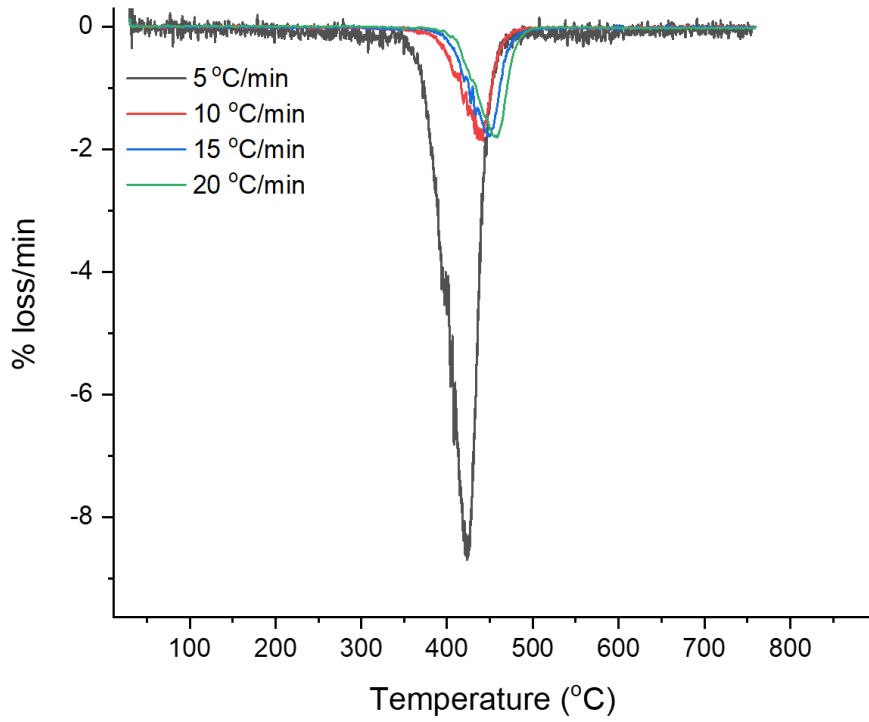


Figure 3.5. DTG plots for 91 % polyester 9 % lycra at different heating rates

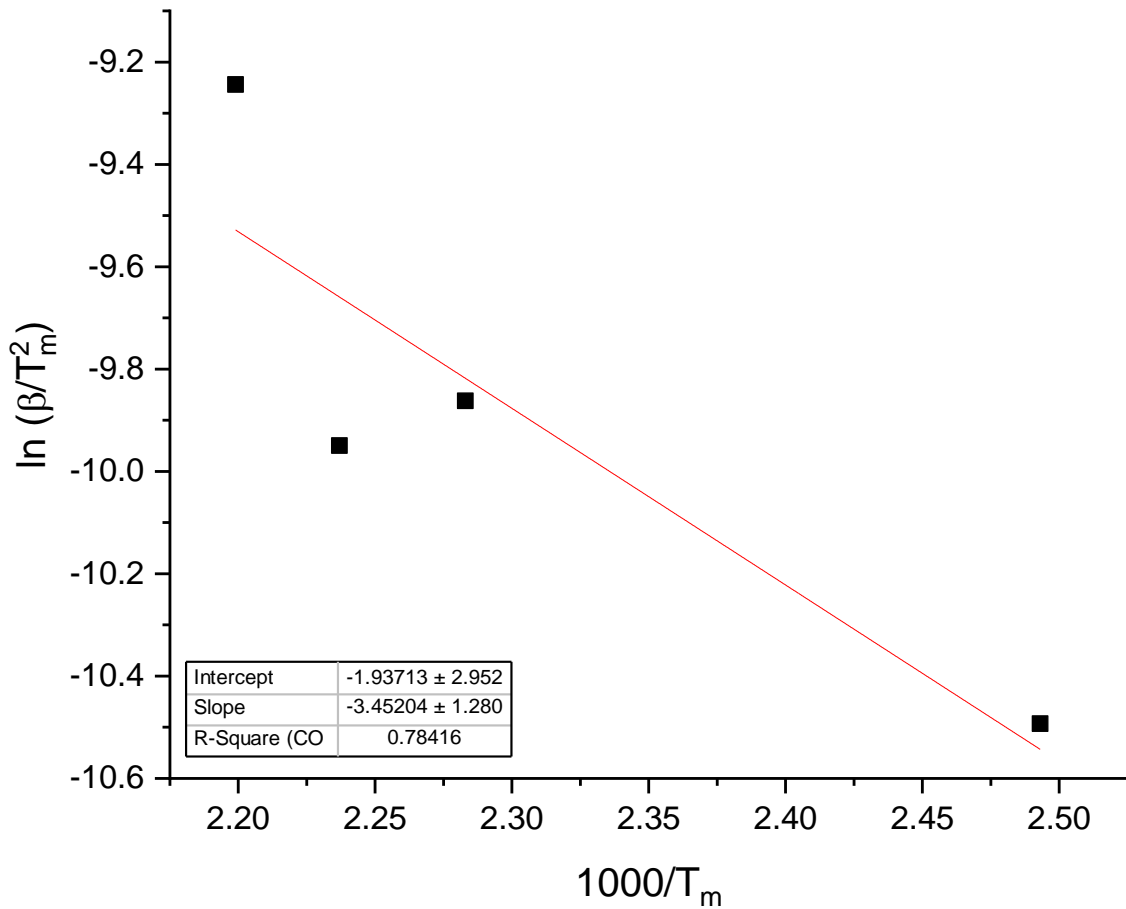


Figure 3.6. Kissinger plot for the 91 % polyester 9 % lycra textile waste sample

Following the identification of the kinetics for the pyrolysis of the polyester/lycra textile waste, the rates of the reaction can be seen, alongside the activation energy, these can be used to present an understanding of how well the reaction progresses with an increase in parameters. In this case, a higher heating rate affects the activation energy. The cotton sample has a lower activation energy than the polyester textile waste, this matches with the TGA data which shows that there is a weight loss curve earlier than that seen for the polyester textile waste sample.

3.3 Gas chromatography to determine the concentration of gas products following pyrolysis of textile waste samples

Gas chromatography was used to identify the gases produced following pyrolysis. Although they cannot be quantified in terms of volumes, they can be quantified in terms of percentage contribution. Therefore, it can be used to determine the relative concentrations of gases, allowing a comparison between different data sets. There were peaks seen for water, and some unknown materials, it is understood that these may be heavier chain hydrocarbons, such as ethane, or acetylene however, as these could not be accurately identified they were assumed to be negligible.

3.3.1 Different sampling approaches for determining the gas concentration in a pyrolysis sample

Initially no additional sampling approaches were implemented, and the evolved gases were allowed to flow from the reactor to the gas chromatographer, however this was seen to be inefficient and the sample could not be accurately ensured to represent the gas phase as accurately evolved. As it was important to determine how the gas phase varied with the reaction time, a different approach was required. The evolution of gases was important as it allowed the monitoring of the reaction progression, as well as allowing the determination of the length of time required to fully pyrolyse the sample.

As stated in section 2.2 the three considered sampling approaches were direct injection, peristaltic pump and the use of a carrier gas; either nitrogen or argon. Due to a greater quantity of feedstock, these reactions were carried out on cotton textile waste at 400 °C with testing being carried out every 15 minutes. The key requirements for the ideal sampling approach are; 1) to allow regular testing to be carried out, 2) to prevent

contamination of the sample, and 3) to ensure a constant flow of pyrolysis gas to be sampled. To monitor these objectives, gas chromatography was used to identify the pyrolysis gases and to determine their relative concentrations.

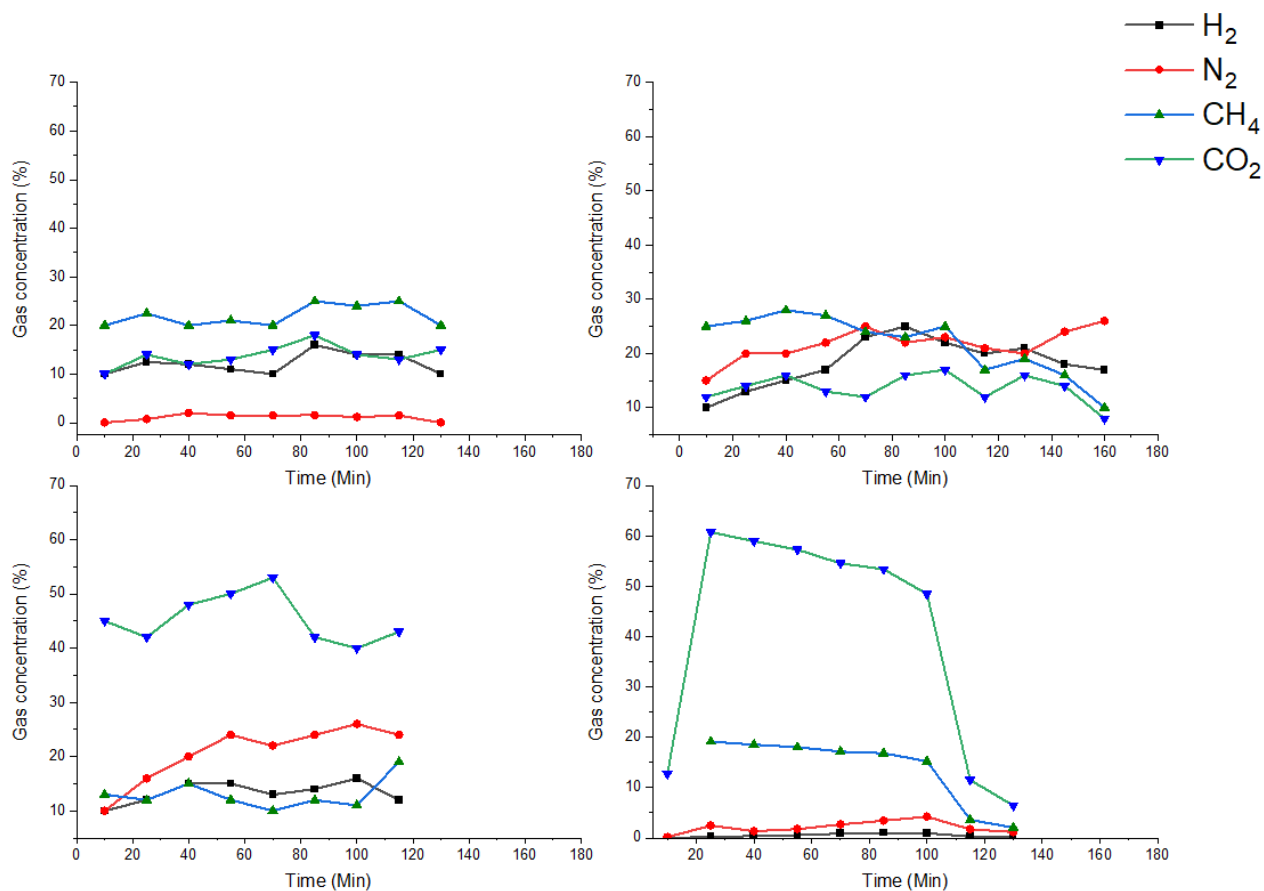


Figure 3.7. The effect on the gas sampling approach on the relative concentration of gases produced where (A) is the evolved gas (B) is the use of a peristaltic pump (C) is using a syringe and (D) is the use of a carrier gas, in this case Ar was used. The gas balance is made of the carrier gas.

A gas syringe was used to take regular samples from the pyrolysis reaction. The needle was inserted into the outlet port of the reactor and a 10 mL sample was drawn, and injected directly to the injection loop, whilst the needle was left in situ. Following injection into the gas chromatographer, the presence of oxygen could be seen, indicating that this method led to the intrusion of air into the pyrolysis reaction, shifting the reaction from pyrolysis to combustion. This was therefore deemed to not be an effective approach for gas sampling. As seen in Figure 3.7, the nitrogen concentration following the use of a syringe is the highest for any approach. As nitrogen is not present in high proportions within the structures of the textile waste, it can be seen that this is an inefficient method for accurately sampling the

gaseous output of pyrolysis. The pierced tubing was replaced and the pyrolysis output was connected to the gas chromatographer, a peristaltic pump (Pharmacia Fine Chemicals Peristaltic Pump P-3) was connected to the outlet of the sampling loop to ensure that the gas was drawn into it. The pump was set to rotate clockwise with a speed of 500 rpm. The sample was injected as usual to the gas chromatographer, and it was seen that there was a large amount of nitrogen and oxygen. Therefore, it was concluded that these settings were too strong and were causing atmospheric air to enter the sample loop through the injector site. By reducing the rpm of the peristaltic pump, the peaks for nitrogen and oxygen decreased but were still present, Figure 3.7 shows the best results for all the samples.

From this it was determined that a carrier gas may be suitable for transporting the evolved pyrolysis gases from the reactor to the gas chromatographer. Due to the nature of pyrolysis an inert gas was required so nitrogen and argon were suggested. These were selected as they were both high purity gases, which do not contain oxygen. A variety of different flow rates were explored, from 5 mL/min to 25 mL/min, with both carrier gases. At all the uses of nitrogen there was an increased nitrogen peak, which increased with the increasing flow rate of the carrier gas. Therefore, as the use of nitrogen as a carrier gas may mask the presence of nitrogen in the actual gas sample, it was discounted. Argon, the reference gas for the gas chromatographer, was used and saw no change in peak sizes, even with higher flow rates. As argon is the reference gas for the thermal conductivity detector, it is acknowledged that some sample dilution may occur. However, it was determined that as long as the flow rate remained constant, this dilution factor could be deemed to be negligible. At the higher flow rates of both argon and nitrogen the peak sizes were seen to be suppressed.

Therefore, for accurate gas readings to determine how pyrolysis gases evolve with increasing time, a flow rate of 10 mL/min was determined to be the most efficient. This was decided as the 5 mL/min led to an unreliable loading showing that it was not strong enough to act as an efficient carrier gas. 10 mL/min was the lowest flow rate that would allow efficient transport of the evolved gases to the sampling loop. The lowest possible efficient flow rate was decided on to ensure that peak dilution was minimized. However, once the gas content was calculated, the percentage contributions were seen to be $100 \pm 5\%$ showing that there was not a significant affect caused by peak dilution. For all pyrolysis

reactions a flow rate of 10 mL/min argon was used to ensure that all results were comparable. The use of a carrier gas can be seen to lead to a higher concentration of CO₂ being collected, which can be assumed to be an accurate representation of the gas produced through the pyrolysis of the textile waste, as this would be expected based on the structure of the cotton sample. The use of a carrier gas allowed for the production of accurate representations of the gases produced through the pyrolysis of textile waste. Interestingly hydrogen concentration is the lowest for the carrier gas approach, however this is to be expected based on the structure of the cotton textile waste, and the preferential formation of methane from these products.

3.3.2 Gas products of pyrolysis of 100 % Cotton textile waste at different temperatures

Pyrolysis of cotton at different temperatures produced different gas compositions. As expected from the TGA data, at lower temperatures there is minimal activity seen. With small amounts of hydrogen, carbon dioxide and carbon monoxide being seen at 300 °C, the proportions of gas produced increases with the higher temperatures, confirming the TGA that pyrolysis occurs at over 350 °C. Higher temperatures will lead to more gases produced as there is more energy to overcome the bond energies.

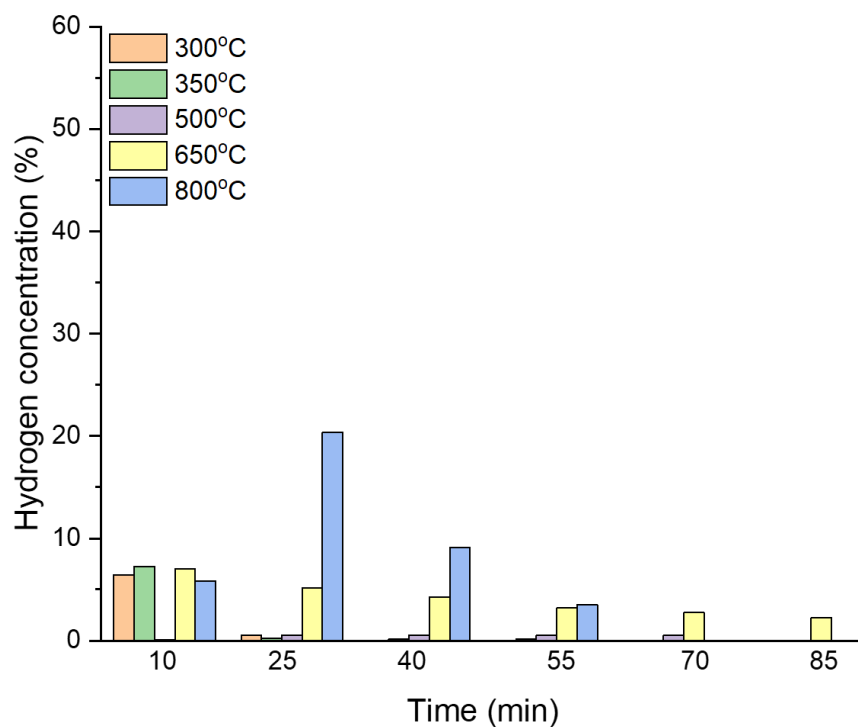


Figure 3.8. Hydrogen production from the fast pyrolysis of 100 % cotton at different temperatures

As shown in Figure 3.8, there is a peak in hydrogen production, reaching 20 % at 25 mins at 800 °C, before it decreases, whereas at other temperatures, the peak hydrogen formation occurs after 10 mins, in the initial pyrolysis zone. This might be due to the higher temperature requiring a longer heating time for the reaction to begin. The higher temperatures produced a higher yield of hydrogen, which is expected due to bond cleavage reactions.

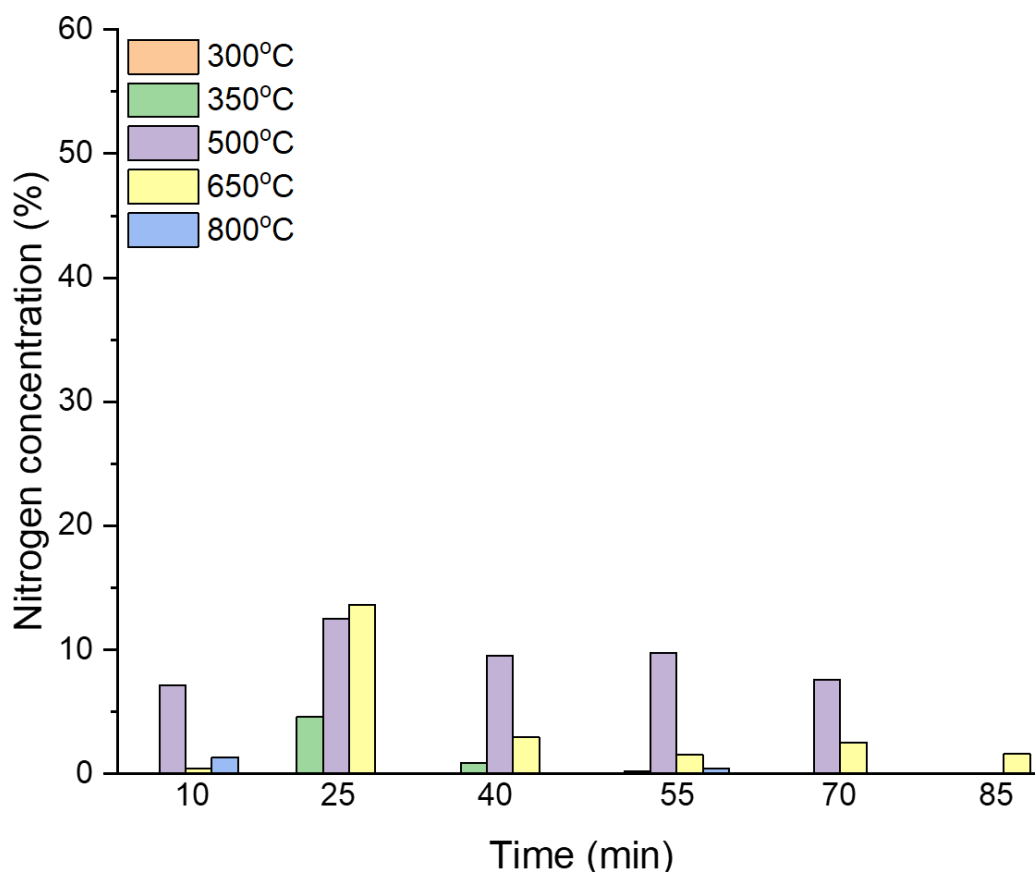


Figure 3.9. Nitrogen production from the fast pyrolysis of 100 % cotton at different temperatures

Nitrogen production was seen to be lower than hydrogen, as seen in Figure 3.9, with a peak at 13.6 % produced at 650 °C after 25 mins. Whilst the maximum produced was seen at 650 °C, the net highest yield was seen at 500 °C with a consistent concentration seen. The lower temperatures, 300 and 350 °C, were seen to not produce any nitrogen. These changes may be due to small quantities of atmospheric nitrogen trapped within the sample, or due to an incorrectly tightened gasket allowing atmospheric nitrogen into the sample. However, this is unlikely as all reactions were carried out in triplicate and nitrogen was seen to occur for all 500 and 650 °C samples.

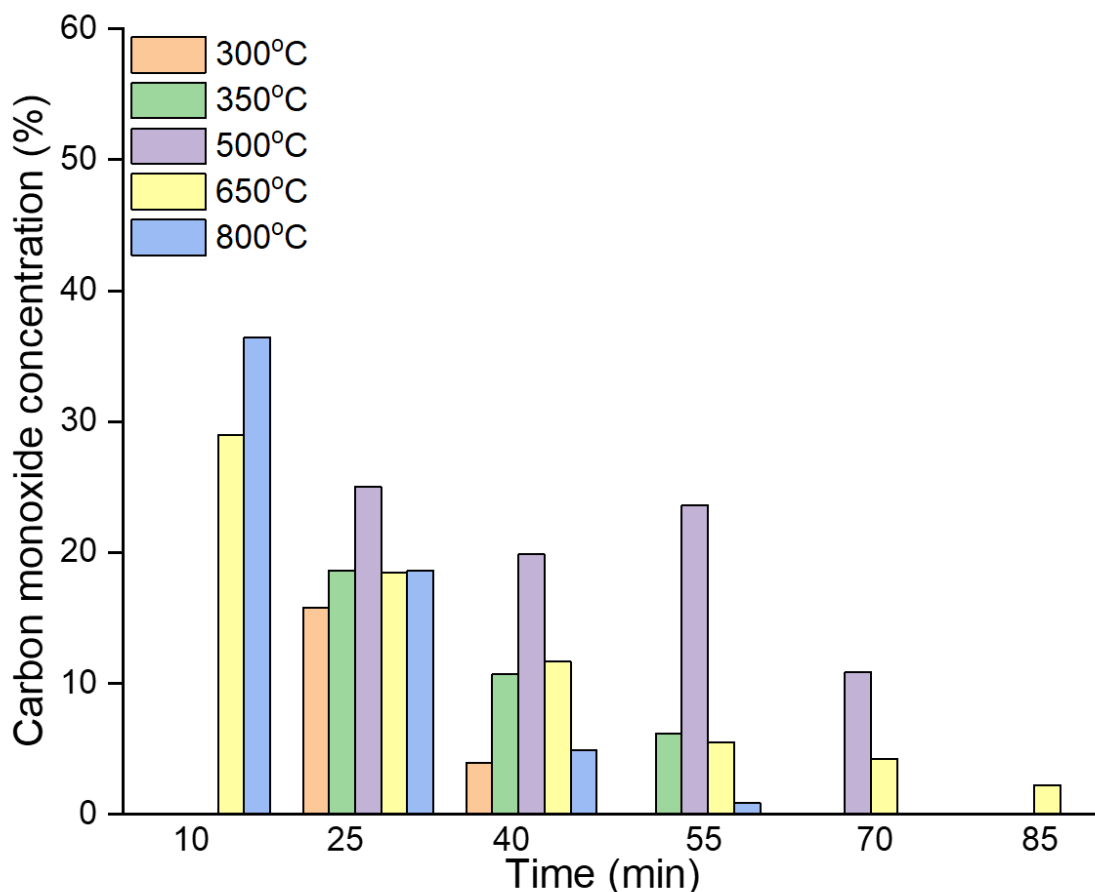


Figure 3.10. Carbon monoxide production from the fast pyrolysis of 100 % cotton at different temperatures

Carbon monoxide was the second highest gas concentration seen, with a peak of 36.5 % after 10 mins at 800 °C. A high quantity of carbon monoxide was produced at 25 mins by all temperatures, showing that it is an easily produced gas. It would be expected that carbon monoxide would have a higher yield than carbon dioxide, due to the reduced atmospheric oxygen present in pyrolysis, however considering Figure 3.10, this is not the case. This increased prevalence of carbon dioxide is due to the lower enthalpy of carbon dioxide, meaning it is more stable and requires less energy to form. The higher yield seen at 800 °C is expected to follow the same pattern as the other high temperature process, where the feedstock is consumed by the higher temperature, meaning that the pyrolysis has a shorter run time.

A consistent production of carbon monoxide is seen at 500 °C, despite seeing no conversion after 10 mins, considering Figure 3.10, it can be noted that carbon dioxide was seen to be

produced after 10 mins, although again at a lower concentration than may be expected. It can therefore be assumed that for these carbon oxygen gases, especially carbon monoxide, a greater energy is required to initiate bond cleavage for the formation of the expected gases.

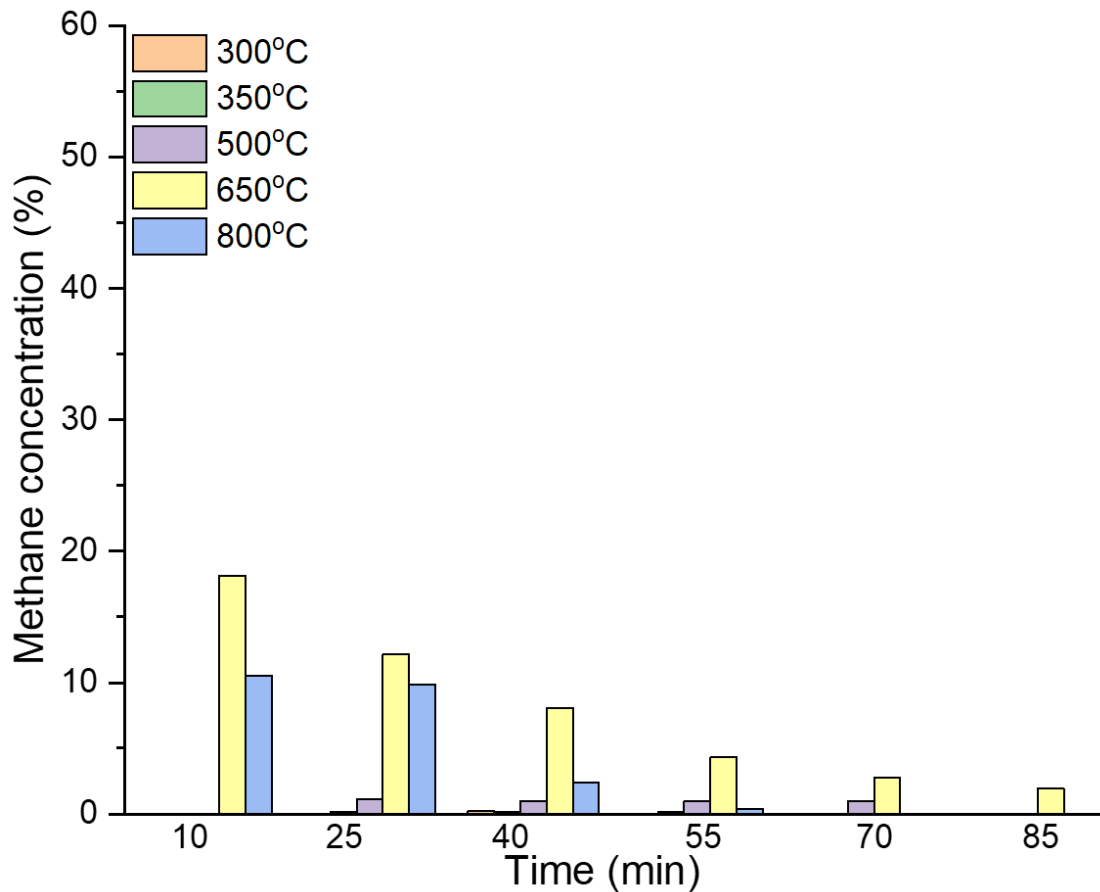


Figure 3.11. Methane production from the fast pyrolysis of 100 % cotton at different temperatures

In literature, methane is the most effective feedstock gas for the formation of carbons. It is seen from Figure 3.11, that only temperatures of over 650°C produced any significant methane. This was attributed to the higher bond enthalpy of C-H and O-H, meaning that more energy is required to release hydrogen. As higher temperatures provide more energy into the system, a higher pyrolysis temperature should allow a higher energy system, breaking the higher enthalpy bonds.

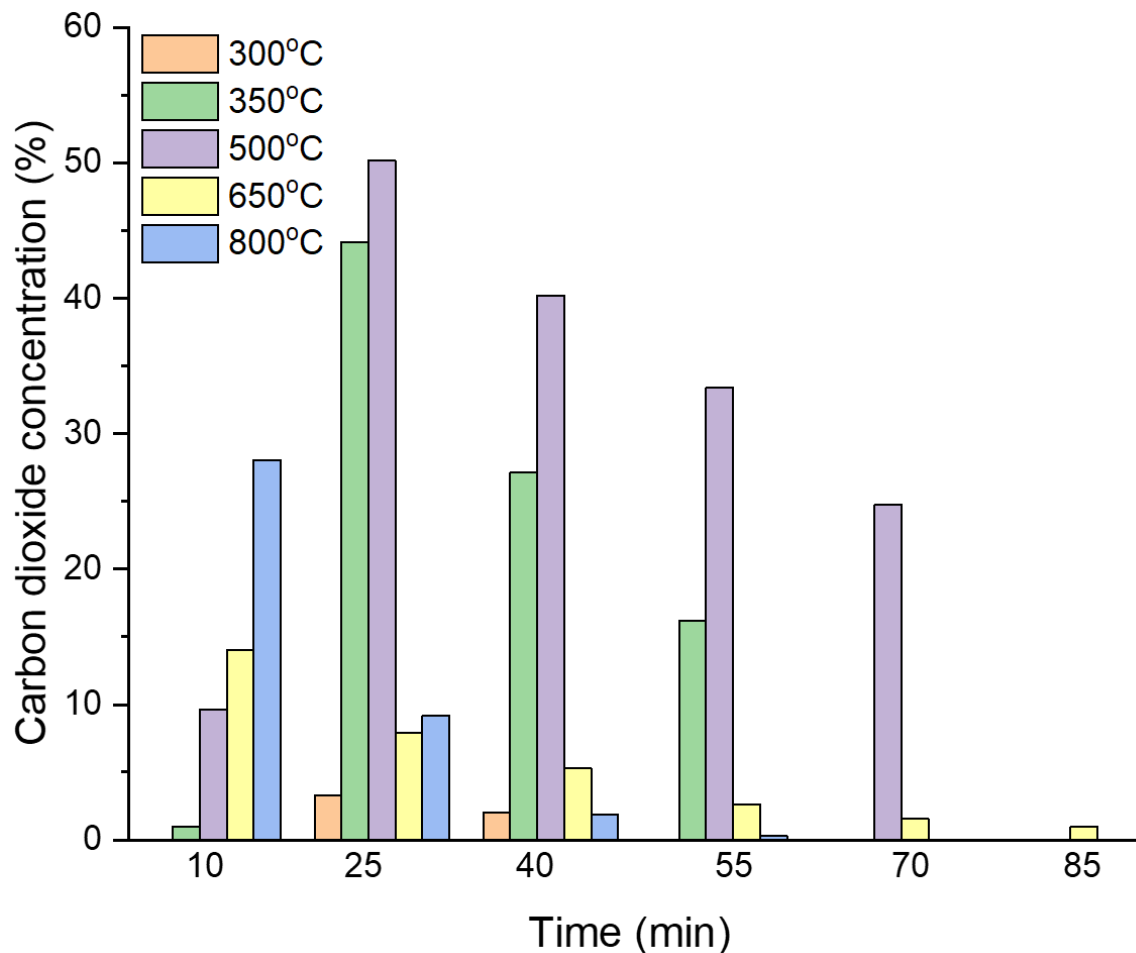


Figure 3.12. Carbon dioxide production from the fast pyrolysis of 100 % cotton at different temperatures

A maximum of 50 % carbon dioxide was seen at 500 °C after 25 mins, Figure 3.12. Similar patterns are seen for 350 °C and 500 °C with a peak after 25 mins before decreasing as time increases. A very small amount of carbon dioxide is seen to be produced at 300 °C, this is attributed to the lack of thermal energy in the system. Carbon dioxide is produced preferentially to carbon monoxide, as it is seen to be more stable, and more desirable, whereas carbon monoxide is formed due to a lack of oxygen in the system.

By changing the temperature of the system, the products produced can be altered to fit the desired outcome. Pyrolysis can be used to affect the changes desired from the products formed, just by altering the temperature the reaction is carried out at. The predominant species seen from cotton pyrolysis were carbon dioxide, carbon monoxide and methane. As these all contain carbon, they can all be reasonably assumed to be efficient feedstock gases for the formation of carbon.

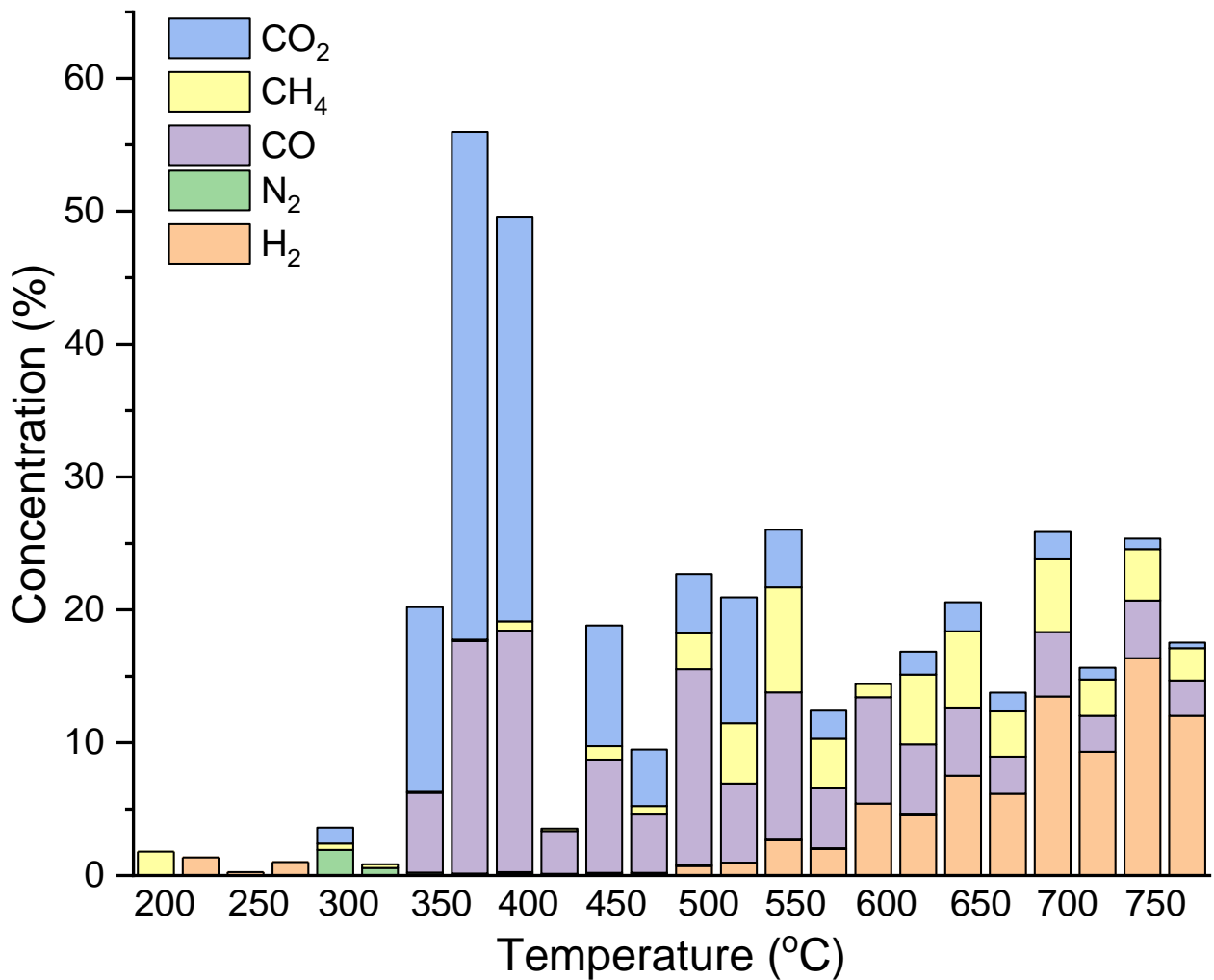


Figure 3.13. The gas concentrations produced through the stepped pyrolysis of 100 % cotton textile waste

The stepped pyrolysis of cotton textile waste, Figure 3.13, shows three main regions of gases produced; a carbon dioxide rich section between 350 and 350 °C, a carbon monoxide rich region between 500 and 600 °C and a hydrogen rich region over 600 °C. These regions are due to the higher availability of oxygen at initiation, whereas as the process progresses there is less oxygen available driving the change to carbon monoxide and then methane.

There is variation seen from the fast pyrolysis compared to the slow pyrolysis, at 350 and 400 °C the fixed temperatures showed a higher yield of carbon monoxide, and minimal carbon dioxide production. This variation could be due to the atmospheric presence of carbon dioxide within the sample, although this would be expected to come off at earlier temperatures. Therefore, it is likely to have evolved from the sample. As the temperature,

and time, increases so does the proportion of carbon monoxide in the sample. This is attributed to a reduction in oxygen seen from this point, favouring other forms of carbon containing gases, similar to incomplete combustion. Finally, at the higher temperatures, there is a greater yield of hydrogen seen, this is assumed to occur as the majority of accessible carbon has been reacted. There is also some evidence that cracking of the heavier pyrolysis oil can occur, as these would be a source of hydrogen, and further carbon, leading to the continued production of methane.

3.3.3 Gas products of pyrolysis of 91 % polyester 9 % lycra textile waste at different temperatures

Based off the TGA data collected, the initial pyrolysis temperature was selected to be 400 °C, with steps of 150 °C for fixed data and continuous stepped with steps of 50 °C. As evidenced throughout Figures 3.14 – 19, it is clear that pyrolysis of the textile waste is not efficient until 450 °C, with most gas production seen at temperatures of 500 °C and above.

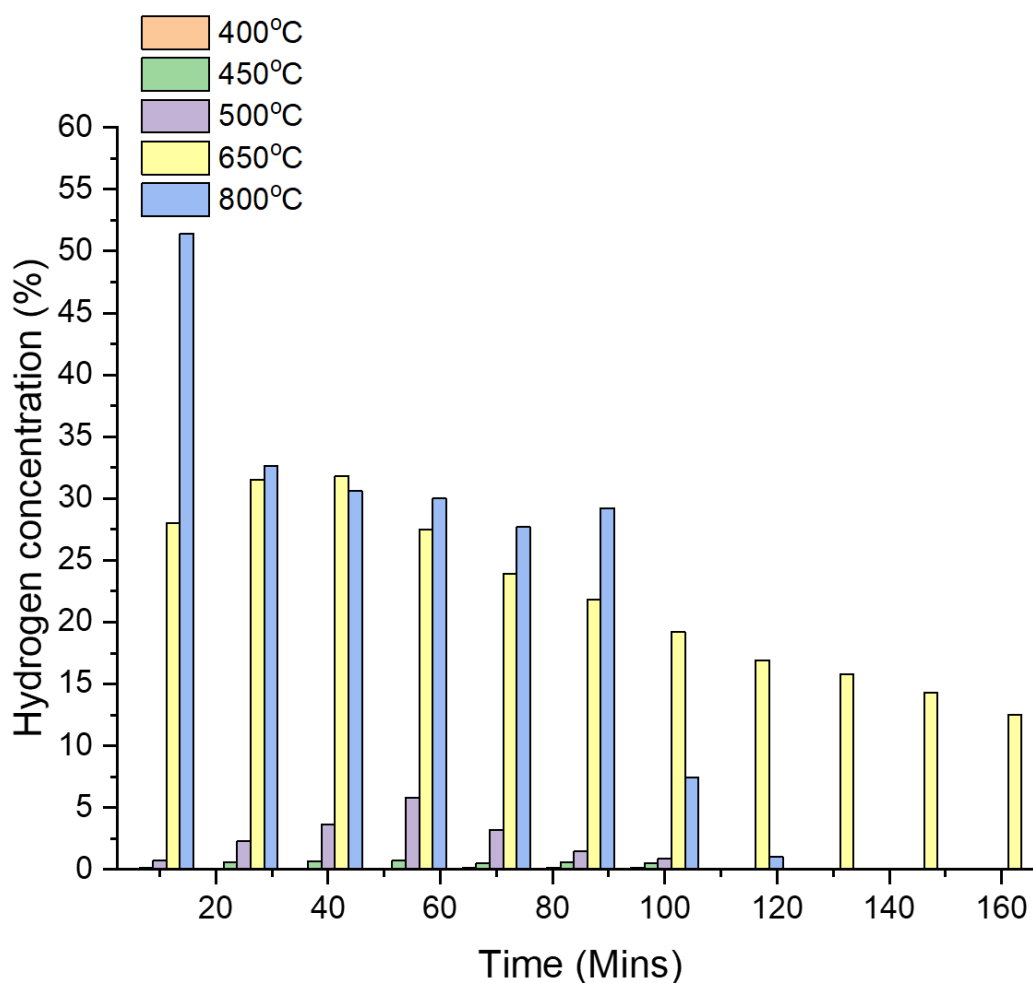


Figure 3.14. Hydrogen generation from the fast pyrolysis of 91 % polyester 9 % lycra mix at differing temperatures

Hydrogen is seen to only be produced at high temperature pyrolysis of the polyester mix. As shown in Figure 3.14, the highest yield of hydrogen is seen after 10 minutes at 800 °C, with a similar pattern seen at 600 °C, although at 600 °C there is a more consistent yield seen. Due to the structure of polyester and lycra, it is expected that due to the bond enthalpies, and potential cracking fragments, that a large amount of energy is required to release the hydrogen.

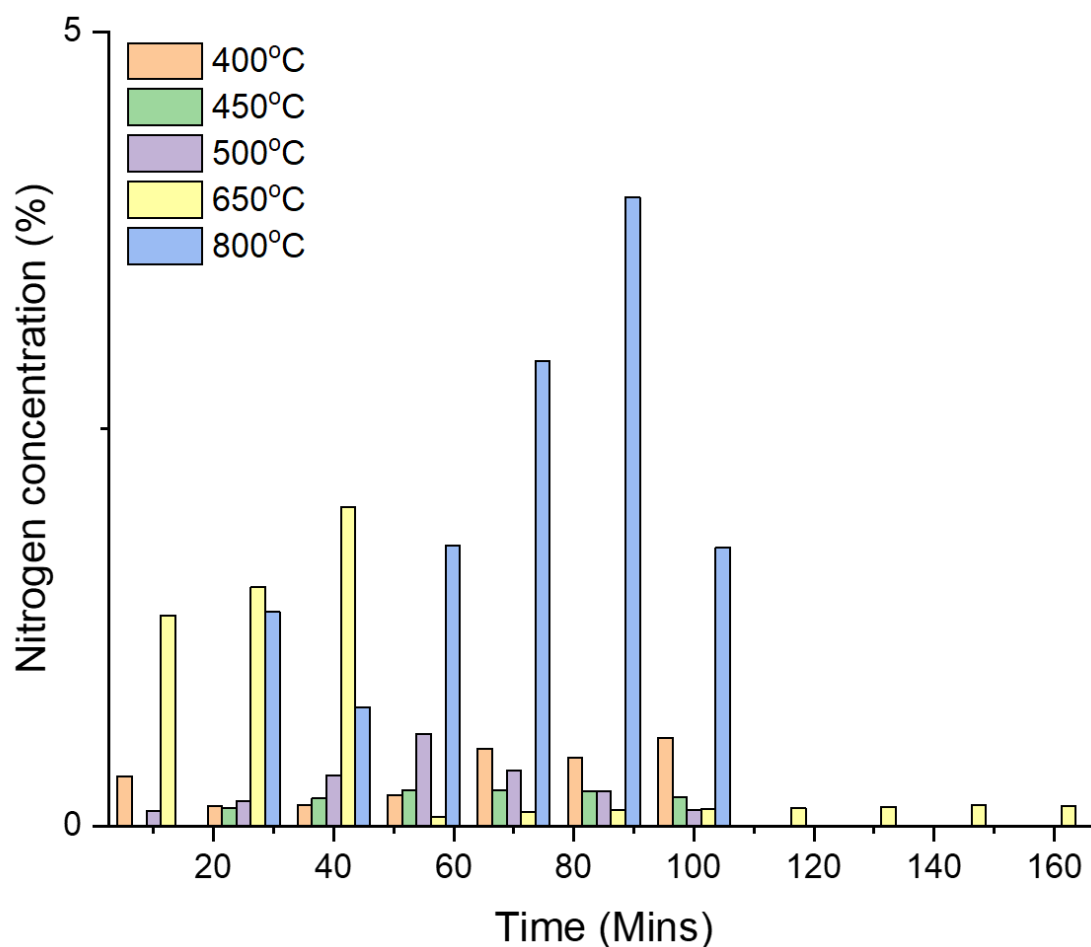


Figure 3.15. Nitrogen generation from the fast pyrolysis of 91 % polyester 9 % lycra mix at different temperatures

Nitrogen levels were seen to be low throughout all polyester/lycra pyrolysis, which despite the presence of nitrogen in lycra, is to be expected. This is due to location of the nitrogen within the compound, a high energy level would be required to separate these, and they preferentially may remain in the oil phase. Any nitrogen produced can be attributed to dyes present within the sample, or trapped atmospheric nitrogen within the sample fibres.

Comparing Figure 3.9 to Figure 3.15, it is clear that either cotton has a higher porosity which has led to nitrogen becoming trapped within the fibres, or that cotton has a higher initial nitrogen content.

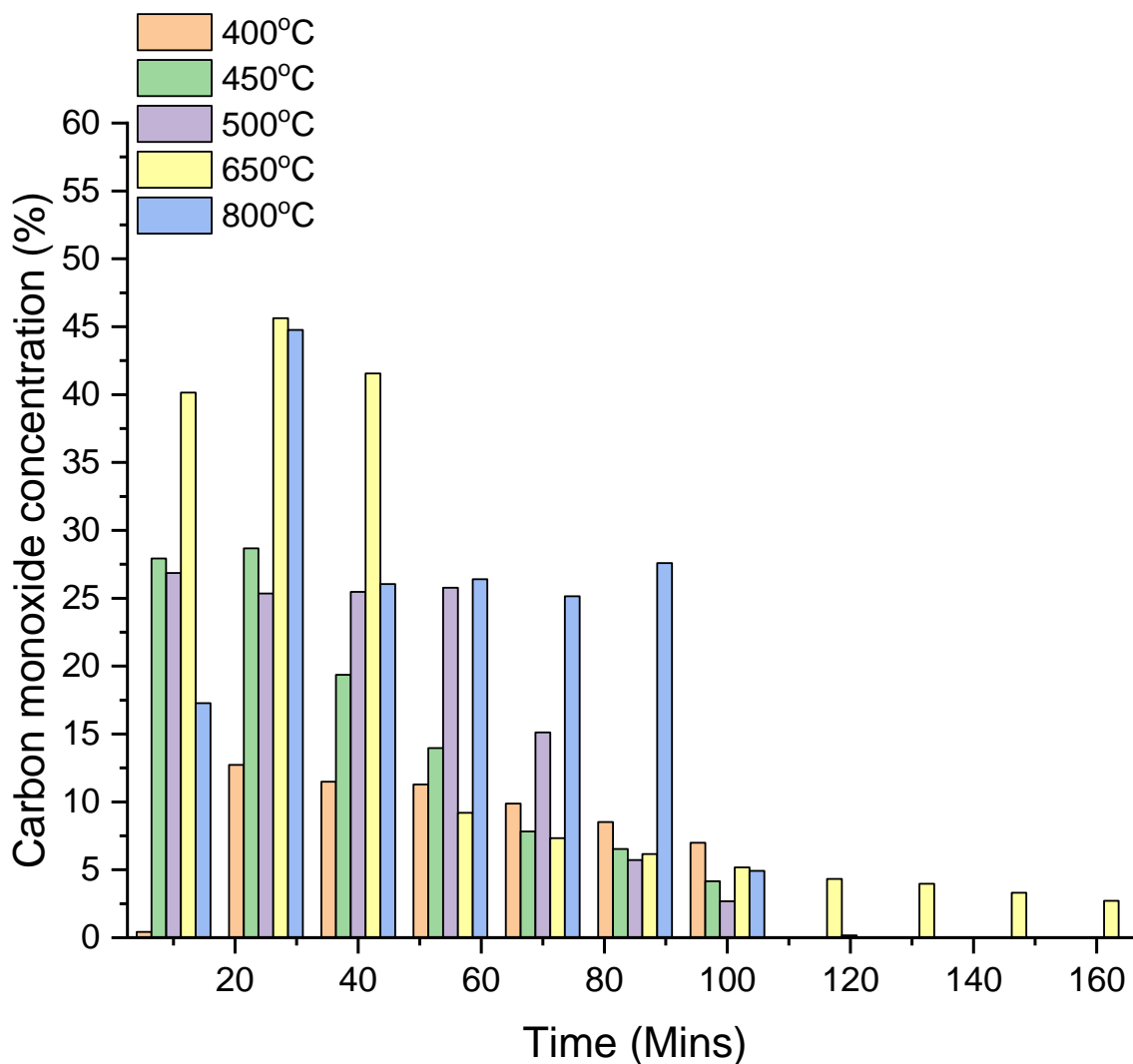


Figure 3.16. Carbon monoxide generation from the fast pyrolysis of 91 % polyester 9 % lycra mix at different temperatures

Carbon monoxide was seen to be produced more efficiently at higher temperatures, specifically 650 °C and 800 °C, although all temperatures produce carbon monoxide. As seen in Figure 3.16, the carbon monoxide is predominately produced at 25 minutes. Considering the structure of the polyester molecule alongside lycra, it can be seen that through fragmentation from thermal decomposition, the molecules can form carbon monoxide, especially at the higher temperatures.

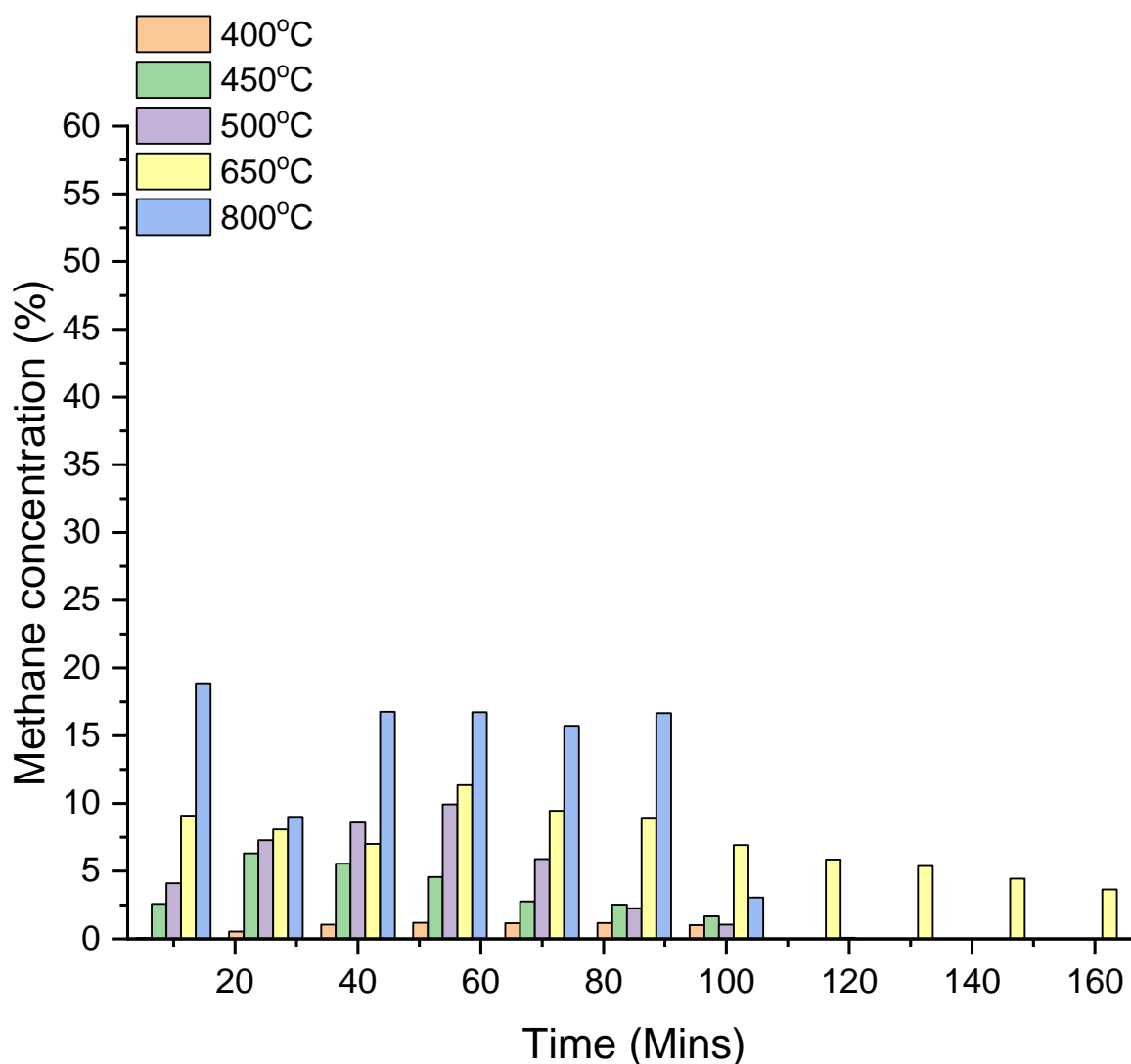


Figure 3.17. Methane generation from the fast pyrolysis of 91 % polyester 9 % lycra mix at different temperatures

Methane, was seen to have the highest yield at 800 °C with a consistent gas generation seen until 100 minutes. As shown in Figure 3.17, the formation of methane is steady before declining towards the end of the reaction. This shows that methane production is a stable process, and able to constantly be formed whilst feedstock remains. Due to the structure of polyester molecules, it is predominately made of carbon and hydrogen, meaning that methane should be preferentially produced. At 400 °C it is seen that there is minimal methane generated, this is in line with the TGA data, there is insufficient energy in the system to produce methane from polyester or lycra.

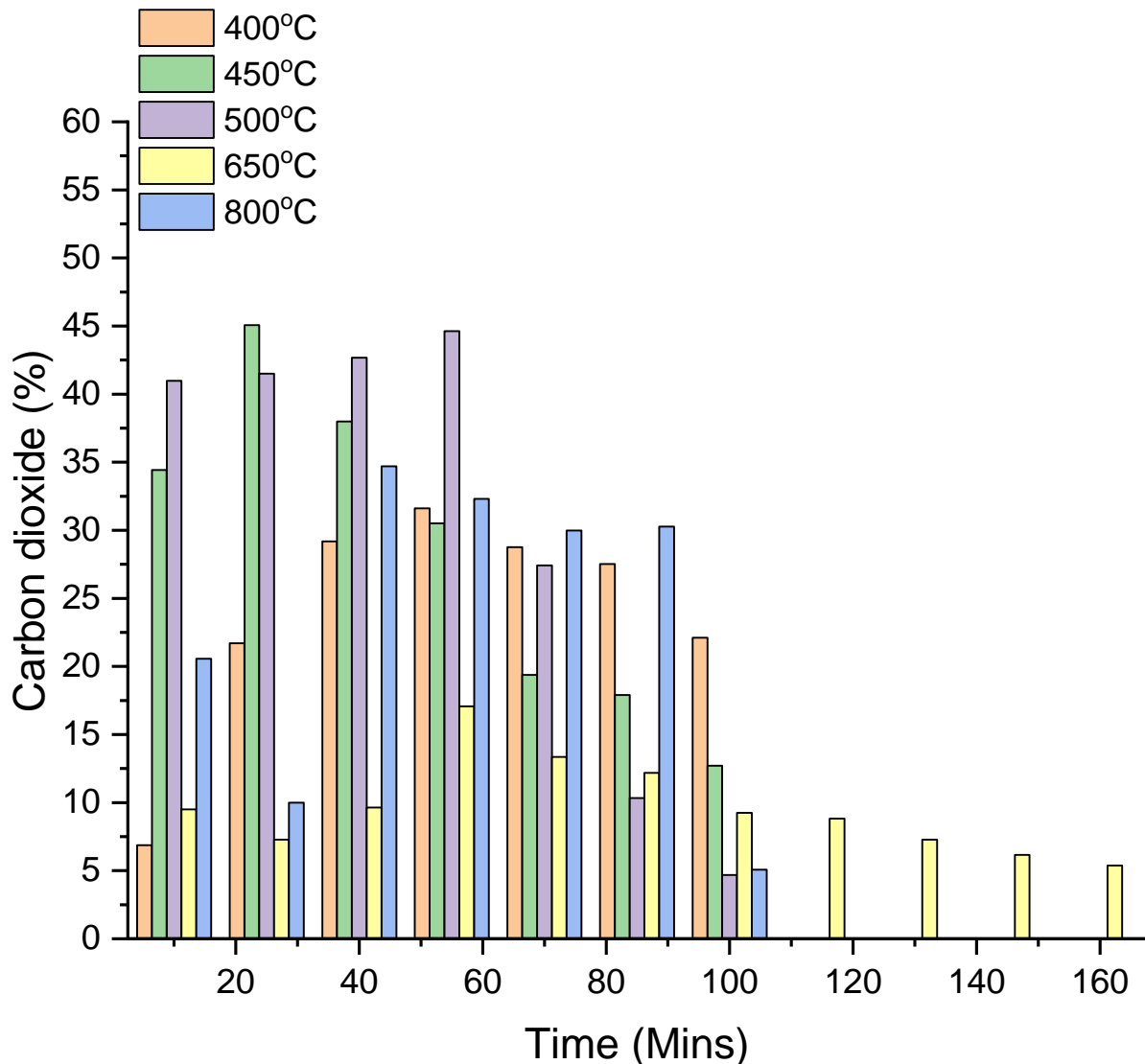


Figure 3.18. Carbon dioxide generation from the fast pyrolysis of 91 % polyester 9 % lycra at different pyrolysis temperatures

Carbon dioxide, similarly to carbon monoxide, sees a higher yield at lower temperatures, compared to other gas types, as shown in Figure 3.18, there is significant production for most temperatures. This may be due to the lower bond enthalpy for C-O bonds, allowing these to be broken at lower temperatures, there may also be atmospheric carbon dioxide trapped within the fibres, although this does not account for the consistent production of carbon dioxide seen at 400 °C. The higher gas production of carbon dioxide over methane is due to the lower bond enthalpy of formation for carbon dioxide.

At 800 °C there is less carbon dioxide formed than carbon monoxide, this may be attributed to the differences in stability and preferential formation. The predominant temperatures

that carbon dioxide was formed at were 450 to 650 °C, this shows that a mid-range temperature can be used for the production of carbon dioxide.

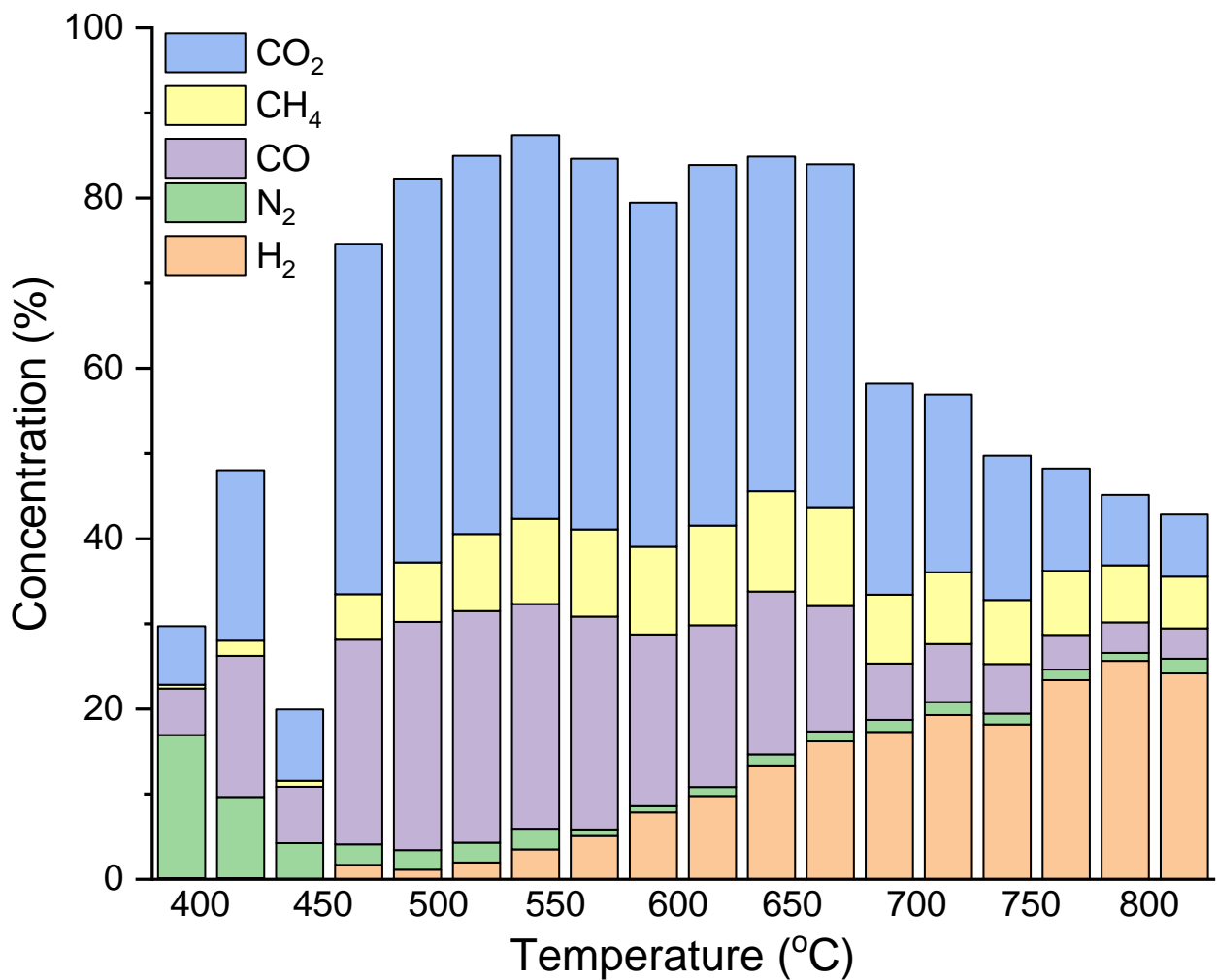


Figure 3.19. The gas production from the stepped pyrolysis of 91 % polyester 9 % lycra textile waste materials

Compared to cotton, the stepped pyrolysis of polyester/lycra mix produces a much higher yield of gases. There are two main regions in the stepped pyrolysis of polyester/lycra mix; one dominated through the production of carbon dioxide and carbon monoxide, and the other characterised through the increased production of hydrogen. As seen in Figure 3.19, the production of methane is constant through all temperatures, this is attributed to the constant formation of carbons, which preferentially form the carbon oxide gases. As the hydrogen levels increase, the carbon oxide levels decrease, this can be attributed to the loss of accessible carbon, leading to a reduction in the formation of methane, and promoting the production of hydrogen.

Atmospheric nitrogen is attributed to the higher yields seen at the lower temperatures, this is evidenced by the sudden decrease seen after 450 °C. Atmospheric nitrogen can become trapped in the fibres of the textile waste, even after flushing the sample with argon.

The stepped pyrolysis of polyester/lycra mix differs from fixed temperature, as methane concentrations are higher at increased temperatures. This implies that as time, as well as temperature, increases that the methane formed is consumed to produce other products. The highest yield of hydrogen is seen at 800 °C at fixed temperatures, and is only seen to be significant over 650 °C, this is in line with the data seen from the fixed temperature pyrolysis seen.

Fixed temperature pyrolysis shows that carbon monoxide is produced earlier than carbon dioxide at higher temperatures, this is seen due to the earlier decrease in carbon monoxide. The reduction in carbon oxides can also be attributed to the consumption of accessible carbon from the feedstock. It should be noted that the fixed temperature pyrolysis only considers how a singular temperature influences the formation of gases rather than considering how increasing the temperature alongside time will influence them. Therefore, considering the variations seen in Figure 3.19, compared to those seen in Figures 3.14 – 3.19, both temperature and time will allow for the control of desired products. There may also be variations seen due to the presence of pyrolysis oils remaining in the reactor, these can be further pyrolysed. This further pyrolysis can alter the gas concentrations seen from the stepped pyrolysis compared to that of the fixed temperatures. As heavier hydrocarbons would be seen in the oil samples, these could be pyrolysed in the reactor to release a greater yield of hydrogen. Temperature has a clear impact on the gases produced from the polyester/lycra feedstock. At higher temperatures, hydrogen production is favoured whereas for lower temperatures carbon dioxide formation is preferred.

The pyrolysis of polyester/lycra mix produced a greater amount of gases, especially for carbon oxygen gases and methane, compared to the cotton feedstock. This means that for the production of carbon, it is assumed that the process will be more efficient using a synthetic textile compared to the natural cotton.

3.4 GC-MS of textile waste samples

The collected oil samples were analysed through gas chromatography-mass spectroscopy. This was the only testing carried out on the oil samples. It was noticed that more oil was produced from the cotton pyrolysis samples, compared to that of polyester, which considering more gas is produced through the pyrolysis of polyester, the primary product of cotton pyrolysis could be attributed to the oils. The spectra produced through GC-MS analysis allowed the identification of compounds within the oil samples, these were categorised due to the most chemically active feature, allowing a comparison between different temperatures, as well as feedstocks.

3.4.1 Pyrolysis oils produced from the pyrolysis of 100 % cotton

The pyrolysis of cotton led to the generation of oils, typically mid to heavy weight hydrocarbons with any other materials that are not volatile enough for the gas phase.

Table 3.3. Gas Chromatography-Mass Spectrometry data for pyrolysis oils produced through the pyrolysis of cotton textile waste at different temperatures

Classification of compound	Contribution (wt.%) of each classification at different temperatures				
	350 °C	500 °C	650 °C	800 °C	Stepped pyrolysis
Aldehyde	3.4	3.4	3.2	2.0	3.6
Ketone	17.2	13.8	17.9	19.8	19.9
Hydrocarbon	16.1	11.5	11.6	8.9	6.0
Cyclic	12.6	24.1	16.8	19.8	26.5
Carboxylic Acid	18.4	8.0	17.9	11.9	15.7
Nitrogen	11.5	11.5	10.5	10.9	13.3
Alcohol	9.2	10.3	8.4	8.9	9.0
Ester	2.3	0.0	3.2	5.0	3.6
Other	9.2	17.2	10.5	12.9	2.4

The GC-MS data shows the primary class of molecule seen in the pyrolysis oils to be cyclic molecules, followed by ketones. These are to be expected based from the structure of cellulose, as with the addition of energy to the cellulose will allow the breakdown of the cyclic molecule. The resultant molecule can be further degraded into the gas phase components, or reform into the oils seen. Light phase oils will condense in the oil traps, whereas heavier oils may have remained in the pyrolysis reactor. These heavier oils may be further pyrolysed, or not been efficiently removed, this may shift the classifications and types of molecules seen within the oil.

As less gas was seen to be produced, and there was a greater yield of oil seen, this indicates that a greater conversion to oil is seen rather than into the gas phase. This exemplifies that heavier molecules are seen from the pyrolysis of cotton, and that under thermal conditions cellulose will preferentially form these volatile, lighter compounds, and agrees with studies on pyrolysis of textile waste [195-197].

There does not seem to be an influence of temperature on the compounds seen, although a general increase in oil formation is noticed in Table 3.3. It is worth noticing that the number of cyclic molecules is reduced at 350 °C compared to the other, higher, temperatures, meaning that the overall energy within the system for the production of these molecules is needed to be higher.

Nitrogen containing compounds, primarily amines, can be associated with the reaction of cracked molecules within the reactor, with atmospheric nitrogen. It may also be an indicator that there were existing nitrogen containing compounds embedded in the textile waste, although as there is a consistent presence of nitrogen seen within the sample it may be possible that ammonia was used in the manufacturing process to treat the cotton fibres.

Ketone formation can be expected due to the presence of glycosidic bond oxygen molecules, which will preferentially form ketones, aldehydes or esters. However, ketones will form preferentially as esters require acids to form, and due to the location of the oxygen atoms, ketones are more likely.

Alcohol formation is probable due to the presence of OH- groups, following cracking of cellulose alcohols can form. These alcohols can be complex, or simple, and often were seen

to involve a cyclic molecule, where this occurred they were classified as alcohols as this is the active component.

Aldehydes are a reportedly common product in the pyrolysis of cellulose based materials. Literature states that at temperatures over 300 °C the depolymerisation of the materials occurs, with simultaneous reactions running [274]. This contributes to the formation of unstable carbonyl and carboxylic groups. All products undergo further fragmentation and dehydration as well as breaks within the C-C linking beginning to occur, leading to the formation of aldehydes, acids and alkyl phenols. Any char material remaining over 380 °C undergoes demethylation and aromatisation forming methane, carbon monoxide and hydrogen. This can be used to understand the formation of the compounds seen in the pyrolysis oils.

There are two main compounds seen throughout all samples; levoglucosan and benzoic acid. 5-methyl-2-furancarboxaldehyde was seen in five of the six temperatures.

Levoglucosan is a product of the pyrolysis of cellulose, and glucose, and is classed as a 1,6-anhydro-derivative of beta-D-glucopyranose. Benzoic acid, typically seen as a pyrolysis product, is used in to produce antifungal preservatives, as well as an intermediate for the synthesis of benzoates. 5-methyl-2-furancarboxaldehyde is used in fragrances, as well as a flavouring agent.

Oil production can be seen to produce a range of materials which can be collected, separated and recycled. Common products can be expected independent of temperature, levoglucosan, benzoic acid and 5-methyl-2-furancarboxaldehyde can all be seen throughout the oil samples. There does not appear to be substantial changes on the products seen with increases in temperatures, although the yield of oil does increase. Therefore, it can be assumed that the production of oil following pyrolysis is independent of temperature.

3.4.2 Oil analysis of pyrolysis oils produced from pyrolysis of 91 % polyester 9 % lycra mix

The GC-MS analysis of oils produced through the pyrolysis of polyester/lycra mix at different temperatures identified a range of different compounds that made up the oil. These were separated into categories based on the chemically active feature. The predominant class of

molecule seen was cyclic, followed by carboxylic acid and hydrocarbons, as seen in Table 3.4.

Table 3.4. Classification of classes of compounds seen following gas chromatography-mass spectrometry analysis of pyrolysis oils produced from polyester/lycra mix

Classification of compound	Contribution (wt.%) of each classification at different temperatures				
	450 °C	500 °C	650 °C	800 °C	Stepped pyrolysis
Aldehyde	4	4	6.5	5.5	6
Ketone	9.5	10	6	7	6
Hydrocarbon	17	17.5	16	12	10
Cyclic	22	22	24.5	26.5	26
Carboxylic Acid	16	20	22	24.5	27
Nitrogen	8	6	6.5	5	4
Alcohol	9.5	10	5.5	6.5	6
Ester	6.5	7	8	7	6
Other	7.5	3.5	5	6	9

The formation of cyclic compounds can occur through either the cracking of the larger polyester or spandex compounds to free the existing cyclic regions, or the reformation of aliphatic hydrocarbons into cyclic forms. As both lycra and polyester contain cyclic regions, it is expected that cyclic molecules will compose a large proportion of the compounds identified. There is a general trend that as the temperature increases, there is a greater proportion of cyclic compounds seen, this can be due to the increased temperatures leading to a raised incidence of the formation of cyclic molecules. A decrease for stepped pyrolysis can be attributed to a general reduction in the oil formation seen from stepped pyrolysis. This furthers the hypothesis that the pyrolysis oils produced, especially heavier ones, are further pyrolysed in the reactor, leading to less oil being collected for this run. The 'other' category was used for samples that did not neatly fit in the other classifications, this was

due to the presence of multiple functional groups which meant the compound has unpredictable behaviours.

Carboxylic acids are formed from the cracking of polyester and lycra molecules leading to the formation of carboxylic acids. These can be simple compounds, or longer chain depending on where the molecule became cracked. Due to the repeated presence of O-C=O groups there is a high probability of the formation of carboxylic acids being synthesised during pyrolysis [274]. The production of carboxylic acids was seen to be constant over all temperatures, although there is a reduction in synthesis seen at 450 °C. This is unexpected due to the high levels within the other temperatures, although could be due to an increased formation of other compounds.

Hydrocarbons are produced from the cracking of the hydrocarbon section of the polyester and lycra molecules. Polyester molecules contain an ethylene chain whilst lycra consists of a long aliphatic hydrocarbon chain. These can both be cracked at any point along the chain, leading to the formation of a variety of different length hydrocarbons. The hydrocarbons can also be formed through the cracking of benzene, although this only becomes likely at high temperatures. As the pyrolysis temperature increases, the long chain hydrocarbons can be further cracked into shorter chain, which is seen through the identification of the compounds within the oils.

Nitrogen compounds, such as amines, are seen to be produced at a low rate. This is attributed to the presence of N-H groups that can be seen within the lycra. The higher yield of nitrogen containing compounds seen at 450 °C may be evidence that the nitrogen containing compounds are preferentially produced at lower temperatures [160]. The presence of dyes in the textile waste can further lead to the production of nitrogen containing compounds.

As discussed in section 3.4.1, the temperature of a reaction can be used to control the products seen in the pyrolysis oils due to decomposition, dehydration and fragmentation. Compared to the cotton pyrolysis oils, there was a greater proportion of cyclic and carboxylic acid compounds seen, whereas cotton saw a higher overall yield for nitrogen containing structures, which is related to the structures of the textiles seen in Figures 1.10 and 1.12. Similarly to cotton, all types of pyrolysis saw the formation of levoglucosan and

benzoic acid. There is also the presence of variants of benzoic acid seen. 4-methyl benzoic acid and 4-ethyl benzoic acid can both be employed in polymer synthesis, contributing to polymer stabilisation. The oils seen can be separated into the individual components for further use.

3.5 SEM to determine the structure of textile waste and the influence of temperature on the structures and defects seen

Scanning electron microscopy images were collected for each pyrolysis temperature, as well as for the original feedstock and stepped pyrolysis, giving information into the effects of temperature on the structure of the internal fibres of the textile waste sample.

3.5.1 Pyrolysis char produced from of 100 % Cotton textile waste at various temperatures

Scanning electron microscopy images for chars produced from the pyrolysis of cotton can be seen in Figure 3.20. The fibre sizes were measured using ImageJ software to determine the impact of the pyrolysis of the structure of the cotton waste. As the temperature increases, the fibres are seen to become more damaged, with a less ordered appearance. In comparison to this, the stepped pyrolysis material retains the structure of the fibres. This can be attributed to the slow pyrolysis, caused by the implemented heating rate from the stepped pyrolysis, leading to a greater preservation of char structure. This is due to the slower formation of gases, causing less strain on the fibres, therefore, causing less damage to the structure of the textile waste. As the temperature increases, the fibres are seen to become more damaged, with a less ordered appearance, in comparison to this, the stepped pyrolysis material retains the structure of the fibres. This can be attributed to the slow heating rate, leading to a greater preservation of char structure. This is due to the slower formation of gases, causing less strain on the fibres, therefore, causing less damage to the structure of the textile waste. The TGA and GC data shows that there is higher activity after 350 °C, which corresponds to the increase in damage seen in the textile fibres. As discussed, the low heating rate of the stepped pyrolysis prevents damage occurring in the char produced, as seen in image f in Figure 3.20. The fixed temperature pyrolysis causes a fast temperature change within the fibres, this will lead to a fast production of gases, which will in turn lead to an increased strain on the fibres, causing the increased damage. As the fixed temperature increases the quality of the char decreases, this can be seen through the

increased damage to the fibres seen, which led to an increase in the brittleness of the char. This can be directly linked to the fast pyrolysis, and heating, of the textile waste, as the stepped pyrolysis, which had a top temperature of 750 °C, does not see the same damage. Therefore, the heating rate can be seen to have an influence on the quality of char formation, this means that the overall quality of the char can be changed through the alteration of heating rate.

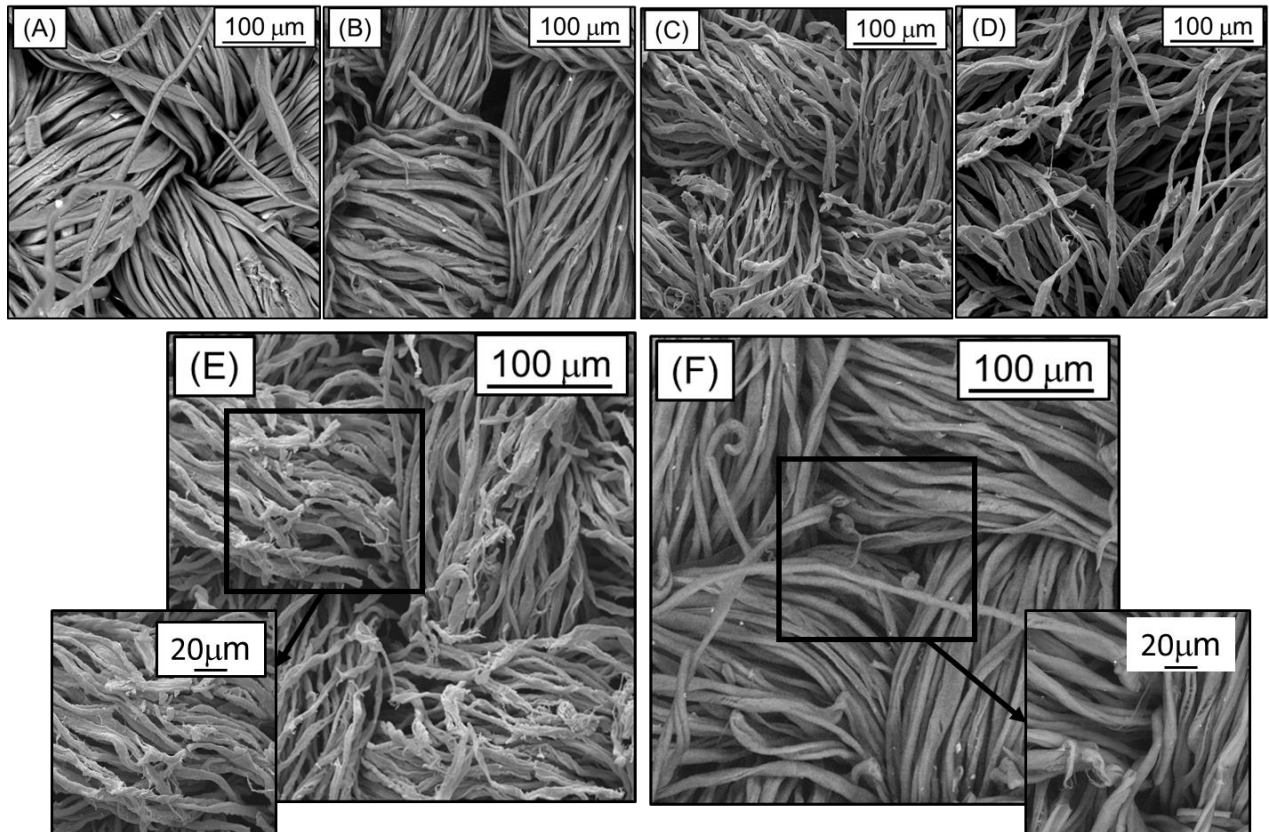


Figure 3.20. Scanning Electron Microscopy images on the chars produced from pyrolysis of cotton at different temperatures (a) raw cotton (b) 350 °C (c) 500 °C (d) 650 °C (e) 800 °C and (f) stepped pyrolysis char

The diameters of the cotton fibres were seen to decrease from 17.50 μm for unreacted cotton, through to 9.03 μm for 800 °C, these were taken as an average from multiple measurements around the image. The diameter of fibre for stepped pyrolysis was 13.21 μm which was comparable to the 13.50 μm seen for pyrolysis char formed at 350 °C. These changes in diameter are associated with the increased damage to the fibres seen in Figure 3.20. The greater damage leads to the fibres to fragment, creating thinner threads from the material bulk. There are small features that can be seen within the SEM images, these may

be remnants of paint, washing powder or other general wear and tear caused through the use of the textile. The features seen in the pyrolysed char were identified as flakes of oil that have embedded within the textile char following pyrolysis.

It can be seen that the overall structure of the fibres is maintained and can be seen to be preserved, even when the fibres are damaged. This can be attributed to the manufacturing process, causing the individual cotton fibres into thicker cotton yarn. Once this is woven, the cotton yarn is tightly held in place. As cotton does not melt at high temperatures, the fibres can be seen to retain the structure from the unreacted cotton, image a in Figure 3.20 shows the original textile structure, and whilst the structuring gets looser, the fibres are still weaved together showing that the overall structure of the chars remains intact.

3.5.2 Pyrolysis char of 91 % Polyester 9 % lycra mix textile waste at various temperatures

The chars produced through the pyrolysis of the polyester/lycra mix can be seen in Figure 3.21. ImageJ could only be used to measure the unreacted polyester/lycra mix, as after this there are no defined fibres.

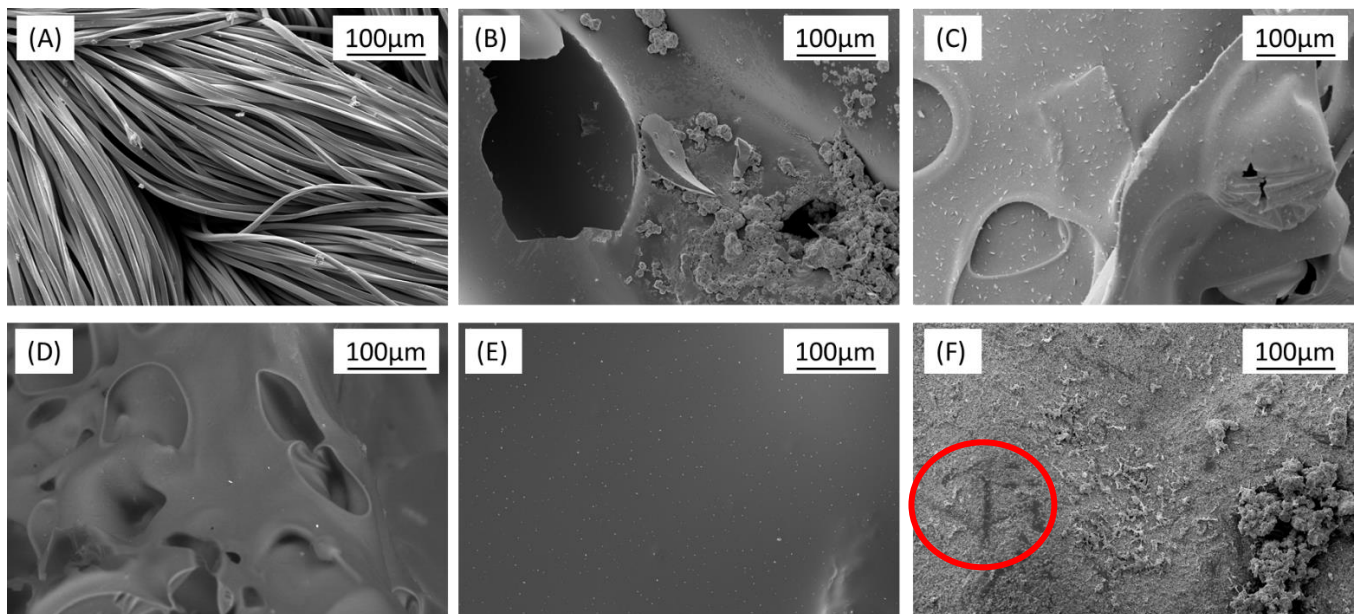


Figure 3.21. Scanning Electron Microscopy images of polyester/lycra mix chars produced through pyrolysis at different temperatures (a) raw polyester/lycra mix (b) 400 °C (c) 500 °C (d) 650 °C (e) 800 °C (f) stepped pyrolysis of polyester/lycra mix

Once the feedstock is heated, the fibre structure is lost and the sample resembles melted plastic. At 400 °C, shown in image B in Figure 3.21, it can be seen that where the sample became liquid and then cooled following the reaction that there are holes. These holes are due to the release of gases from within the sample, and can be seen through temperatures between 400 °C and 650 °C. The features seen, such as those embedded within the char produced at 500 °C and 800 °C are due to oil becoming trapped within the char whilst both are still liquid. As the liquid char is cooling, the oil becomes trapped within leading to these features. At 400 °C and 500 °C there is evidence of gas leaving the char during the cooling phase, displayed through the holes and bubbles on the surface. These holes and bubbles show that the material is in a liquid form whilst the gas evolves. As there are none of these features visible for 800 °C and the stepped pyrolysis it can be seen to have a relationship with temperature, and lower temperatures will be more susceptible. At 800 °C there are no features seen, due to the high pyrolysis temperature, the polyester/lycra mix remains in a liquid state for longer, allowing any defects caused by the release of gas to be engulfed with the liquid feedstock.

Stepped pyrolysis is seen to not have a smooth surface, although this may be a superficial coating. This may be caused by oil condensing within the reactor after the char has cooled and coating the char. The identified feature on image f in Figure 3.21, can be seen to reveal the expected smoother surface as seen in the fixed temperature pyrolysis, furthering that this is a superficial coating.



Figure 3.22. Lower magnification image of unreacted polyester/lycra textile waste feedstock

ImageJ analysis on the unreacted PE showed fibres of an average of 8.91 μm . The fibres appear more uniform than those seen in Figure 3.20 with the natural cotton fibres, which is to be expected from a synthetic material. A lower magnification image in Figure 3.22 shows that the polyester/lycra fibres are plaited, as opposed to the weaving seen in the cotton sample. This is due to the differences in manufacturing processes, and the requirements of the final product. In Figure 3.22 there are loose fibres that are not involved within the bulk material, these are caused through wear and tear during the life cycle of the textile.

As both polyester and lycra melt at higher temperatures, it is expected that the intrinsic structure will be lost at heating, especially compared to that of the cotton sample. The chars produced by the pyrolysis of cotton will have fewer future applications than those produced by the pyrolysis of cotton, especially the stepped pyrolysis. However, this shows how the choice of textile material will allow the tuning of the products and for this research the gas phase is the product of interest.

3.6 Energy dispersive X-ray spectroscopy for inorganic elemental analysis of char produced from textile waste pyrolysis

Energy dispersive x-ray spectroscopy (EDS) was carried out in tandem with the scanning electron microscopy image collection. As the sample is placed on a carbon tape, there may be a higher reported value for carbon, which will affect the other samples as the proportions are given as wt. % of the total mass.

3.6.1 Elemental analysis on chars produced from the pyrolysis of 100 % Cotton textile waste using EDS

The EDS shows that as the temperature increases, the proportion of carbon in the sample increases. In Figure 3.23 there is a clear increase in carbon content from 48.8 wt. % at 350 °C to 73.7 wt. % at 500 °C. This may be due to the aforementioned carbon tape leading to a disproportionate carbon content, although it is expected due to the consumption of oxygen within the sample during pyrolysis.

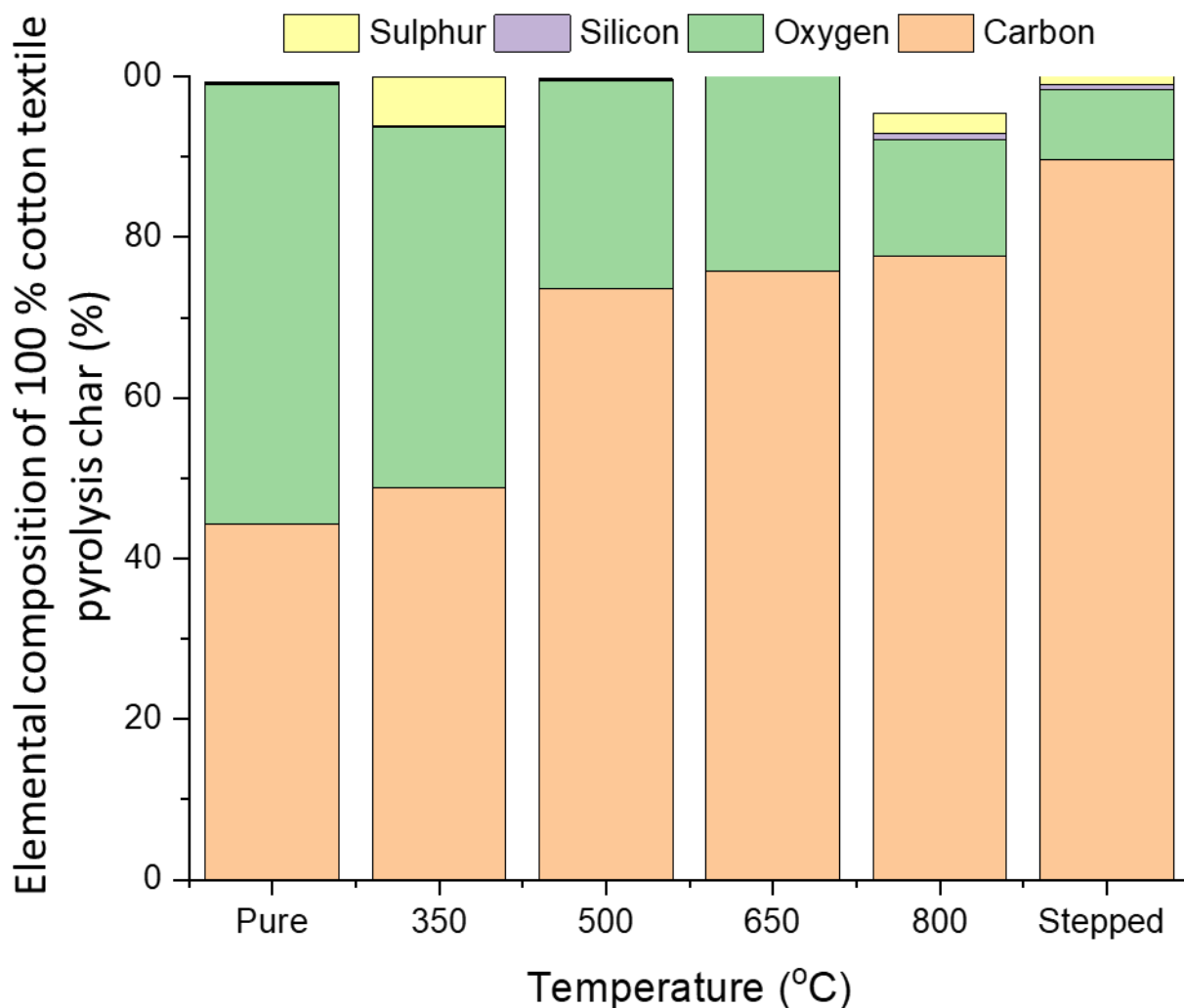


Figure 3.23. Energy Dispersive Spectroscopy data analysis on cotton chars produced at different temperatures during pyrolysis of 49.5 °C/min

Both the cotton char and feedstock are seen to be predominately carbon and oxygen rich. During the pyrolysis of the material, the carbon content increases in the sample. The stepped pyrolysis char contains the highest wt. % of carbon at 89.61 wt. %. This may be due to the higher final temperature causing a greater loss of other elements during the pyrolysis. The presence of silicone and sulphur seen in the char materials can be attributed to contaminants within the plates due to incorrect cleaning. They may also be due to the presence of oil flakes within the char, which were seen in some SEM images, as shown in Figure 3.20, as there is no significant, consistent, presence seen, they can be assumed to be negligible to the overall sample. As pyrolysis is carried out in the absence of oxygen, any available oxygen will be consumed preferentially. As the EDS data shows that the

proportions seen for 350 °C pyrolysis is similar to that of the unreacted cotton, it is further evidence, alongside the TGA and GC data that pyrolysis is inefficient at this temperature. This decrease in oxygen with increasing temperature is expected as the oxygen is consumed through the heating rate. A higher temperature leads to a greater consumption of oxygen from the textile and will affect the composition of the char.

3.6.2 Inorganic elemental analysis on chars produced from the pyrolysis of 91 % Polyester 9 % lycra textile waste using EDS

Similar to the trend shown in Figure 3.24, as the temperature of pyrolysis increases, so does the carbon content of the char. The pure feedstock is shown to have a higher starting carbon content, which due to the structure of polyester and lycra compared to cotton is to be expected.

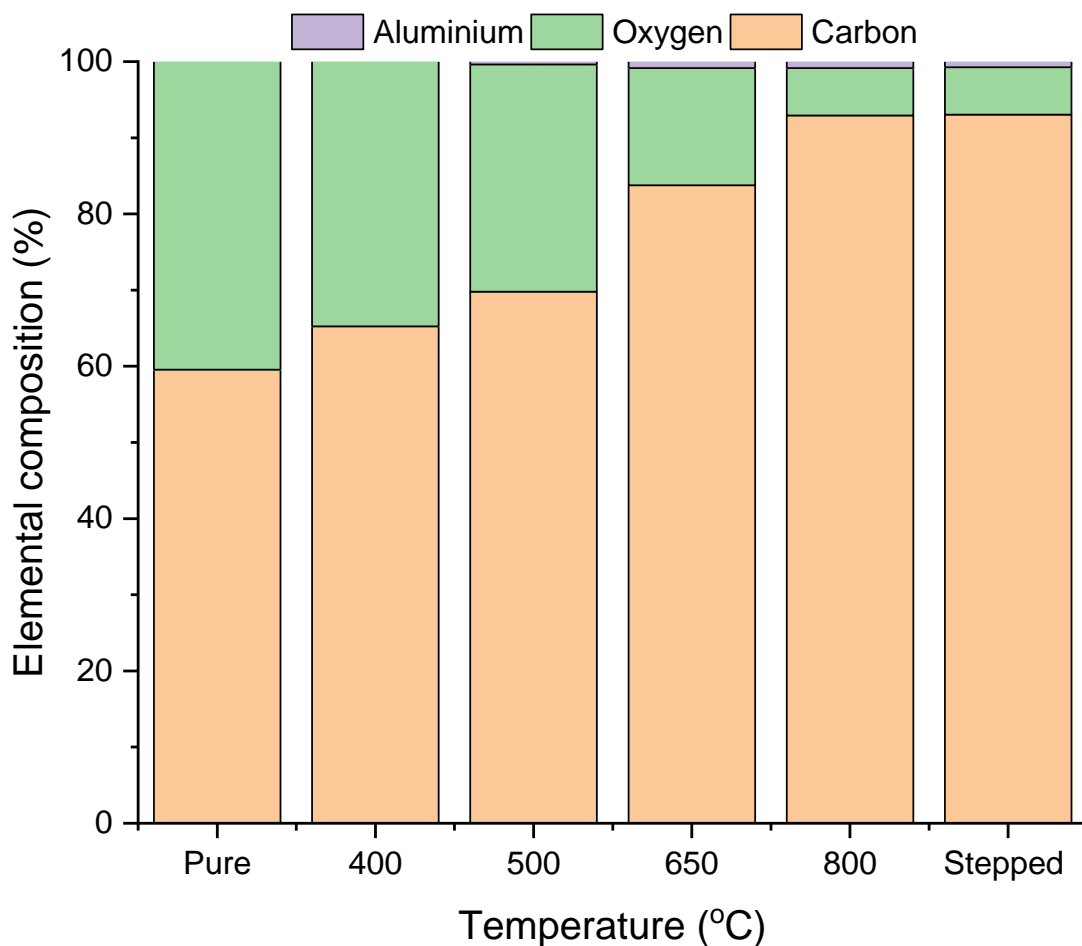


Figure 3.24. Energy Dispersive Spectroscopy analysis on chars produced from fast pyrolysis of polyester/lycra at different temperatures

As seen in Figure 3.24, there is a slow increase in the carbon content from 59.47 wt. % for the unreacted polyester/lycra mix through to 69.79 wt. % at 500 °C before a large jump to 83.77 wt. % and 92.93 wt. % for 650 °C and 800 °C respectively. This change, whilst partially due to the presence of the carbon tape used to secure the sample, can also be attributed to the increased carbon content of the sample. As the pyrolysis temperature increases, oxygen will be consumed faster within the system, and there will be less remaining oxygen within the sample. Stepped pyrolysis had the highest carbon content at 93.05 wt. % meaning that proportionally there was less oxygen, although this is similar to that seen for char produced through pyrolysis at a fixed temperature of 800 °C. This shows that the higher final temperature has allowed a greater rate of consumption of the oxygen in the sample.

The presence of aluminium that can be seen at the higher temperatures could be contaminants within the plate, or from the tools used to remove the sample from the reactor. It is unlikely to be from the produced oils or dyes, although aluminium can be used to ensure colour-fastness within textiles. As Figure 3.21 shows, the polyester/lycra feedstock loses the original structure and forms flakes of char, this shows the change in morphology which can be associated with the changes in the elemental composition. Through these structural changes, any atmospheric oxygen present within the fibres of the feedstock will be seen to be released, whilst the oxygen within the structure will remain as part of the char, albeit in small quantities.

3.7 Fourier-transform infrared spectroscopy (FT-IR) for the determination of structural bonds comprising the structure of chars produced from the pyrolysis of textile waste feedstocks

Fourier-transform infrared spectroscopy (FT-IR) analysis was used to determine the properties of the bonds seen within the chars, and original feedstocks. This allows a greater understanding of how the internal bonding of the chars is affected by the changes in heating rate and final temperatures.

3.7.1 Structural properties of chars produced through the pyrolysis of 100 % cotton textile waste

FT-IR was carried out on the cotton chars to give information on the structure and bonding features seen. The plots can be seen in Figure 3.25, and show a reduction in the

transmittance range which shows that there are less features visible, and that the whole frequency passes through the sample without impediment.

Based on the reported structure of cellulose, the expected peaks were identified in Table 3.5. The bending and stretching vibrations mean that the same feature will lead to more than one peak. Bending vibrations occur due to a change in angle, whilst the stretching vibrations occur due to a change in bond length.

Table 3.5. Table showing the expected peaks from cotton char Fourier-transform infrared spectroscopy [269].

Feature	Wavelength (cm⁻¹)	Bending or stretching
O-H	3550-3200	Stretching
C-H	3000 - 2840	Stretching
C-H	1450	Bending
O-H	1390 - 1310	Bending
C-O	1085 - 1050	Stretching

The pure cotton shows the greatest level of interaction with the infrared radiation, and allows the identification of peaks, and the relevant features. The first peak can be seen as a broad peak around 3320 cm⁻¹ which is associated with O-H bonds which can be seen in the structure of cellulose, a second peak is identified at 2903 cm⁻¹ which relates to C-H bonding, again these are present within cellulose. A peak at 1450 cm⁻¹ is related to C-H bonds, around 1250 cm⁻¹ to 1100 cm⁻¹ there are multiple peaks seen which relate to the C-O bonds seen in cellulose.

At the fixed temperature 350 °C pyrolysis char, there is a decrease in transmittance seen, meaning there is less occurring within this sample. There is a shallow, broad peak seen at 3350 cm⁻¹ and 2490 cm⁻¹ which reference O-H and C-H stretching vibrations. There is a strong peak around 1620 cm⁻¹ which is related to C=C stretching bond, typically in an unsaturated ketone, followed by a broad peak at 1050 cm⁻¹ which is associated with C-O primary alcohols. This shows that the bonding seen within the char changes with the increased pyrolysis temperature.

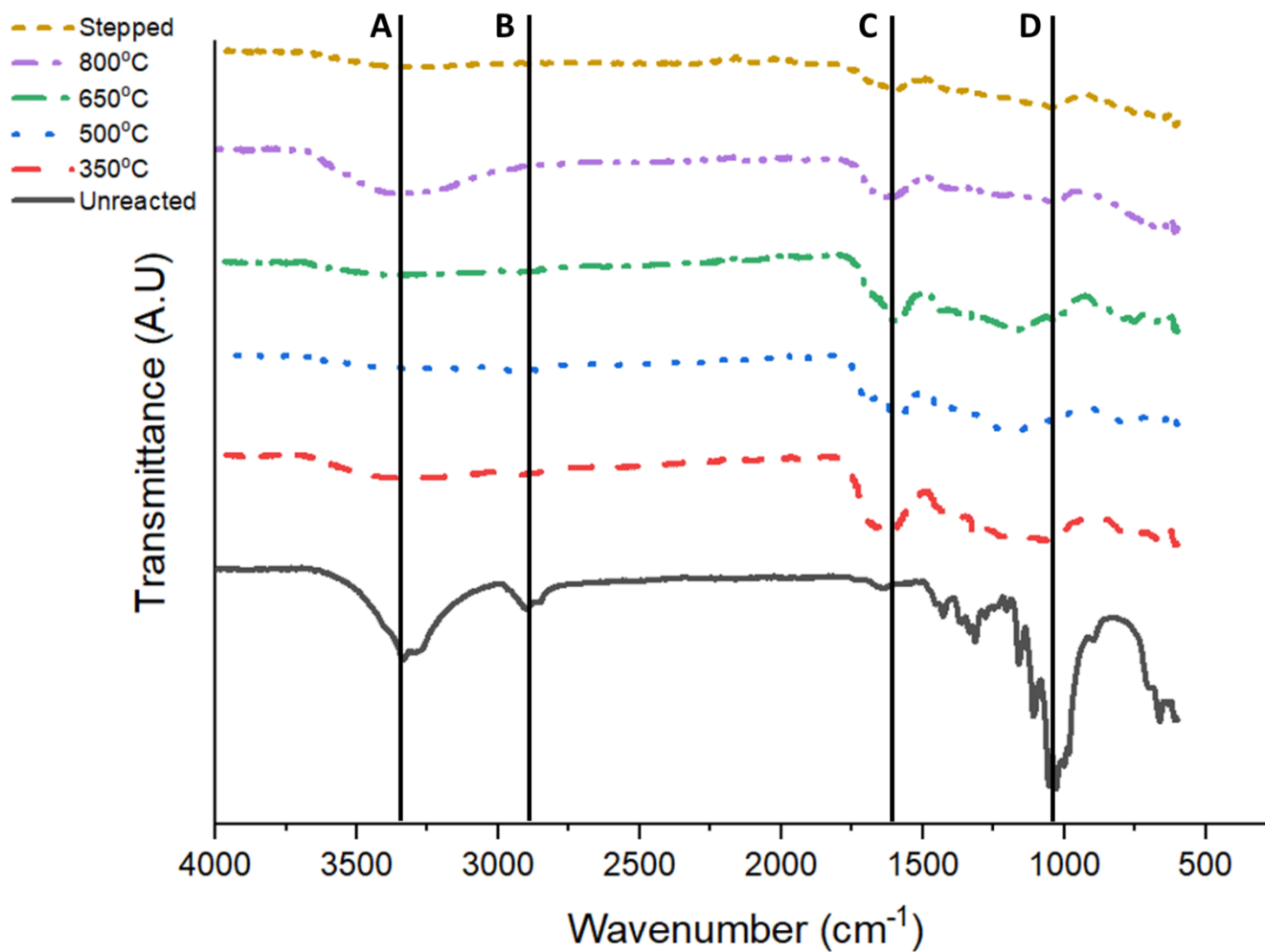


Figure 3.25. Fourier-Transform Infrared Spectroscopy data carried out on cotton chars produced at different pyrolysis temperatures where the labelled bands relate to O-H bonding (A), C-H bonding (B), C=C bonding (C) and C-O bonds (D).

The transmittance remains low for all the fixed temperature pyrolysis chars, the 500 °C char showed shallow peaks at 3310 cm⁻¹ and 2930 cm⁻¹ which are associated with the O-H and C-H stretching respectively. There is a distinct peak at 1700 cm⁻¹ which is reported as the C-H bending in an aromatic compound followed by a peak at 1600 cm⁻¹ which is related to the C=C stretching within the char. The 650 °C fixed temperature cotton pyrolysis char sample retains a broad, shallow peak at 3350 cm⁻¹ relating to O-H stretching, with the next peak seen at 1600 cm⁻¹ which is identified as C=C stretching. The final significant peak is seen at 1170 cm⁻¹ which is identified as C-O stretching for aliphatic ethers. At the highest fixed temperature pyrolysis, 800 °C, there is a broad peak seen at 3300 cm⁻¹ relating to O-H stretching and a single peak at 1610 cm⁻¹ related to the C=C stretching.

Whilst consistent peaks are seen; in particular the O-H stretching and C-O stretching, there is a change within the internal structure as the fixed pyrolysis temperature changes. Initially the major change is the C=C peak around 1620 cm⁻¹ showing a change in the bonding within the formed char, this peak remains visible throughout all the fixed temperature chars. It can therefore be assumed that during heating the cyclic structure is broken and bonds are reformed leading to the formation of C=C bonds.

Analysis of the stepped pyrolysis cotton char has peaks at 1048 cm⁻¹, 1601 cm⁻¹ and 3234 cm⁻¹ which are associated with CO-O-CO stretching, C=C stretching and O-H stretching respectively. This shows similarities with the chars produced at higher temperature pyrolysis. Although the presence of CO-O-CO stretching shows a difference in bond changes through heating, this variance can be attributed to the applied heating rate.

3.7.2 Structural properties of chars produced through the pyrolysis of 91 % polyester 9 % lycra textile waste

The expected peaks for polyester/lycra can be seen in Table 3.6. These are identified from the bonding seen within the structures of the feedstock materials. The plots can be seen in Figure 3.26, showing a decrease in the transmittance of the char, due to a reduction in the bonding seen for the polyester/lycra pyrolysis char.

Table 3.6. Expected peaks for the Fourier-transform infrared spectroscopy of polyester/lycra chars produced at different temperatures [269].

Feature	Wavenumber (cm⁻¹)	Bonding or stretching
C=O	1818 - 1650	Stretching
C-O	1310 - 1050	Stretching
C-H	3333 – 2695	Stretching
C-H	1465 – 1380	Bending
N-H	1650 - 1580	Bending
C-N	1250 - 1020	Stretching

These identified peaks can be used to determine the bonding seen within the char materials. For the pure polyester/lycra mix there is a sharp peak seen at 1710 cm⁻¹ which is related to C=O bonding, with other peaks seen at 1240 cm⁻¹, 1090 cm⁻¹, 1020 cm⁻¹ and 722 cm⁻¹ with a small, shallow peak seen at 2950 cm⁻¹. These relate to C-O, C-N, an additional C-N, C-H bond and a shallow O-H peak. It is worth noting that due to the sharp peaks seen for the pure polyester/lycra mix compared to the pure cotton, there is less hydrogen bonding present for polyester/lycra textile waste. This is expected due to the structures of these molecules, as well as the intramolecular bonding seen. At 400 °C fixed temperature pyrolysis, the transmittance of the char decreases and there are no significant peaks seen, this may be due to the nature of the char, which as seen in Figure 3.21 shows no structure, and has a visual appearance of being smooth with a shiny surface. This can interfere with the infrared, leading to an incorrect spectrum. Some peaks are seen for the char produced at 500 °C, although the transmittance is lower than that seen for the pure feedstock. Peaks are seen at 1680 cm⁻¹, 1430 cm⁻¹, 1280 cm⁻¹ and 729 cm⁻¹, relating to C=O, C-H, C-O and another C-H bond respectively. These show that the structure of the char still retains a similar structure as the unreacted feedstock. Visibly, the char produced at 500 °C was seen to be more matte than the chars produced at other temperatures, which explains why a spectrum could be seen. All other temperatures showed no significant peaks, and had a very low transmittance, which can be attributed to both the visual properties of the char, as well as the change in structure that is caused by the pyrolysis of the feedstock. This shows that

there are no significant bonds seen, or that it may be predominantly C-C bonds, which are notoriously difficult to accurately, and reliably, identify.

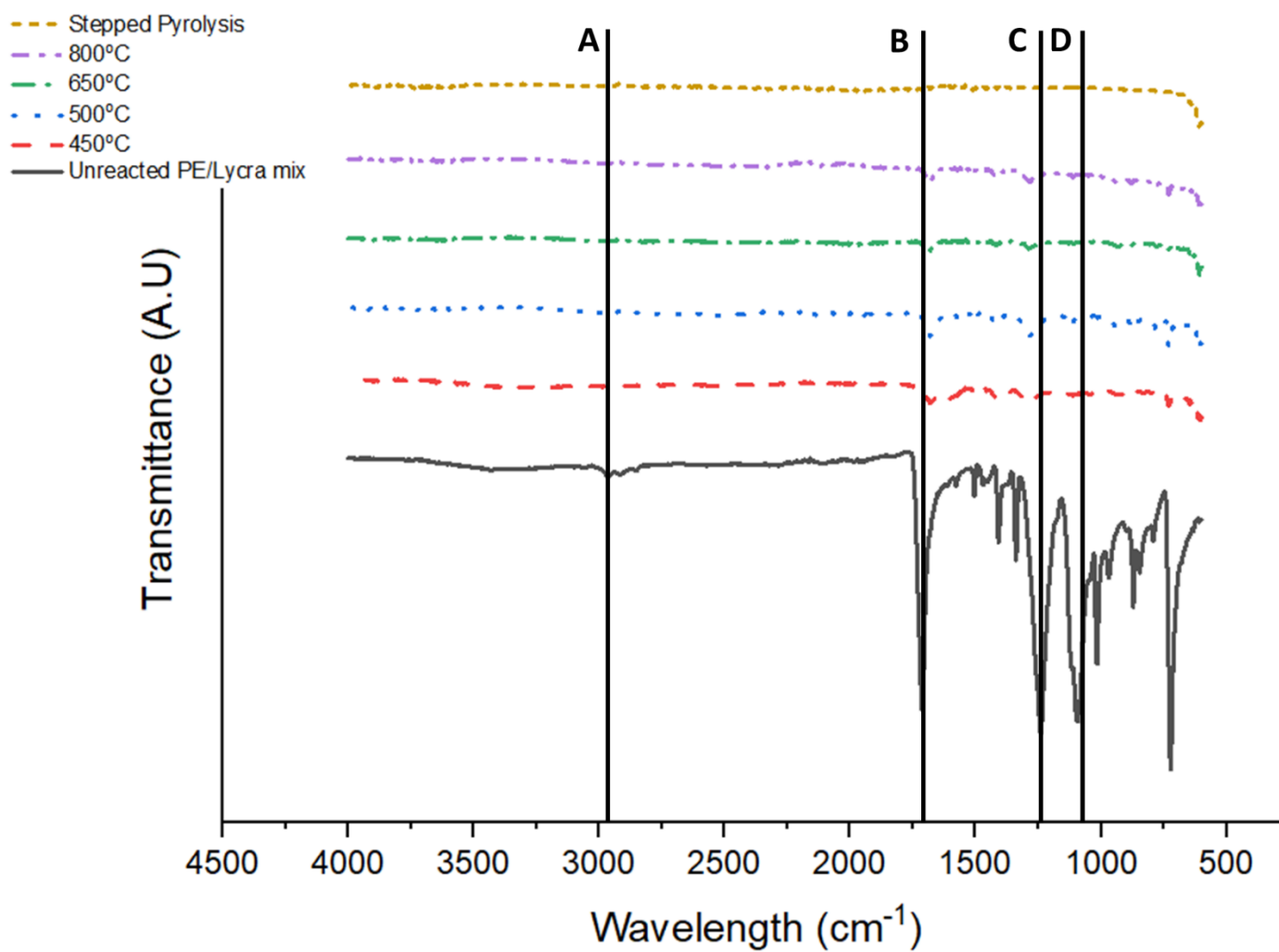


Figure 3.26. Fourier-transform infrared spectroscopy data for the chars produced at varied temperatures of pyrolysis of polyester/lycra textile waste where the labelled bands relate to O-H bonds (A), C=O bonds (B), C-O bonds (C) and C-H bonds (D)

3.8 Elemental analysis to determine the CHN and oxygen content of chars produced through the pyrolysis of textile waste at different temperatures.

The elemental analysis was carried out to identify the relative quantities of carbon, nitrogen and oxygen within a sample. This will allow an understanding of how the pyrolysis temperature will alter the structure, and composition of the char. This approach will only consider the organic elements through combustion, whilst the inorganics were determined through energy dispersive spectroscopy.

3.8.1 Elemental analysis of chars produced through the pyrolysis of 100 % cotton textile waste

As seen in Table 3.7, the elemental analysis allowed the composition of the cotton chars to be determined. As the pyrolysis temperature increased, the carbon content also increased, from 43 wt. % for the unreacted feedstock, through to a peak carbon content seen at 500 °C with 81.6 wt. %, before a decrease is seen through to 71.9 wt. % at 800 °C. Considering the changes in bonding seen with increased temperatures in Figure 3.25, it is expected that there would be a greater carbon content as the temperature increased, as shown in Figure 3.23. However, the elemental analysis that is shown in Table 3.7, is more accurate, and less likely to be affected by contaminants. There is an agreement that the carbon content will initially increase with higher temperatures, however, it may be that after a certain point there is an increased consumption of the carbon within the structure, to the point where the elemental composition changes, and starts to decrease. For the cotton pyrolysis chars produced at 800 °C and through stepped pyrolysis, the hydrogen content increases from a low of 2.15 wt. % at 650 °C to 4.52 and 4.58 wt. % at 800 °C and stepped pyrolysis respectively. This increase may be due to oils becoming embedded in the cotton char, leading to an increase in hydrogen seen. Nitrogen content is stable from the unreacted sample at 0.15 wt. % through to 0.13 wt. % for the 800 °C char before falling to 0.07 wt. % for the stepped pyrolysis char. This decrease shows that the nitrogen is intrinsically linked within the structure of the polyester chars and only decreases with slow heating rates.

Table 3.7. CHN analysis of 100 % cotton chars produced at different pyrolysis temperatures

Sample	Carbon content (wt.%)	Hydrogen content (wt.%)	Nitrogen content (wt.%)	Oxygen content (wt.%)
Raw cotton	43	6.52	0.15	49.21
300 °C 100 % cotton	66.1	4.57	0.13	28.76
350 °C 100 % cotton	72.5	4.86	0.12	21.40
500 °C 100 % cotton	81.6	3.41	0.12	18.35
650 °C 100 % cotton	78.5	2.15	0.12	17.44
800 °C 100 % cotton	71.9	4.52	0.13	22.34
Stepped pyrolysis	71.4	4.58	0.07	22.84

As the stepped pyrolysis has a similar elemental composition to the char produced at 800 °C, this shows that despite a different in structure seen in Figure 3.20, the elemental composition is similar. As both these samples were heated to high temperatures, this implies that the higher temperatures lead to similar char composition.

The oxygen content, calculated by difference, of the cotton char is seen to decrease initially with an increase in pyrolysis temperature, from 49.21 wt. % for the unreacted feedstock to 17.44 wt% at 650 °C which is also seen in Figure 3.25, with a decrease in C-O and O-H bonds seen, supporting a similar decrease in the weight percent of hydrogen seen with the same temperature increase. At 800 °C the oxygen content increases to 22.34 wt. % with the stepped pyrolysis having 22.84 wt. % oxygen, this is again supported by Figure 3.25, with a peak for the O-H bonding being seen. This increase in oxygen is due to the reforming of alcohol groups from the deposition of oils and secondary pyrolysis leading to further reactions that were not expected. There is no increased bonding seen for C-O bonds showing that only the alcohol groups are reformed at the higher temperatures.

There will be incombustible inorganics remaining within the sample following combustion using the LECO Truspec. This ash content produced can be used to determine the oxygen content using Equation 6. The ash content was found to be 1.11 wt. % following the ashing of a sample of 100 % cotton in oxygen, this represents the inorganic portion of the textile sample.

3.8.2 Elemental analysis of chars produced through the pyrolysis of 91 % polyester 9 % lycra textile waste

The elemental analysis of the polyester/lycra mix can be seen in Table 3.8. This gives information on how the pyrolysis process affects the char composition at different temperatures.

Table 3.8. Elemental analysis of polyester/lycra mix chars produced at different pyrolysis temperatures

Sample	Carbon content (wt.%)	Hydrogen content (wt.%)	Nitrogen content (wt.%)	Oxygen content (wt.%)
Raw 91 % polyester 9 % lycra	61.6	4.84	0.19	32.93
400 °C 91 % polyester 9 % lycra	85.7	4.02	0.90	8.94
500 °C 91 % polyester 9 % lycra	87.5	3.67	0.87	7.52
650 °C 91 % polyester 9 % lycra	88.5	3.25	0.9	6.91
800 °C 91 % polyester 9 % lycra	89.8	2.98	0.89	5.89
Stepped pyrolysis	90	2.8	1.04	5.72

As seen in Figure 3.24 and Table 3.8 and compared to Figure 3.23 and Table 3.7 the carbon content of the unreacted polyester/lycra textile waste is higher than that of cotton. This is expected due to the structures of both polyester and lycra. The hydrogen content is lower for unreacted polyester/lycra compared to that of cotton, which is expected due to the structure of cellulose compared to the PET and lycra. The ash content was found to be 0.44 wt.% representing the inorganic content of the 91 % polyester 9 % lycra textile waste sample. Table 3.8 shows that with the increasing pyrolysis temperature there was an

increasing carbon content in the char material, with a significantly lower oxygen content when compared to the cotton char.

3.9 Nitrogen physisorption, porosity and surface area of chars produced through the pyrolysis of textile waste at different temperatures

The surface area and porosity of the chars were determined through the use of nitrogen physisorption. This allows an understanding of how the porosity and surface area of the char material is affected by different pyrolysis temperatures. The adsorption plots can be used to give information on the pore size of the material. Type I is seen for microporous solids, and is characterised by a concave shape for the relative pressure. Type II is seen for non-porous, or macroporous, materials, it is identified through a shallow 's' shape. Type III indicates unrestricted multilayer formation and is seen where the isotherm is convex to the relative pressure, and is also associated with non-porous or macroporous materials. Both type IV and V are related to mesoporous solids, and are characterised with a hysteresis loop being visible when both the adsorption and desorption are plotted, although the adsorption is seen to a more defined 's' shape. The final type is the VI which is defined by a series of steps, which correlate to the monolayer capacity for each adsorbed layer. Type VI are associated with uniform non-porous surfaces [275].

3.9.1 Porosity and surface area of chars produced from pyrolysis of 100 % cotton textile waste

The isotherms produced through the analysis of cotton chars at different pyrolysis temperatures are shown in Figure 3.27. It can be seen that the chars produced at fixed temperatures 650 and 800 °C as well as pure cotton, have similar adsorption patterns, showing that they will have similar porosity.

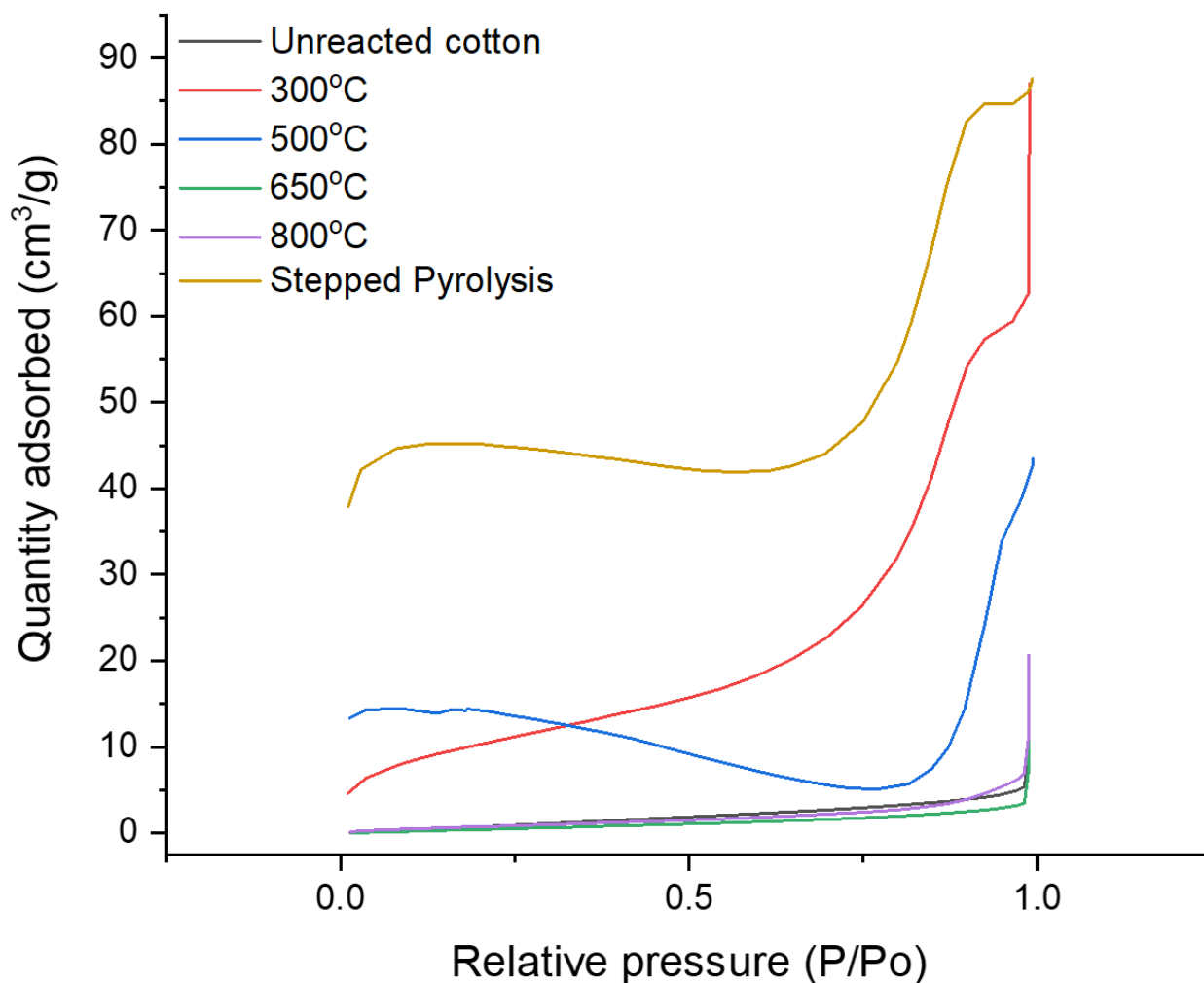


Figure 3.27. Absorption for the chars produced from pyrolysis of cotton textile waste at different temperatures of fast pyrolysis, from unreacted feedstock to 800 °C as well as the slow pyrolysis sample

Figure 3.27 shows that the pure cotton, 650 and 800 °C pyrolysis chars can be assigned as type VI mesoporous, having pores larger than 2 nm but smaller than 50 nm, which is supported from the data seen in Table 3.9. Pure cotton and chars produced at 650 and 800 °C do not fit the type VI mesoporous isotherm, Figure 3.28 shows these in more detail. They appear to resemble closest the type III isotherm, meaning a macroporous, or non-porous material, this means that there is a low surface area for these three samples. This is supported by the surface area seen in Table 3.9, but the pore size suggests a mesoporous material. Therefore, the isotherms can be assumed to show a visual indication of these properties, but need to be considered with the plotted data to be truly useful.

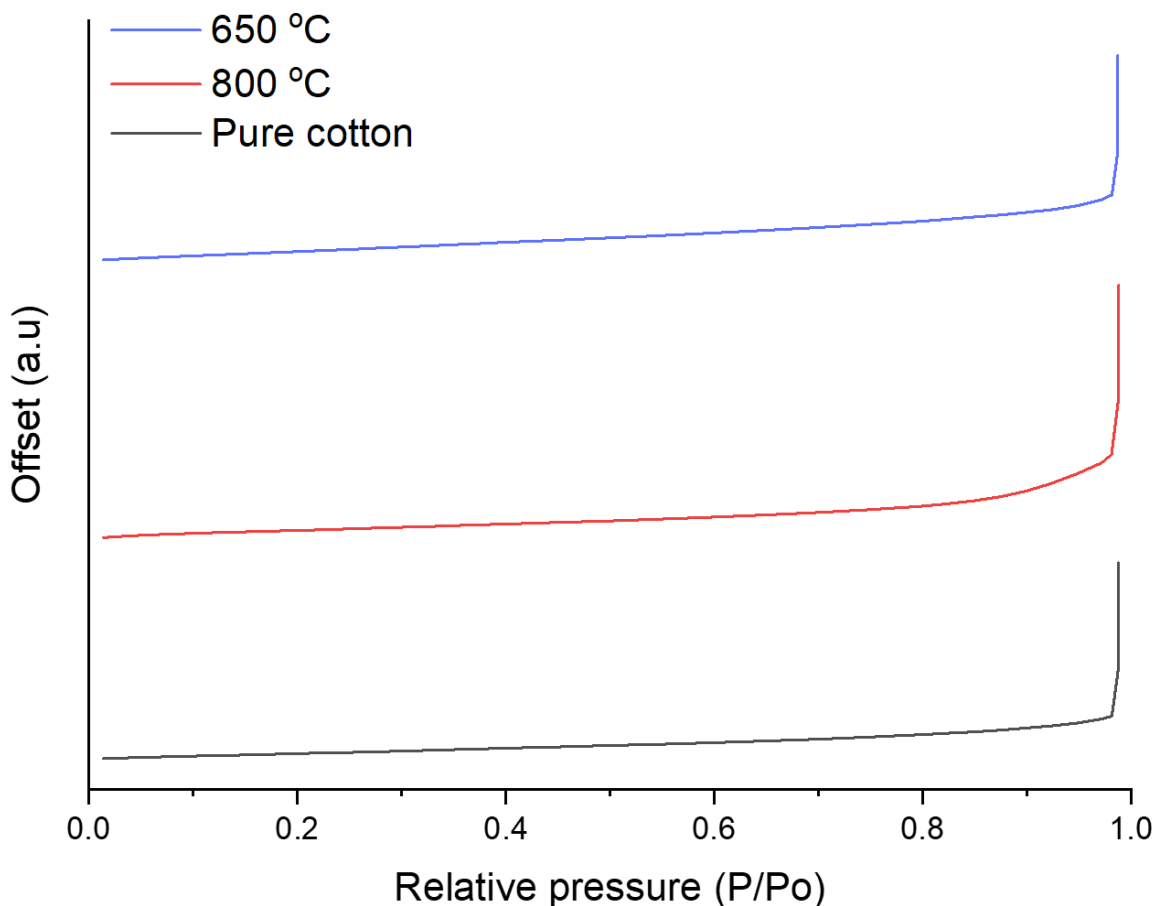


Figure 3.28. Offset adsorption isotherms for cotton chars produced through high temperature fast pyrolysis, as well as the unreacted feedstock

Once the full adsorption and desorption have been plotted, BJH and BET equations can be applied to calculate the surface area, pore volume and pore size of the char. As seen in Table 3.9, there is an initial increase in surface area with the rise in temperature, from 5.89 m^2/g to 48 m^2/g at 350 $^\circ\text{C}$, although at 500 $^\circ\text{C}$ the surface area is still 38.94 m^2/g . At 650 and 800 $^\circ\text{C}$ the surface area decreases down to 3.89 m^2/g and 3.50 m^2/g respectively.

The initial increase in surface area can be attributed to the reduction of weaker-bonded groups that are consumed, increasing the surface area [276]. The pore size is expected to decrease with increasing surface area, as a larger pore size implies a smaller number of pores on the material, whilst a smaller pore size will lead to an increase in the pore number, increasing the surface area. This is seen to be true, with a change from 19.12 nm for the unreacted cotton, before decreasing to 14.88 nm at 350 $^\circ\text{C}$. The decrease of pore size with increased surface area can be associated with the loss of volatiles and moisture from the

surface of the fibres, this then produces a greater number of pores, which will be small in size. As the temperature increases further, the structure of the fibres becomes more damaged, as seen in Figure 3.20, causing the pores to collapse and connect, leading to the increased pore size.

The stepped pyrolysis char, despite having a top pyrolysis temperature of 750 °C, has the highest surface area of 136.07 m²/g. As slow pyrolysis is seen to preserve the structure of the char, the surface area is expected to be high, as the loss of volatiles within the sample causes the increase of the surface area, however, at the higher temperatures, this structure is maintained. Therefore, the pore sizes are conserved. Comparing Figure 3.20 images e and f, the integrity of the stepped pyrolysis structure can be seen. The pore sizes given in Table 3.9 are an average of the BJH plots, therefore it can be expected that there should be the presence of macropores due to the structure of the cotton char that can be seen in Figure 3.20, there may be adsorption of nitrogen within the spaces between the fibres.

Table 3.9. Surface area, pore size and pore volume calculated from the physisorption of nitrogen at different temperatures on chars produced through the pyrolysis of cotton at different temperatures

Temperature condition	Surface area (m²/g)	Pore volume (cm³/g)	Pore size (nm)
Pure cotton	5.89 ± 0.10	0.025	19.147
300 °C	36.42 ± 0.22	0.130	12.337
350 °C	48.21 ± 0.22	0.179	14.883
500 °C	38.94 ± 2.08	0.050	18.465
650 °C	3.89 ± 0.25	0.024	29.367
800 °C	3.50 ± 0.09	0.032	27.732
Stepped pyrolysis	136.07 ± 4.82	0.078	11.452

The pore volume will typically increase with an increased surface area, and with an inverse relationship to the pore size. At the higher temperatures of 500 to 800 °C the decrease in pore volume can be due to collapse of pores due to the damaged fibres, this will couple with the pore size increase as the pores will become shallower yet have a larger opening, explaining the lower surface area.

3.9.2 Porosity and surface area of chars produced from pyrolysis of 91 % polyester 9 % lycra textile waste

The porosity of the polyester chars did not seem to change with temperature, with a low porosity seen for the unreacted material as well as the chars formed (Figure 3.29). For the chars produced at pyrolysis temperatures over 450 °C there was no adsorption seen, which is to be expected due to the structure of the textile. As the sample is heated up, the highly synthetic content starts to melt, producing a pore-less material. Figure 3.21 shows the surface of the char sample, and from 500 to 800 °C there are no significant features so there was no measured physisorption of nitrogen leading to no measured surface area. The stepped pyrolysis char shows some surface texture which could allow the adsorption of nitrogen on the surface of the char. Therefore, it can be seen that the initial structure of the textile waste can influence the surface area of the resultant char. As the polyester material is synthetic, and polymer based, the resultant char acts like a melted plastic, which in turn limits the porosity of the sample.

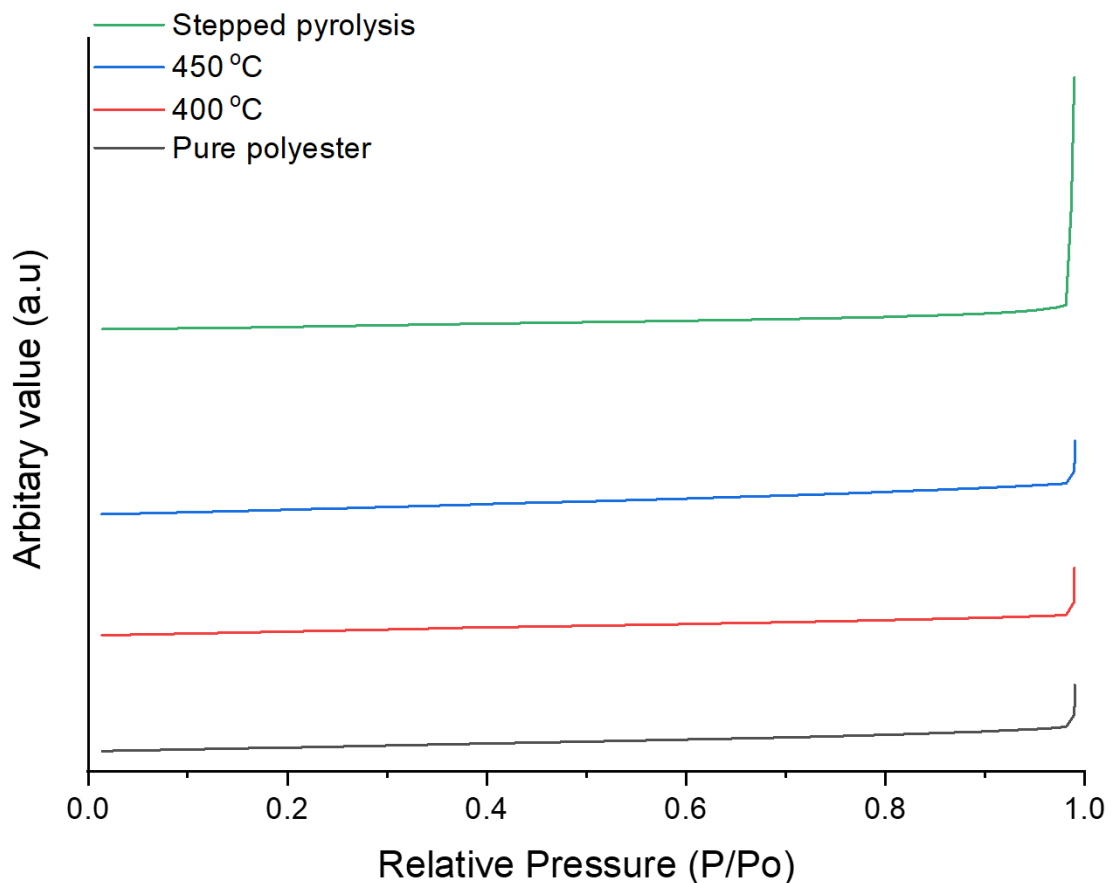


Figure 3.29. Adsorption isotherm for polyester textile char samples following pyrolysis at different temperatures

The chars produced through the pyrolysis of polyester/lycra textile waste showed limited porosity, based off the adsorption of nitrogen on the surface. This may be due to the nature of the polyester/lycra fibres, which were seen to be very smooth which will limit the physisorption of nitrogen. This translates to a reduced surface area as the pyrolysis temperature increases, Table 3.10, which is due to the decreasing pore size as the polymer fibres begin to melt. As the polyester/lycra starts is heated, the fibres are seen to melt and the surface area decreases from 9.21 m²/g for the unreacted polyester/lycra sample, to 5.93 m²/g for the 400 °C pyrolysis temperature, whilst the pore size does increase by 1 nm in this temperature range. This may indicate that as the temperature of the pyrolysis increases, extra pores may become visible as the surface coating is melted off. This change may be related to a sampling issue, whereby the sample has broken revealing internal air bubbles formed during the pyrolysis of the char. These air bubbles may lead to the increased surface area of 7.46 m²/g for the char produced at 450 °C. All the char samples for the

polyester/lycra textile waste samples can be seen to had a much lower surface area at the same pyrolysis temperature. The unreacted polyester/lycra sample does have a higher surface area compared to that of the cotton, which may be due to defects seen within the surface of the polyester/lycra fibres.

Table 3.10. Surface area, pore volume and size for the physisorption of nitrogen at different temperatures on chars produced through the pyrolysis of polyester at different temperatures

Temperature condition	Surface area (m²/g)	Pore volume (cm³/g)	Pore size (nm)
Pure PE/lycra sample	9.21 ± 3.56	0.012	15.035
400 °C	5.93 ± 0.88	0.012	16.306
450 °C	7.46 ± 2.02	0.013	12.218
Stepped pyrolysis	Bulk	Bulk	Bulk

The physisorption of nitrogen on the stepped pyrolysis char sample produced an isotherm, but the calculations could not be applied due to the bulk nature of the material. There was no accurate approach to calculate these methods which means that it is assigned as a bulk material. As the samples between 500 and 800 °C showed no adsorption isotherm they can also be assumed to have bulk properties for surface area, pore volume and pore size.

3.10 Conclusions

The pyrolysis of textile waste gives three products; gas, oil and char. Following analysis, it is clear that the temperature of pyrolysis will affect the quality of the products, as well as the original feedstock. Depending on the desired products, these parameters can be altered. As the fixed temperature of the pyrolysis increased, the char yield was seen to decrease with an increased production of oil.

For cotton, the main gas that was produced through any pyrolysis temperature were the carbon dioxide and monoxide gases, which based on the ultimate elemental analysis is to be expected. Although the higher temperature pyrolysis does favour a greater production of hydrogen and methane compared to the lower temperatures, with the highest hydrogen yield of 20 % seen at 800 °C and 18 % methane at 650 °C. The stepped pyrolysis showed three clear regions; carbon dioxide rich between 350 and 350 °C, carbon monoxide rich

between 500 and 600 °C and hydrogen rich over 600 °C. Although, it is expected that at the higher temperatures there is a secondary pyrolysis of the produced oils occurring, as the heavier pyrolysis oils will remain within the reactor. For cotton pyrolysis oils, there is no significant change in the proportions of the classification of molecule seen, with cyclic molecules having the highest contribution independent of reaction temperature, and all the oils contained levoglucosan and benzoic acid. Therefore, it can be assumed that an alteration of the temperature will not significantly affect the oil production at lab scale.

The chars formed from the pyrolysis of cotton textile waste showed that temperature will have a significant impact on the structure, and composition of the char. At higher temperature fixed pyrolysis, there is visible damage to the fibres, and the importance of applying a heating rate on the conservation on structure, and surface area is clear. The cotton chars also show the relationship of temperature with the surface area of the fibre. As volatile components decrease and the carbon content initially increases so does the surface area and pore volume whilst the pore size decreases. Although stepped pyrolysis, as an example of slow pyrolysis, maintains the structure of the char, as well as increasing the surface area from the unreacted material. The surface area for the unreacted cotton was $5.89 \pm 0.10 \text{ m}^2/\text{g}$ which increased to $136.07 \pm 4.82 \text{ m}^2/\text{g}$ for the stepped pyrolysis char. Considering the Fourier-transform infrared spectroscopy on the cotton chars, the bonding changes with an increase in temperature. From the 350 °C pyrolysis and upwards there is the presence of C=C bonds, which was not seen in the presence of the unreacted material, or the structure of cellulose. Therefore, it can be assumed that the cyclic cellulose regions are broken with the application of heat, to reform into C=C bonds. It is unknown the extent of this change within the overall structure of the material.

The TGA data showed that pyrolysis would start from 350 °C for cotton textile waste which was confirmed following experimental investigation. There was no significant gas formation below 350 °C, as exemplified by the stepped pyrolysis, although the char will be affected by the temperature, pyrolysis of the sample will not occur. The polyester/lycra mix was seen to require a higher temperature for the pyrolysis to occur, at around 400 °C, this is due to the stronger bonds within the sample, requiring a greater energy to overcome. This was confirmed by both the TGA and gas chromatography readings, as well as the higher

activation energy seen for the polyester/lycra sample compared to that of the cotton sample.

Due to the nature of polyester and lycra, it was expected that both would melt once heated rather than form a porous material, and this was shown in Figure 3.21. The initial structure is lost as soon as the sample is heated to 400 °C and above, this is seen in stepped pyrolysis as well. The Fourier-transform infrared spectroscopy showed that the polyester/lycra chars retained minimal bonds, although this may be due to the surface of the polyester/lycra char reflecting the infrared beam rather than internal bond changes. There appears to be C-N bonds seen within the unreacted feedstock, which are then lost during pyrolysis, showing that the C-N bonds are the first to be lost during pyrolysis.

The carbon content of the unreacted polyester/lycra material was higher than that of cotton, 61.6 wt. % compared to 43 wt. %, which is expected due to the structures seen. This can be seen in the dominance of carbon containing gases; methane, carbon dioxide and carbon monoxide. The polyester/lycra textile waste sees a similar pattern to that of cotton, where there is an increase in carbon content within the chars as the temperature increases. Whereas the cotton carbon content decreases past 500 °C, the carbon content of polyester/lycra mix is seen to plateau after a certain point, without decreasing. This may be due to the higher initial carbon content forming the skeleton of the polyester structure which cannot be removed even with increasing temperatures.

The oil formation from the pyrolysis of polyester/lycra mix is seen to be predominately cyclic and carboxylic acid molecules, with a similar content of each classification for each temperature, meaning that similarly to cotton, there is no significant impact on oil production through the changing of temperature. It can be seen that based on the individual structures of both polyester and lycra alongside cotton, that certain products can be controlled with changing temperatures. For example, if a high yield of carbon dioxide or monoxide gas is required, then a higher fixed pyrolysis temperature of cotton is required, which in turn will lower the surface area of the char produced. If a high surface area char is required then a slow pyrolysis approach should be used.

Chapter 4 - Production, and optimisation, of carbon using catalytic chemical vapour deposition

4.1 Introduction

The formation of carbon was carried out using chemical vapour deposition over a nickel catalyst to produce a carbon deposition layer. Different parameters were selected, and explored to promote the synthesis of carbon. The pyrolysis temperatures of the cotton and polyester/lycra feedstocks were varied, alongside the chemical vapour deposition temperature and carrier gas flow. The nickel catalyst was selected due to literature showing an increased yield for the production of carbon nanomaterials [82, 85, 91, 99] although selectivity was low with nanofibers, nanotubes and graphene seen to be produced. The catalyst was synthesised as set out in section 2.1 before being tested using x-ray diffraction to determine the crystallinity of the sample, as well as the lattice structure, which was supported from transmission electron microscopy.

Scanning electron microscopy allowed the topography of the catalyst to be explored whilst the energy dispersive x-ray spectroscopy showed the inorganic composition of the catalyst, allowing the surface loading to be determined whilst inductively coupled plasma spectroscopy was used to determine the total metal content. The porosity and surface area were determined through nitrogen physisorption. The SEM images were used to measure the catalyst particle sizes, to determine the uniformity of the synthesised catalysts and to visualise how the catalyst clusters formed. Once the catalyst was characterised chemical vapour deposition was used to produce carbon nanomaterials. The process was optimised to ensure that the maximal carbon yield can be seen from the carbon containing gases produced from the pyrolysis of the textile waste.

Literature shows that small carbon chains are the most effective for the production of carbon through chemical vapour deposition [86, 92, 93, 104] with the presence of hydrogen increasing the yield of carbon nanomaterials. Therefore, the gases produced through the pyrolysis of textile waste can be used to produce carbon. As a control sample, pure methane was used to synthesise carbon over the nickel catalyst, the structure of the resultant carbon nanomaterials was compared to the structures produced from the CVD of the textile waste pyrolysis gases. Following carbon synthesis, the produced carbon nanomaterials were characterised. The samples underwent X-ray diffraction to determine if the carbon was amorphous or crystalline, and to see if the catalyst material was altered during CVD. The surface area and porosity of the carbon was investigated using nitrogen physisorption, this

will give information into the future applications, and how well the carbon will impregnate an epoxy matrix. Scanning electron microscopy showed the structure of the produced carbon, with higher resolution images being produced through transmission electron microscopy (TEM), allowing the identification of the type, or types, of carbon nanomaterial produced. TEM can also be used to determine the growth type of the carbon on the metal catalyst. Where possible the carbon nanostructures were measured using ImageJ software to give detailed information on the structure.

It is worth noting that a methane control sample was produced, this has been referred to in the text as 'methane sample'. As stated in literature [53, 62, 69] methane gives the highest quality carbon nanomaterials and so was used as a reference for the textile waste carbon nanomaterial samples.

4.2 Nickel alumina catalysts used for catalytic chemical vapour deposition

It was decided that a nickel alumina catalyst would be the most efficient for the formation of carbon from the carbon containing gases. It was determined that a metal loading of over 70 % would be the most efficient for this conversion and so theoretical loadings of 70 % Ni, 80 % Ni and 90 % Ni with the remainder being alumina. A higher metal loading should allow a greater activity to be seen, in this case this would allow a better yield of carbon. Ni and Al nitrate salts were selected to limit the contamination that can be caused by chloride salts due to the preferential binding. The solubility of nitrate salts is high enough to prevent residual nitrates within the sample.

4.2.1 X-ray diffraction of nickel catalysts

Once passivated, and fully dried, the catalysts were analysed using x-ray diffraction. This allowed the degree of crystallinity to be identified, as well as to determine if the nickel metal had oxidised during the synthesis. Figure 4.1 shows that the catalyst has a majority crystalline nature, exemplified by sharp peaks, if the sample were amorphous then the peaks would be broad. The individual peaks seen were identified as nickel and alumina [277, 278].

Despite x-ray diffraction not being a quantitative method, the intensity can be used to determine if the proportions change. As can be seen in Figure 4.1 the 70 % nickel sample has clearer alumina peaks when compared to the 90 % nickel sample. This is caused by the

relative intensity of the nickel peaks increasing, and those for alumina decreasing. Electron diffraction was used to confirm the crystal structure of the catalyst. The planes of the crystal showed the (111) (200) and (220), confirming the presence of the Ni metal and the (312) plane for the alumina was also seen. The (525) plane for the alumina cannot be seen, this may be as the predicted distance from the centre of the electron beam to the (525) point would be greater than that imaged.

Scherrer equation is used to determine the crystallite size as seen in Equation 7.

$$\tau = \frac{K\lambda}{\beta \cos\theta} \quad \text{Equation 7.}$$

Where:

- τ is the mean crystallite size
- K is a dimensionless shape factor (0.89)
- λ is the wavelength used in the XRD, in this case Cu is 0.1542 nm
- β is the full width at half maximum, calculated through manual integration (radians)
- θ is the diffraction angle for the associated peak ($^{\circ}$)

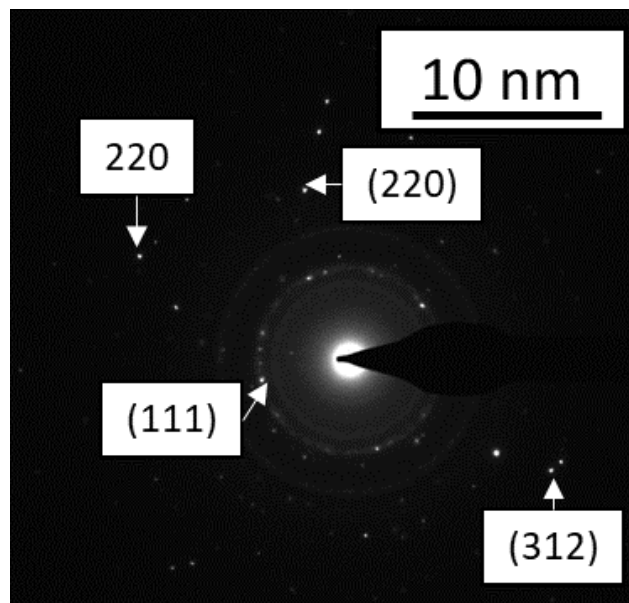
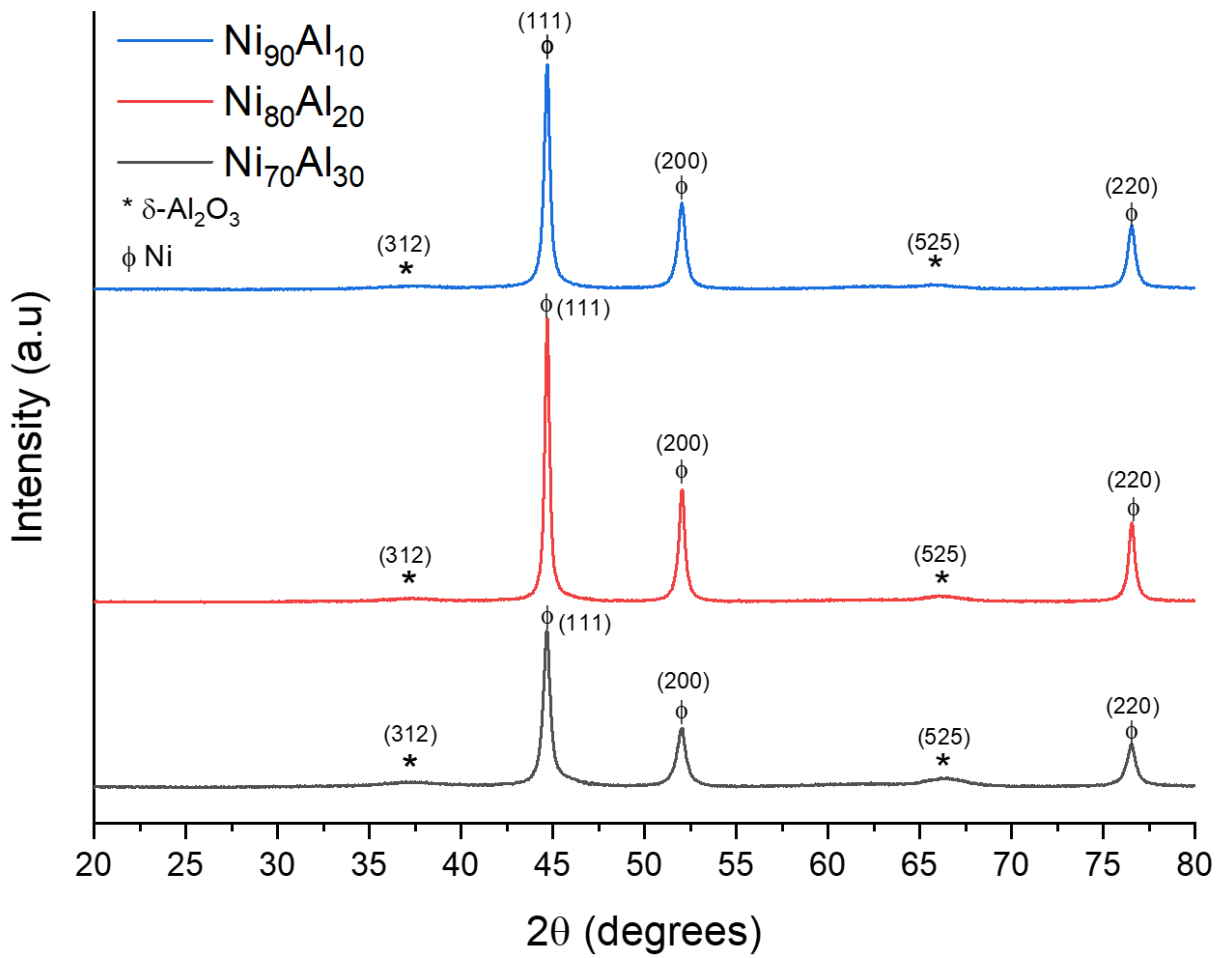


Figure 4.1. X-ray diffraction and an example of electron diffraction for different metal loaded catalyst powders, metal loadings were seen to be 70 % Ni, 80 % Ni and 90 % Ni. The hkl peaks were assigned based off the ICDD's PDF-2 2023 database.

Scherrer's equation, equation 7, was used to determine the crystallite size for the catalysts showing that the average crystallite size for the 90 % nickel sample was 24.9 nm with 80 % nickel having an average crystallite size of 28.64 nm and the 70 % nickel sample having an average size of 30.35 nm. This shows that with the higher support content, there is a higher crystallite size, this is because the alumina is causing a greater level of agglomeration by surrounding the nickel nanoparticles. At the higher metal content, the catalyst crystallite size decreases, due to the higher metal loading and a reduced support structure content. Measurements taken from the TEM images confirmed these measurements, showing that the 90 % nickel had the smallest crystallite size, this is confirmed in Figure 4.4.

4.2.2 Microscopy and elemental analysis of nickel catalysts

Scanning electron microscopy was used to determine the microstructure of the catalysts, followed by energy dispersive x-ray spectroscopy to determine the inorganic elements present within the catalyst. This testing was carried out following grinding of the catalyst, to achieve a greater level of homogeneity of sizes, to ensure a greater level of consistency during experimental work. As can be seen in Figure 4.2, the particle sizes are not uniform, the 70 % and 80 % catalyst show some homogeneity within the sample whilst the 90 % nickel sample shows a mix of large and small particles. These were measured using ImageJ to determine the variance of size within the sample. The distribution of the length of the particles can be seen in Figure 4.3, where it is clear that there is a greater spread of particle sizes for the 90 % and 70 % nickel catalyst, with a standard deviation of 32.71 and 34.92 respectively whilst 80 % nickel catalyst only had a standard deviation of 18.54. There were more particles seen through the analysis of 80 % and 90 % nickel catalysts, than that for the 70 % nickel, this might be due to the human error in the grinding process, as well as the higher proportion of alumina in the catalyst. The most populous size of particle for the 70 % nickel catalyst is between 100 and 120 μm whereas the 80 % nickel catalyst has a mode size of 40 to 60 μm and for the 90 % nickel catalyst the most common size is between 20 and 40 μm . Meaning that a large portion of the sample has similar particle sizes. The 70 % Ni catalyst has no overlap with the other catalysts, with the majority of the particles being between 70 and 150 nm. This larger particle size is likely directly related to the grinding of the post-reduction catalyst, however, it may also be due to the greater amount of support structure leading to agglomeration.

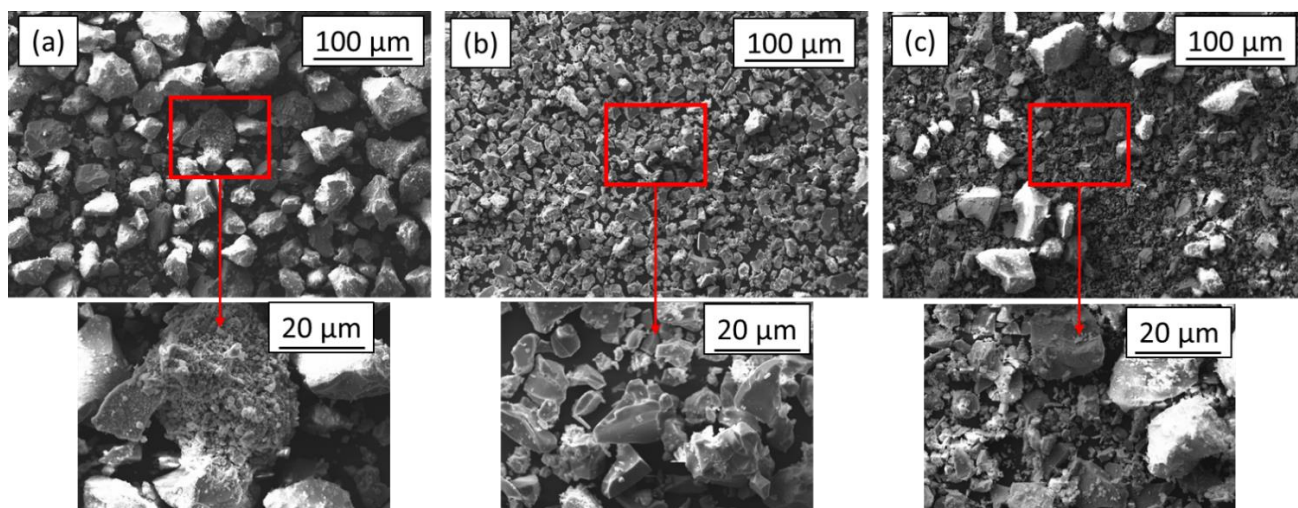


Figure 4.2. Scanning electron images of the catalyst at different metal loadings (a) 70 % nickel 30 % alumina (b) 80 % nickel 20 % alumina and (c) 90 % nickel 10 % alumina

As can be seen in the higher magnification insert images shown in Figure 4.2, none of the catalyst particles are uniformly smooth. There are deposits of smaller particles on the surface of the larger ones, which could be caused by the grinding of the catalyst. The microscopy also shows that there is some uniformity between all catalyst samples in terms of particle shape, with similar profiles seen with each metal loading.

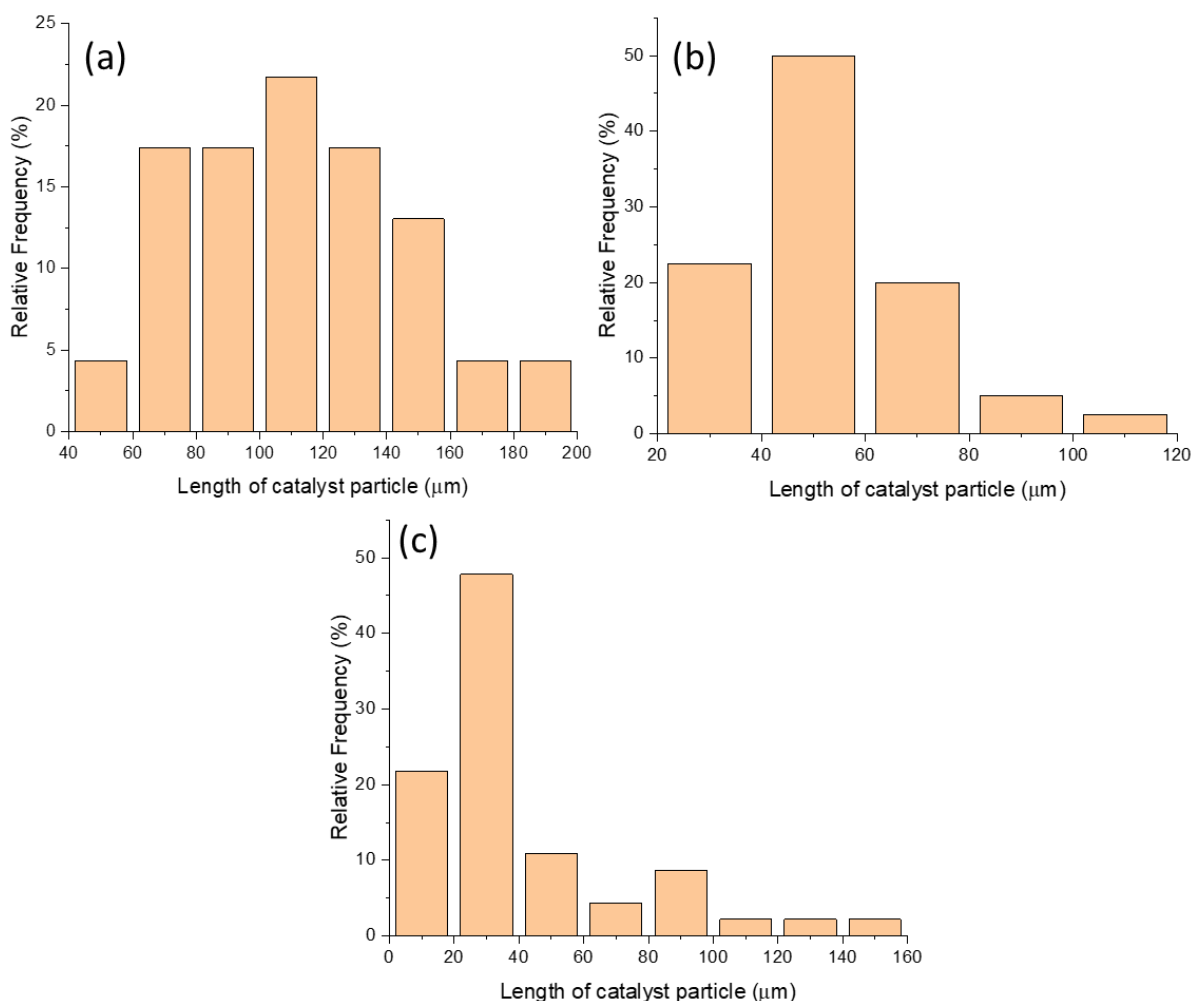


Figure 4.3. Catalyst cluster size distributions, for different metal loading for catalysts (a) 70 % nickel 30 % alumina (b) 80 % nickel 20 % alumina and (c) 90 % nickel 10 % alumina

Using the transmission electron microscopy, the metal nanoparticles that comprise the catalyst can be seen, as shown in Figure 4.4, with the particle size distribution shown in Figure 4.5. Visually there are no significant changes to the particle sizes with increased metal loading. Although the cluster of the alumina support structure surrounding the metal nickel particles can be seen to decrease, leading to smaller catalyst particles. This is supported by the changing average particle length seen in Figure 4.3. This suggests that the greater metal loading, which naturally leads to a reduced support loading, will affect the catalyst cluster size. Figure 4.4 shows that there is inherent inhomogeneity within the size of the metal nanoparticles, especially that of nickel. There were occasions where alumina sheets were seen to be formed for the 70 % Ni sample, these were destroyed by the electron beam during imaging so it can be assumed that these are not stable. The Ni

nanoparticles are seen to be faceted, which as discussed in Section 1.4.1.3 can lead to the formation of carbon nanofibers, as opposed to carbon nanotubes.

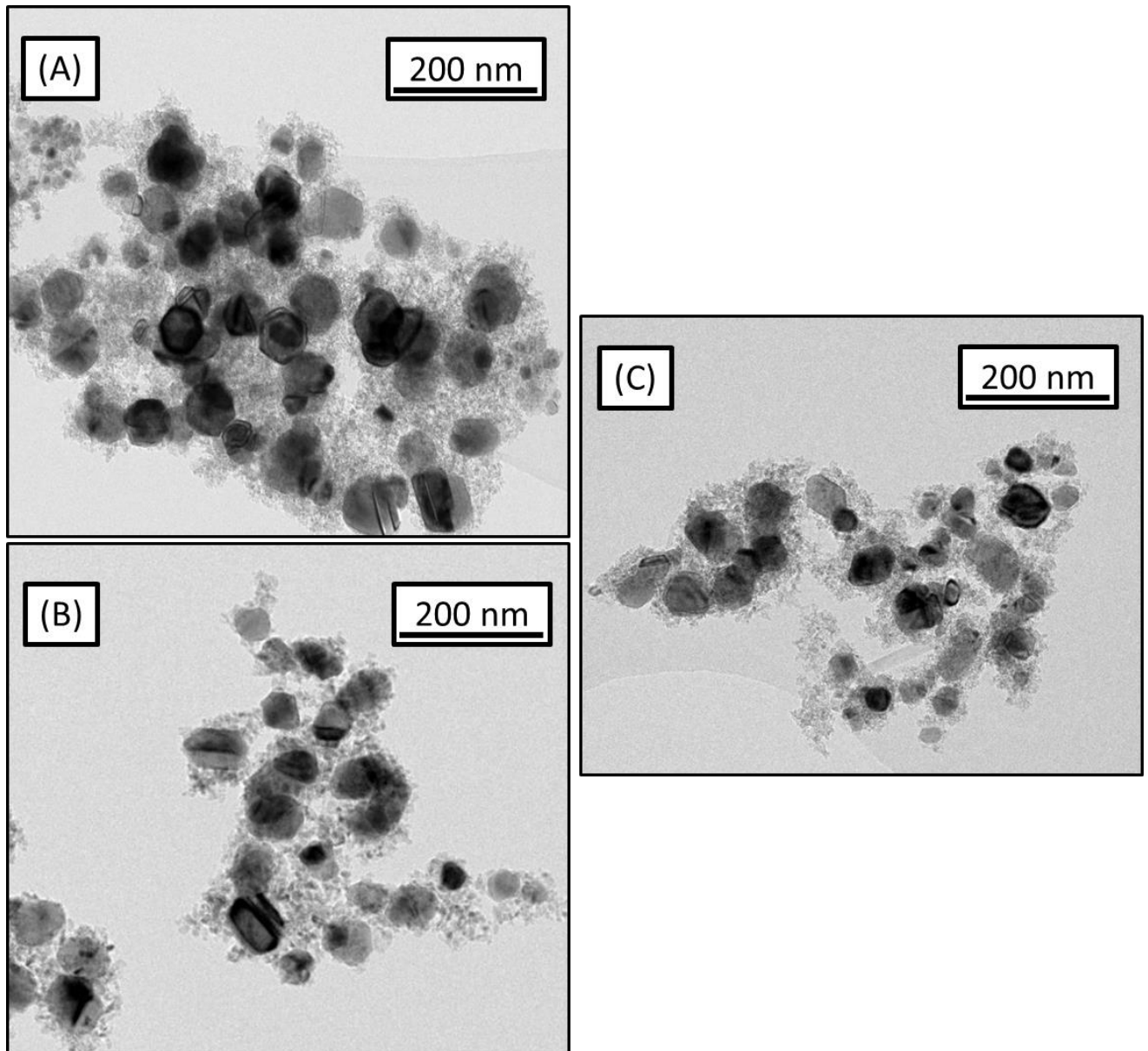


Figure 4.4. Transmission electron microscopy image of the (A) 70 % Ni 30 % alumina sample (B) 80 % Ni 20 % alumina and (C) 90 % Ni 10 % alumina sample

Considering the nanoparticle size distribution, Figure 4.5, it can be seen that the size of the alumina nanoparticles decreases with an increase in the alumina loading from a frequency of 25 % in the 2 – 2.5 nm at 30 % alumina to 30 % 4 – 6 nm at 10 % alumina. For both the 70 and 80 % nickel samples, the most frequent measurement of the Ni nanoparticle was 30 to 40 nm which increased to 60 to 70 nm for the 90 % Ni sample. The Ni nanoparticles measured within the 90 % catalyst, Figure 4.5, shows that there is a greater variance of particles with a similar frequency, between 30 and 60 nm and 70 to 80 nm all have a

frequency of 15 %. This means that there is a greater lack of homogeneity for the 90 % Ni sample.

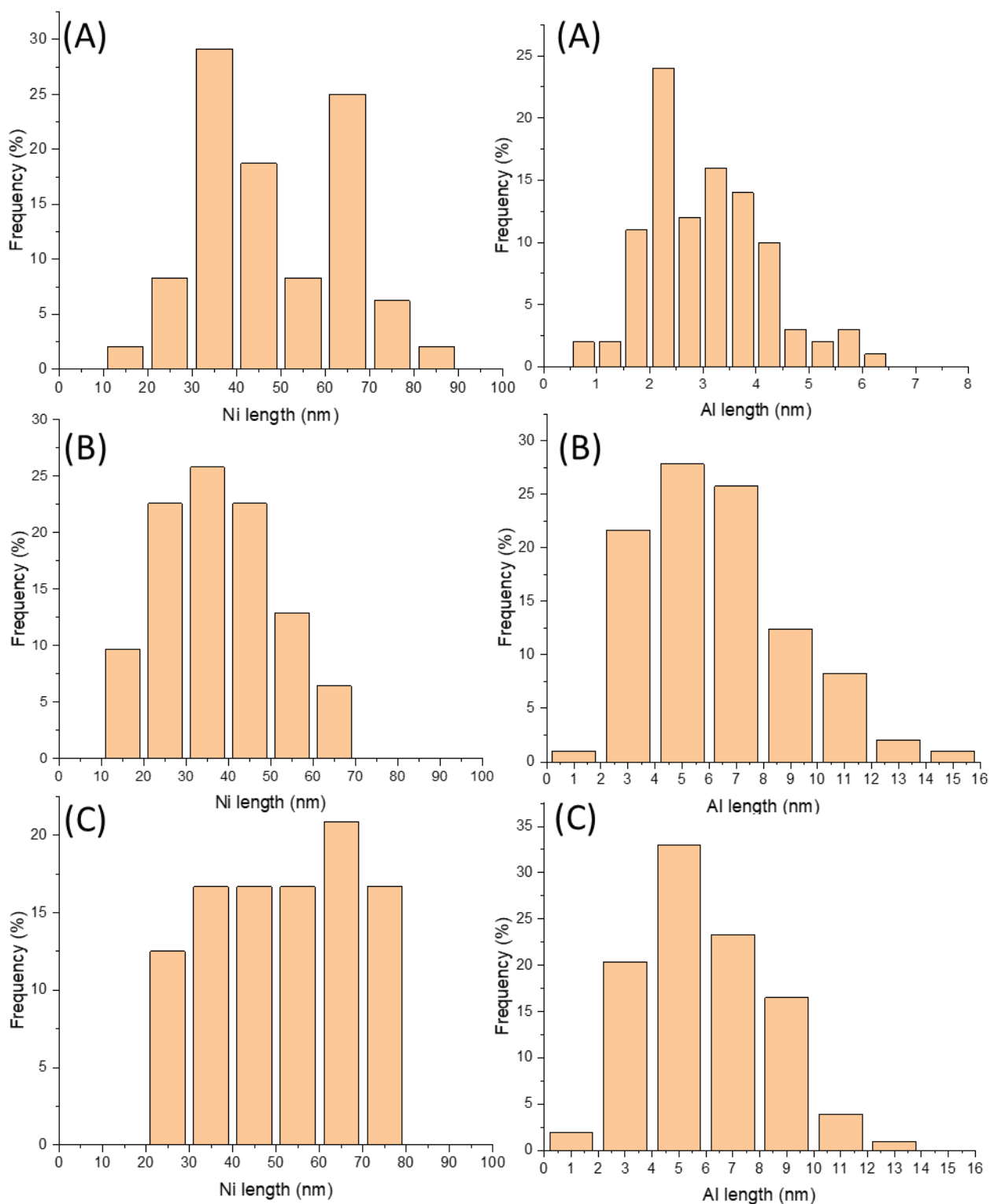


Figure 4.5. Particle size distribution for nickel and alumina nanoparticles within (A) 70 % nickel 30 % alumina catalyst (B) 80 % nickel 20 % alumina catalyst (C) 90 % nickel 10 % alumina catalyst

Elemental analysis was carried out during the scanning electron microscopy process. The theoretical loadings of 70, 80 and 90 % nickel can be compared to the measured values, these are displayed in Figure 4.6. It is worth noting that the EDS will only determine the surface layer of the catalyst, without penetrating deeper within the particles. This gives information on the initial proportions of the metal active sites available, as during catalyst use cracks may form, leading to the internal structure to be exposed for further reactions. There is an increase in the measured loading with the theoretical loading, although all are measured as lower than the expected loading. As the lower metal loadings there is an increase in the oxygen content on the surface of the catalyst, which is in line with the higher aluminium content seen, as the aluminium support is in the form alumina oxide. The differences between the theoretical and measured values are likely caused due to agglomeration and variations within the formation of the catalyst. As only a small portion of the catalyst was tested, this may not be a full representation of the metal loading.

There is a greater variance seen in the recorded weight percentages of nickel, especially compared to alumina. This greater increase in variance in the oxygen content can be due to the surface oxidation that can occur due to improper storage, as well as different proportions of full conversion to Al_2O_3 of the catalyst support structure. The standard deviation of the weight % of nickel in the catalyst is 5.25 for 70 % nickel, increasing to 9.52 for 80 % nickel and decreasing to 6.49 for 90 % nickel. This shows that the 80 % nickel catalyst has the least homogeneity within the sample, this may be due to the grinding process revealing more of the surface area, whereas the sample containing larger samples will contain more nickel internally, which will not be measured through EDS. Different sites on the same sample were measured, ensuring a spread of data was collected. However, this also shows that the catalyst loading is not homogenous and will vary across the surface of the catalyst material, especially for the 80 % nickel catalyst.

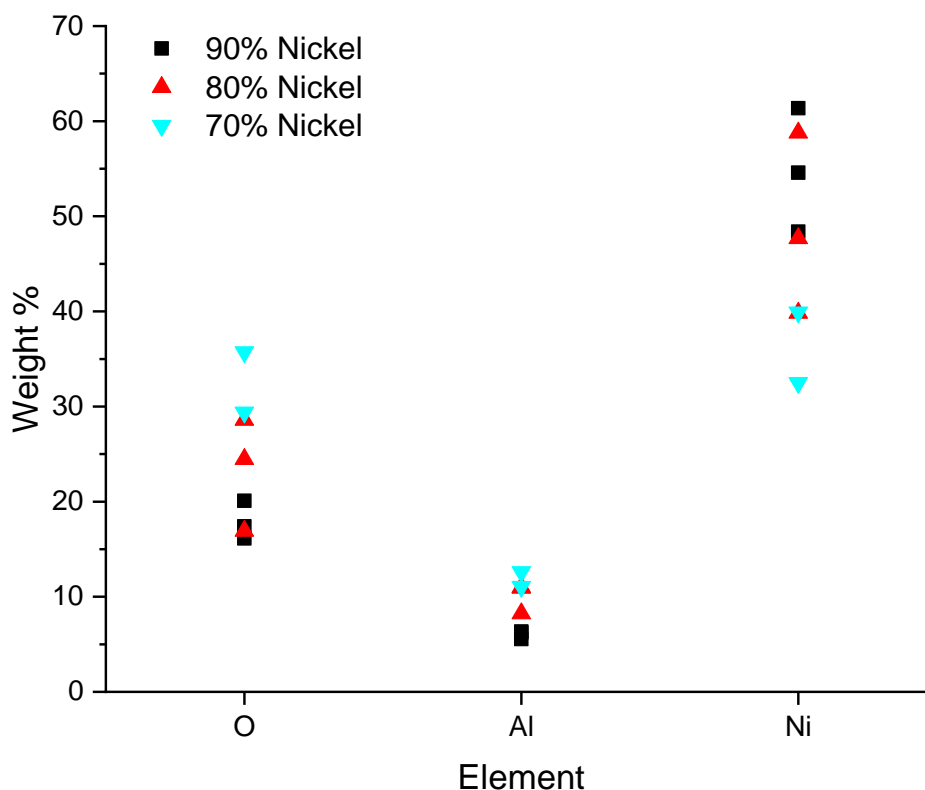


Figure 4.6. Energy dispersive x-ray spectroscopy elemental analysis on the different metal loadings of the catalysts produced with theoretical yields of 90, 80 and 70 % Nickel. Multiple measurements were taken and presented to show the range of data collected.

There may be a limit in the available metal loading on the support structure, causing excess to be washed off. Figure 4.6 shows that the maximal loading of nickel on the alumina oxide support at the surface of the catalyst should be considered to be around 60 %. It appears that the oxygen content varies, which as the catalyst support has been identified as Al_2O_3 , Figure 4.1, is expected, although not to this extent. The molecular mass of alumina is 101.96 g/mol with oxygen contributing 44.13 wt.% towards this. Even with the 30 % alumina support for the 70 % catalyst there should only be a maximum of 15 wt.% contribution from oxygen. This means that because the higher oxygen content within the sample it can be assumed that some oxidation of the sample has occurred, this may mean that the passivation of the sample has been incomplete, or that during storage oxidation has begun to occur. This indicates that following the storage of the catalyst the activity may be decreased due to the increased oxygen content. The process by which the nickel and alumina interacted was determined to be a nickel doped with aluminium to prevent

agglomeration. Figure 4.7, alongside Figure 4.4, shows that the nickel present in the catalyst is in nanoparticle form as there are clear boundaries between each nanoscale particle.

HAADF imaging was coupled with EDS to map the elemental surface of a 90 % Ni catalyst sample. Due to time limitations this could not be repeated for all samples. Figure 4.7 shows that there are clear nickel metal particles supported by a sea of aluminium and oxygen.

There is almost 100 % overlap between the oxygen and aluminium so it can safely be assumed that an aluminium oxide has been formed. It can be assumed that this is the same for all the catalyst samples, whereby the active component is supported and is accessible for the formation of carbon during the CVD process.

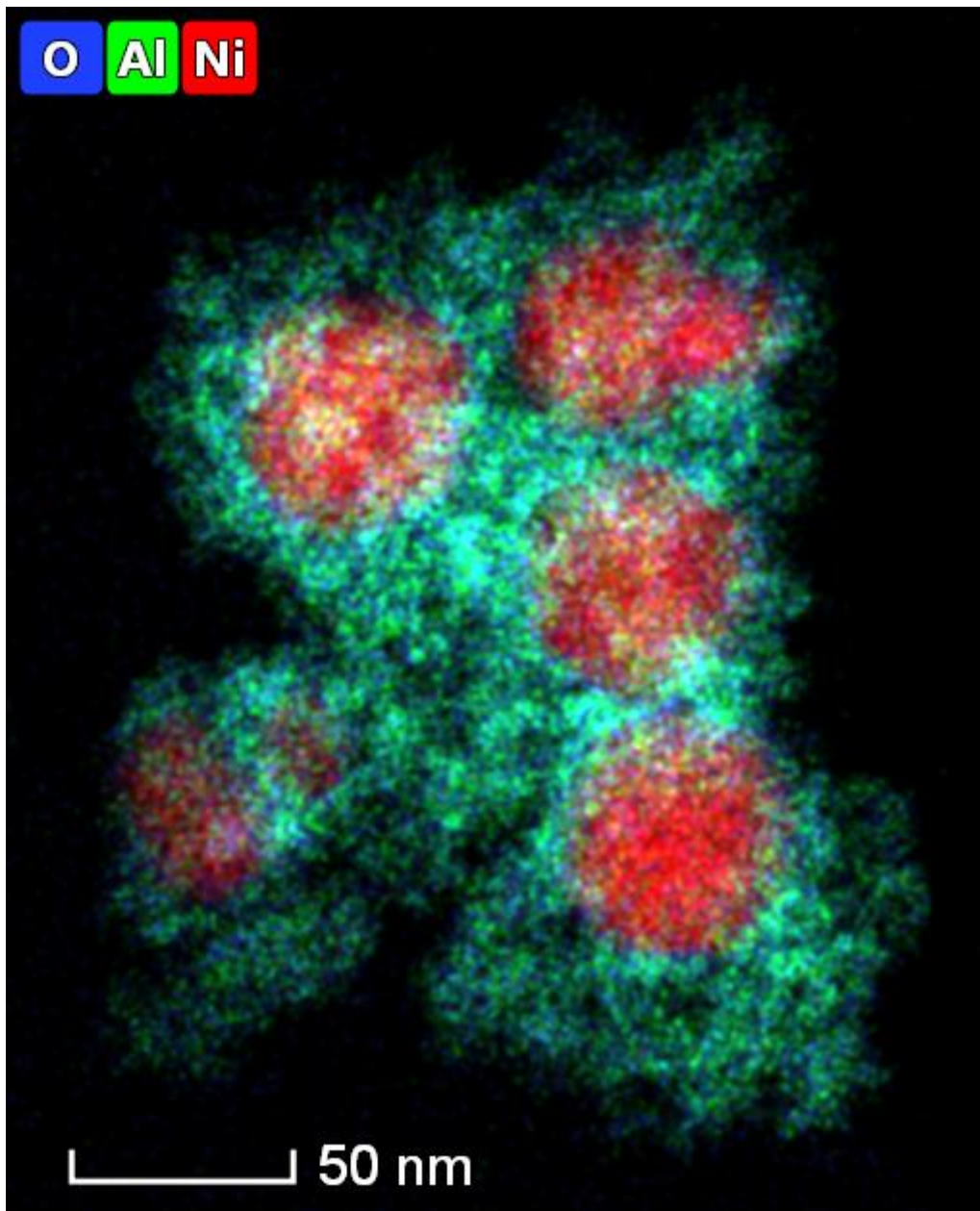


Figure 4.7. Elemental map of the 90 % Ni 10 % alumina sample

To confirm the internal content of the catalyst, the sample was digested and analysed using inductively coupled plasma mass spectrometry. The results of this are shown in Table 4.1. As can be seen there are other elements present that were not expected, these can be due to trace metal salts on the glass ware which will not affect the overall metal concentration, or due to contaminants on the cones in the detector of the mass spectrometer. The total nickel content shown in Table 4.1 is higher than that seen in Figure 4.6, meaning that the internal nickel may be masked by the alumina support. The aluminium content appeared to be similar to that seen in Figure 4.6, however the oxygen content could not accurately be

measured, although the aluminium was measured in oxygen to quantify any aluminium oxide. Therefore, it can be seen that the coprecipitation method will allow the production of catalysts with high metal loadings. Whilst the theoretical measurements do not match the experimental, there is a definite increase in the nickel content of the catalyst. As the total contributions of the metals is not 100 % this can be attributed to the presence of oxygen that was not measured, which is supported through the EDS analysis in Figures 4.6 and 4.7.

Table 4.1. Table showing the elemental composition of different catalyst materials

Sample	Wt. % Ni	Wt. % Al	Other elements present
90 % Ni	75.5 ± 18.9	15.5 ± 8.5	Cu, Zr, Ba
80 % Ni	66.5 ± 25.7	16.3 ± 6.8	Cu, Zr, Ba
70 % Ni	57.8 ± 17.5	25.2 ± 6.5	Cu, Zr, Ba

4.2.3 Porosity and surface area of produced catalysts

A key factor in the length of time a catalyst will remain active is the surface area and porosity of the material. As these influence the active sites that are available for reactions to occur. However, in the case of CCVD this does not have as much of an influence as the growth mechanism during deposition will drive the reaction and is more dependent on the feedstock composition. The isotherms produced through the adsorption and desorption of nitrogen on the catalyst surface show that all the catalysts have a type V isotherm, Figure 4.8, indicated through the hysteresis loop, this mesoporosity is supported through the pore size in Table 4.2. A type V isotherm indicates that the sample is mesoporous but with a weak interaction. This weak interaction means that the nitrogen will not strongly bind to the surface of the sample and can easily be removed.

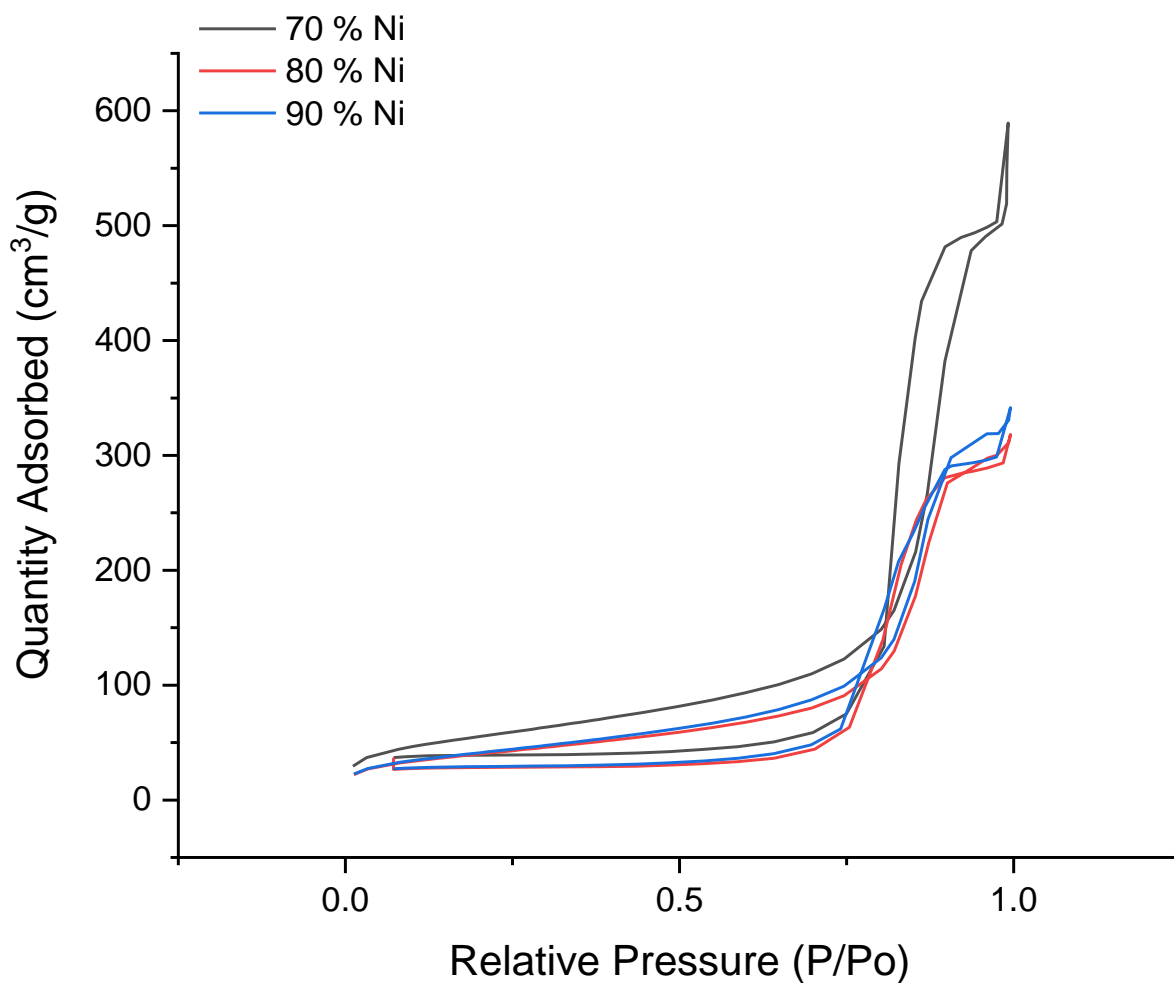


Figure 4.8. Adsorption and desorption of nitrogen on the surface of the produced catalyst

The surface area of the catalyst, Table 4.2, is highest for the 70 % nickel catalyst, at 197.82 m²/g, whereas the other two samples are more comparable at 143.32 and 148.55 m²/g for 80 and 90 % nickel respectively. The 80 and 90 % nickel catalysts are comparative in terms of surface area, pore volume and size with minimal variation, this matches the size distributions and visual images, as they are similar with only around 10 nm between the average particle size, compared to the 80 nm difference with the 70 % nickel sample.

Table 4.2. Surface area, pore volume and pore size for the produced catalysts

Catalyst sample	Surface area (m²/g)	Pore volume (cm³/g)	Pore size (nm)
70 % Ni	197.82 ± 0.55	0.897	15.43
80 % Ni	143.32 ± 0.39	0.483	11.77
90 % Ni	148.55 ± 0.44	0.521	11.62

4.2.4 Activity of the nickel alumina catalysts

The activity of the catalysts was tested to determine the which composition would be the most effective for the synthesis of carbon from the pyrolysis gases. The 70 % Ni catalyst lasted 7.5 hours, Figure 4.9, with a maximum conversion seen of 25 %, the 80 % Ni catalyst showed an activity of 12 hours and a maximum conversion of 30 % whilst the 90 % Ni showed activity for 20 hours with a maximum conversion of 32 %. Therefore, it is clear that the 90 % Ni catalyst was the most efficient for the conversion of methane. The 90 % Ni catalyst also produced the highest yield of carbon following the end of activity, this was seen to be 1.98 g with 1.08 g and 0.97 g for 80 and 70 % respectively. This is expected, as a higher activity should lead to an increased yield due to a longer time for the reaction to occur.

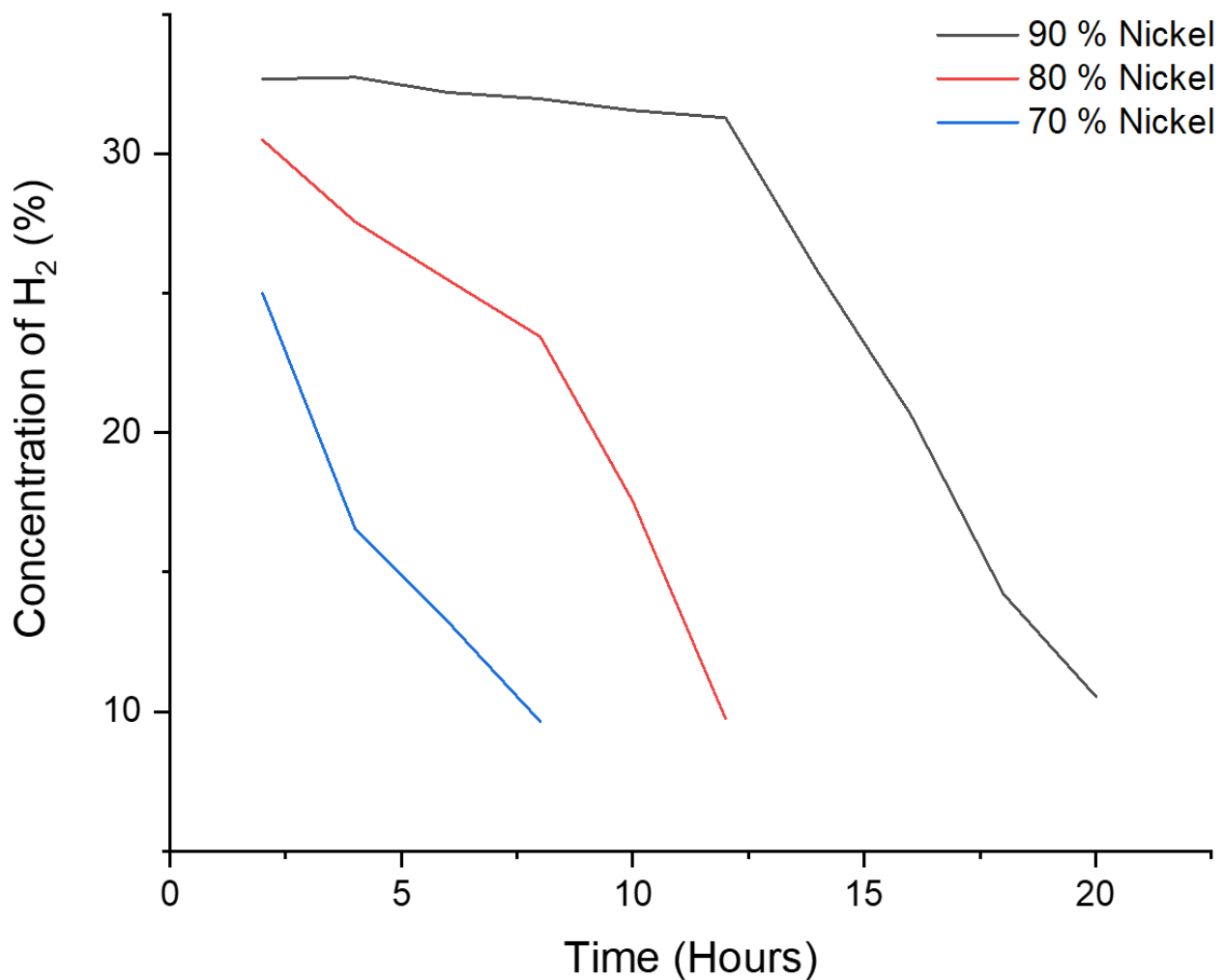


Figure 4.9. Plots showing the conversion of methane to hydrogen at different catalyst metal loadings as a way to determine the activity of the catalyst

As seen in Figure 4.9, the 90 % Ni catalyst showed a greater initial stability of conversion, for the first 12 hours, before exhibiting a steep decline in activity, whilst the 80 % nickel catalyst showed no stability, and showed a steady deactivation from the peak conversion. Although the peak conversion of methane into hydrogen is similar for both the 80 and 90 % nickel, the activity profiles are different, showing that the 90 % nickel catalyst will provide a longer lasting conversion, and therefore will show a greater resistance from deactivation following the deposition of carbon through the conversion of methane. The 70 % nickel shows a lower conversion of the 100 % methane to hydrogen, as well as deactivating earlier, and exhibiting a steeper reduction in the activity. These changes in activity may be due to the particle size, as seen in Figure 4.3, the 70 % nickel catalyst has larger particles, which in turn may reduce the surface area, limiting the activity as there will be fewer locations on the surface that are

able to catalyse the reaction. The 90 % nickel sample however, showed a variety of particle sizes and distributions, seen in Figure 4.3, although the average particle size was measured to be 40 nm. This means there should be a greater surface area, and therefore the activity is greater due to this. This range of particle sizes may be the reason that the 90 % nickel sample can resist deactivation longer than the other catalysts, as there is a greater spread of sizes, meaning that as deposition increases, the particles deactivate at different rates, giving a stable conversion for the initial 12 hours. Once deposition of the carbon starts to increase, deactivation will occur rapidly, similarly to the other metal loaded catalysts. From this, it can be seen that to ensure a high carbon yield, which is linked to the conversion of methane to hydrogen, the 90 % nickel sample is more effective. It is undetermined whether this is due to the particle size distribution or the higher metal loading, or a combination of both. A higher yield, alongside a higher length of activity can be seen to show a higher rate of activity compared to the other catalyst samples. It is worth noting that despite being labelled as 70 to 90 % Ni catalysts these are the theoretical loadings, and in reality, the metal loading is lower, suggesting that the variation within catalyst performance is likely due to the difference in particle sizes.

4.3 Optimisation of the deposition of carbon from a variety of feedstocks over a catalyst

To determine the optimal parameters for the deposition of carbon on the catalyst, design of experiments was implemented. Identified variables were the pyrolysis temperature, catalyst type, chemical vapour deposition temperature and carrier gas flow rate as well as feedstock type. Before CVD was carried out, the pyrolysis process was optimised. The optimal pyrolysis temperature for the two feedstocks was determined through the analysis of the gas chromatography data, the selected temperature was that with the highest carbon containing gas content. This was identified as 600 °C for both the cotton and polyester/lycra textile waste feedstocks. Therefore, these temperatures were set as the pyrolysis temperatures for the textile feedstock. 600 °C was chosen over the 800 °C as it will also be less energy intensive and therefore cheaper.

To monitor the extent of the reaction, gas chromatography monitored the gas output, allowing the status of the catalyst to be seen. To determine the overall efficiency of the reaction, the mass of carbon produced was considered, as this is the desired product of the

reaction. The 90 % Ni catalyst showed the greatest deposition of carbon before deactivation and was therefore selected for all reactions. A high, middle and low point was identified for the temperature and flow rate and a binary set for the feedstock. These parameters were selected as they will have the greatest impact on the process, and therefore, the results seen. The recommended temperature for nickel catalysts is between 700 and 900 °C [243] with chemical vapour deposition carried out at a variety of temperatures from 600 °C [279] to 1000 °C [280] so it was decided to test these temperature extremes with a mid-point for a reference. As the temperature will affect the deposition rate, as well as the longevity of the catalyst, this is an important consideration. The flow rate was selected to investigate if it would lead to significant decreases in concentration within the gas phase, as well as to determine if it was required to ensure a constant flow of the evolved gases. The feedstock should influence the carbon containing gas due to the different structures seen within the textile samples, therefore it is important to determine which is optimal for the production of carbon.

Table 4.3. The optimisation parameters and results for the production of carbon from the pyrolysis to chemical vapour deposition of textile waste feedstocks

Temperature (°C)	Flow rate (mL/min)	Feedstock	Mass of carbon (g)
600	0	Polyester	0.027 ± 0.512
		Cotton	0.016 ± 0.021
600	10	Polyester	0.253 ± 0.120
		Cotton	0.045 ± 0.960
600	20	Polyester	0.063 ± 0.098
		Cotton	0.004 ± 0.021
800	0	Polyester	0.000 ± 0.003
		Cotton	0.018 ± 0.023
800	10	Polyester	0.009 ± 0.006
		Cotton	0.000 ± 0.003
800	20	Polyester	0.049 ± 0.023
		Cotton	0.005 ± 0.009
1000	0	Polyester	0.034 ± 0.067
		Cotton	0.015 ± 0.076
1000	10	Polyester	0.014 ± 0.053
		Cotton	0.000 ± 0.003
1000	20	Polyester	0.002 ± 0.008
		Cotton	0.000 ± 0.002

It is clear from Table 4.3 that the optimal conditions for the production of carbon is a temperature of 600 °C with a flow rate of 10 mL/min and a feedstock of polyester. It was expected that polyester would produce a higher carbon yield due to the higher content of carbon containing gases. Although polyester is seen to produce the highest yield of carbon, this is only 6.25 % yield from the textile waste feedstock. Where samples are seen to produce 0.000 g of carbon, this was due to recovery only consisting of the mass of catalyst, with no evidence of carbon deposition. These were attributed to the higher reaction temperature causing the catalyst to be less efficient and preventing the deposition of

carbon. A carrier gas flow rate of 0 mL/min was determined to not ensure that there was a constant movement of the pyrolysis gases over the catalyst leading to a reduced carbon production. The 20 mL/min carrier gas flow rate also does not allow enough time for the reaction of the carbon containing gas and the catalyst, but due to the faster travel of these samples. There is a higher carbon yield at most parameters for the polyester samples when compared to that seen for cotton. This means that to produce the maximal amount of carbon, polyester should be used as the feedstock. This is to be expected due to the higher carbon containing gases produced through the pyrolysis of polyester as seen in Figures 3.4 to 3.8.

Therefore, for the optimal production of carbon through the use of chemical vapour deposition of the carbon containing pyrolysis gases from the pyrolysis of textile waste samples should be carried out using polyester feedstock pyrolysed at 600 °C with a carrier gas flow rate of 10 mL/min and a chemical vapour deposition temperature of 600 °C.

4.4 X-ray diffraction of synthesised carbons from pyrolysis-CVD

Powder x-ray diffraction was carried out on the carbon samples produced from chemical vapour deposition, as seen in Figure 4.10. It can be seen that there is a presence of nickel carbide in the cotton textile waste sample, as well as that produced from methane, this may be due to the operating conditions or contaminants within the reactor. The intensities of the 91 % polyester 9 % lycra carbon and 100 % cotton samples were seen to be reduced, this was due to the small sample size available for testing, as such there was a greater amount of noise seen in the baseline, which could cause some peaks to be obscured. Due to the strong peaks seen for crystalline nickel, any smaller less intense peaks can become lost within the baseline, or even be covered by peaks at the same point. This is exemplified through the double peaks seen for nickel carbide and nickel at 43 to 45 degrees, the poor peak separation is caused by overlapping peaks. This is to be expected due to the similarities in the nickel and nickel carbide crystallinity. As pyrolysis oils are produced during the pyrolysis of textile waste samples there is the chance that these oils may impact the crystallinity of the sample as the oil filters were not seen to be impenetrable.

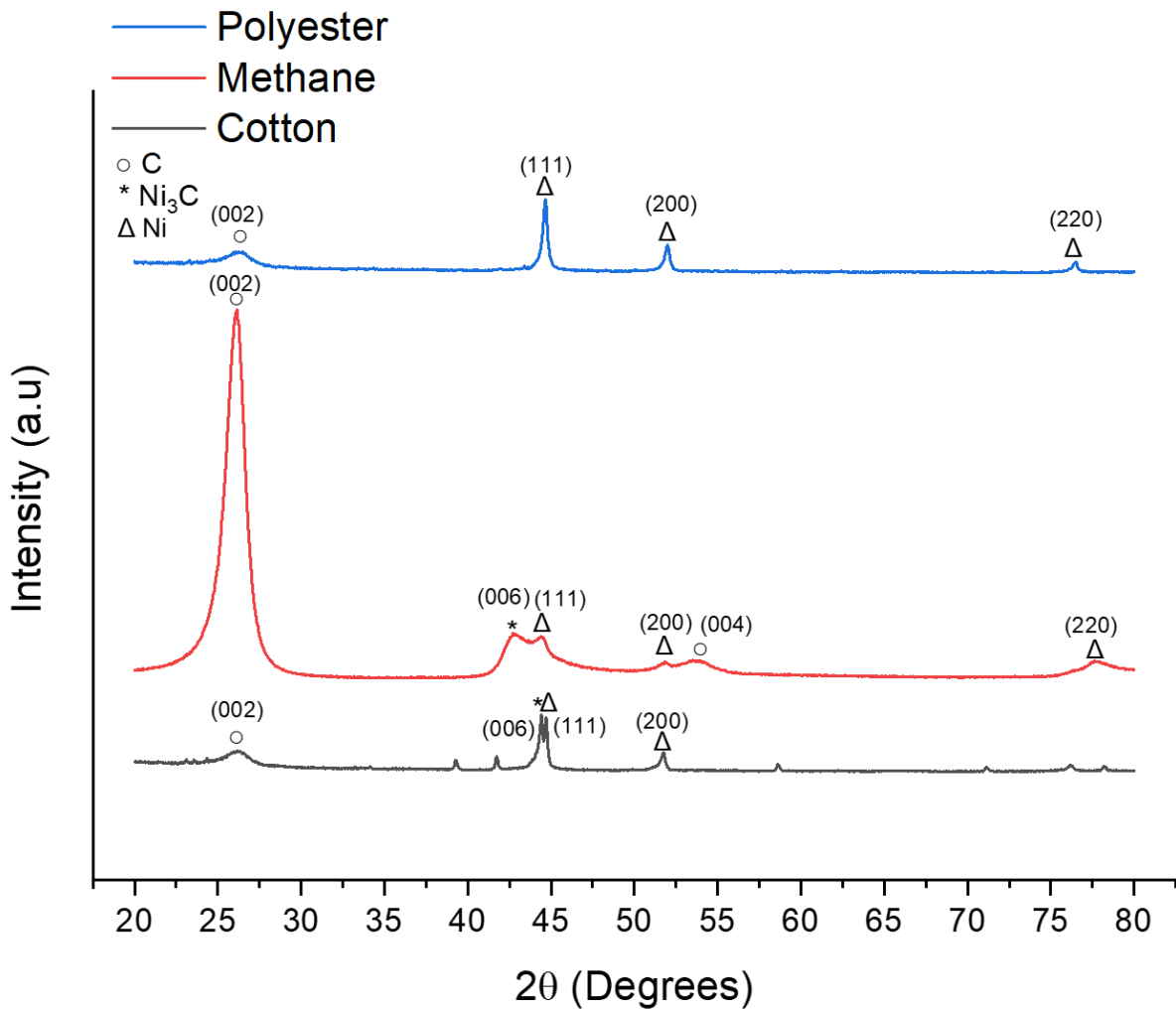


Figure 4.10. Powder x-ray diffraction plot showing the components, and relative crystallinity, of the carbons produced through the pyrolysis to chemical vapour deposition of 91 % polyester 9% lycra cotton and methane. The peaks have been assigned hkl values based on the ICDD's PDF-2 2023 database.

The peaks seen in Figure 4.10 were compared to those seen in literature to confirm the ICDD's database. The presence of nickel carbide within the produced carbon indicates that a secondary reaction occurred on the nickel catalyst. There is evidence that nickel carbide can form due to carburization of nickel films in the presence of carbon monoxide at 350 °C [281] which due to the conditions of the chemical vapour process could occur as a secondary reaction. As the pyrolysis of cotton was carried out at 600 °C, where the predominant gas produced is carbon monoxide it is feasible that an increased rate of carburization occurred on the nickel catalyst. The polyester sample did not see this same carburization reaction which could be due to the increased hydrogen content dampening the reaction on the

nickel metal substrate. There is some evidence of nickel carbide seen for the carbon produced from the pure methane sample, as evidenced by the (006) peak seen at 42.67 degrees. The presence of methane can cause an increase in carburization following the reduction of an oolitic hematite to iron [282], therefore, if the catalyst was further reduced to metallic nickel the decomposition of methane could lead to carburization, although the study found 750 °C to be optimal for this decomposition, the behaviour was seen to occur from 600 °C. Electron diffraction was used to further explore the crystal structure of each of the carbon samples, for the cotton and polyester the presence of Ni was confirmed, however this was not seen for the methane carbon sample, confirming the TEM images that there were no metal nanoparticles in this sample. The electron diffraction confirmed that the carbon produced had the same crystal structure for each feedstock. There were no (110) or (006) Ni₃C particles seen, meaning that the presence of nickel carbide may be due to contamination, or was removed during the sample preparation.

The Scherrer equation, Equation 7, was used to determine the crystallite size of the carbon nanomaterials. The crystallite size for cotton, polyester and methane samples were determined to be 12.66 nm, 27.56 nm and 5.62 nm respectively. Showing that the carbon size is influenced by the feedstock gas, this may be due to the presence of lighter pyrolysis oils in the sample, which may coat the catalyst sample and the resultant carbon material. As the Scherrer equation is based on the largest peak, this may also indicate that as the predominant peak for the cotton and polyester carbon samples is the metal nickel, this influences the calculated full width half maximum and in turn the average crystallite size.

4.5 Surface area and physisorption of synthesised carbons

The adsorption of nitrogen on the surface of the synthesised carbons is shown in Figure 4.11, the samples show a type III isotherm, indicating that there is no identifiable monolayer formation, with weak adsorbent-adsorbate interactions and clusters of adsorbed molecules on favoured sites. The carbons can therefore be assumed to have limited porosity.

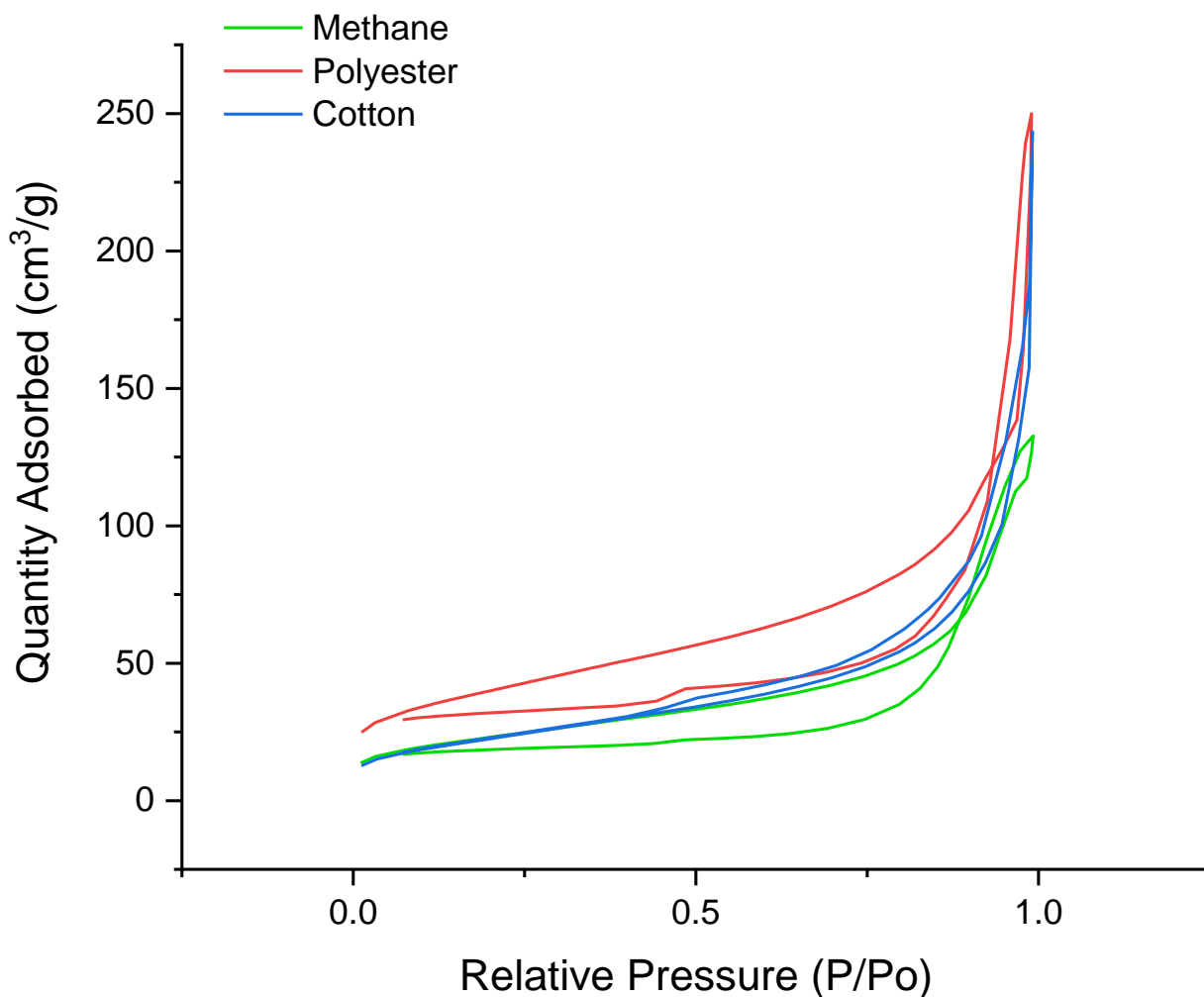


Figure 4.11. Nitrogen physisorption for carbon samples produced through chemical vapour deposition of pyrolysis gases

The two carbon samples produced from the textile waste pyrolysis were seen to adsorb a greater quantity of nitrogen compared to that produced through synthesis with methane. The methane and cotton textile samples were seen to have similar surface area measurements, 82.31 and 82.41 m²/g respectively, as seen in Table 4.4, whilst the polyester/lycra and cotton samples both had pore volumes of 0.37 cm³/g. Overall, there is no significant variation within the measured properties for the carbon samples indicating that the feedstock type does not greatly influence the surface area of the sample.

Table 4.4. Surface area, pore volume and size measurements for the produced carbon from CVD

Carbon sample	Surface area (m²/g)	Pore volume (cm³/g)	Pore size (nm)
Methane control sample	82.31 ± 0.25	0.198	10.32
91 % polyester 9 % lycra	91.56 ± 0.41	0.37	12.02
100 % cotton	82.41 ± 0.44	0.37	17.62

4.6 Scanning Electron Microscopy of carbon nanofibers

Scanning electron microscopy was used to examine the carbon produced through the chemical vapour deposition process. As can be seen in Figure 4.12, there are differences between the different carbon source gases, showing that the gas composition will influence the carbon nanostructure. The polyester/lycra carbon and the cotton carbon materials show a carpet of the small, protruding carbon nanomaterials coating the surface of the catalyst, whilst the carbons seen from methane are in thicker clumps. The lower magnification images are coated in gold to ensure a clearer image of the nanostructure, whilst those at the higher magnification are uncoated to allow an accurate measurement of the fibres, as the gold will increase the diameter of the fibres. These fibres were measured using ImageJ to determine the width of the fibres, unfortunately due to the fibre entanglements present in the sample it was impossible to accurately measure the nanofiber lengths.

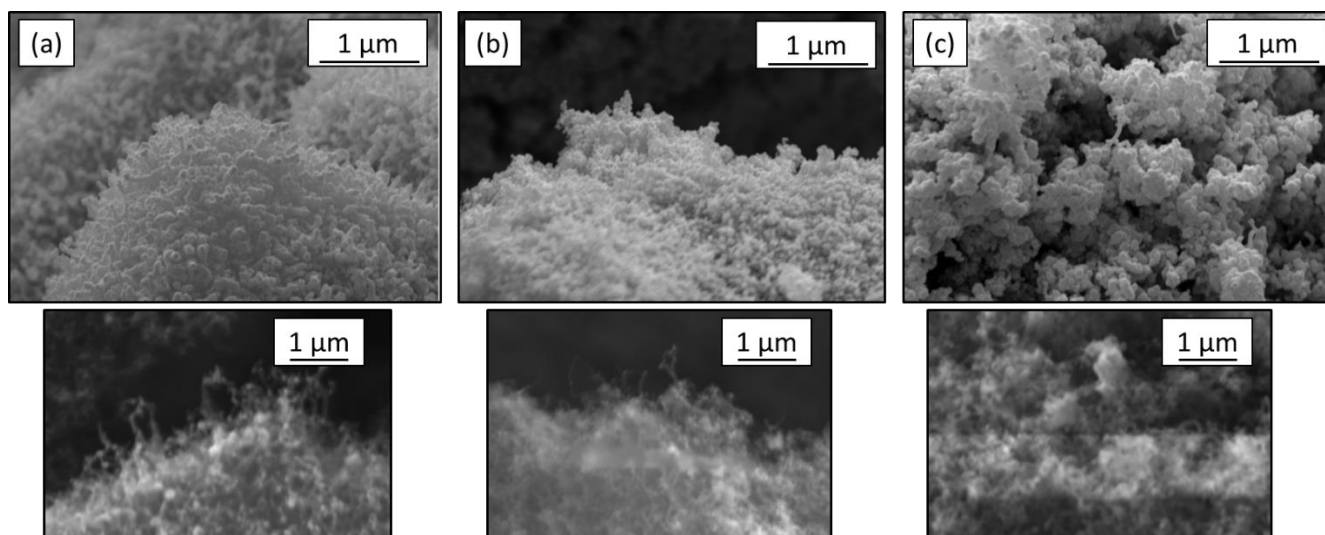


Figure 4.12. Scanning electron microscopy images of carbon produced through chemical vapour deposition of carbon containing gases, or a reference gas, over a 90 % nickel 10 % alumina catalyst with (a) polyester/lycra textile waste (b) cotton textile waste and (c) methane gas

It can be seen in the higher magnification, uncoated methane sample that there is a high density of carbon seen to grow off the catalyst. This agrees with the higher yield of carbon seen for the methane sample, as a higher density will lead to less individual fibres seen. For the polyester/lycra and cotton carbon samples, the growth of the carbon can be seen to follow the shape of the catalyst, whilst for the methane grown carbon there is no such distinction. This may indicate a different growth mechanism, which can be identified using transmission electron microscopy, or it may show that the density of the carbon deposition is higher. The runs of the polyester/lycra and cotton pyrolysis to chemical vapour deposition lasted on average 95 and 85 mins respectively, whilst the methane carbon deposition lasted for 12 hours on average. There was more variation in the time for the reactions containing the pyrolysis gases, which is to be expected as the gas output is dependent on the quantity of the feedstock, which will vary due to human error. Therefore, the limiting factor for the synthesis of carbon nanomaterials from the pyrolysis of textile waste can be attributed to the feedstock quantity whilst methane was limited by the catalyst. In the lab scale process there was no option to be able to add more textile sample to the reactor without introducing oxygen into the system.

The feedstock gas can be seen to have a great impact on the carbon nanomaterial produced, Figure 4.13 shows that there is a distinct difference between the three feedstock

materials. As shown in Figures 3.8 to 3.12 and Figures 3.14 to 3.18 the cotton textile sample has a greater proportion of oxygen containing gases, this appears to change the structure of the resultant carbon nanomaterials. The cotton nanostructured carbon can be seen to have a greater concentration of metal nanoparticles remaining compared to the carbon produced from the polyester/lycra and methane feedstocks. However, the textile waste produced carbon nanofibers can be seen to have a significant interaction with the metal catalyst nanoparticles whereby the nanomaterial grows around it, this is likely due to a relationship with the oxygen containing gases and the metal nanoparticle. As shown in Figure 4.13 and 4.14 the diameter of the carbon nanofiber is greater for the cotton feedstock compared to that produced from the waste polyester feedstock. The cotton feedstock also led to a greater level of disorganisation compared to the other carbon nanomaterials produced, which explains the larger diameter. Figure 4.13 confirms that the CVD process used in this situation leads to the formation of the carbon nanofibers, identified by the angle of the carbon deposition on the metal nanoparticle. Nanofibers are produced due to the faceted nanometals, and these can be seen in Figure 4.13 where the metal nanoparticle remaining at the end of the nanofiber can be seen to have had an impact on the diameter of the nanofiber. The carbon nanofibers also appear to have a hollow interior, this is especially clear for the carbon nanofibers produced from the polyester and carbon feedstocks. This may allow gas to be trapped within the centre of these. The nanofibers produced from the methane were seen to have slightly thicker ends where the metal nanoparticle has been lost. It can be seen from the angle of the growth of the carbon layers that the growth mechanism of the polyester and cotton feedstock carbon is tip growth, as the carbon sheets grow out from the nickel catalyst nanoparticle. There are kinks within the length of the nanofiber for the two textile feedstock materials, this occurs during the growth phase of the nanofibers and is due to the shedding of the carbon stored within the catalyst particle. This means that the length of the nanofibers produced will have a relationship with the capacity of the catalyst to store carbon, as well as the carbon content of the feedstock gas.

Considering Figure 4.13, the carbon nanoparticles produced from the methane are longer fibres that appear to not be clustered together. This may be due to the more complete reaction as the methane CVD had the longest run time, whereas for the textile waste samples there may be incomplete conversion leading to the shorter carbon nanofibers as

well as the presence of the nickel nanoparticles remaining in the carbon samples. As the polyester/lycra sample had the second longest reaction time, this may explain why the cluster of carbon nanomaterial seen in image A of Figure 4.13 has a lower density than that seen in image C. The reaction time therefore can be assumed to have an effect on the carbon nanomaterial seen.

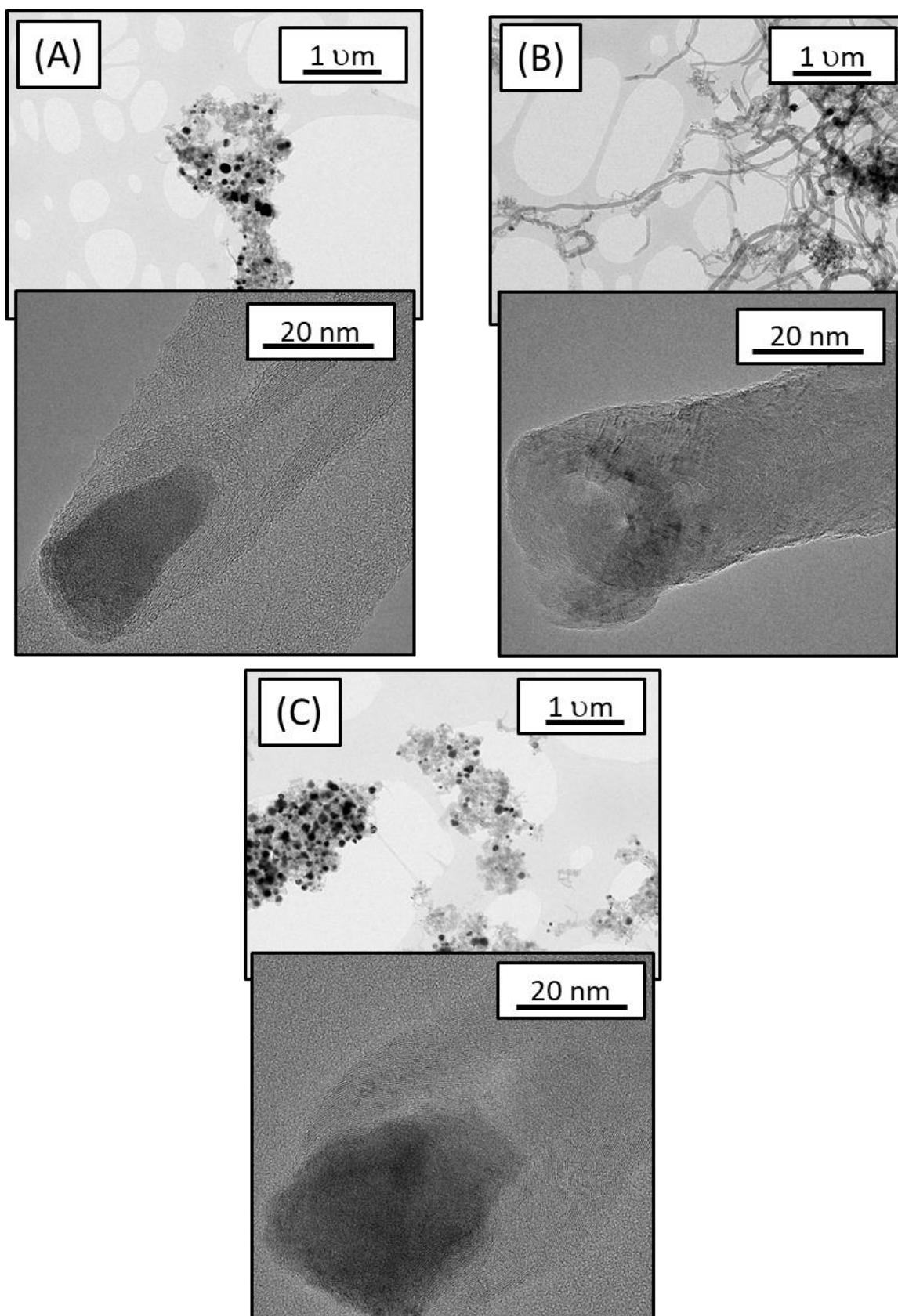


Figure 4.13. Transmission electron microscopy images of carbon nanofibers produced from (A) polyester feedstock (B) methane feedstock and (C) cotton feedstock. All were deposited on a 90 % Ni catalyst.

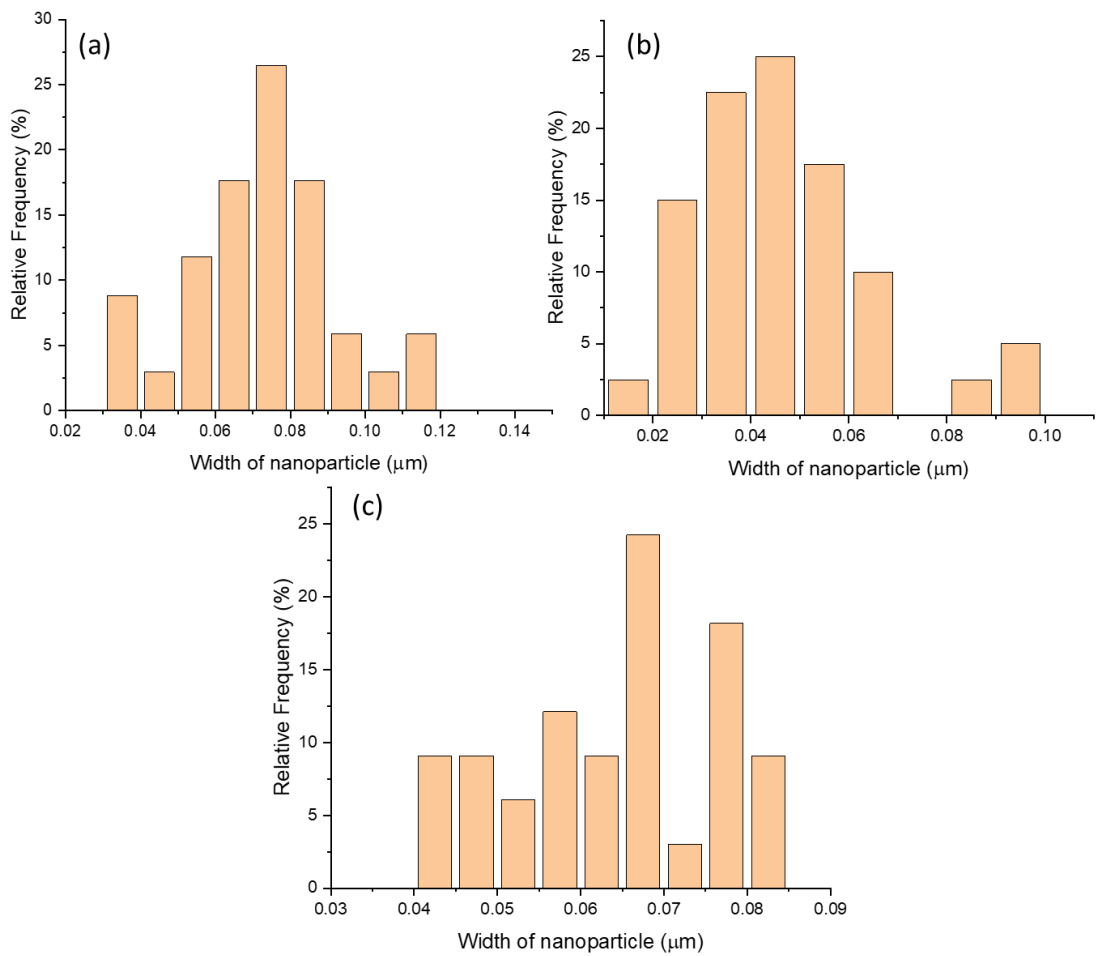


Figure 4.14. Distributions of the width of different carbon fibres produced through the chemical vapour deposition of (a) methane (b) cotton pyrolysis gases (c) polyester/lycra pyrolysis gases over a 90 % nickel 10 % alumina catalyst

The distributions for the carbon fibres can be seen in Figure 4.14. These show that the carbon produced from polyester/lycra textile waste has a smaller variation in the carbon nanoparticle width, showing a more uniform sample, whilst the carbon produced from pure methane and the cotton pyrolysis gas mix has a greater spread of widths seen. This is partially due to the entanglement, meaning that the individual fibres cannot be measured accurately, however it is clear that the fibres have a denser footprint when produced from methane compared to pyrolysis of cotton or polyester/lycra, this is shown in both Figure 4.12 and 4.14, as the mean nanoparticle width is measured to be 0.072 μm whilst cotton and the polyester/lycra pyrolysis to chemical vapour deposition were measured to be 0.047 and 0.064 μm respectively. This can be seen to be due to the increase in deposition seen for polyester compared to cotton, as the yield was higher, as seen in Table 4.3.

4.7 Infrared spectroscopy of the different carbons produced from different feedstocks

As shown in Figure 4.15, the spectra for the cotton, methane carbon and polyester carbon all show very similar peaks. The $C\equiv C$ bonds seen at peak A can be attributed to the carbon nanofiber internal bonds. Whilst it would be expected that the internal bonds of the sample would be single C-C bonds it may be that the overlapping of multiple fibres has caused a peak to occur at this point. The transmittance seen for the carbon sample is much lower than that seen for any other, meaning that the intensity of any peaks is much lower. The features that are seen for the methane carbon sample show a lower transmission rate than that seen for the other carbon samples. This means that this sample will have less bonds that adsorb at this wavelength.

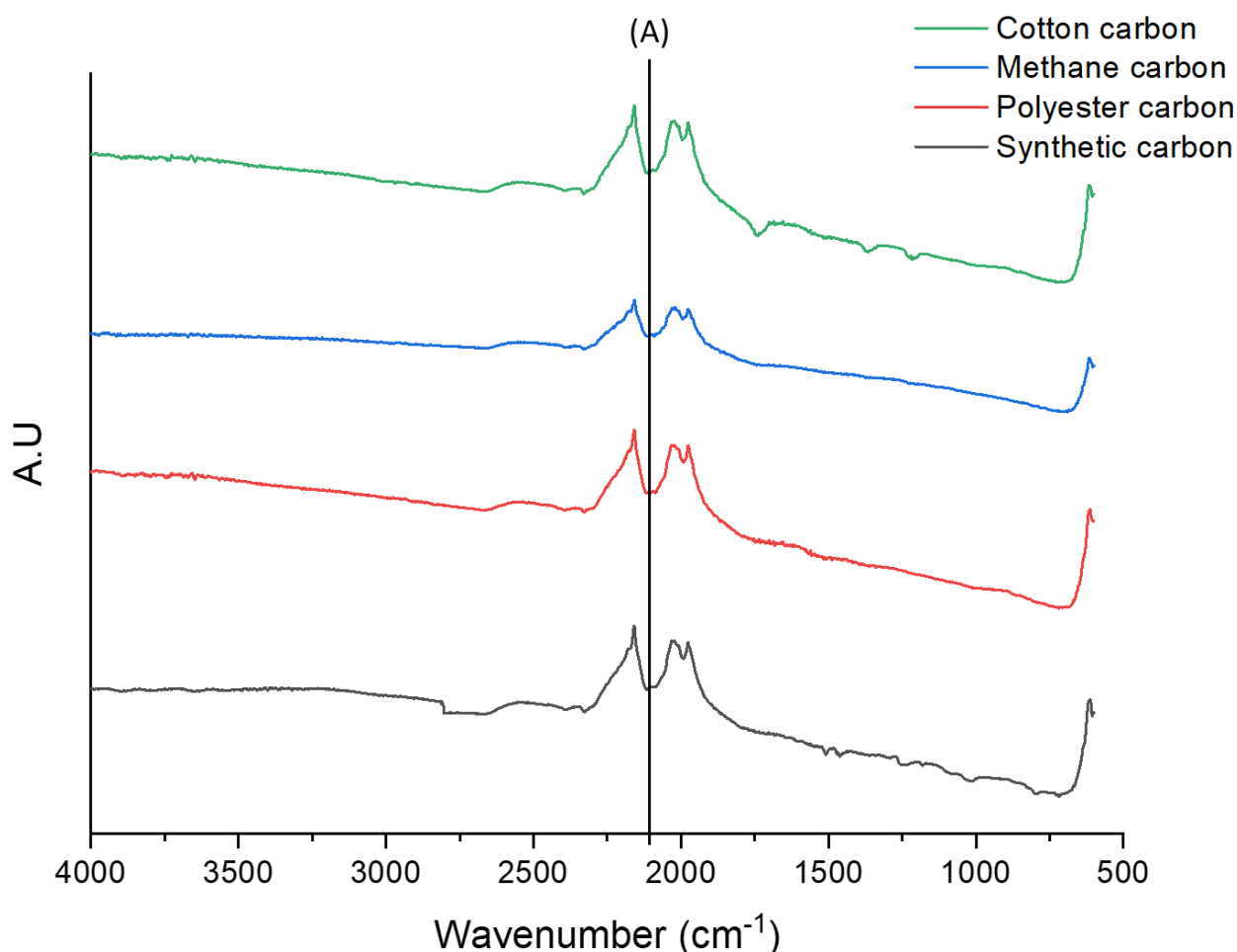


Figure 4.15. Fourier-Transform infrared spectroscopy of carbons produced from different feedstocks showing (A) $C\equiv C$ stretching

4.8 Comparison between polyester/lycra carbon and the synthetic gas mix carbon

Due to limitations of the feedstock material, a synthetic gas mix was designed to mimic the gas concentration seen at the peak production from polyester/lycra mixed textile waste. This allowed a constant production of carbon, without a reliance on the quantity of feedstock. It was determined that only the polyester/lycra textile waste should be used for the production of carbon due to the higher yield, giving a higher economic feasibility and making a more viable option for industrial applications. The chemical vapour deposition of the synthetic gas mix had a longer duration compared to the pyrolysis to chemical vapour deposition of polyester/lycra, lasting 7 hours, confirming that the limiting factor is not the activity of the catalyst, but the feedstock availability. The yield of carbon reflected this increased duration with the average yield being 0.453 g compared to the 0.063 g shown in Table 4.3.

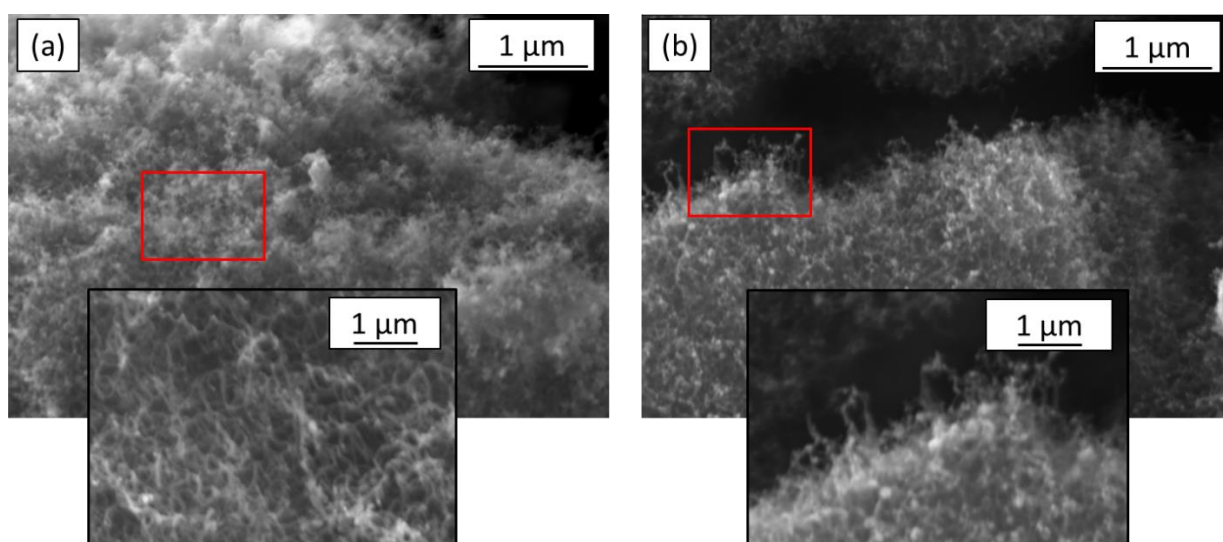


Figure 4.16. Scanning electron microscopy images of carbon produced through chemical vapour deposition over 90 % nickel 10 % alumina catalyst of (a) a synthetic gas mix to mimic that of the polyester/lycra textile waste gas phase and (b) pyrolysis of polyester/lycra textile waste

This increase in yield does not seem to lead to an increase in nanoparticle width, as the mean width was seen to be 0.054 µm, identified in Figure 4.17, which is less than that seen for the carbon produced from polyester. The scanning electron microscopy images, shown in Figure 4.16, show that carbon nanofibers are produced, although it is clear that there is a greater yield of the carbon produced through the synthetic gas mix, due to the density of fibres seen. The relative length of the fibres cannot be compared due to the locations that

the microscopy images were taken. The synthetic gas mix carbon images were taken from a central point on the catalyst whilst the polyester/lycra pyrolysis carbon sample was taken from the edge of the catalyst. Therefore, despite the nanoparticles appearing longer in image a of Figure 4.16 compared to image b this cannot be measured.

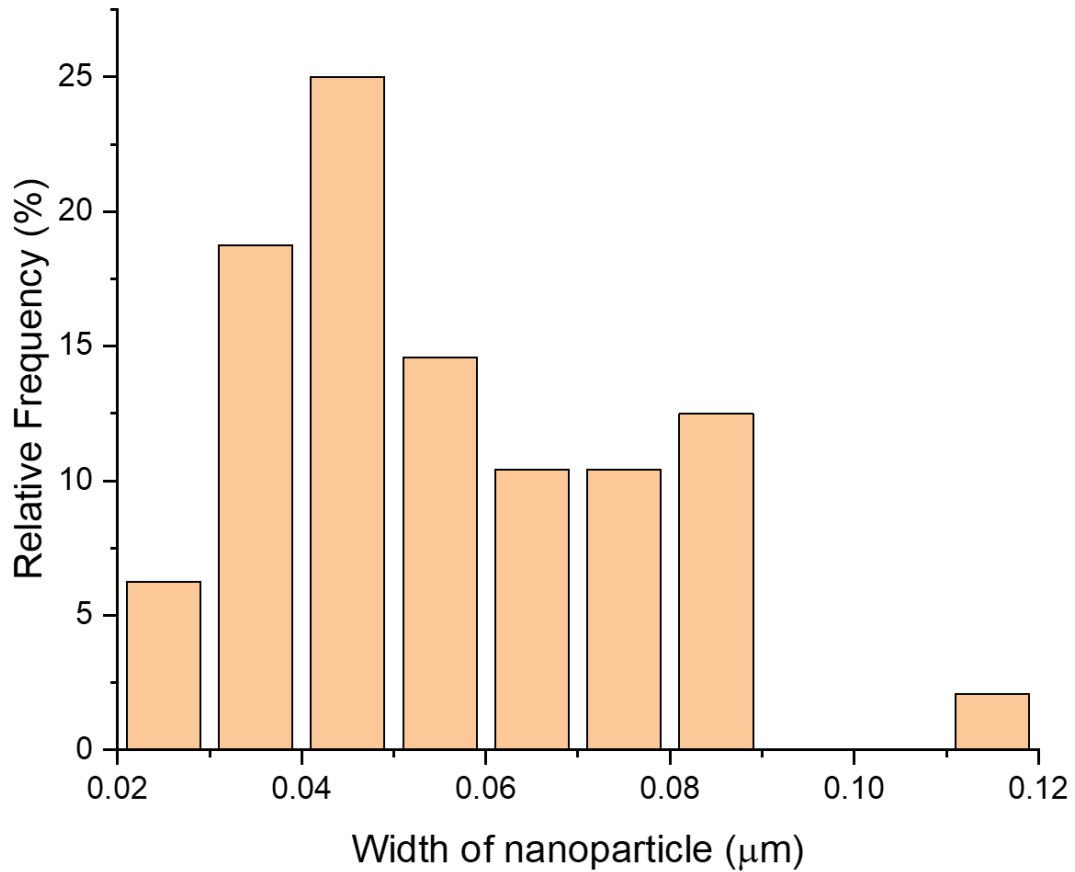


Figure 4.17. Distribution of the widths of nanoparticles seen in the carbon produced through the chemical vapour deposition of a synthetic gas mix to mimic that of the polyester/lycra textile waste gas phase over a 90 % nickel 10 % alumina catalyst at 600 °C

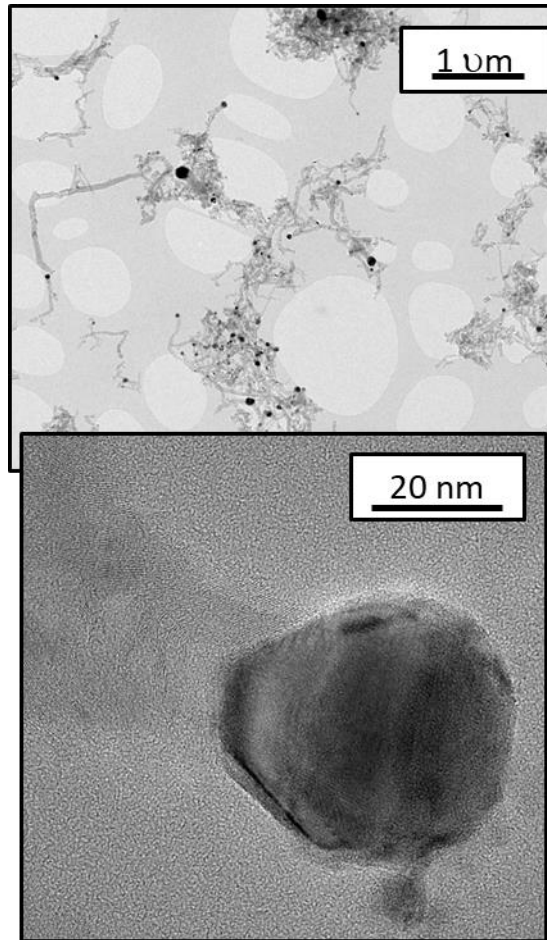


Figure 4.18. Transmission electron microscopy of carbon nanofibers produced from a synthetic gas mix

As can be seen in Figure 4.18, the carbon nanofibers produced are comparable to those seen in image A in Figure 4.13, showing that the synthetic gas mix successfully mimics that of the polyester/lycra textile waste. As the structure of the textile waste and synthetic gas mix nanofibers are similar, it can be assumed that the presence of the nickel nanoparticle is due to the oxygen containing gases, rather than being due to the incomplete reaction. However, this phenomenon is not fully understood, and would require more investigation to explain. The average diameter of the carbon nanofibers produced from the polyester were 3.69 nm whilst those produced from the synthetic gas mix were 3.72 nm showing that these have similar physical attributes. Due to the tangled nature of the nanofibers it is difficult to determine the length of these samples. However, it can be seen that the clusters of nanofibers are comparable between the synthetic gas mix and the polyester/lycra feedstock.

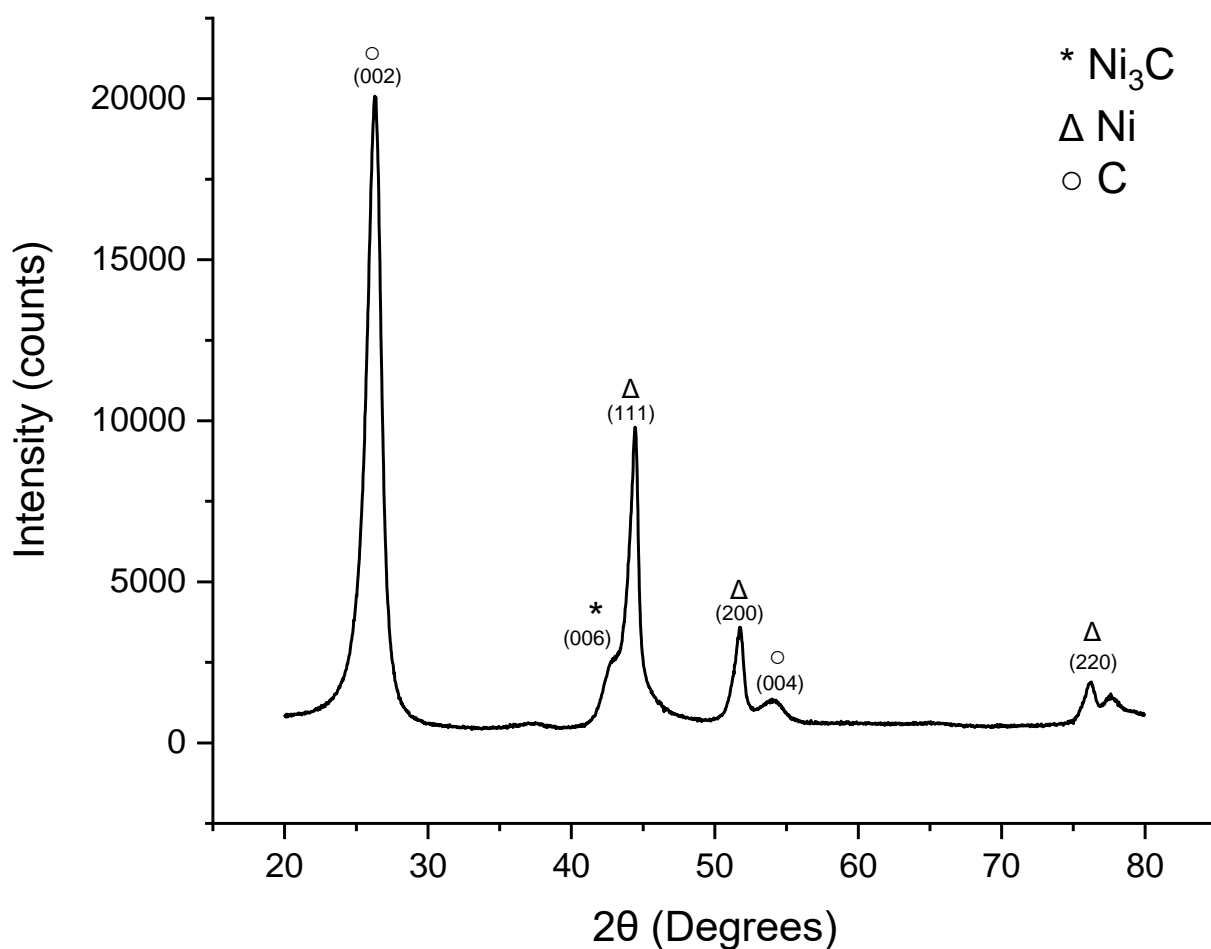


Figure 4.19. Powder x-ray diffraction of the carbon produced from the synthetic gas mix designed to mimic the gases produced through the pyrolysis of 91 % polyester and 9 % lycra textile waste with hkl values assigned based on the ICDD's PDF-2 2023 database.

Figure 4.19 shows the presence of nickel carbide, which was not seen in the powder x-ray diffraction of the carbon produced from the direct pyrolysis of the polyester/lycra textile waste sample. The electron diffraction taken on the carbon sample confirms the presence of (002) (111) and (220) planes, as shown in Figure 4.20. There was no evidence of the nickel carbide in the electron diffraction, showing that this may have been contamination, or to not occur homogeneously over the whole sample. The (002) peak is related to the presence of carbon within the sample, and is seen to be the most significant peak for both the synthetic gas mix and the methane gas mix, showing that there may be a slight reduction in the quantity of nickel metal remaining in the sample.

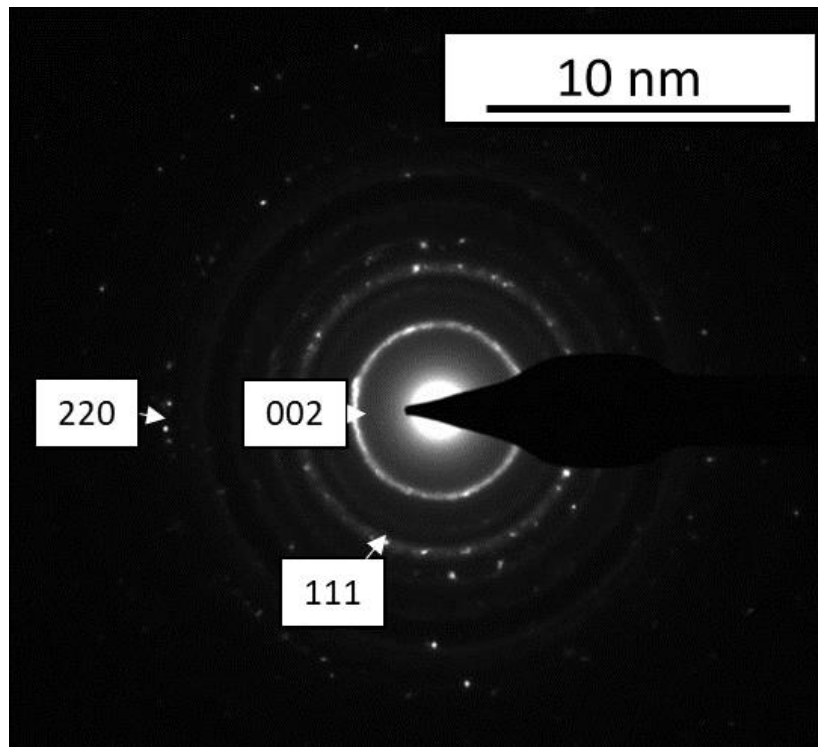


Figure 4.20. Electron diffraction pattern for the synthetic carbon with labels showing the identified hkl values

The crystallite size of the synthetic carbon mix was found to be 8.35 nm, which is smaller than the carbon produced from the polyester textile waste pyrolysis. This difference may be related to the lack of oils, but also that the largest peak for the synthetic carbon was a carbon peak, rather than the nickel peak which was seen to be the largest for the polyester carbon sample.

Nitrogen physisorption of the synthetic gas carbon found that the surface area was $90.188 \pm 0.36 \text{ m}^2/\text{g}$ with a pore volume of $0.25 \text{ cm}^3/\text{g}$ and a pore size of 9.55 nm. This shows that it is smaller than that of the carbon produced from the polyester textile waste, but has a larger surface area than the other two samples.

4.9 Conclusion

The production of different weight loaded nickel catalysts showed that, despite a discrepancy between the theoretical and experimental loadings, that the co-precipitation method would accurately produce high nickel content catalysts. Unfortunately, experimental loadings will be lower than the theoretical loadings as human error, instrumentation error and inefficient processes can lead to differences in the metal loadings. The 90 % Ni catalyst showed a larger average particle length of 60 to 70 μm

compared to that of 70 and 80 % Ni samples, 30 to 40 μm for both, meaning that the diameter of carbon nanofibers produced using the 90 % nickel sample will be larger. The surface area measurements were seen to be comparable for both 80 and 90 % Ni, 143.32 and 148.55 m^2/g respectively, whilst the 70 % Ni sample had a higher surface area of 197.82 m^2/g . This may be due to the increased aluminium support network, and was not seen to improve the performance as the 70 % Ni catalyst deactivated after 7.5 hours. The synthesis of carbon nanoparticles using catalytic chemical vapour deposition is dependent on the catalyst used, the feedstock gas as well as the parameters of the reaction. Whilst the optimised parameters showed the greatest improvement in carbon production, it does remain a low yield, a maximum yield of 0.253 g. This was attributed to the feedstock being fully consumed. Therefore, due to limitations in the quantity of textile available a synthetic gas mix was utilised to ensure that there was a constant gas stream over the catalyst. A 90 % nickel 10 % alumina catalyst was determined to be the most effective catalyst for the synthesis of the carbon nanomaterial due to the increased activity when compared to the other metal loaded catalyst. The different feedstock material led to changes in the visible forms of the carbon to be altered. A higher oxygen content can be seen to cause a greater level of metal nanoparticle remaining in the resultant carbon nanofibers, whilst the methane feedstock led to carbon nanomaterials without any metal.

The cotton feedstock had the highest content of non-methane gases, which appears to have led to the formation of some amorphous carbon as well as carbon onions with layers of carbon surrounding the metal nanoparticle. This implies that the presence of oxygen in the feedstock gas will lead to the disorganisation of the produced carbon, this may be due to the competing oxidation of the catalyst. Therefore, a pyrolysis temperature of 600 $^{\circ}\text{C}$ should be used to produce the carbon-containing gas, with a chemical vapour deposition temperature of 600 $^{\circ}\text{C}$ and a 90 % Ni catalyst to produce the carbon. It was deemed that a synthetic gas mix was required to ensure a greater production of the carbon nanomaterial as using the polyester/lycra feedstock led to a limited gas production preventing full decomposition of carbon on the catalyst. The carbon produced from the polyester/lycra textile waste has significant similarities to that produced using the synthetic gas mix. Therefore, to produce the quantity required for the production of the composite material, the synthetic mix was used preferentially to ensure that enough carbon was produced.

Chapter 5 - The mechanical properties of the composite materials

5.1 Introduction

To produce the composite materials a bisphenol A diglycidyl ether was combined with the (C12-14)alkylglycidyl ether to produce the resulting epoxy matrix material. The bisphenol A was selected due to its presence in offshore wind turbine components, especially blades [283]. This was combined with the produced carbon nanomaterials to yield the epoxy composite materials with varying carbon loading. To determine whether the addition of the carbon material affected the mechanical properties and strength of the sample, mechanical testing was carried out. The testing will allow the different properties of the composite material to be explored, and compared to determine the differences seen through the addition of the carbon additive material. Three processes were selected for testing of this composite material; tensile testing, three-point bending and accelerated weathering. Tensile testing will show the composite material's resistance to load being applied to each end of a sample, allowing the ductility of the sample to be considered [272]. A greater resistance to the applied load shows a stronger internal network, leading to a better material. Three-point bending determines how resilient a material is to a load applied perpendicular to the sample, focusing the load on one length of the test sample [284]. Three-point bending can allow the calculation of the flexural modulus, which theoretically should be similar to that of the Young's Modulus, however in practice this will not be the case. Polymers, under which the epoxy matrix is classed, behave differently to metals which the theory is based on. Metals will generally have a greater range of elastic deformation before the permanent damage occurs, whereas polymers will have more time-dependent viscoelasticity properties, meaning that polymer samples can appear more brittle than metal samples depending on the load rate of the test [285]. To uncover how the composite material will be influenced and affected by weathering, for example if it were to be used in offshore wind turbine blades, accelerated weathering is used. There are a few different approaches to consider; xenon arc, UV exposure or carbon arc with the addition of salt sprays or sands to cause corrosion [286]. As the composite materials are aimed to improve the performance of offshore wind turbine blades, it was determined that the use of ISO 12944-9:2018 would be the most applicable ensuring that both UV, condensation and salt sprays would be used to mimic the external offshore conditions as accurately as possible [273, 287]. Accelerated weathering tests cannot accurately replicate the conditions that a material will be exposed to, but can be used to determine the suitability for an

environment. Following the weathering tests other mechanical properties can be re-tested to see the impact of the weathering, and therefore the suitability of the material in this environment. In this case tensile testing was identified as the desired test following the accelerated weathering as it will consider the bulk properties of the whole material, and allow the calculation of Young's Modulus and the resultant comparison to see the impact of the weathering process. Scanning electron microscopy was carried out on the remnants of the composite material to identify the fracture point, and to investigate how the face of the breaking point was affected. TGA was also used on the post-test fragments, to limit the production of excess epoxy, to determine if the presence of the carbon material will influence the thermal degradation of the epoxy sample. Where possible all the mechanical tests were carried out in triplicate to allow for the exploration of the variance within the samples, however, for the materials produced from the synthetic gas mixture only one sample could be produced for each test due to cost and time limitations.

5.2 Determination of the tensile strength of the composite material

The tensile strength of the composite samples found that there was a general decrease with an increase of the control carbon, synthesised from methane, which is exemplified in Figure 5.1. Due to the nature of tensile testing, there is an inherent lack of reproducibility [37], this is especially noticeable in the graph for the 2 wt.% methane carbon (MC) in epoxy composite, as there is a greater variance within the data with a standard deviation of 259.7 whereas the 3.5 wt.% MC sample has a standard deviation of 121.7 showing that the samples for the 3.5 wt.% MC samples has less variance in the load required to reach the tensile load of the composite material. Unfortunately, due to the time limitations and the low yield, only one sample for each synthetic carbon loading was produced. This means that there is a higher risk of error, as there is no comparison between samples. The variance within the loading of the sample can be assigned to human error, the presence of microfractures already existing within the sample as well as an incompletely mixed sample. Human error will lead to the samples having some variance within the thickness of the gauge, which in turn will lead to variances with the tensile strength, these may be minimal but have a great impact on the repeatability of the tensile load. There may also be differences with the mixing of the carbon sample with the epoxy resin, and variations within the ratio of curing agent with the bisphenol A, both of these will alter the mechanical

properties of the produced composite material. Increasing the proportion of hardener will make the sample more brittle whilst a lower proportion of hardener will lead to a more flexible sample. During the manufacture of the composite materials, air is introduced into the epoxy resin during the mixing of the carbon to ensure a homogenous sample, however despite the sample being degassed, pockets of air can form which will lead to points of weakness within the sample. As these spots of weakness cannot be accurately mapped within the composite, it cannot be accurately used to transcribe the cause of failures occurring earlier. Microfractures can occur within the sample during the curing phase, caused through the release of any encapsulated air, or due to any temperature changes during curing. For the pure epoxy sample, the early failure is likely due to a difference in the gauge thickness of the sample, or poor curing, as there will be less chance of the air being entrapped and surrounding carbon particles and leading to weaknesses. It can be seen that for one sample of 0.5 wt.% methane carbon impregnated in the epoxy composite, a different loading rate was used, this was caused by human error, and will not affect the load at which the sample was overcome by the tensile load. At the pre-breaking loads for some samples, there are some fluctuations on the plot, this is caused by the sample slipping within the clamp, causing the load measurement to be changed, this slippage will not impact the overall tensile strength of the composite material.

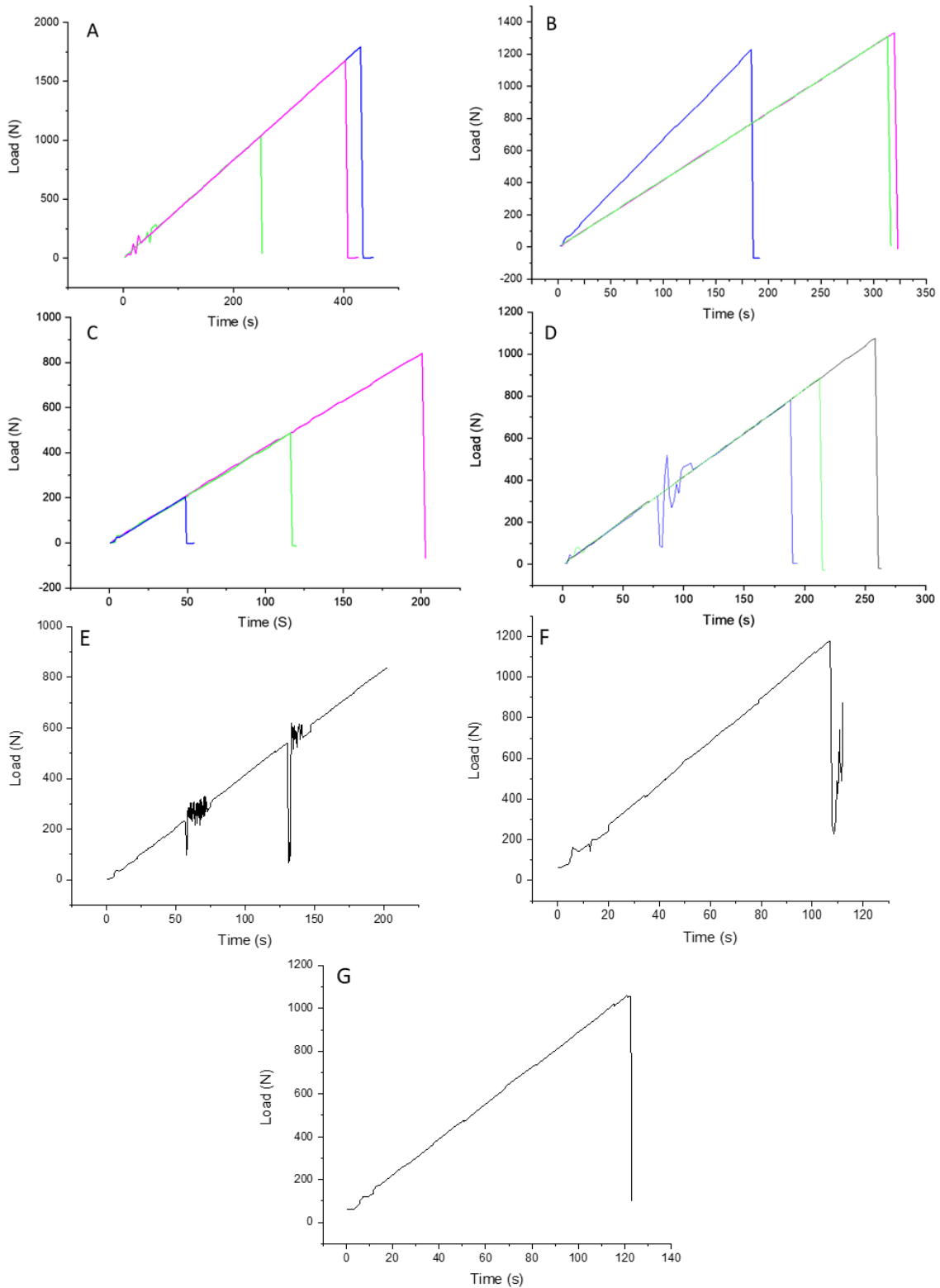


Figure 5.1. Plots to show the maximum tensile loading (stress) before failure for composite materials at different carbon loadings (a) pure epoxy sample (b) 0.5 wt.% carbon in the epoxy sample (c) 2 wt.% carbon in the epoxy sample and (d) 3.5 wt.% carbon in the epoxy sample (e) 0.5 wt.% synthetic carbon (f) 2 wt.% synthetic carbon (g) 3.5 wt.% synthetic carbon

The loading for the samples was used to determine the stress, strain and Young's modulus, seen in Table 5.1, which allows for a greater understanding of the physical and mechanical properties of the epoxy composite materials. It was reported that the cured bisphenol A would have a tensile strength equivalent to 56 N/mm^2 which as the sample gauge will have an area of 36 mm^2 gives 2016 N [288]. The samples tested through the LLOYDS EZ50 were between 1026.2 and 1792.1 N , which indicates that during the process of producing the epoxy sample, the sample was not correctly degassed, leading to defects within the composite. It can be seen from Figure 5.1 that the maximum tensile load for the $0.5 \text{ wt.}\%$ MC sample is measured as 1332.4 N with a minimum load seen to be 614.5 N showing a decrease across the spread of data with the addition of carbon to the epoxy matrix. The spread of data for the $2 \text{ wt.}\%$ MC containing composite material was seen to be greater than that for any other sample, with the lowest tensile load being 201.4 N and the greatest being 839.7 N , which is less than that seen for the $0.5 \text{ wt.}\%$ MC composite samples. The $3.5 \text{ wt.}\%$ MC loaded composite had a peak tensile load of 1074.9 N with the lowest load being 780.1 N .

For the synthetic carbon the maximum load for $0.5 \text{ wt.}\%$ synthetic carbon (SC) composite was 837 N , with 1056 N as the maximum load for the $2 \text{ wt.}\%$ SC composite and 1175 N for the $3.5 \text{ wt.}\%$ SC sample. The carbon produced from the synthetic gas mix can be seen to have the maximum load for the $3.5 \text{ wt.}\%$ SC loaded sample, which was seen to be similar to the average load to the $3.5 \text{ wt.}\%$ methane carbon sample. The greatest difference in maximal loads is between the $2 \text{ wt.}\%$ samples, where the methane carbon had a maximal load of 839.7 N which is significantly lower than the 1056 N from the synthetic carbon mix, this may be due to the lack of repeats causing a false higher result. It can be seen that all the tensile loading abilities of the carbon containing composites is lower than that seen for the pure epoxy sample, however there is overlap with the 0.5 and $3.5 \text{ wt.}\%$ MC loaded samples, meaning that the addition of the carbon will not significantly reduce the performance of the epoxy material. The $2 \text{ wt.}\%$ methane carbon composite sample saw no overlap in tensile load with the pure epoxy, showing that it has reduced the tensile performance of the composite material.

Comparatively to the methane control samples, with a greater carbon loading there is an increase in the maximal load of the composite material. This may be due to the different

properties of the carbon nanofibers, or the presence of the metal nanoparticles that remain within the composite material. The loading profiles of these samples show that they are a brittle material, as there is no necking seen, on the sample or on the graphs shown in Figure 5.1, once the maximum loading of the sample is reached, it fractures. This property is not seen to change with an increased loading of the carbon sample within the epoxy matrix. This continued brittleness shows that the carbon does not lead to any increased elasticity within the sample, which is expected as carbon nanofibers are not known for their elasticity, and as the presence of reinforcement agents is designed to impart the mechanical properties of the additive material, it is clear that the carbon nanomaterial has no higher elasticity than that of the epoxy.

$$\sigma = F/A \quad \text{Equation 8.}$$

The tensile stress was calculated using Equation 8 where;

σ is stress (MPa)

F is the force applied (N)

A is the cross-sectional area of the test sample (mm²)

$$\varepsilon = \frac{\Delta L}{L} \quad \text{Equation 9.}$$

Tensile strain is determined through Equation 9 where;

E is strain

ΔL is the change in length of the sample at a given moment (mm)

L is the original length of the test sample (mm)

$$E = \frac{\sigma}{\varepsilon} \quad \text{Equation 10.}$$

Young's Modulus is calculated using Equation 10 where;

E is the young's Modulus (MPa)

σ is stress (MPa)

ϵ is strain

Table 5.1. Stress, strain and Young's Modulus for composite samples that contain either no carbon, 0.5 wt.% carbon, 2 wt.% carbon or 3.5 wt.% carbon from different feedstocks

Sample	Maximum stress (MPa)	Strain	Young's Modulus (MPa)
Pure epoxy 1	49.78	1.666	298.67
Pure epoxy 2	28.78	0.13	2213.68
Pure epoxy 3	46.64	1.61	288.49
0.5 wt.% MC 1	38.78	0.078	495.03
0.5 wt.% MC 2	37.00	0.07	531.10
0.5 wt.% MC 3	17.06	0.058	295.76
2 wt.% MC 1	23.31	0.036	641.44
2 wt.% MC 2	13.50	0.067	202.50
2 wt.% MC 3	5.67	0.046	1231.88
3.5 wt.% MC 1	21.67	0.317	684.21
3.5 wt.% MC 2	29.83	0.057	520.35
3.5 wt.% MC 3	24.61	0.049	498.87
0.5 wt.% SC	23.28	0.042	559.60
2 wt.% SC	24.19	0.054	431.43
3.5 wt.% SC	28.17	0.048	586.85

The maximum stress and strain of each sample can be seen in Table 5.1, alongside the calculated Young's Modulus. It can be seen that there is a general decrease in the maximal stress the sample can withstand with an increase in the carbon loading. As there is a consistent decrease for the 2 wt.% MC loading sample, it is not due to human error in one

sample, which can be seen to cause the pure epoxy 2 sample to show significant differences in the stress and strain compared to the other two pure epoxy samples. The 0.5 wt.% MC loaded carbon sample 3 also shows the presence of incorrect manufacturing leading to variations with the stress and strain compared to the other samples. There may be air bubbles surrounding the impregnated carbons or other microdefects caused during curing which will cause weaknesses in the sample. At 0.5 wt.% MC the additional carbon may not significantly influence the mechanical properties of the sample, as the loading of the carbon may not have led to the disruption of the matrix enough to influence the mechanical properties, whilst at 2 wt.% MC the carbon loading can disrupt the epoxy structure enough to reduce the mechanical properties, but the loading is insufficient to impart improved mechanical properties on the composite material. By 3.5 wt.% methane carbon loading the mechanical properties are seen to increase, this shows that the reinforcement filler material is beginning to improve the reduction in mechanical properties seen. For the synthetic carbon composites, there is a smaller spread of values, with a standard deviation of 2.4 whilst for the methane carbon composites there is a standard deviation of 8.5 across the averages. This shows that the synthetic carbon samples have a reduced impact on the tensile strength of the sample. All three of the synthetic carbon composite samples have comparable tensile strength to the 3.5 wt.% MC sample. The stress is reduced from the average of 30.93 MPa for the 0.5 wt.% MC loaded samples to 25.36 MPa for the 3.5 wt.% methane carbon samples, which is an increase of the 2 wt.% MC loaded sample average stress measurement of 13.56 MPa. The strain seen for the different samples appears more constant, although there is a decrease from the maximum strain seen for the pure epoxy compared to that seen for the composite material. Strain will show how much the sample extends as the load is applied, and so can be used to support the determination of the ductility of the composite.

As the strain is seen to be highest for the pure epoxy samples, they can be assumed to have the greatest ductility of the samples seen, at 1.66, 0.13, and 1.61 with one of these being significantly lower, in line with the stress seen, which shows that presence of defects within the sample will affect both the stress and strain measurements. For the majority of the other samples, the strain measurements are seen to be between 0.036 and 0.078, with a further high of 0.317 for sample 1 of the 3.5 wt.% MC loaded, showing that this sample

shows a greater ductility compared to the others. The strain calculated for the SC composite materials are comparable to those generated from the other samples, at 0.042 to 0.048, showing that the changes within the microstructure of the nanomaterials does not have an influence on the strain. As the other values of maximum strain are relatively consistent it shows that the ductility of the samples at every carbon loading is comparable, and that increasing the carbon loading in the composite does not affect this.

A higher Young's Modulus will show a stiffer material that will show less changes to the shape and size when under an elastic load. It can be seen that as a whole the Young's Modulus is lowest for the pure epoxy samples, at 29.87 and 28.85 MPa, the defective sample had a Young's Modulus of 221.37 MPa, showing a higher relative flexibility within this sample but that the defective sample would show a lower level of deformation under load. In general, the Young's Modulus results for the 0.5 wt.% and 3.5 wt.% MC composite materials were similar, from 49.5 to 68.42 MPa, showing similar reactions to being under load. The 0.5 wt.% MC sample 3 showed a Young's Modulus of 29.58 MPa which was lower than the other samples, due to a lower stress measurement compared to the other samples in this group, whilst retaining a similar strain, this leads to the sample showing a greater ability to be deformed following the same loading. It can be assumed that if the carbon were poorly dispersed within the sample then this would influence this variance in Young's Modulus seen, however, there was no evidence of this happening for this sample. The sample may have had a different sample thickness at the breakage point, which would not be accounted for in the calculations of stress and strain, this accumulated error would carry into the calculation of Young's Modulus. The synthetic carbon samples showed a reasonably high level of stiffness, especially compared to the pure epoxy samples. The Young's Modulus for the 0.5 wt.% SC epoxy samples was calculated to be 559.60 MPa compared to the MC composite has an average Young's Modulus of 440.66 MPa showing the synthetic carbon imparts a greater stiffness. Again, there is a great variance seen for the 2 wt.% MC loaded samples, with a range from 20.25 MPa to 123.12 MPa, showing defects within these samples. These defects could be due to differences within the gauge width which would alter the cross-sectional area due to lips forming during degassing and subsequent curing, or the vacuum desiccator being shifted, preventing the sample from curing flat. To prevent this affecting the calculations, the individual samples were measured

using callipers to ensure an accurate calculation of stress and strain could be made, this limited the impact of changes in width of the sample affecting the overall calculation. The variation in the Young's Modulus seen for the 2 wt.% MC sample is likely related to the presence of air bubbles caused by air being trapped within the sample by the carbon nanoparticles. The degassing of the sample may not have fully remove air pockets surrounding the carbon, which will lead to points of weakness, affecting the stress and strain, and therefore the Young's Modulus.

Therefore, it can be seen that the increased load of the carbon in the epoxy sample will influence the mechanical properties of the composite, although not necessarily for the better, an increased loading appears to cause the material to become more brittle, this was especially seen for the 2 wt.% MC carbon sample. These variances may be due to particle agglomeration within the composite material, preventing the influence of the imparted mechanical properties from improving the bulk properties. There were some differences in the behaviour seen from the addition of the synthetic carbon compared to the methane carbon. These differences could be associated with the presence of the metal nanoparticles remaining within the carbon samples, and distorting the internal matrix structure, leading to a greater level of defects.

5.3 Determination of the flexural strength of the composite material

Compression testing, similarly to tensile strength, shows low level of repeatability [289] due to the presence of human error, machine error and microdefects within the produced sample. Similarly to the tensile testing, the maximum loading for the samples was seen to be for the pure epoxy, shown in Figure 5.2, with a decrease in the load being seen once the carbon has been mixed into the sample. The rate of load addition is kept constant to ensure the results generated are comparable, meaning that the plots can be used to determine that the maximal loading for the pure epoxy is between 98 and 147 N whilst for a 0.5 wt.% carbon composite this range is from 104.4 to 125 N, with the 2 wt.% MC composite and the 3.5 wt.% MC composite having ranges of 45.3 to 70.7 N and 93.6 to 125.3 N respectively. To determine the spread of data the standard deviations were calculated showing the pure epoxy exhibited the greatest spread of variance with 62.23 whilst the 0.5 wt.% MC composite only had a standard deviation of 7.87, with 3.5 wt.% MC and 2 wt.% MC having 15.08 and 28.73 correspondingly. Similarly, to the synthetic composites tested for tensile

strength, due to the limitations regarding the use of carbon monoxide, there was only one of each weight loading produced. The differences in these measurements could be due to all the same defects considered in Section 5.1, as these will affect the flexural strength of the sample as well as the tensile strength.

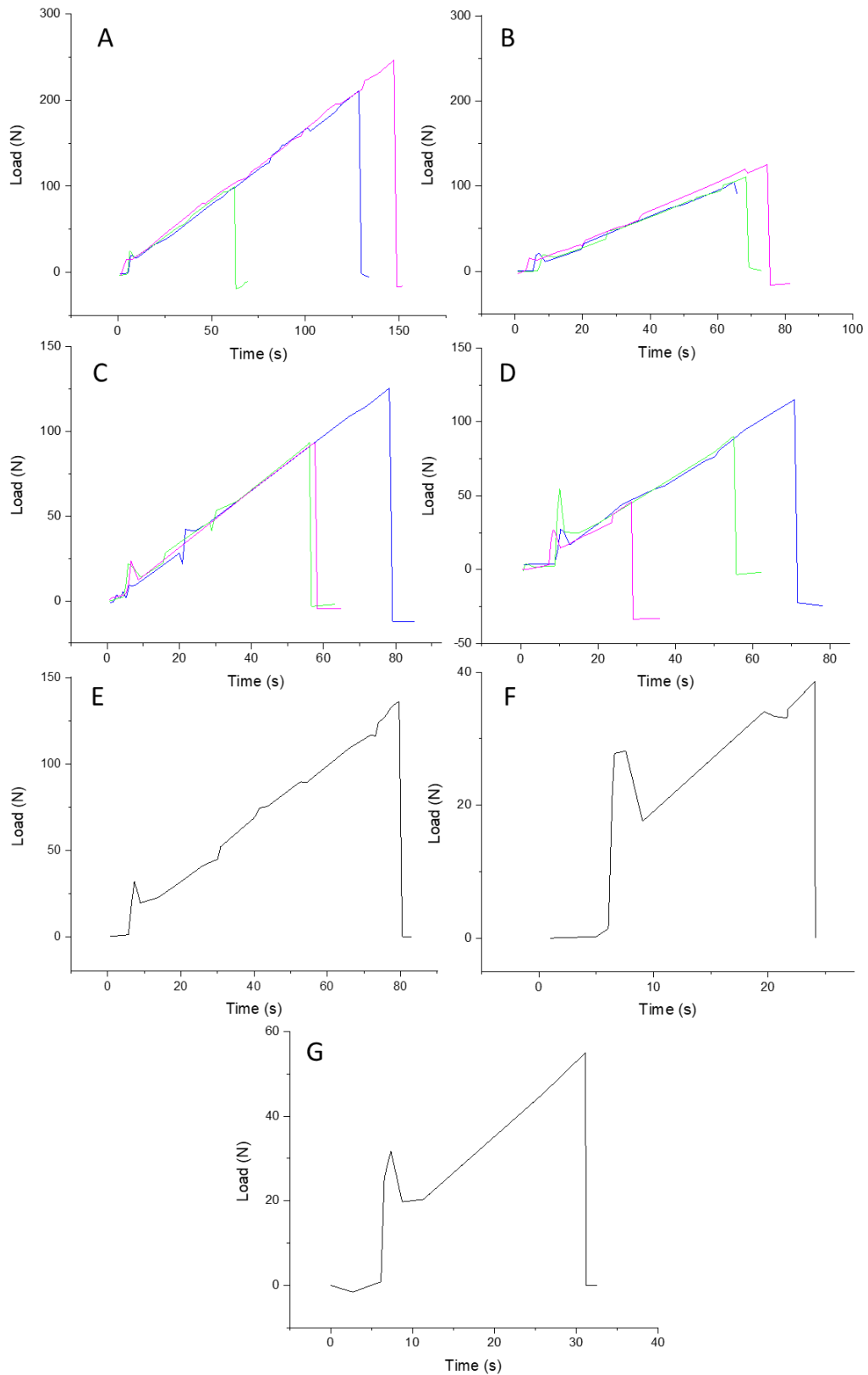


Figure 5.2. Results of 3-point bending tests to determine the flexural strength of a composite material made of (a) pure epoxy and composite materials of pure epoxy and (b) 0.5 wt.% methane carbon (c) 2 wt.% methane carbon (d) 3.5 wt.% methane carbon (e) 0.5 wt.% synthetic carbon (f) 2 wt.% synthetic carbon and (g) 3.5 wt.% synthetic carbon

The reported flexural strength of the pure epoxy sample was determined to be 1368 N for these samples [288], this was seen to be significantly higher than the measured values. However, it can be seen that the loading ability of the pure epoxy is higher than that seen for the composite materials formed, indicating that the carbon loading of the sample will reduce the flexibility of the samples. There was some sample slippage seen at the early points of the testing, however, as the rate of loading remains constant, these will not affect the overall flexural properties, such as maximal loading, flexural stress, flexural strain and flexural modulus. Sample slippage can be caused by movements within the load cell and attachments, especially at the start. Considering the results for the pure epoxy and 0.5 wt.% MC loaded composite, a change in the loading rate can be seen close to the failure point, this occurs due to the material flexing with the increased load, which in turn can cause some inaccuracies within the measurements of the loading rate. It can also be seen to occur as the sample starts to reach the end of the elastic potential, preventing it from withstanding the pressure of the loading. When the sample reaches this point, small cracks will start to occur which will contribute to the overall failure of the composite materials, once the cracks propagate through the whole sample, the load will overcome the structure, leading to the failure of the material. Theoretically the addition of a carbon reinforcing agent was expected to aid in the prevention of crack propagation, however considering Figure 5.2, it can be seen that this was not the case. The addition of carbon to the epoxy matrix has led to an increased brittleness of the material, which could be due to agglomerated carbon samples, or poor distribution. To limit the effect of these issues, the carbon sample was ground to a fine powder before being incorporated into the epoxy matrix, however this could still lead to agglomeration of the nanomaterials, leading to disruptions in the epoxy matrix, weakening the bulk material.

Table 5.2. Calculation of the maximal flexural stress, strain and flexural modulus from different composite materials composed of epoxy and varying loadings of carbon nanomaterials

Sample	Flexural Stress (MPa)	Flexural Strain	Flexural Modulus (MPa)
Pure epoxy 1	0.35	0.095	875.0
Pure epoxy 2	0.17	0.031	415.1
Pure epoxy 3	0.41	0.096	1027.0
0.5 wt.% MC 1	0.21	0.057	535.6
0.5 wt.% MC 2	0.18	0.136	462.1
0.5 wt.% MC 3	0.21	0.038	522.7
2 wt.% MC 1	0.21	0.036	523.6
2 wt.% MC 2	0.16	0.025	388.9
2 wt.% MC 3	0.17	0.026	388.2
3.5 wt.% MC 1	0.19	0.019	477.1
3.5 wt.% MC 2	0.15	0.031	375.8
3.5 wt.% MC 3	0.08	0.035	365.6
0.5 wt.% SC	0.23	0.147	566.7
2 wt.% SC	0.06	0.031	160.8
3.5 wt.% SC	0.09	0.042	229.5

The calculation of flexural stress, strain and modulus are different from those for tensile testing, and the equations are as follows [290, 291].

$$\sigma_f = \frac{My}{I} \quad \text{Equation 11.}$$

Flexural stress was calculated from Equation 11 where;

σ_f is the flexural stress (MPa)

M is the internal bending moment

Y is the perpendicular distance from neutral axis to a point on the section (mm)

I is the moment of inertia of the section area about a neutral axis

Flexural strain is calculated through the use of Equation 12

$$\epsilon_f = \frac{6Dd}{L^2} \quad \text{Equation 12.}$$

Where;

ϵ_f is the flexural strain

D is the maximum deflection of the centre of the test beam (mm)

d is the depth of the sample gauge (mm)

L is the length of the sample material (mm)

$$E_f = \frac{L^3 F}{4bd^3} \quad \text{Equation 13.}$$

The flexural modulus is calculated through Equation 13 where;

E_f is the flexural modulus (MPa)

L is the length of the test sample (mm)

F is the force applied to the test sample (N)

b is the width of the test sample (mm)

d is the depth of the test sample (mm)

The flexural loading plots, Figure 5.2, showed the maximal loadings for each composite material and allowed the calculation of the flexural stress, strain and flexural modulus, shown in Table 5.2, with the equations seen above. These calculations allow the mechanical properties of the composite materials to be understood, and how the flexural properties can vary depending on the loading of carbon within an epoxy matrix. The flexural stress and strain are calculated from the maximal force applied to the composite material before fracture, showing the maximum stress and strain each sample can withstand following the application of a bending force. Flexural stress is also referred to as the flexural strength, and relates to how well a sample can withstand the pressure of bending, a higher value shows a greater resistance to fracture. It can be seen that the pure epoxy has the highest flexural stress results, at an average of 0.31 MPa whilst 0.5 wt.% MC, 2 wt.% MC and 3.5 wt.% MC

loaded composites had results of 0.2, 0.18 and 0.14 MPa respectively. It can be seen that the pure epoxy has the highest result, meaning the lowest flexibility and a greater resistance to bending, although the pure epoxy sample 2 showed a lower flexural stress result at 0.17 MPa compared to the other readings of 0.41 and 0.35 MPa. The 0.5 wt.% SC sample showed the second highest flexural stress, with the 2 wt.% and 3.5 wt.% SC samples both being lower than that seen for their MC counterparts. This could be due to the presence of air within the sample where the sample was not fully degassed, and the increased metal content within the SC samples could lead to more air trapped in pockets. Air will lead to points of weaknesses, as well as distortions in the matrix, and will ultimately lead to failures within the sample.

When 0.5 wt.% MC is added to the composite material, it can be seen that there is a decrease in the flexural strength from the pure epoxy flexural strength of 0.31 MPa to 0.2 MPa, this decrease shows that the sample is comparably easier to bend under an applied force. However, this coupled with the lower maximal loading seen in Figure 5.2 shows that the sample will load less before it succumbs to the applied load under flex. This decrease in strength can be attributed to the presence of the carbon sample, which will distort the matrix enough to weaken the sample with a weight loading of carbon that is too low to impart the mechanical properties to the bulk material. As the carbon loading increases to 2 wt.% MC the flexural stress that the sample can withstand decreases further, to an average of 0.18 MPa, which alongside the maximal loading seen being 70.7 N, shows that the sample will have less resistance to bending under an applied load, this is seen as well in the 2 wt.% SC sample where there is a decrease to 0.06 MPa. This further reduction in strength can be assigned to the further disruptions in the bonding of the epoxy through the addition of a greater loading of carbon. As the carbon disrupts the epoxy network it can lead to voids, crosslinking defects and debonding, each of which will lead to the weakening of the overall structure [292]. This variance can be attributed to the distribution of the carbon within the composite. When the weight loading was 0.5 wt.% for both carbon types, the distribution did not appear to significantly cause variance within the calculated flexural strength, which may be as it is less significant to the overall sample, leading to limited agglomeration, preventing further voids and point defects forming. With the 2 wt.% loaded samples, agglomeration can start to occur which will lead to greater disruptions of the crosslinking

network of the epoxy matrix. The increase in the flexural stress seen at the 3.5 wt.% MC loaded sample can be used to determine the start of the positive influence of the carbon nanomaterials within the epoxy composite, although this is still lower than that seen for both 0.5 wt.% loaded samples. Therefore, it can be seen that whilst the initial increase of carbon added to the epoxy sample leads to a decrease in performance, the flexural stress is seen to begin to recover at the addition of 3.5 wt.% MC although this was not seen to be the same for the synthetic carbon samples.

The flexural strain, similarly to the strain seen in section 5.2, considers how the length of the sample will be affected by the addition of a load, a higher value will show a greater level of bending seen within the sample with an applied load. Similar to the stress results, the strain results are calculated from the maximal load seen on the sample. There is an anomalous point for the 0.5 wt.% MC 2 sample where a flexural strain of 0.136 is seen, this can be attributed to an error in the ratio of hardener to epoxy, leading to a more flexible sample, increasing the extension of the sample under load, whilst not affecting the strength of the sample, as it withstood a load of 110 N. The pure epoxy samples saw a greater change in the length of the sample during the application of a load, whilst the 2 wt.% MC samples showed the least change in deflection at an applied load. The 2 wt.% MC loaded sample therefore shows significant defects leading to failure before the sample bends, showing the related properties of the flexural stress and strain. The lower flexural stress means that the sample is not as resistant to bending whilst the flexural strain shows that the length of the sample does not significantly change under load, indicating a brittle sample. The 3.5 wt.% methane carbon loaded samples showed an increase in the flexural strain compared to the 2 wt.% MC loaded samples, which can be seen to be the impact of the increased carbon loading leading to the imparting of the mechanical properties from the carbon materials to the epoxy material. This shows that at the 3.5 wt.% MC loading the benefits provided from the additive carbon will start to overcome the issues caused through the formation of voids, defects and air pockets during the curing process. The synthetic carbon 2 wt.% and 3.5 wt.% loading samples were seen to be comparable to that of the MC composites, but the 0.5 wt.% SC composite had a higher strain than the pure epoxy with a value of 0.147, similar to the anomalous data point for the 0.5 wt.% MC composite. However, due to a lack of

repeated measurements, it is unclear if this would be the same for all 0.5 wt.% SC composites.

The flexural modulus shows how resistant a material is to bending, and considers both the load applied and the change in shape of the sample during the application of the load. For the pure epoxy samples, the results showed a spread of results from 415.1 to 1027.0 MPa, and an average of 772.3 MPa. The higher the flexural modulus, the higher the resistance to bending, meaning a stiffer, less flexible material. The highest flexural modulus was seen for the pure epoxy sample 3 with a measurement of 1027.0 MPa, showing it is the least flexible sample. As a greater weight percent of carbon is added to the epoxy matrix, there is a greater chance for the disruption of the crosslinked network, leading to voids. At the 3.5 wt.% MC loaded sample, the flexural modulus is between 365.6 and 477.1 MPa with an average of 402.6 MPa, showing that the addition of carbon will influence the flexural modulus seen. The 3.5 wt.% sample showed the least spread of data, with only 112 MPa between the minimum and maximum flexural modulus seen, showing the highest reproducibility for all the produced composites. This reproducibility could be due to a stabilising effect from the addition of the carbon to the epoxy sample, less variance in the ratio of epoxy to hardener or more uniformity within the sample. It is likely that all three of these will contribute to the reduced spread of flexural modulus seen. The 0.5 wt.% methane carbon sample had an average flexural modulus of 506.76 MPa. This situates the flexural modulus for the 0.5 wt.% MC samples as stiffer than those of the pure epoxy, with 3.5 wt.% and 2 wt.% MC samples being the highest stiffness samples. This shows that the 0.5 wt.% MC loaded sample does not disrupt the matrix to cause significant voids or breakages, leading to poor mechanical properties, whilst the 2 wt.% MC sample is weaker, which is attributed to the formation of voids surrounding agglomerated carbon nanomaterials. The 3.5 wt.% MC sample shows an improvement in the mechanical properties when compared to the 2 wt.% MC sample, which shows that the issues with agglomeration and void formation have started to be overcome by this increased carbon loading. For the synthetic carbon composite, the 0.5 wt.% sample was comparable to the data seen for the 0.5 wt.% MC with 566.7 and 506.8 MPa respectively, whilst the 2 and 3.5 wt.% SC composites showed a much lower flexural modulus, meaning that the material is less resistant to bending when a force is applied.

Theoretically the flexural modulus and Young's Modulus should be comparable, and whilst there is some level of similarity between the two measurements, it can be seen that the composite materials produced have a greater resistance to tensile testing when compared to flexural testing. However, all the samples can be seen to be stiff with the pure epoxy sample having the greatest loading potential when considering the loads that the samples withstood during testing. It appears that the bisphenol A and carbon composite materials have a greater affinity to tensile testing due the lower Young's Modulus showing a greater level of flexibility. A lower Young's Modulus and flexural modulus will lead to an increased likelihood of the sample recovering following stresses applied in these directions, for example following an impact, or during the use of a material. Whilst the results for both Young's Modulus and flexural modulus show that the sample is relatively brittle and stiff, it can be seen that this is less so in the tensile plane compared to the resistance to bending. For tensile testing, the 2 wt.% methane carbon loading sample shows the greatest variance and stiffness, meaning it is the most brittle sample, and can be assumed to contain the greatest number of defects and voids, despite best efforts during the manufacture of the samples. The 0.5 wt.% methane carbon loaded sample shows the greatest similarity to the results for the pure epoxy, indicating that there is insufficient carbon to alter the internal structure of the epoxy matrix sample significantly, whilst the 3.5 wt.% MC sample shows improvements in the mechanical properties when compared to the 2 wt.% MC sample but not yet reaching those seen for the 0.5 wt.% MC sample. This increase for the 3.5 wt.% MC sample can be attributed to the beginnings of the carbon nanomaterials imparting mechanical properties, and reinforcing the epoxy matrix. There were differences seen for the synthetic carbon composites, although these were seen to be predominantly in the flexural tests, showing that the change in the nanostructured carbon can lead to a lower resistance to bending under load. This may be due to changes in the inherent mechanical properties of the carbon nanomaterials, or the presence of the nickel metal nanoparticles leading to increased brittleness. The maximal loading is seen to be greater for the tensile testing, by a significant factor, which is due to the loading of the sample. During tensile testing, the whole sample is involved in the resistance to loading, whilst for the three-point bending test the loading is focused on half of the sample, although this is taken into consideration during the calculation of the respective modulus. It can be seen that the addition of carbon to the epoxy sample will influence, and impact, the mechanical

properties of the resultant composite materials, with the weight loading further impacting the properties seen.

5.4 Accelerated weathering and post weathering tensile testing

The different composite samples underwent 672 hours of weathering to determine how efficiently the samples would resist the effects of exposure to salt spray and UV radiation. It is worth noting that there was only one sample each for the synthetic carbon epoxy due to the increased time and cost of production of these and that during transit some damage was caused, which will not affect the accelerated weathering but did prevent the tensile strength being recorded for one sample. It appears that the pure epoxy and all 0.5 wt.% carbon composites are affected by the accelerated weathering as there is a colour change that occurs as seen in Figure 5.3. However, due to the nature of the carbon, it is unclear if this resistance to colour change is due to the carbon improving the resistance to the weathering or if the carbon masks these effects. There was no significant degradation following the addition of the salt spray, this shows that the epoxy-carbon composite materials are not degraded through a salt spray atmosphere. The surfaces of the post-weathered samples are seen to have become slightly matte following exposure to the salt spray. However, there are no significant changes to the surface appearance following the exposure. If the samples were not resistant to weathering it would be expected that the surface of the material would be worn down and the shape of the sample would be changed.




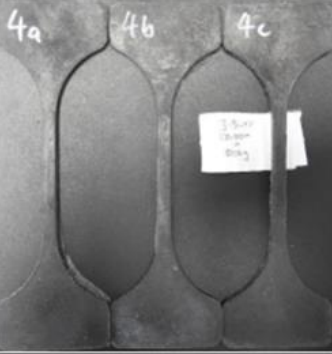



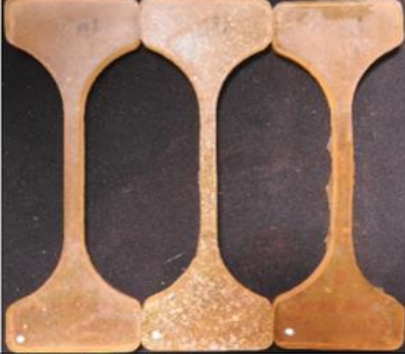

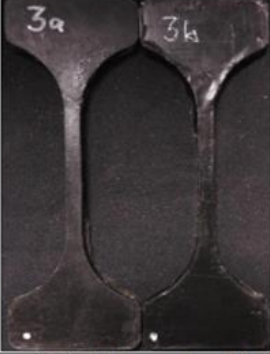



<p>1. Unfilled epoxy (3 off).</p>	<p>2. 0.5% Carbon filled epoxy (3 off). Note samples have damage on gauge lengths.</p>	<p>3. 2% Carbon filled epoxy (2 off).</p>	
			
<p>4. 3.5% Carbon filled epoxy (3 off).</p>	<p>5. 0.5% Syn carbon filled epoxy (1 off).</p>	<p>6. 2% Syn carbon filled epoxy (1 off). Sample heavily warped.</p>	<p>7. 3.5% Syn carbon filled epoxy (1 off).</p>
			
<p>1. Unfilled epoxy. Samples have yellowed & become cloudy.</p>	<p>2. 0.5% Carbon filled epoxy. Note samples have damage on gauge lengths. Some yellowing & clouding seen.</p>	<p>3. 2% Carbon filled epoxy. No significant visible changes. Some gummy residues.</p>	
			
<p>4. 3.5% Carbon filled epoxy. No significant visible changes.</p>	<p>5. 0.5% Syn carbon filled epoxy. Some yellowing seen.</p>	<p>6. 2% Syn carbon filled epoxy. Sample heavily warped. No significant visible changes.</p>	<p>7. 3.5% Syn carbon filled epoxy. No significant visible changes.</p>
			

Figure 5.3. Images of epoxy samples before and after accelerated weathering, the individual samples are labelled in the image, where the type of carbon is not specified it is methane produced carbon.

Once the weathering was carried out, the post-weathered samples underwent tensile testing which can be compared to those carried out on the original samples. The rate of loading was different to that of the non-weathered tensile testing, however this should not affect the peak load that the sample can withstand. Unfortunately, the 2 wt.% synthetic carbon sample was too deformed for testing and therefore cannot be compared.

Table 5.3. Stress and Young's Modulus for different carbon composite materials following accelerated weathering

Sample	Stress (MPa)	Young's Modulus (MPa)
Pure epoxy 1	40.68	2521.37
Pure epoxy 2	33.92	2149.36
Pure epoxy 3	37.70	2447.47
0.5 wt.% MC 1	21.16	2004.05
0.5 wt.% MC 2	28.95	2653.53
0.5 wt. % MC 3	22.55	1831.34
2 wt.% MC 1	33.79	2066.05
2 wt.% MC 2	34.97	2150.61
3.5 wt.% MC 1	28.70	2845.55
3.5 wt.% MC 2	23.67	1472.04
3.5 wt.% MC 3	23.49	2003.32
0.5 wt.% SC	30.76	1992.94
3.5 wt.% SC	14.69	2401.33

There is a decrease in the maximal stress for the pure epoxy and the 0.5 wt.% MC sample. For the pure epoxy there was a decrease from an average stress of 41.73 to 37.43 MPa and for the 0.5 wt.% methane carbon composite from 30.95 to 24.22 MPa following the weathering. For the 2 wt.% methane carbon composite the sample showed an increase in the tensile strength from 14.16 to 34 MPa, and the 3.5 wt.% methane carbon composite showed no increase but also no decrease. For the 2 wt.% methane carbon composite, there

were only two samples available for the post-weathering testing which may affect the average. However, both individual measurements are higher than that seen for the non-weathered samples so it can be assumed that there is no negative impact from the weathering. From this it can be assumed that the addition of the carbon material will stabilise the effect of weathering on the epoxy composite.

The Young's Modulus increased for all samples, due to the increase in strain and decrease in the maximal loading. This means that all the samples have become stiffer following weathering. This means that micro-cracks and fractures may have been formed during the freeze cycles, this will impair the ductility of the sample. Confirming that the accelerated weathering had the greatest impact on the pure epoxy samples, the greatest increase in the Young's Modulus was seen from an average of 933.4 to 2447.47 MPa following the weathering. Therefore, the presence of the carbon within the epoxy composite increases the resistance to weathering, by preventing the composite from becoming more brittle. Considering the actual maximal loadings seen during testing, the greatest decrease was seen for the pure epoxy sample with an average loading of 1342.61 N seen, a 156.52 N difference from the pre-weathered samples. For the 0.5 wt.% samples there was a 127.19 N decrease for the MC composite and a 25 N increase for the SC sample. The 2 wt.% MC composite samples showed a 52 N increase whilst the 3.5 wt.% samples showed a 15 and 138 N decrease for the MC and SC composites respectively.

5.5 Comparison of mechanical properties between different tests

The different mechanical properties of the composite materials were compared and can be seen in Figure 5. 4. This shows that the greatest error seen within the pre-weathering sample was in the pure epoxy, this can be attributed to the anomalous data point of 2218 MPa. For the post-weathering tensile testing, it can be seen that the highest range of data can be seen for the 3.5 wt.% MC composite. This may be due to unknown impacts of the weathering of the samples for example; microcracks, air intrusion and fracture sites. Once these are put under pressure the sample will fail under a lighter load. In general, the maximum loading was lower following weathering, with the greatest decrease being seen for the pure epoxy sample with a decrease of 10 MPa. There was an increase in the stress for 2 wt.% MC from pre- to post-weathering, 17 to 32 MPa, however, the error for this sample was high in the pre-weathering testing.

The flexural testing showed a reduced level of error when compared to the tensile testing, this can be assigned to the reduced machinery error, as the sample is not held in clamps. The positioning of the sample clamps may have increased the pressure on the sample gauge which would in turn limit the repeatability of the testing. The pure epoxy sample retains the greatest level of error, similar to the pre-weathering samples, which indicates that there is consistency within the mixing and curing steps during the formation of the composite material. However, in the flexural and pre-weathering testing there is a clear decrease in the maximal load that the composite material can withstand as the carbon loading increases.

The post-weathering sample showed less of a trend, with high maximal stress loading being seen for pure epoxy, 2 wt.% MC and 0.5 wt.% SC composite materials. The lowest point was 15 MPa loading for the 3.5 wt.% SC. This may be due to the potential failure modes as discussed earlier.

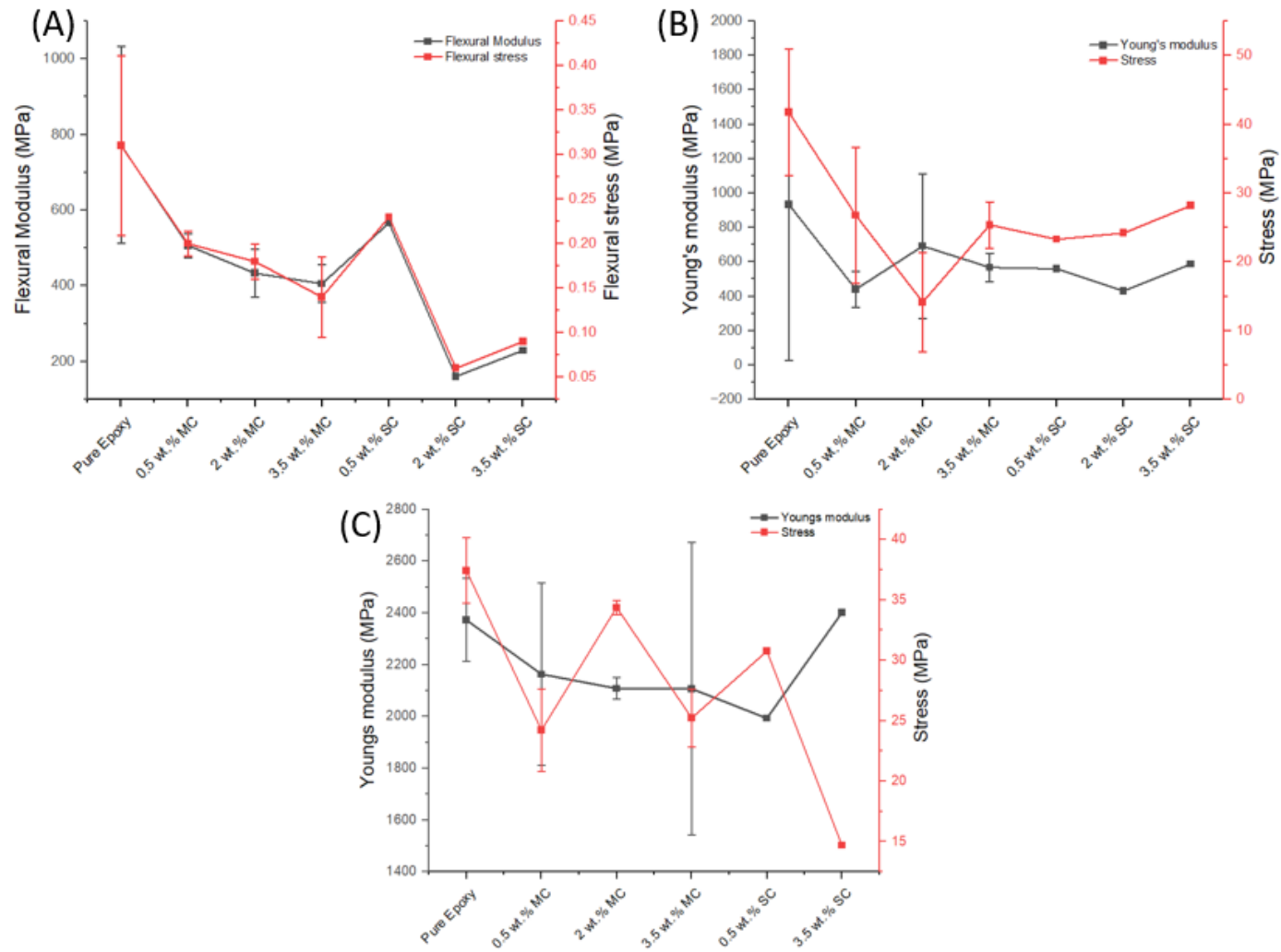


Figure 5.4. Comparison of different test parameters (A) Compression (B) Pre-weathering (C) Post-weathering on the Young's Modulus and Maximal Stress of composite materials

5.6 Scanning Electron Microscopy on fractured composite materials

Images were only taken on the tensile fracture faces of the composite sample, as the broken flexural segments were too broken to accurately identify a fracture point. As can be seen in Figure 5.5, there is an initial point of impact, and radiating out from this are cracks. Often directly surrounding the impact point there is a smooth region. This smooth region may arise from the shearing of the surface with the fracture force, or due to the fracture site being at a higher point due to the application of tensile force protecting the immediate surroundings. It can be seen in the 2 wt.% methane carbon loaded composite, that there are impurities within the sample, cotton fibres appear within the sample, likely from the PPE worn during sample preparation. This is also seen in the 3.5 wt.% methane sample, although the fibre is smaller. This human error will not affect the mechanical properties of the composite material. In the 2 wt.% methane sample, it can clearly be seen that there are microcracks within in the composite surface, however as this is following testing, it cannot be determined if this is due to the tensile testing. These deeper microcracks may be due to pockets of air surrounding the impregnated carbon, forming during the curing stage. However, as they are only significantly noticeable within the 2 wt.% methane sample it can be assumed that this may be an individual sample error, over a process error. This greater prevalence of errors and cracks within the sample could be the cause for the reduced mechanical properties seen for the 2 wt.% methane composite samples. The 0.5 wt.% MC sample has an overall smoother fracture face surface, which may be due to the lack of carbon within the sample, leading to less void spaces within the composite. The 3.5 wt.% MC sample has a less smooth fracture face than the 0.5 wt.% sample, but has less features than the 2 wt.% MC sample. This may show a greater level of impregnation, and incorporation, of the carbon within the composite material.

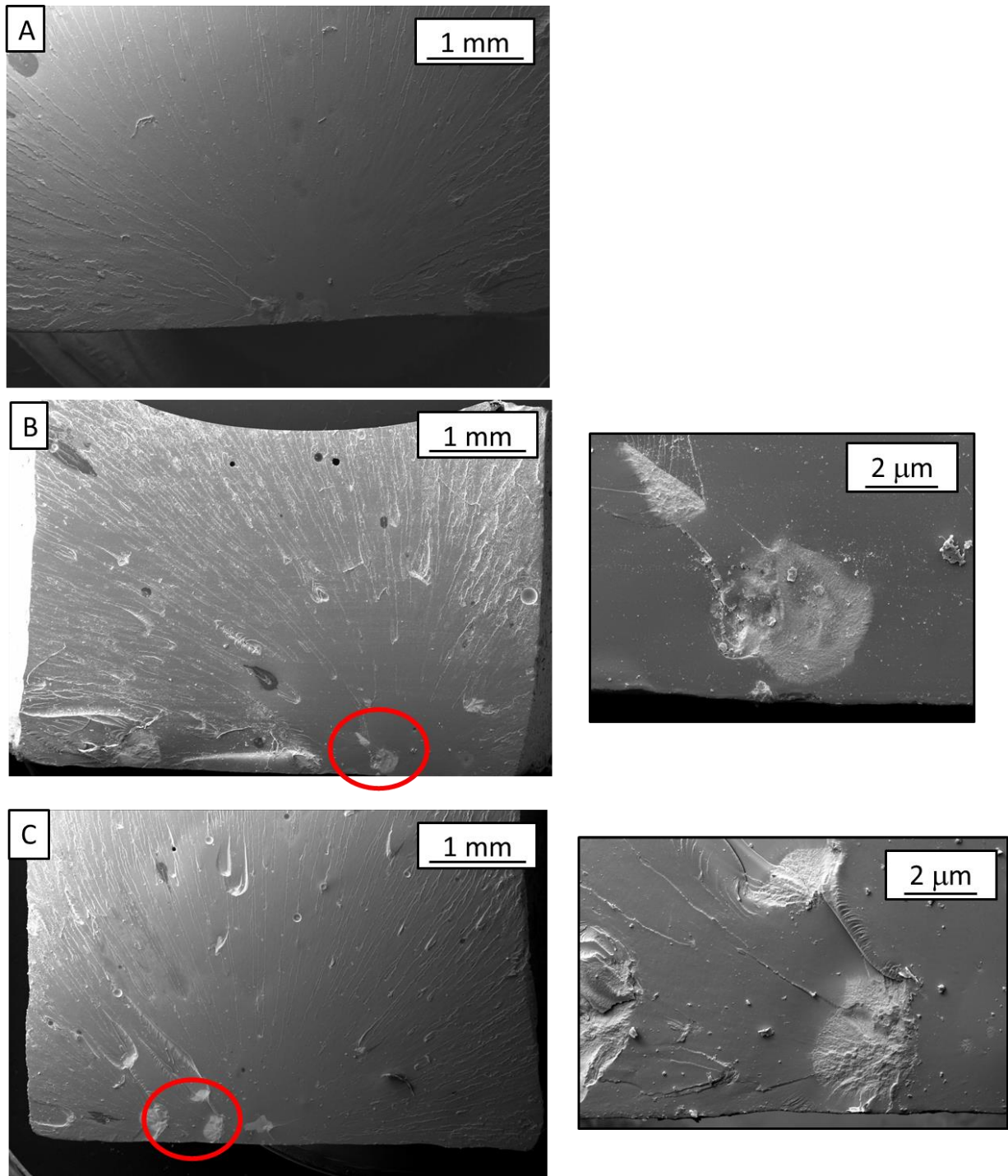


Figure 5.5. SEM images showing the tensile fracture sites of (A) 0.5 wt.% methane carbon loaded into epoxy (B) 2 wt.% methane carbon loaded into epoxy and (C) 3.5 wt.% methane carbon loaded into epoxy

The fracture points can be identified as the epicentre of the region of the smooth section, all fracture points were seen to occur at the lower edge of the sample, but were not seen to be central on the test gauge. This indicates that during the application of a load on the

composite material, even when this load is tensile in nature, the external edges are the weak point where the fracture propagation will occur. The fracture point is also seen to be more textured than other points on the fracture face, this may be due to the force being applied to this point causing heat to build up and cause deformation. These points of weakness may be initiated through small air bubbles on the surface to the sample. Where these occur, the sample will have fewer completed networks within the body of the composite, leading to a reduction of the resistance capacity for the composite. Following the fracture cracks can be seen to spread out in a star-burst pattern surrounding this smooth central point, leading to the failure of the sample as the cracks reach the edges of the sample. The profiles of these cracks widen as the carbon loading increases, however, the frequency of them decreases. This may show the beginnings of the imparted mechanical properties of the carbon addition on the composite material, with a reduced number of cracks forming, or the broader cracks can indicate the shearing of material into larger chunks, caused by impurities, and contaminants, causing weaknesses within the composite. The presence of contaminants should be limited as the carbon contained in the composite was not produced using pyrolysis gases, limiting the risk of oils in the sample, which in turn should reduce the contaminants within the sample.

For the SEM images of 2 and 3.5 wt.% methane carbon loaded samples, there are small holes seen in the surface of the fracture site. Unfortunately, the SEM cannot determine the distribution, and impregnation of the carbon within the composite surface as it is purely a topological test. But these small holes are likely related to the presence of carbon within the sample, and are the pockets of air surrounding them, which are exposed through the fracturing of the test sample. The greatest deformation seen in a fracture face is for the 2 wt.% MC sample which is consistent with the lower mechanical properties. It is unclear whether the defects seen in the fracture face have caused the reduced mechanical properties or if these formed following the application of load.

The top edge of the 2 wt.% MC sample is seen to be bowed, which will lead to a different distribution of pressure once the load is applied. This bowing is likely caused through the curing process causing shrinkage to occur, this is due to human error and despite best efforts cannot always be mitigated against. The shrinkage is also caused during degassing, where a sample will overflow the mould due to expansion and then following the release of

the vacuum, will lose sample mass and lead to shrinkage. This phenomenon may lead to slight variations within the weight percent loading, however, these should not be significant and were determined to not affect performance.

5.7 Thermogravimetric analysis of composite materials

Thermogravimetric analysis was used to determine if the addition of the carbon nanomaterial would affect the thermal degradation profile. To prevent excess plastic generation, the samples tested were samples that had mechanical testing carried out on them, as these tests would not affect the thermal degradation properties. As can be seen in Figure 5.6, there is more variance in the thermal degradation of the pure epoxy sample, for both the DTG and TGA curve. All samples, apart from one of the pure epoxy samples, show two weight loss peaks, the anomalous pure epoxy sample shows three. As these are all positioned in the same location, it can be determined that they are all the same points occurring. The first DTG peak is seen to occur at around 355 to 360 °C with the second occurring between 434 and 438 °C. The first derivative weight loss is 4.52 and 2.97 %/min for both peaks for the 0.5 wt.% MC carbon loaded composite in comparison to 4.42 and 2.99 %/min for the pure epoxy, showing that there is a slight difference in the first peak, but that the second appears to be unchanged through the addition of the carbon nanomaterial. For the 2 wt.% MC loaded sample the peaks were measured to be 4.28 and 3.09 %/min whilst for the 3.5 wt.% MC sample the peaks were 4.33 and 2.91 %/min respectively. The greatest variation is seen in the first peak size between the different loadings of carbon nanomaterials. As the temperature range for the peaks within all the samples was comparable, it can be assumed that the peaks are caused by the decomposition of the same features of the epoxy matrix, and it is just the rate of decomposition that is altered. For the 0.5 wt.% SC sample the peaks were measured at 4.1 and 3.3 %/min. For the 2 and 3.5 wt.% SC samples the peaks were measured to be 3.7 and 3.2 %/min and 3.9 and 3.2 %/min respectively. This shows that the synthetic carbon samples show slightly different weight loss curves, but they occur at the same temperatures. This shows that the addition of the synthetic carbon has altered the rate of weight loss in these areas, however, as the temperature locations of the peaks remains the same, and there is not a significant change in the weight loss per minute it can be assumed that this is instrumental error. There are two clear weight loss peaks in the DTG data, which is not represented in the TGA curve.

Literature shows that the pure bisphenol A epoxy has a DTG peak at 340 °C which was determined to be due to the degradation of the internal ether bonds, whilst a second peak at 435 °C was attributed to severing of the C-C bond connecting the benzene ring [293, 294]. These DTG peaks were not as well defined as the ones seen in Figure 5.5, although this may be due to the heating rate of the literature study being 10 °C/min and 20 °C/min whereas the data collected in the research was collected at 5 °C/min. A lower heating rate will allow more data to be collected, in higher detail. It can be determined that the addition of the carbon material to the epoxy sample, at least at the tested weight percentages, will not significantly alter the degradation of the epoxy sample, although the peaks appear more repeatable following this addition, but this is likely due to human error rather than imparted properties.

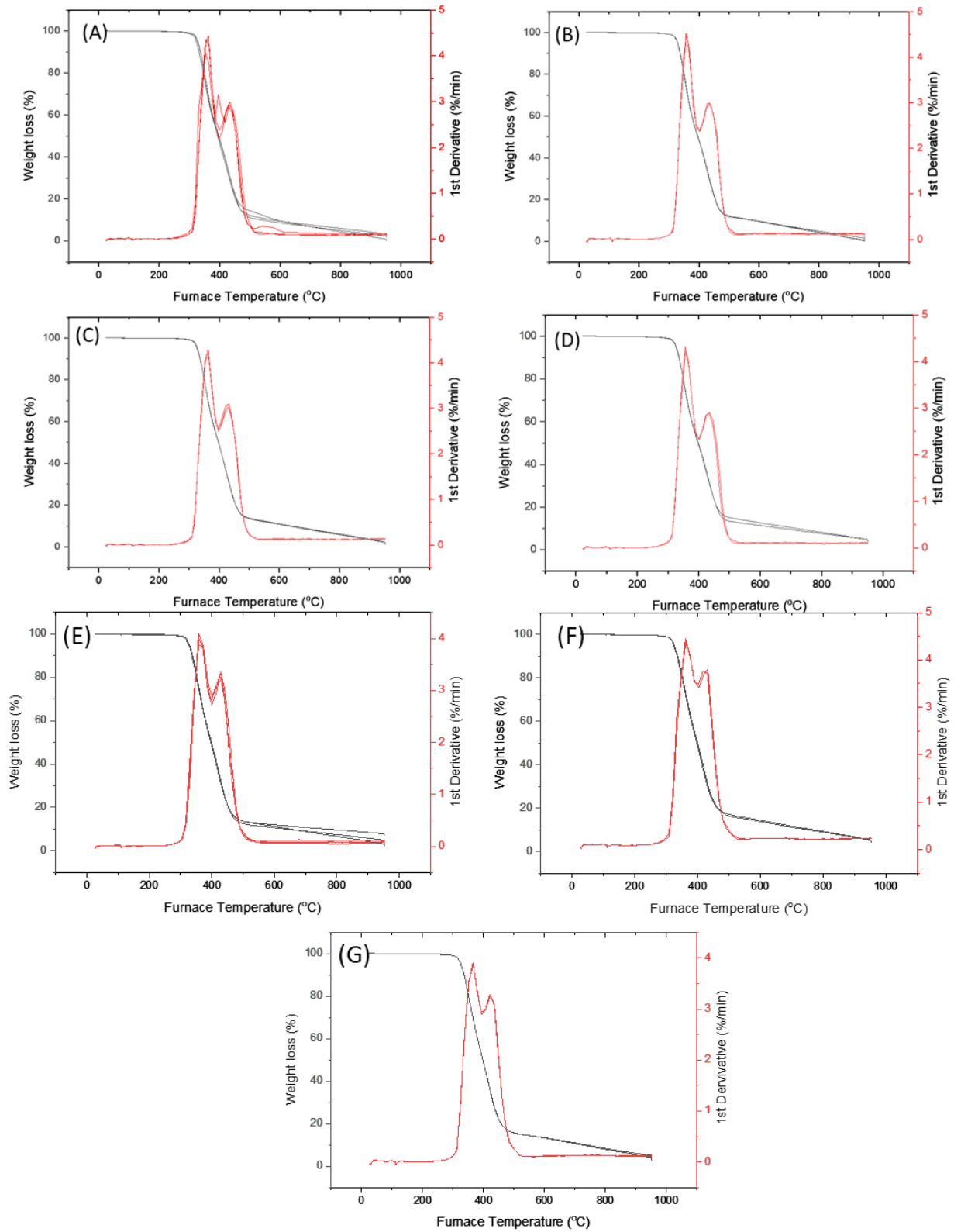


Figure 5.6. TGA and DTG curves for different composite materials where (A) pure epoxy (B) 0.5 wt.% methane carbon (C) 2 wt.% methane carbon (D) 3.5 wt.% methane carbon (E) 0.5 wt.% synthetic carbon (F) 2 wt.% synthetic carbon and (G) 3.5 wt.% synthetic carbon

The TGA curves show no significant changes through the addition of carbon nanomaterials to the epoxy, the different temperature points can be seen in Table 5.4. There is minimal variation between each composite materials type for each of the measured temperature points. This further shows that the addition of carbon to the epoxy does not affect the thermal degradation of the sample.

Table 5.4. Thermogravimetric Analysis temperature results for different carbon composite materials

Sample	T _{onset} (°C)	T _{hl} (°C)	T _{end} (°C)
Pure epoxy	311	399.5	951
0.5 wt. % MC	315	396	945
2 wt. % MC	308	397.3	951
3.5 wt. % MC	314	396.8	950
0.5 wt.% SC	306	400	950
2 wt. % SC	309	390	951
3.5 wt. % SC	311	392	949

The remaining masses, all under 2 % of the initial mass, show that the sample is predominantly organic in nature. Based on the T_{onset}, T_{hl} and T_{end} values, there is no significant effect on the TGA plot from the addition of the carbon nanomaterial into the epoxy matrix. Whilst there is a slight increase in the second peak seen for the synthetic carbon samples, it is not significant enough to be assigned to a different reaction.

Therefore, it can be concluded that the addition of carbon at 0.5, 2 and 3.5 wt.% will not affect the thermal degradation properties of the composite sample. There is no evidence of other peaks in the DTG curves, meaning that the impregnated carbon is not decomposed as an extra step, unless there is overlap between carbon – epoxy bonds and the internal C-C bonds breaking. This potential overlap is unlikely as any bonding formed should be physical rather than chemical, as the carbon is impregnated within the epoxy, and would lead to an increased %/min weight loss, which is not seen. Therefore, it can be assumed that the carbon encapsulated in the sample is not significant enough to trigger a change in the mass loss peak.

5.8 Infrared spectroscopy for the determination of bonds within the carbon composite material

The FT-IR carried out on the epoxy samples can be seen in Figure 5.7, it is clear that with the addition of the nanostructured carbon materials there is a reduction in the transmission, meaning that the features are less clear at the higher loadings. This reduction in transmission may be due to the change in opacity of the samples, reducing the light, although, as seen in Figure 4.15 the carbon spectra has common peaks within the epoxy resin, meaning the addition of the carbon to the sample will not show in the spectra. For the methane carbon samples, there is a higher transmission, especially for the 0.5 wt.% MC sample. The different bond modes were explored by Ullah et al, [295], the rings that form the bisphenol A show the greatest contribution to the infrared spectroscopy shown in Figure 5.6. The two C-H stretching modes seen at peaks A and B are the result of multiple peaks occurring in the same wavelength, as the bisphenol A molecule is large there will be multiple bonds contributing, especially the C-H or C-C modes. H-C-H, C-C-H and C-C stretching occur around 1508 cm^{-1} which was assigned peak C in Figure 5.6. The C-C bonds are predominately within the ring system which leads to the multiple C-C peaks shown at peaks C, D, E, F and G. These peaks show both the in-plane and out of plane bending modes which can occur when there are complex carbon rings. There are minimal changes seen from the addition of the carbon nanomaterial to the epoxy, which is expected due to the spectra seen in Figure 4.15. Due to this it can be seen that there are no new bonds formed during the curing of the bisphenol A and the carbon nanomaterial.

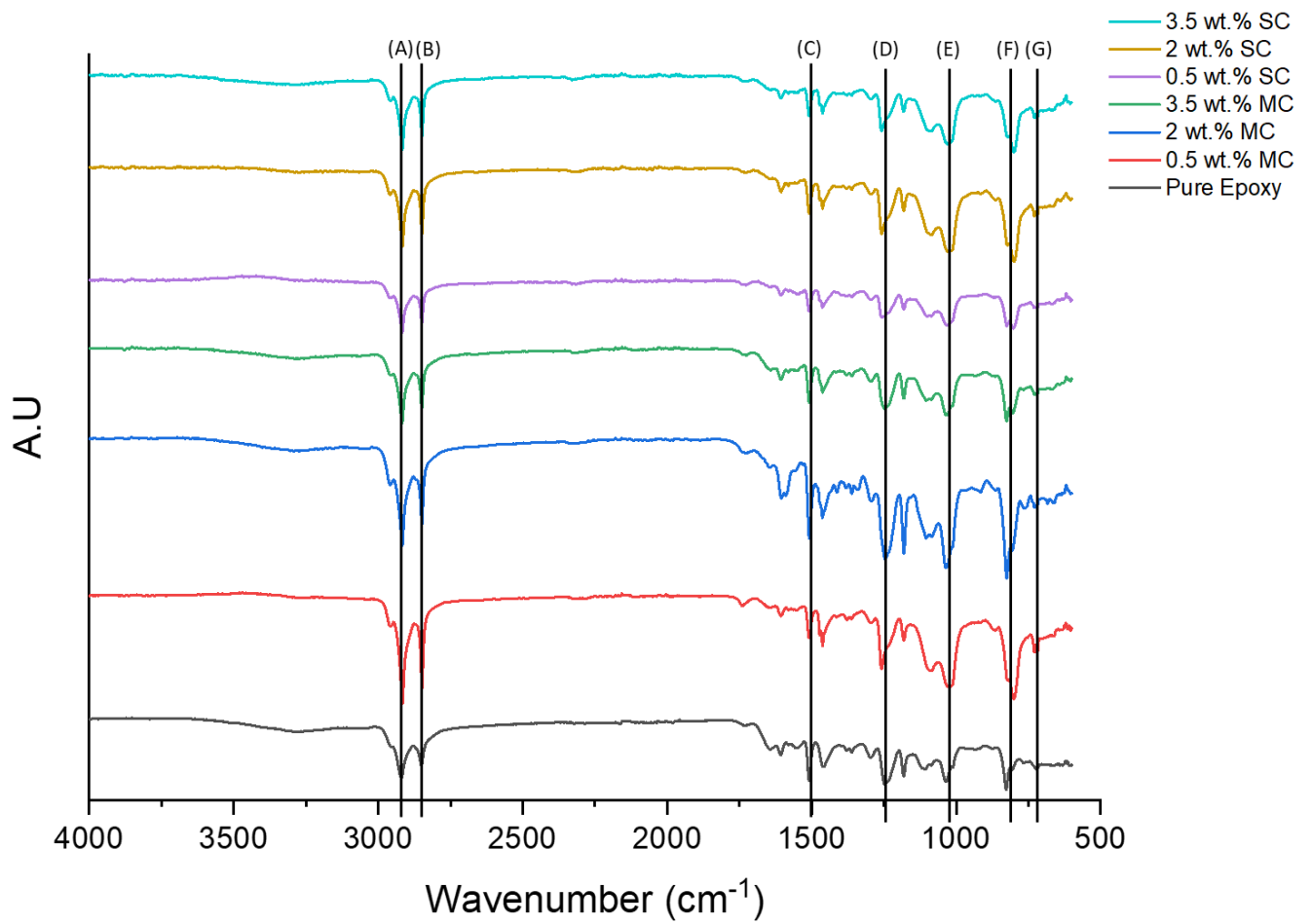


Figure 5.7. Fourier-Transform infrared spectroscopy for different carbon composite materials where (A) is CH stretching (B) is CH stretching (C) is HCH, CCH and CC stretching (D) is CCH and out of ring CC stretching (E) is CC stretching in-ring (F) is CO and CC stretching in rings and (G) is torsions in the rings and CC out of plane bending

5.9 Conclusions

The mechanical properties of the epoxy were seen to be negatively impacted through the addition of a low weight percentage amount of carbon material. The ability to withstand tensile stress was seen to decrease at all weight loadings from an average of 41.78 MPa for the pure epoxy control sample to 25.36 MPa for the 3.5 wt% methane carbon composite. The inherent errors of the mechanical testing can be seen in the data, as there is significant variation within some of the measurements, but the trend shows that the addition of the carbon nanomaterials will reduce the resistance to both bending and tensile loads. This means that the maximal tensile loading capacity is reduced, for the pure epoxy this was on average 1499.13 N which decreased to 1084.19 and 838.8 N for the 0.5 wt.% MC and SC respectively. This trend of decrease continues for both the 2 wt.% samples with the MC sample having an average of 509.03 N maximum loading and the SC sample showing a load capacity of 1175.32 N. For the 3.5 wt.% samples 913.81 and 1056 N maximal loads were seen for the MC and SC samples respectively.

For the compression testing the maximal loading for the pure epoxy was measured to be 185.51 N, showing that the epoxy samples are brittle and will not see much resistance to bending loads. The 0.5 wt.% samples saw a maximum bending load of 113.73 and 136.23 N for the MC and SC samples respectively. The 2 wt.% methane carbon sample showed a maximal bending capacity of 103.53 with the SC sample having a load capacity of 38.5 N. This shows that the addition of carbon to the epoxy matrix leads to a more brittle sample, this is due to the carbon particles disrupting the epoxy matrix, preventing effective cross-linking to be formed. This is confirmed by the further decrease in the bending load capacity seen for the 3.5 wt.% samples; the MC composite showed a maximum load of 83.34 N and the SC composite had a capacity of 55 N.

The presence of carbon within the epoxy did reduce the effects of weathering on the carbon composite materials. Whilst all the samples showed a decrease in the tensile properties, the decrease was greatest for that of the pure epoxy sample. The maximal loading for the pure epoxy showed a 156.52 N decrease whilst for the 0.5 wt.% samples there was a 127.19 N decrease for the MC composite and a 25 N increase for the SC sample. The 2 wt.% MC composite samples showed a 52 N increase whilst the 3.5 wt.% samples showed a 15 and

138 N decrease for the MC and SC composites respectively. This indicated that the presence of the carbon within the epoxy sample offers some resistance to weathering effects on the epoxy sample. The changes in the epoxy loading were seen to not impact the thermal decomposition of the composite materials, as the DTG curves remained constant throughout all the samples. As there is no change in the positioning, or significant changes within the first derivative values for each, it can be assumed that the thermal degradation of the sample is not influenced by the addition of the carbon materials. The FT-IR also shows that the presence of the carbon within the sample will not affect the bonding seen within.

Chapter 6 - Conclusions and future work

6.1 Conclusions

The novel use of pyrolysis of textile waste as a feedstock for the synthesis of carbon nanofibers has been explored within this thesis. Due to the high content of polyester in the textile waste stream, 80 % of the 92 million tonnes, alternatives to landfill must be explored. Whilst polyester is beginning to be recycled, pyrolysis offers a chance to recover more useful products such as carbon containing gases, oils and char materials. Adopting the methods shown in Chapter 2 can assist the fast fashion industry in improving circular economy and satisfying some United Nation Sustainable Development Goals, in particular goals 7 and 12. Goal 7 considers access to clean energy whilst goal 12 considers sustainable consumption, as this project is aiming to produce wind turbine blades from waste textile waste materials it is clear how these two are achieved. The pyrolysis of textile waste would produce carbon containing gases which when flowed over a 90 % Ni catalyst would lead to the chemical vapour deposition of carbon. The resultant carbon nanofibers were mixed with a bisphenol A diglycidyl ether in differing proportions and the mechanical properties of the resultant composite were tested. Due to the increased resistance to weathering seen for the carbon composite materials, they have potential to be used to protect the leading edge of an offshore wind turbine blade.

6.1.1 The potential for using pyrolysis techniques for the re-use of polyester/lycra and cotton textile waste

The products of the pyrolysis of textile waste were oils, gases and char materials. Feedstock typology influences the gas phase composition. Cotton textile waste leads to a greater yield of carbon monoxide compared to polyester/lycra textile waste, which produced both carbon monoxide and carbon dioxide at fast pyrolysis to a fixed temperature. The pyrolysis of cotton with a heating rate of 2.5 °C/min produced a high yield of carbon dioxide whilst for the polyester/lycra textile waste there was significant production of both carbon monoxide and dioxide. This slow pyrolysis shows that, especially for the polyester/lycra sample, there was an effective secondary pyrolysis. In this case heavier oils were pyrolysed, altering the gas composition at higher temperatures. For the polyester/lycra textile waste sample, pyrolysis temperatures between 450 and 650 °C showed the greatest gas yield which was dominated by carbon dioxide and carbon monoxide. Pyrolysis temperatures over 650 °C showed an increase in the production of hydrogen. For the cotton sample the overall gas

yield was lower at all temperatures. The highest gas yield was seen between 350 and 400 °C, confirming that polyester/lycra has a higher activation energy, with a primarily carbon dioxide composition. At the higher temperatures there was an increase in the hydrogen content seen for both the cotton and polyester/lycra samples. This shows that, by altering the temperature and heating rate, the output gas phase can be manipulated.

During the pyrolysis of the textile waste, oil is formed from the heavier components of the gas phase, these are the parts that condense when they are cooled. For the cotton textile waste material, all the oil samples for the fixed pyrolysis temperatures and slow pyrolysis contained levoglucosan, benzoic acid and 5-methyl-2-furancarboxyaldehyde. The polyester/lycra samples also all contained benzoic acid and levoglucosan, but do not show the presence of 5-methyl-2-furancarboxyaldehyde. For both textile waste samples, the most common classification for these oils were cyclic and carboxylic acids. This shows that the actual oils produced cannot be controlled for, their production is independent on the pyrolysis temperature, and the feedstock material has only limited impact.

Due to the difference in nature of the textile waste samples considered in this research, natural vs synthetic, the char materials following pyrolysis had different characteristics. The char produced from synthetic polyester/lycra showed limited porosity and surface area. The polymeric nature of the fibres led the material to melt, preventing the formation of a porous char. The char produced by the cotton sample however, showed that the slow pyrolysis process preserved a high surface area. The higher temperature fast pyrolysis of cotton textile waste led to the collapse of the pore structure, reducing the surface area of these samples. Elemental analysis showed that, for both samples there was an initial increase in the carbon content with temperature, with decreasing oxygen but this plateaus over 500 °C. The cotton sample contains a maximum of 81.6 wt.% carbon whilst the polyester/lycra sample has a maximum of 90.3 wt.% carbon. FT-IR on the resultant chars confirmed a change in bonding with an increase in the pyrolysis temperature. For the cotton sample, there was a significant decrease in the O-H and C-O bonds with C=C bonds being formed at increased temperature. For the polyester/lycra sample, there were minimal bonds. It is assumed that this means that there are non-polar C-C bonds which would not show on infrared spectroscopy.

The pyrolysis of the textile waste can be used to produce useful products. Product typography can be tuned depending on required parameters, but that depends on the nature of the original feedstock. If a high surface area char is desired, slow pyrolysis of a natural textile is best, but if a higher gas yield is required, then pyrolysis of a synthetic textile gives the best outcome.

6.1.2 The production of carbon from pyrolysis of textile waste

The synthesis of carbon from the pyrolysis of textile waste was optimal with a 90 % Ni 10 % Al catalyst using polyester/lycra synthetic textile as a feedstock. A higher active metal loading coupled with the increased gas yield from the polyester/lycra sample, produced a higher quality carbon nanomaterial when compared to that produced from the cotton sample. The carbon produced from the pyrolysis of the cotton textile waste had a lower level of order when compared to that produced from the polyester/lycra sample. The highest yield of carbon was produced from the methane control sample, producing a mix of carbon nanofibers and carbon nanotubes. The carbon produced through the chemical vapour deposition of pyrolysis gas from the cotton textile showed there were large disordered carbon structures formed around the catalyst nanoparticles. This is attributed to a higher oxygen content in the gas phase, as well as a reduced gas yield, which may prevent the formation of the longer carbon nanofibers seen in the other samples. To create a higher yield of carbon, a synthetic gas mix was designed to mimic that seen from the pyrolysis of the polyester/lycra mix. Following characterisation, it was seen that the produced carbons were comparable.

The catalyst sample had faceted edges leading to the synthesis of angled carbon walls, and for all the cotton, polyester/lycra and synthetic gas mix the metal nanoparticles were still present in the sample. However, the carbon nanofibers produced from the methane control sample did not contain any metal nanoparticles. It is assumed this is related to the presence of oxygen in the samples, however further work is required to fully confirm this. The powder x-ray diffraction showed the samples were all crystalline in nature, with electron diffraction supporting this. The width of the carbon fibres produced from the synthetic gas mix was narrower than the nanofibers produced from the cotton and polyester/lycra feedstock. This could be due to the inhomogeneous nature of the catalyst surface leading to a greater variance within the diameters. Unfortunately, the carbon samples were too tangled to

measure the length. Through the utilisation of textile waste as a feedstock for the production of carbon nanomaterials the aims of this thesis were reached, as well as SDG goal 12.

6.1.3 The mechanical properties of the carbon-epoxy composite material

The measured mechanical properties of the carbon-epoxy composites made decreased with the addition of the nanostructured carbon. For tensile strength the pure epoxy samples were the highest performing with an average Young's Modulus of 293.58 MPa . This shows the material retains some flexibility. The increase in the Young's Modulus seen with the addition of the carbon material shows there is an increase in brittleness. The synthetic gas mix carbon composite samples appear to have a Young's Modulus comparable to that seen in the carbon composite made from the methane control. The 0.5 wt. % samples were all seen to have a lower Young's Modulus than any of the 3.5 wt. % carbon loaded samples. This shows that lower levels of carbon impregnation in the composite leads to a lower change in the tensile strength of the material. This may be due to the lack of disruption of the matrix, leading to less points of defects throughout the sample. The variance seen between the Young's Modulus of the carbon produced from two different feedstocks for the 2 wt.% samples may be due to human error, although it may also be due to the lack of repeats for the synthetic carbon samples. The MC 2 wt.% samples had the greatest spread of results showing there was an inherent lack of consistency. There may have been issues with the carbon nanomaterials causing air pockets, which would cause an artificially high Young's Modulus as the sample would become more brittle.

For the flexural test, again the pure epoxy sample showed the greatest resistance with an average flexural modulus of 722.36 MPa to bending whilst the 2 wt.% SC sample showed the least resistance to bending with a flexural modulus of 160.8 MPa. The 0.5 wt.% samples for the carbon produced from each feedstock showed comparable results, at 506.8 and 566.7 MPa for the MC and SC samples respectively. These show the second and third highest results, agreeing with the tensile testing that the 0.5 wt.% samples show the greatest similarity to the pure epoxy samples. The 2 wt.% samples for both the feedstock materials had the lowest flexural moduli showing the least resistance to bending following the application of a load. This agrees with the differences in the tensile testing, that there is the

greatest variance within this 2 wt.% loaded sample. This phenomenon is considered less likely to be due to human error and can be attributed to the weight loading of the sample. However, it is unclear why this is occurring. The fracture sites analysed by SEM showed there was a clear impact location surrounded by a smooth surface with limited striations before an outer ring with more markings. This shows that when the test sample fails the impact causes a section to shear off, leading to this smooth area, whilst the impact penetrates deeper into the composite.

Despite the presence of the carbon materials appearing to reduce the tensile and flexural strength of the sample, their addition reduced the impact of accelerated weathering. The pure epoxy samples showed the greatest visible change with the samples becoming yellowed following exposure to the salt spray. This continues to the Young's Modulus, where there is an eight-fold increase showing there is a significant decrease in resistance to tensile loading following weathering. In comparison, the highest increase for the carbon reinforced samples was only 5.6 times for the 0.5 wt.% MC loaded sample. For all other samples, whilst there was still an increase in the Young's Modulus, it was lower than for the pure epoxy sample. This shows the addition of the nanostructured carbon will limit the effects of weathering on the sample.

The loading of carbon in these samples was too low for a change in the thermal degradation to be seen. The DTG curves for the carbon composites matched the pure epoxy sample showing that there was no change in the thermal properties. This means that the use of the carbon produced through the methods described within this thesis can be used to reinforce composite materials against the effects of weathering. The process of producing carbon materials from waste textile, whilst producing a lower yield compared to that seen from pure methane, can be used to divert textile waste from landfill. Whilst the produced carbon containing composite cannot be used to impart mechanical strength, it could be used as a coating to reduce the impact of weathering on offshore wind turbine blades. This would be especially beneficial as leading edge protection.

6.2 Future work

To complete the study set out here, further work should be carried out to explore the effects of higher loading of carbon in an epoxy composite on the mechanical properties of

the sample. Surface treatment should also be carried out, to determine if this will improve the network linkages between the carbon and the epoxy matrix. This would improve the mechanical properties by allowing stronger bonding to be formed between the carbon and epoxy, preventing the disruptions that have been discussed in Chapter 5. Currently there has not been much interest in the modification of carbon nanofibers, with most of the work being focussed on carbon nanotubes. One study considered that the oxidation of the carbon nanofibers enables the deposition of catalytically active materials and successfully showed that nitric acid would oxidise the surface [296]. Following on from this, different functionalisation approaches could be considered such as chelating phosphine and ammonium or sulphuric acid, or more mechanical approaches, such as electroplating and chemical vapour deposition of thin layers of the desired material [297-300]. The functionalisation of the surface properties improves the bonding ability of the carbon nanofibers with the epoxy matrix.

As only two textile waste materials have been explored in this thesis, a greater range of textile types should be explored. It is recommended that synthetic fibres are of more interest than natural fibres due to the higher proportion of methane in the sample, and their higher presence in textile waste streams. Pure polyester, spandex, nylon or polyurethane would be good candidates to consider for future pyrolysis exploration for the CVD process.

To further optimise the commercial economics of the pyrolysis process, the potential uses of the excess heat energy released should be explored. This could be commercial greenhouses, communal facilities or district heating systems. As the pyrolysis process occurs in a closed system there would be a low risk of damage to health caused by this approach.

Mechanical properties of the carbon nanofibers produced should be explored to determine their potential for imparting strength into the composite material. This should include tensile strength as well as compression. Hardness would also be an important consideration to determine the potential of the carbon nanofibers to prevent crack propagation. This would establish any potential benefits of the addition of the carbon material to the epoxy matrix to reduce OPEX costs by improving the mechanical properties of the blade.

Reference list

1. McKay, D., et al., *Exceeding 1.5°C global warming could trigger multiple climate tipping points* Science 2022. **377**(1171).
2. Smith, J., et al., *Assessing dangerous climate change through an update of the Intergovernmental Panel on Climate Change (IPCC) "reasons for concern"*. PNAS, 2009. **106**(106).
3. Reichle, D., *Anthropogenic alterations to the global carbon cycle and climate change*, in *The Global Carbon Cycle and Climate Change*, R. D, Editor. 2020, Elsevier.
4. Swim, J., S. Clayton, and G. Howard, *Human Behavioral Contributions to Climate Change*. American Psychologist, 2011. **66**(4).
5. Kuylenstierna, J., E. Michalopoulou, and F. Dixon. *Why we must reduce methane emissions now to solve the climate crisis*. 2021 [cited 2023 01/02].
6. Intergovernmental Panel on Climate Change, *Anthropogenic and Natural Radiative Forcing in Climate Change 2013 – The Physical Science Basis: Working Group I Contribution to the Fifth Assessment Report of the Intergovernmental Panel on Climate Change*. 2014, Cambridge University Press: Cambridge.
7. Tian, H., et al., *A comprehensive quantification of global nitrous oxide sources and sinks*. Nature, 2020. **586**(7828): p. 248-256.
8. United Nations, *Kyoto Protocol*, F.C.o.C. Change, Editor. 1997.
9. United Nations. *Kyoto Protocol - Targets for the first commitment period*. 2020 [cited 2020 06/01/2020]; Available from: <https://unfccc.int/process-and-meetings/the-kyoto-protocol/what-is-the-kyoto-protocol/kyoto-protocol-targets-for-the-first-commitment-period>.
10. Harris, K., *Energy Trends*, E.a.I.S. Department for Business, Editor. 2022.
11. Ragheb, M., *Economics of Wind Power Generation*, in *Wind Energy Engineering*, L. T, Editor. 2017, Academic Press
12. Fonseca, L., J. Domingues, and A. Dima, *Mapping the Sustainable Development Goals Relationships*. Sustainability, 2020. **12**(8).
13. United Nations Development Programme. *The SDGs in Action*. 2023 [cited 2023 03/07]; Available from: <https://www.undp.org/sustainable-development-goals>.
14. IRENA, *Renewable Power Generation Costs in 2021*. 2022, International Renewable Energy Agency: Abu Dhabi.
15. BVG Associates, *Guide to an offshore wind farm*. 2018, The Crown Estate.
16. Kirschke, D. *Composite materials for the wind energy industry*. 2019 08/01/2020]; Available from: <https://www.openaccessgovernment.org/composite-materials-wind-energy/76762/>.
17. Saroen Global, *Sections of a wind turbine blade*. 2015: Saroen Global.
18. Independent statistics and analysis, *Levelised cost and levelised avoided cost of new generation resources in the annual energy outlook 2019*, U.S.E.I. Administration, Editor. 2019.
19. Shennan, C., *Prepreg and Infusion: Processes for Modern Wind Turbine Blades*. 2013, HEXCEL.
20. Greaves, P., *Design of offshore wind turbine blades, in Offshore wind farms*. 2016, Woodhead Publishing.
21. National Research Council, *Manufacturing processes for rotor blades - current manufacturing processes*, in *Assessment of research needs for wind turbine rotor materials technology*. 1991, The National Academies Press: Washington DC.
22. Siemens Gamesa, *IntegralBlade*, S. Gamesa, Editor. 2002.
23. Burgarella, B., et al., *Micromechanical modelling of matrix cracks effect on shear and transverse response for unidirectional composites with a full field approach*. Composite Structures, 2019. **208**: p. 338 - 345.

24. Malhotra, P., et al., *A review and design study of blade testing systems for utility-scale wind turbines*. Renewable and Sustainable Energy Reviews, 2012. **16**: p. 284 - 292.
25. Fagan, E., et al., *Physical experimental static testing and structural design optimisation for a composite wind turbine blade*. Composite Structures, 2017. **164**: p. 90 - 103.
26. Steel, W. *Substructure Testing Paving the Way to Longer Wind Turbine Blades*. 2016 [cited 2020 21/06]; Available from: <https://www.renewableenergyworld.com/2016/02/09/substructure-testing-paving-the-way-to-longer-blades/#gref>.
27. Odegard, G. and M. Kumosa, *Determination of shear strength of unidirectional composite materials with the Iosipescu and 10 off-axis shear tests*. Composites Science and Technology, 2000. **60**: p. 2917 - 2943.
28. Ullah, H. and V. Silberschmidt. *Analysis of impact induced damage in composites for wind turbine blades*. in *Power Generation Systems and Renewable Energy Technologies*. 2015. Islamabad.
29. Park, J., et al., *Linear vibration analysis of rotating wind-turbine blades*. Current Applied Physics, 2010. **10**: p. 332 - 334.
30. Power, E. *Blade vibration testing requires specialised approach*. 1995 [cited 2020 21/06].
31. Berring, P., et al., *Torsional Performance of Wind Turbine Blades - Part I: Experimental Investigation*, in *International Conference on Composite Materials*. 2007: Kyoto.
32. Zhang, Z., et al., *Coupled-Mode Flutter of Wind Turbines and its Suppression Using Torsional Viscous Dampner*. International Journal of Hydrogen Energy, 2019. **44**: p. 9291 - 9306.
33. Zhang, Z., B. Chen, and R. Nielsen, *Coupled-Mode Flutter of Wind Turbines and its Suppression Using Torsional Viscous Dampner*. Procedia Engineering, 2017. **199**: p. 3254 - 3259.
34. Richards, D., P.-E. Verrien, and M. Dann, *Torsional Testing of a Wind Turbine Blade*, in *Europäisches Patentamt*, W. Vestas, Editor. 2017.
35. Dolinski, L. and M. Krawczuk, *Analysis of Modal Parameters Using a Statistical Approach for Condition Monitoring of the Wind Turbine Blade*. Applied Sciences, 2020. **10**(17).
36. Maclean-Blevins, M., *Material selection - Which plastic to use?*, in *Designing Successful Products with Plastics*. 2018, William Andrew. p. 19 - 50.
37. Singh, G., et al., *Interlaboratory Round Robin Study of Axial Tensile Properties of SiC/SiC Tubes* Applied Ceramic Technology, 2018. **15**(6).
38. Ashwill, T. and J. Paquette, *Composite Materials For Innovative Wind Turbine Blades*. 2008: Albuquerque.
39. Nasrollahzadeh, M. and Z. Issaabadi, *An introduction to Nanotechnology*, in *An Introduction to Green Nanotechnology*. 2019, Academic Press.
40. Foroutan, M., V. Naeni, and M. Ebrahimi, *Carbon nanotubes encapsulating fullerene as water nano-channels with distinctive selectivity: Molecular dynamics simulation*. Applied Surface Science, 2019. **489**: p. 198 - 209.
41. Bhavani, K., T. Anusha, and P. Brahman, *Fabrication and characterization of gold nanoparticles and fullerene-C60 nanocomposite film at glassy carbon electrode as potential electro-catalyst towards the methanol oxidation*. Hydrogen Energy, 2019. **44**: p. 25863 - 25873.
42. Dubrovsky, R., V. Bezmelnitsyn, and A. Eletsii, *Plasma fullerene production from powdered carbon black*. Carbon, 2004. **42**: p. 1063 - 1066.
43. Royal Society of Chemistry. *Arc-Discharge Method*. 2020 [cited 2020 21/06]; Available from: <https://www.rsc.org/publishing/journals/prospect/ontology.asp?id=CMO:0002240>.
44. Loos, M., *Production of CNTs and Risks to Health*, in *Carbon Nanotube Reinforced Composites*. 2015, William Andrew. p. 103 - 123.
45. Ma, P. and Y. Zhang, *Perspectives of carbon nanotubes/polymer nanocomposites for wind blade materials*. Renewable and Sustainable Energy Reviews, 2014. **30**: p. 651- 660.

46. Hsu, S. and P. Luo, *From Nanoarchitectonics to tissue architectonics: Nanomaterials for tissue engineering*, in *Advanced Supramolecular Nanoarchitectonics*. 2019, William Andrew.
47. Kuz'min, M., M. Kuz'mina, and A. Kuz'mina, *Production and properties of aluminum-based composites modified with carbon nanotubes*. *Materials Today*, 2019. **19**: p. 1826 - 1830.
48. Booker, R. and E. Boysen, *Nanotechnology for Dummies*. 2 ed. 2005, Hoboken: Wiley.
49. Gong, J., et al., *Catalytic carbonization of polypropylene by combined catalysis of activated carbon with Ni₂O₃ into carbon nanotubes and its mechanism*. *Applied Catalysis A*, 2012. **449**: p. 112 - 120.
50. VM, S., et al., *Role of Reaction and Factors of Carbon Nanotubes Growth in Chemical Vapour Decomposition Process Using Methane - A Highlight*. *1D Nanomaterials* 2010. **2010**: p. 11.
51. Nessim, G., *Properties, synthesis and growth mechanisms of carbon nanotubes with special focus on thermal chemical vapor deposition*. *Nanoscale*, 2010. **2**: p. 1306 - 1323.
52. Wang, J., et al., *Carbon nanotubes production from catalytic pyrolysis of waste plastics: The influence of catalyst and reaction pressure*. *Catalysis Today*, 2019.
53. Bajad, G., et al., *Production of liquid hydrocarbons, carbon nanotubes and hydrogen rich gases from waste plastic in a multi-core reactor*. *Journal of Analytical and Applied Pyrolysis*, 2017. **125**: p. 83 - 90.
54. Bajad, G., et al., *Processing of mixed-plastic waste to fuel oil, carbon nanotubes and hydrogen using multi-core reactor*. *Chemical Engineering & Processing: Process Intensification*, 2017. **121**: p. 205 - 214.
55. Veksha, A., A. Giannis, and V. Chang, *Conversion of non-condensable pyrolysis gases from plastics into carbon nanomaterials*. *Journal of Analytical and Applied Pyrolysis*, 2017. **124**: p. 16 - 24.
56. Mancillas-Salas, S., et al., *Production of few-layer graphene by wet media milling using organic solvents and different types of graphite*. *Ceramics International*, 2020. **46**: p. 2413 - 2420.
57. Huang, Y., et al., *Effect of airborne contaminants on the macroscopic anti-wear performance of chemical vapor deposition graphene*. *Surface and Coatings Technology*, 2020. **383**: p. 125 - 276.
58. Luan, Y., et al., *Arc-discharge production of high quality fluorine-modified graphene as anode for Li-ion battery*. *Chemical Engineering Journal*, 2019.
59. Liu, S., et al., *A review of extending performance of epoxy resins using carbon nanomaterials*. *Composites Part B*, 2018. **136**: p. 197 - 214.
60. Kinloch, I., et al., *Composites with carbon nanotubes and graphene: An outlook*. *Science*, 2018. **362**: p. 547 - 553.
61. Gavrilov, A., et al., *Study of the mechanisms of Filler Reinforcement in Elastomer Nanocomposites*. *Macromolecules*, 2014. **47**: p. 5400 - 5408.
62. Agnelli, S., et al., *Interactive effects between carbon allotrope fillers on mechanical reinforcement of polyisoprene based nanocomposites*. *eXPRESS Polymer Letters*, 2014. **8**: p. 436 - 449.
63. Prasad, S., et al., *Engineered nanomaterials: nanofabrication and surface functionalisation, in Emerging Applications of Nanoparticles and Architecture Nanostructures*. 2018, Elsevier. p. 305 - 340.
64. Bokobza, L. and M. Kolodziej, *On the use of carbon nanotubes as reinforcing fillers for elastomeric polymers*. *Polymer International*, 2006. **55**: p. 1090 - 1098.
65. Boonbumrung, A., P. Sae-ou, and C. Sirisinha, *Reinforcement of Multiwalled Carbon Nanotube in Nitrile Rubber: In Comparison with Carbon Black, Conductive Carbon Black, and Precipitated Silica*. *Journal of Nanomaterials*, 2016.
66. Zhao, C., et al., *Spontaneous and specific myogenic differentiation of human mesenchymal stem cells on polyethylene glycol-linked multi-walled carbon nanotube films for skeletal muscle engineering*. *Nanoscale*, 2015. **7**: p. 18239 - 18249.

67. Pastorin, G. and Y. Ren, *Incorporation of hexamethylmelamine inside capped carbon nanotubes*. *Advanced Materials*, 2008. **20**(11).
68. Zhong, W., et al., *CFD simulation of dense particulate reaction system: Approaches, recent advances and applications*. *Chemical Engineering Science*, 2016. **140**: p. 16-43.
69. Loh, K., et al., *Clinical applications of Carbon Nanomaterials in Diagnostics and Therapy*. *Advanced Materials*, 2018. **30**(47).
70. Bakry, R., et al., *Medicinal applications of fullerenes*. *International Journal of Nanomedicine*, 2007. **4**: p. 639 - 649.
71. Creative Diagnostics. *Properties and Applications of Carbon Nanoparticles*. 2020 [cited 2020 22/06].
72. Banerjee, J., K. Dutta, and D. Rana, *Carbon Nanomaterials in Renewable Energy Production and Storage Applications*, in *Emerging Nanostructured Materials for Energy and Environmental Science*. 2019, Springer. p. 51 - 104.
73. Thines, R., et al., *Application potential of carbon nanomaterials in water and wastewater treatment: a review*. *Journal of the Taiwan Institute of Chemical Engineers*, 2017. **72**: p. 116 - 133.
74. Yin, Z., et al., *The Application of Carbon Nanotube/Graphene-Based Nanomaterials in Wastewater Treatment*. *Small*, 2019. **16**.
75. Hassan, A., H. Elkady, and I. Shaaban, *Effect of Adding Carbon Nanotubes on Corrosion Rates and Steel-Concrete Bond*. *Scientific Reports*, 2019. **9**.
76. Jain, P., B. Patidar, and J. Bhawsar, *Potential of Nanoparticles as a Corrosion Inhibitor: A Review*. *Journal of Bio- and Tribo- Corrosion*, 2020. **6**: p. 42 - 54.
77. Liu, Z., et al., *CVD Synthesis of Graphene*, in *Thermal Transport in Carbon-Based Nanomaterials* Z. G, Editor. 2017, Elsevier
78. Yan, K., et al., *Designed CVD growth of graphene via process engineering* *Accounts of chemical research*, 2013. **46**(10).
79. Srivastava, A., et al., *Novel Liquid Precursor-Based Facile Synthesis of Large-Area Continuous, Single and Few-Layer Graphene Films*. *Chemistry of Materials* 2010. **22**(11): p. 3457 - 3461.
80. Li, X., et al., *Large-Area Synthesis of High-Quality and Uniform Graphene Films on Copper Foils*. *Science*, 2009. **324**(5932): p. 1312-1314.
81. Zhang, X., et al., *Roles of CuO and Cu₂O in graphene growth on a copper substrate*. *Applied Surface Science*, 2022. **576**(A).
82. Zhao, X. and L. Gou, *Comparative analysis of graphene grown on copper and nickel sheet by microwave plasma chemical vapor deposition* *Vacuum*, 2018. **153**: p. 48 - 52.
83. Leidinger, P. and S. Gunther, *Insight into the Thermodynamics of Graphene Growth on Copper*. *Journal of Physical Chemistry C*, 2021. **125**(23).
84. Losurdo, M., et al., *Graphene CVD growth on copper and nickel: role of hydrogen in kinetics and structure* *Physical Chemistry Chemical Physics*, 2011(46).
85. Rybin, M., et al., *In Situ Control of CVD Synthesis of Graphene Film on Nickel Foil*. *Physica Status Solidi B*, 2018. **255**.
86. Azira, A. and M. Rusop. *Chemical properties of carbon nanotubes prepared using camphoric carbon by thermal-CVD*. in *AIP conference proceedings*. 2010.
87. Baddour, C., et al., *A simple thermal CVD method for carbon nanotube synthesis on stainless steel 304 without the addition of an external catalyst*. *Carbon*, 2008. **47**: p. 313 - 317.
88. Fleming, E., et al., *Thermal conductivity of carbon nanotubes grown by catalyst free chemical vapor deposition in nanopores*. *Carbon*, 2019. **145**: p. 195 - 200.
89. Delzeit, L., et al., *Multiwalled carbon nanotubes by chemical vapor deposition using multilayered metal catalysts*. *Journal of Physical Chemistry*, 2002. **106**: p. 5629 - 5635.
90. Rao, F., T. Li, and Y. Wang, *Effect of hydrogen on the growth of single-walled carbon nanotubes by thermal chemical vapor deposition* *Physica E: Low-dimensional systems and nanostructures*, 2008. **40**: p. 779 - 784.

91. Venkatesan, S., et al., *Effect of chemical vapor deposition parameters on the diameter of multi-walled carbon nanotubes*. 2018.
92. Shukrullah, S., et al., *Effect of Ethylene Flow Rate and CVD Process Time on Diameter Distribution of MWCNTS*. *Materials and Manufacturing Processes*, 2016. **31**: p. 1537 - 1542.
93. Zhangyi, C., et al., *Effect of acetylene flow rate on morphology and structure of carbon nanotube thick films grown by TCVD*. *Frontiers of Materials Science in China*, 2007. **1**: p. 92 - 96.
94. Dahmen, K.H., *Chemical Vapor Deposition*, in *Encyclopedia of Physical Science and Technology*, R. Meyers, Editor. 2003, Academic Press. p. 787 - 808.
95. Kuvshinov, G., et al., *Peculiarities of filamentous carbon formation in methane decomposition on Ni-containing catalysts*. *Carbon*, 1998. **36**(1-2): p. 87-97.
96. Restivo, J., O. Soares, and M. Pereira, *Processing Methods Used in the Fabrication of Macrostructures Containing 1D Carbon Nanomaterials for Catalysis Processes*, 2020. **8**(11).
97. Manafi, S. and S. Badiie, *Production of Carbon Nanofibres Using a CVD Method with Lithium Fluoride as a Supported Cobalt Catalyst*. *Advances in Materials Science and Engineering*, 2008.
98. Li, M., et al., *Synthesis of carbon nanofibers by CVD as a catalyst support material using atomically ordered Ni₃C nanoparticles*. *Nanotechnology*, 2016. **27**(50).
99. Zheng, G., et al., *A model for the structure and growth of carbon nanofibers synthesized by the CVD method using nickel as a catalyst*. *Carbon*, 2004. **42**.
100. Suda, Y., *Chemical Vapor Deposition of Helical Carbon Nanofibers*, in *Chemical Vapor Deposition for Nanotechnology*, M. P, Editor. 2018, Intechopen
101. Shoukat, R. and M. Khan, *Synthesis of vertically aligned carbon nanofibers using inductively coupled plasma-enhanced chemical vapor deposition*. *Electrical Engineering* 2017. **100**: p. 997 - 1002.
102. Elamin, M., et al., *Preparation of Large Carbon Nanofiber on a Stainless Steel Surface and Elucidation of their Growth Mechanisms*. *Zeitschrift fur Naturforschung A*, 2018. **74**(3).
103. Nolan, P., D. Lynch, and A. Cutler, *Carbon Deposition and Hydrocarbon Formation on Group VIII Metal Catalysts*. *The Journal of Physical Chemistry*, 1998. **102**(21).
104. Vlnes, F. and A. Gorling, *Template-Assisted Formation of Fullerenes from Short-Chain Hydrocarbons by Supported Platinum Nanoparticles*. *Angewandte Chemie*, 2011. **50**(20).
105. Kleckley, S., et al., *Fullerenes and Polymers Produced by the Chemical Vapor Deposition Method*, in *Synthesis and Characterisation of Advanced Materials* S. M, G. D, and M. R, Editors. 1997, American Chemical Society
106. Wang, X., et al., *Synthesis of Fe-included onion-like Fullerenes by chemical vapor deposition*. *Diamond and Related Materials* 2006. **15**(1): p. 147 - 150.
107. Kang, J., et al., *Direct synthesis of fullerene-intercalated porous carbon nanofibers by chemical vapor deposition*. *Carbon*, 2012. **50**(14).
108. House of Commons, *Fixing Fashion: Clothing consumption and sustainability* 2019.
109. Textile Exchange, *Preferred fiber and materials* 2019.
110. Grand View Research, *Textile Market Size, Share and Trends Analysis Report By Raw Material (Woolm Chemical, Silk), By Product (Natural Fibers, Polyester), By Application (Household, Technical), By Region, And Segment Forecasts 2021 - 2028*. 2021.
111. British Fashion Council., *The economic value of the UK's fashion industry in 2015*. 2016.
112. LABFRESH. *Fashion Waste Index*. 2020 [cited 2021 08/03]; Available from: <https://labfresh.eu/pages/fashion-waste-index?lang=en&locale=en>.
113. Textile Exchange, *The Life Cycle Assessment of Organic Cotton Fiber - A Global Average* 2014.
114. Beall, A. *Why clothes are so hard to recycle*. 2020 [cited 2021 13/07]; Available from: <https://www.bbc.com/future/article/20200710-why-clothes-are-so-hard-to-recycle>.
115. Ellen MacArthur Foundation., *A new textiles economy: Redesigning fashion's future* 2017.

116. Wojciechoska, E., *How circular economy can effect the pattern of textile system, with particular focus on fashion and carpet industry*, in *School of Government 2021*, LUISS.
117. EuRIC Textiles, *Handling and Sorting Specifications for re-use and recycling of used textiles 2021*, EuRIC: Brussels
118. Murthy, H., *Introduction to Textile Fibres*. 2015, New York: WPI Publishing.
119. Kozłowski, R. and M. Mackiewicz-Talarczyk, *Handbook of Natural Fibres* Vol. 1. 2020: Elsevier
120. East, A., *3 - Polyester fibres in Synthetic Fibres*, M. J, Editor. 2004, Woodhead
121. Liu, Y., *Chemical Composition and Characterisation of Cotton Fibres*, in *Cotton Fiber: Physics, Chemistry and Biology*, D. Fang, Editor. 2018, Springer.
122. Dochia, M., et al., *Cotton fibres*, in *Handbook of Natural Fibres* R.M. Kozłowski, Editor. 2012, Woodhead Publishing: Duxford, UK. p. 14 - 16.
123. Hearle, J., *Fibre structure: its formation and relation to performance in Handbook of textile fibre structure 2009* Woodhead Publishing in Textiles
124. Kirchain, R., et al., *Sustainable Apparel Materials 2015*, Massachusetts Institute of Technology
125. East, A., *The structure of polyester fibres in Handbook of textile fibre structure*. 2009, Woodhead Publishing in Textiles
126. Shen, L., E. Worrel, and M. Patel, *Open-loop recycling: A LCA case study of PET bottle-to-fibre recycling* Resources, Conversation and Recycling, 2010. **55**: p. 34 - 52.
127. McCullough, H. and D. Sun, *An Investigation into the Performance Viability of Recycled Polyester (R-PET) from Virgin Polyester (V-PET)*. Journal of Textile Science and Fashion Technology, 2019 **2**(4).
128. Richards, A., *Nylon fibres*, in *Synthetic Fibres* J. McIntyre, Editor. 2005, Woodhead Publishing. p. 20 - 94
129. Thiemens, M. and W. Trogler, *Nylong Production: An Unknown Source of Atmospheroc Nitrous Oxide*. Science, 1991. **251**: p. 932 - 934.
130. Nunez, C. *Carbon dioxide levels are at a record high. Here's what you need to know*. 2019 12/01/2020]; Available from: <https://www.nationalgeographic.com/environment/global-warming/greenhouse-gases/>.
131. Covavisaruch, S., *Recycling of Nylon 6 Scraps* Ecomaterials 1994: p. 267 - 272.
132. MacGregor, J., *Acrylonitrile in the Textile Industry*. The Journal of the Society of Dyers and Colourists, 1959. **75**: p. 181 - 189.
133. Deshpande, S., *Ecofriendly dyeing of synthetic fibres* Indian Journal of Fibre and Textile Research 2001. **26**: p. 136 - 142.
134. Grishanov, S., *Structure and properties of textile materials in Handbook of Textile and Industrial Dyeing* M. Clark, Editor. 2011, Woodhead publishing
135. Weil, E., *Reaction polymers* Journal of Polymer Science Part A: Polymer Chemistry 1992. **31**: p. 1097
136. Ulrich, H., *Chemistry and technology of isocyanates* 1996: Wiley.
137. Sharmin, E. and F. Zafar, *Polyurethane: An Introduction in Polyurethane* 2012, InTech Open
138. Luo, Y., *Comprehensive Handbook of Chemical Bond Energies* 2007: CRC Press
139. Huang, J., et al., *Theoretical studies on bond dissociation enthalpies for model compounds of typical plastic polymers* IOP Conference Series: Earth and Environmental Science, 2018. **167**.
140. Ragusa, A., et al., *Plasticenta: First evidence of microplastics in human placenta*. Environment International, 2021. **146**.
141. Falco, D.D., et al., *The contribution of washing process of synthetic clothes to microplastic pollution*. Scientific Reports, 2019. **9**.
142. Henry, B., K. Laitala, and I. Klepp, *Microfibres from apparel and home textiles: Prospects for including microplastics in environmental sustainability assessment*. Science of the Total Environment, 2019. **652**: p. 483-494.

143. De Falco, F., et al., *Evaluation of microplastic release caused by textile washing processes of synthetic fabrics*. Environmental Pollution, 2018. **236**: p. 916 - 925.
144. Falco, F.D., et al., *Microfiber Release to Water, Via Laundering, and to Air, via Everyday Use: A Comparison between Polyester Clothing with Differing Textile Parameters*. Environmental Science and Technology, 2020. **54**: p. 3288 - 3296.
145. Creed, S., *Valuing Our Clothes: the cost of UK fashion*. 20127, wrap,.
146. Christie, R., *Environmental Aspects of Textile Dyeing* ed. C. R. 2007: Woodhead Publishing
147. Kant, R., *Textile dyeing industry an environmental hazard*. Natural Science, 2012. **4**: p. 22 -26
148. Lellis, B., et al., *Effects of textile dyes on health and the environment and bioremediation potential of living organisms* Biotechnology Research and Innovation 2019. **3**(2): p. 275 - 290
149. Yaseen, D. and M. Scholz, *Textile dye wastewater characteristics and constituents of synthetic effluents: a critical review*. International Journal of Environmental Science and Technology, 2018. **16**: p. 1193 - 1226
150. Wilhelm, F., *Pollution of Aquatic Ecosystems I*, in *Reference Module in Earth Systems and Environmental Sciences* 2009, Academic Press. p. 110 - 119.
151. Hu, Z. and D. Grasso, *Water Analysis | Chemical Oxygen Demand*, in *Encyclopedia of Analytical Science*, W. P, T. A, and P. C, Editors. 2005, Elsevier.
152. Beldean-Galea, M., F. Copaciu, and M. Coman, *Chromatographic Analysis of Textile Dyes* Journal of AOAC International, 2019. **101**(5): p. 1353 - 1370.
153. Temesgen, F., N. Gabbiye, and O. Sahu, *Biosorption of reactive red dye (RRD) on activated surface of banana and orange peels: Economical Surfaces and Interfaces*, 2018. **12**: p. 151 - 159.
154. Tahir, M., H. Bhatti, and M. Iqbal, *Solar Red and Brittle Blue direct dyes adsorption onto Eucalyptus angophoroides bark: Equilibrium, kinetics and thermodynamic studies* Journal of Environmental Chemical Engineering, 2016. **4**: p. 2431 - 2439.
155. Gupta, V., *Fundamentals of Natural Dyes and Its Application on Textile Substrates in Chemistry and Technology of Natural and Synthetic Dyes and Pigments* 2019 Intech Open
156. Moldoveanu, S., *Pyrolysis of Carboxylic Acids*, in *Techniques and Instrumentation in Analytical Chemistry* 2010, Elsevier
157. Yousef, S., et al., *A new strategy for using textile waste as a sustainable source of recovered cotton* Resources, Conversation and Recycling, 2019. **145** p. 359 - 369.
158. Yousef, S., et al., *A sustainable bioenergy conversion strategy for textile waste with self-catalysts using mini-pyrolysis plant* Energy Conversion and Management, 2019. **196**: p. 688 - 704.
159. Horrocks, A., *Technical fibres for heat and flame protection* in *Handbook of technical textiles* A. Horrocks and S. Anand, Editors. 2016, Woodhead.
160. Yasin, S., et al., *Spouted-Bed Gasification of Flame Retardant Textiles as a Potential Non-Conventional Biomass*. Applied Sciences, 2020. **10**: p. 16.
161. Sumner, M., *Written evidence submitted by Dr Mark Sumner, University of Leeds*. 2018.
162. Chinasamy, J. 'A monstrous disposable industry': *Fast facts about fast fashion*. 2019 [cited 2021 13/07/21]; Available from: <https://unearthed.greenpeace.org/2019/09/12/fast-facts-about-fast-fashion/>.
163. Mazibuko, M., et al., *Investigating the natural degradation of textiles under controlable and uncontrollable environmental conditions* Procedia Manufacturing, 2019. **35**: p. 719 - 724.
164. Chamas, A., et al., *Degradation Rates of Plastics in the Environment* ACS Sustainable Chemistry and Engineering, 2020. **8**: p. 3494 - 3511
165. Li, L., M. Frey, and K. Browning, *Biodegradability study on Cotton and Polyester Fabrics*. Journal of Engineered Fibres and Fabrics, 2010. **5**: p. 42 - 52
166. Kaartinen, T., J. Sormunen, and K. Rintala, *Case study on sampling, processing and characterisation of landfilled municipal solid waste in the view of landfill mining*. Journal of Cleaner Production, 2013. **55**: p. 56 - 66.

167. Chandler, N., *Landfills: Environmental Impacts, Assessment and Management* Environmental Research Advances 2017: Nova Publishers.
168. Epa. *Global Greenhouse Gas Emissions Data*. 2019 12/01/2020]; Available from: <https://www.epa.gov/ghgemissions/global-greenhouse-gas-emissions-data>.
169. Spuijbroek, M., *Textile Waste in Mainland China*. 2019, Ministry of foreign affairs
170. Department for Environmental, F.a.R.A., *UK statistics on waste*. 2022.
171. Watson, D., et al., *Used Textile Collection in European Cities*, ECAP, Editor. 2018.
172. EPA, *Textiles: Material-Specific Data*. 2020.
173. Jiang, Z., Z. Guo, and C. Xiao, *Preparation and properties of bottle-recycled polyethylene terephthalate (PET) filaments*. *Textile Research Journal*, 2018. **89**(7).
174. Notman, N., *Recycling clothing the chemical way* *Chemical World* 2020. **17**(2).
175. Busilienne, G. *The Effect of Fibre Composition and Washing Conditions upon Hand Properties of Knitted Materials*. in *International Conference on Natural Fibres - Sustainable Materials for Advanced Applications* 2013.
176. Royal Society of Chemistry. *Science to enable sustainable plastics in 8th chemical sciences and society summit (CS3)*. 2020. London.
177. Wang, Y., *Recycling in Textiles* 2006: Woodhead Publishing.
178. Moharir, R., P. Gautam, and S. Kumar, *Waste Treatment Processes/Technologies for Energy Recovery*, in *Current Developments in Biotechnology and Bioengineering* K. S, K. R, and P. A, Editors. 2019, Elsevier.
179. Cheremisinoff, N., *Handbook of Air Pollution Prevention and Control*. 2002, Butterworth Heinemann: USA.
180. Bartl, A., *Textile Waste*, in *Waste*, L. T and V. D, Editors. 2011, Academic Press
181. Frith Resource Management LTD, *Incineration of Municipal Solid Waste*, F.a.R.A. Department for Environmental, Editor. 2013.
182. Hanif, M., et al., *Effects of Pyrolysis Temperature on Product Yields and Energy Recovery from Co-Feeding of Cotton Gin Trash, Cow Manure, and Microalgae: A Simulation Study* *PLoS ONE*, 2016. **11**: p. 1 - 11.
183. Miranda, R., et al., *Pyrolysis of textile wastes I: Kinetics and yields*. *Journal of Analytical and Applied Pyrolysis*, 2007. **80**: p. 489 - 495.
184. Adeleke, K., O. Itabiyi, and O. Ilori, *Design, Simulation Analysis and Performance Evaluation of a Fluidised Bed Reactor for the Pyrolysis of Biomass*. *American Journal of Engineering Research* 2018. **7**: p. 138 - 145.
185. Jamradlowdluk, J. and C. Lertsatotthanakorn, *Characterisation and Utilisation of Char Derived from Fast Pyrolysis of Plastic Wastes*. *Procedia Engineering*, 2013. **69**: p. 1437 - 1442.
186. Trubetskaya, A., et al., *Effect of fast pyrolysis conditions on biomass solid residues at high temperatures*. *Fuel Processing Technology*, 2016. **143**: p. 118 - 129.
187. Hoekstra, E., et al., *Fast pyrolysis in a novel wire-mesh reactor: Design and initial results*. *Chemical Engineering Journal*, 2012. **191**: p. 45 - 58.
188. Pandey, D., A. Daverey, and K. Arunachalam, *Biochar: Production, properties and emerging role as a support for enzyme immobilization*. *Journal of Cleaner Production*, 2020. **255**.
189. Gupta, G. and M. Mondal, *Pyrolysis: an alternative approach for utilization of biomass into bioenergy generation*, in *Biofuels and Bioenergy*, G. B, S. R, and Z. Z, Editors. 2022, Elsevier
190. Ronsse, F., et al., *Production and characterization of slow pyrolysis biochar: influence of feedstock type and pyrolysis conditions*. *GCB-Bioenergy*, 2012. **5**(2).
191. Wall, L., *The Mechanisms of Pyrolysis, Oxidation, and Burning of Organic Materials* NBS Special Publication 1970.
192. Souza, C.d.S., et al., *Induced changes of pyrolysis temperature on the physiochemical traits of sewage sludge and on the potential ecological risks* *Scientific Reports*, 2021. **11**(974).
193. Pecha, M. and M. Garcia-Perez, *Pyrolysis of lignocellulosic biomass: oil, char, and gas, in Bioenergy*, A. Dahiya, Editor. 2020, Elsevier.

194. Abdullah, N., et al., *Influence of temperature on conversion of plastic waste (polystyrene) to liquid oil using pyrolysis process*, in *2nd international Tropical Renewable Energy Conference 2017*, IOP Science Indonesia
195. Ruiz, B., et al., *Employment of conventional and flash pyrolysis for biomass wastes from the textile industry with sustainable prospects*. *Journal of Analytical and Applied Pyrolysis*, 2023. **169**.
196. Barisci, S. and M. Oncel, *The disposal of combed cotton wastes by pyrolysis* *International Journal of Green Energy*, 2014. **11**: p. 255 - 266.
197. Alongi, J., G. Camino, and G. Malucelli, *Heating rate effect on char yield from cotton, poly(ethylene terephthalate) and blend fabrics*. *Carbohydrate Polymers*, 2013. **92**: p. 1327 - 1334.
198. Park, C., et al., *Pyrolysis of Polyethylene Terephthalate over Carbon-Supported Pd Catalyst*. *Catalysts*, 2020. **10**(5).
199. Wen, C., et al., *The pyrolysis and gasification performances of waste textile under carbon dioxide atmosphere* *Journal of Thermal Analysis and Calorimetry*, 2017. **128**: p. 581 - 591.
200. Jia, H., et al., *Catalytic Fast Pyrolysis of Poly (Ethylene Terephthalate) (PET) with Zeolite and Nickel Chloride*. *Polymers*, 2020. **12**(3).
201. Li, C., et al., *Catalytic pyrolysis of polyethylene terephthalate over zeolite catalyst: Characteristics of coke and the products*. *International Journal of Energy Research*, 2021. **45**(13).
202. Joo, J., et al., *Pyrolysis of Denim Jeans Waste: Pyrolytic Product Modification by the Addition of Sodium Carbonate*. *Polymers* 2022. **14**(5035).
203. Balcik-Canbolat, C., et al., *Pyrolysis of commingled waste textile fibres in a batch reactor: Analysis of the pyrolysis gases and solid product*. *International Journal of Green Energy*, 2017. **14**: p. 289 - 294.
204. Clark, J. *Types of Catalysis*. 2013 [cited 2020 27/11]; Available from: <https://www.chemguide.co.uk/physical/catalysis/introduction.html>.
205. QS Study. *Experiment Explanation by Catalytic Adsorption Theory*. 2020 [cited 2020 27/11]; Available from: <https://www.qsstudy.com/chemistry/experiment-explanation-by-catalytic-adsorption-theory>.
206. Tian, H., et al., *Recent Advances on the Design of Group VIII Base-Metal Catalysts with Encapsulated Structures* *ACS Catalysis* 2015. **5**: p. 4959 - 4977.
207. Lu, Y., H. Jin, and R. Zhang, *Evaluation of stability and catalytic activity of Ni catalysts for hydrogen production by biomass gasification in supercritical water*. *Carbon Resources Conversion*, 2019. **2**: p. 95 - 101.
208. Qi, S., et al., *Nano-sized nickel catalyst for deep hydrogenation of lignin monomers and first-principles insight into the catalyst preparation* *Journal of Materials Chemistry*, 2017(8).
209. Yusuf, M., et al., *Contemporary trends in composite Ni-based catalysts for CO₂ reforming of methane*. *Chemical Engineering Science* 2021. **229**.
210. Jung, S., et al., *CO₂-cofeeding catalytic pyrolysis of macademia nutshell*. *Journal of CO₂ Utilization*, 2020. **37**: p. 97 - 105.
211. Hu, N., et al., *Ni-Cu/Al₂O₃ catalysts for the selective hydrogenation of acetylene: a study on catalytic performance and reaction mechanism* *New Journal of Chemistry*, 2019(46).
212. Gawande, M., et al., *Cu and Cu-Based Nanoparticles: Synthesis and Applications in Catalysis* *Chemical Reviews* 2016. **116**: p. 3722 - 3811.
213. Shi, X., et al., *Copper catalysts in semihydrogenation of acetylene: from single atoms to nanoparticles* *ACS Catalysis*, 2020. **10**: p. 3495 - 3504.
214. Vedrine, J., *Heterogeneous Catalysis on Metal Oxides* *Catalysts* 2017. **7**.
215. Sierra-Salazar, A., et al., *Unconventional Pathways for Designing Silica-Supported Pt and Pd Catalysts with Hierarchical Porosity*, in *Horizons in Sustainable Industrial Chemistry and Catalysis* S. Albonetti, S. Perathoner, and E. Quadrelli, Editors. 2019, Elsevier. p. 377 - 397.

216. Luo, W., et al., *Zeolite-supported metal catalysts for selective hydrodeoxygenation of biomass-derived platform molecules*. *Green Chemistry*, 2019. **21**.
217. Moteki, T., et al., *Zeolite surface as a catalyst support material for synthesis of single-walled carbon nanotubes* *The Journal of Physical Chemistry*, 2011. **115**.
218. Deelan, T.v., C. Mejia, and K.d. Jong, *Control of metal-support interactions in heterogeneous catalysts to enhance activity and selectivity*. *nature catalysis* 2019. **2**.
219. Lam, E. and J. Luong, *Carbon Materials as Catalyst Supports and Catalysts in the Transformation of Biomass to Fuels and Chemicals*. *ACS Catalysis*, 2014. **4**: p. 3393 - 3410.
220. Gong, Y., et al., *Graphitic Carbon Nitride polymers: promising catalysts or catalyst supports for heterogeneous oxidation and hydrogenation*. *Green Chemistry*, 2015. **17**.
221. Chaudhary, V. and S. Sharma, *An overview of ordered mesoporous material SBA-15: synthesis, functionalization and application in oxidation reactions* *Journal of Porous Materials*, 2016. **24**: p. 741-749.
222. Howard, L., C. Hammond, and A. Buchard, *Polymer-supported metal catalysts for the heterogenous polymerisation of lactones* *Polymer Chemistry*, 2019. **10**.
223. Yao, D., et al., *Co-Precipitation, impregnation and so-gel preparation of Ni catalysts for pyrolysis-catalytic steam reforming of waste plastics* *Applied Catalysis B: Environmental*, 2018. **239**: p. 565 - 577.
224. Hutchings, G. and J. Vedin, *Heterogeneous Catalyst Preparation*, in *Basic Principles in Applied Catalysis* M. Baerns, Editor. 2004, Springer: Berlin.
225. Schwarz, J., C. Contescu, and A. Contescu, *Methods for preparation of catalytic materials* *Chemical Reviews*, 1995. **95**: p. 477 - 510.
226. Dervin, S. and S. Pillai, *An Introduction to Sol-Gel Processing for Aerogels in Sol-Gel Materials for Energy, Environment and Electronic Applications*. 2017, Springer.
227. Pakhomov, N. and R. Buyanov, *Current Trends in the Improvement and Development of Catalyst Preparation Methods*. *Kinetics and Catalysis*, 2005. **46**: p. 669 - 683.
228. Jong, K.d., *Deposition Precipitation*, in *Synthesis of Solid Catalysts*, K.d. Jong, Editor. 2009, Wiley.
229. Quin, K., et al., *Understanding the deposition-precipitation process for the preparation of supported Au catalysts* *Journal of Molecular catalysis A: Chemical*, 2010. **320**: p. 97 - 105.
230. Lee, M.v.d., et al., *Deposition Precipitation for the Preparation of Carbon Nanofiber Supported Nickel Catalyst*. *JACS Articles*, 2005. **127**: p. 13573 - 13582.
231. Bartholomew, C., *Mechanisms of catalyst deactivation*. *Applied Catalysis A*, 2001. **212**: p. 17 - 60.
232. Rostrup-Nielsen, J., *Sulfur Poisoning*, in *NATO Advanced Study Institute on Catalyst Deactivation*, J. Figueiredo, Editor. 1981: Portugal.
233. Wise, H., *Mechanisms of Catalyst Poisoning by Sulfur Species*. *Studies in Surface Science and Catalysis*, 1991. **68**: p. 497 - 504.
234. Xu, T., et al., *Thermal oxidation to regenerate sulfone poisoned Pd-based catalyst: effect of the valence of sulfur*. *RSC Advances*, 2014. **63**.
235. Trimm, D., *Deactivation and Regeneration*, in *Handbook of Heterogeneous Catalysis* G. Erti, H. Knozinger, and J. Weitkamp, Editors. 1997.
236. Ostrovskii, N., *New models of catalyst deactivation by Coke: II. Coking of supported platinum catalysts*. *Kinetics and Catalysis*, 2001. **42**: p. 326 - 333.
237. Y. Dai, et al., *The physical chemistry and materials science behind sinter-resistant catalysts*. *Chem Soc Rev*, 2018. **47**.
238. Barreiro, E., et al., *Spatial, temporal and quantitative assessment of catalyst leaching in continuous flow*. *Catalysis today*, 2018. **308**: p. 64 - 70.
239. Sadaba, I., et al., *Deactivation of solid catalysts in liquid media: the case of leaching of active sites in biomass conversion reactions* *Green Chemistry*, 2015. **17**.

240. Al-Fatesg, A., et al., *Decomposition of methane over alumina supported Fe and Ni-Fe bimetallic catalyst: Effect of preparation procedure and calcination temperature*. Journal of Saudi Chemical Society, 2018. **22**: p. 239 - 247.
241. Kruissink, E., L.v. Reijen, and J. Ross, *Coprecipitated Nickel-Alumina Catalysts for Methanation at High Temperature*. Journal of the Chemical Society, Faraday Transactions 1: Physical Chemistry in Condensed, 1981. **77**: p. 649 - 663.
242. Nele, M., et al., *Preparation of high loading silica supported nickel catalyst: simultaneous analysis of the precipitation and aging steps*. Applied Catalysis A, 1999. **178**: p. 177 - 189.
243. Lim, Y., et al., *Enhanced Carbon Nanotubes Growth Using Nickel/Ferrocene-Hybridized Catalyst*. ACS Omega, 2017. **2**(9).
244. Yang, R., K. Chuang, and M. Wey, *Effects Of Nickel Species On Ni/Al₂O₃ Catalysts In Carbon Nanotube And Hydrogen Production By Waste Plastic Gasification: Bench And Pilot Scale Tests* Energy and Fuels, 2015. **29**: p. 8178 - 8187.
245. Snow, N., *Gas Chromatography in Modern Instrumental Analysis*, S. Ahuja and N. Jespersen, Editors. 2006, Elsevier.
246. McNair, H., J. Miller, and N. Snow, *STATIONARY PHASES*, in *Basic Gas Chromatography*. 2019. p. 69-86.
247. Shellie, R., *Gas Chromatography in Encyclopedia of Forensic Science* J. Siegal, P. Saukko, and M. Houck, Editors. 2013, Academic Press.
248. Sevcik, J., *Detectors in Gas Chromatography*. 1976: Elsevier Science.
249. Poole, C., *Gas Chromatography | Detectors*, in *Encyclopedia of Analytical Science*, W. P, T. A, and C. Poole, Editors. 2005, Elsevier.
250. Hubschmann, H., *Handbook of GC-MS: Fundamentals and Applications*. third ed. 2015: Wiley.
251. Turner, D., et al., *Gas Chromatography-Mass Spectrometry: How Do I Get the Best Results?* 2019: Royal Society of Chemistry.
252. Henry, A., *Mass Spectrometer Optimization*. 2020, Agilent.
253. Thomas, S., *Mass Spectrometry in Contemporary Practice in Clinical Chemistry*, W. Clarke and M. Marzinke, Editors. 2019, Academic Press.
254. Reed, S., *Scanning electron microscopy*, in *Electron Microprobe Analysis and Scanning Electron Microscopy in Geology*, S. Reed, Editor. 2009, Cambridge University Press
255. Ul-Hamid, A., *A Beginners' Guide to Scanning Electron Microscopy*. 2018: Springer Cham.
256. Adams, F. and C. Barbante, *Chapter 7 - Electron-Based Imaging Techniques*, in *Comprehensive Analytical Chemistry*, A. F and B. C, Editors. 2015, Elsevier. p. 269-313.
257. Zhao, J. and X. Liu, *Electron microscopic methods (TEM, SEM and energy dispersal spectroscopy)*, in *Reference Module in Earth Systems and Environmental Sciences*. 2022, Elsevier.
258. Prime, R., et al., *Thermogravimetric Analysis (TGA)*, in *Thermal Analysis of Polymers: Fundamentals and Applications*, M. J and P. R, Editors. 2008, John Wiley and Sons.
259. Basu, P., *Analytical Techniques*, in *Biomass Gasification, pyrolysis and Torrefaction*, B. P, Editor. 2018: Elsevier.
260. Ebnasajjad, S., *Surface and Material Characterization Techniques*, in *Handbook of Adhesives and Surface Preparation* E. S, Editor. 2011, Elsevier.
261. Saadatkah, N., et al., *Experimental methods in chemical engineering: Thermogravimetric analysis—TGA*. The Canadian Journal of Chemical Engineering, 2020. **98**(1): p. 34-43.
262. Pourhakkak, P., et al., *Fundamentals of adsorption technology in Adsorption: Fundamental Processes and Application*, M. Ghaedi, Editor. 2021.
263. Tien, C., *Introduction to Adsorption*. 2018: Elsevier.
264. Langmuir, I., *The Vapor Pressure of Metallic Tungsten*. Physical Review Journals Archive, 1913. **2**(5).

265. Monson, P., *Understanding adsorption/desorption hysteresis for fluids in mesoporous materials using simple molecular models and classical density functional theory*. Microporous and Mesoporous Materials, 2012. **160**(15): p. 47 - 66.
266. Lundstedt, C., *BET Theory and how its used to calculate surface area*. 2019.
267. Ambroz, F., et al., *Evaluation of the BET Theory for the Characterisation of Meso and Microporous MOFs*. Small Methods, 2018. **2**(11).
268. Holbrook, R., et al., *Overview of Nanomaterial Characterisation and Metrology*, in *Characterisation of Nanomaterials in Complex Environmental and Biological Media*. 2015, Elsevier.
269. Stuart, B., *Infrared Spectroscopy: Fundamentals and Applications*. 2004: John Wiley & Sons.
270. Griffiths, P. and J. de Haseth, *Fourier Transform Infrared Spectrometry*. 2nd Edition ed. 2006: John Wiley & Sons.
271. Cantor, B., *Bragg's Law: Diffraction*, in *The Equations of Materials 2020*, Oxford University Press
272. Davis, J., *Tensile Testing*. 2004, Ohio: ASM International.
273. Standardisation., I.O.f., *Paints and varnishes — Corrosion protection of steel structures by protective paint systems — Part 9: Protective paint systems and laboratory performance test methods for offshore and related structures*, in *ISO 12944-9:2018*. 2018.
274. Nam, H., et al., *Chemical composition of pyrolysis oil through thermal decomposition of sugarcane biomass*. Vietnam journal of chemistry, 2020. **58**: p. 770-778.
275. Smart, S., et al., *Porous ceramic membranes for membrane reactors*, in *Handbook of Membrane Reactors* B. A, Editor. 2013, Woodhead Publishing.
276. Debiagi, P., et al., *Yield, Composition and Active Surface Area of Char from Biomass Pyrolysis* Chemical Engineering Transactions, 2018. **65**.
277. Wang, H., et al., *Large scale synthesis and characterisation of Ni nanoparticles by solution reduction method* Bulletin of Material Science, 2008. **31**: p. 97 - 100.
278. Leyva-Ramos, R., et al., *Fluoride Removal from Water Solution by Adsorption on Activated Alumina Prepared from Pseudo-Boeshmite*. Journal of Environmental Engineering and Management Journal, 2008. **18**: p. 301 - 309
279. Li, Z., et al., *Low-Temperature Growth of Graphene by Chemical Vapor Deposition Using Solid and Liquid Carbon Sources* ACS Nano, 2011. **5**(4).
280. Brukh, R. and S. Mitra, *Mechanism of carbon nanotube growth by CVD*. Chemical Physics Letters, 2006. **424**.
281. Kleefeld, J. and L. Levenson, *Nickel carbide: Its formation and characterization by transmission electron diffraction, Auger electron spectroscopy and electron spectroscopy for chemical analysis* Thin Solid Films, 1979. **64**(3).
282. Wang, H., et al., *The effect of methane decomposition on the formation and magnetic properties of iron carbide prepared from oolitic hematite`*. RSC Advances, 2017. **7**: p. 3921 - 3927.
283. Committe, E.R., *Epoxy Resins In Wind Energy Applications*. 2015.
284. International Organisation for Standardisation., *Plastics - Determination of flexural properties*. 2019.
285. Pelleg, J., *Mechanical Properties of Materials* Solid Mechanics and Its Applications 2013: Springer Dordrecht.
286. Pickett, J., *Weathering of Plastics in Handbook of Environmental Degradation of Materials* K. M, Editor. 2018, Elsevier.
287. Robinson, R., *Accreditation of Mechanical Testing Laboratories*, in *Mechanical Testing and Evaluation* H. Kuhn and D. Medlin, Editors. 2000, ASM International.
288. MG Chemicals, *Translucent Epoxy Encapsulating and Potting Compounf 832C Technical Data Sheet*. 2016.

289. Luecke, W., et al., *Repeatability and reproducibility of compression strength measurements conducted according to ASTM E9 2009*, National Institute of Standards and Technology
290. American Society for Testing and Materials, *Standard Test Methods for Flexural Properties of Unreinforced and Reinforced Plastics and Electrical Insulating Materials in D790-17*. 2017.
291. Licari, J. and D. Swanson, *Test and Inspection Methods*, in *Adhesives Technology for Electronic Applications* L. J and S. D, Editors. 2011, Elsevier.
292. Fu, Y. and X. Yao, *A review on manufacturing defects and their detection of fiber reinforced resin matrix composites*. Composites Part C: Open Access, 2022. **8**.
293. Fu, J., et al., *Morphology, toughness mechanism, and thermal properties of hyperbranched epoxy modified diglycidyl ether of bisphenol A (DGEBA) interpenetrating polymer networks*. Polymers for Advanced Technologies 2008. **19**(19): p. 1597 - 1607.
294. Liang, h., et al., *Mechanism Identification and Kinetics Analysis of Thermal Degradation for Carbon Fiber/Epoxy Resin*. Polymers, 2021. **13**(4).
295. Ullah, R., I. Ahmad, and Y. Zheng, *Fourier Transform Infrared Spectroscopy of "Bisphenol A"*. Journal of Spectroscopy, 2016. **2016**.
296. Din, I., et al., *Surface modification of carbon nanofibers by HNO₃ treatment*. Ceramics International, 2016. **42**(1): p. 966 - 970.
297. Klein, k., et al., *Surface characterization and functionalization of carbon nanofibers*. Journal of Applied Physics, 2008. **103**(6).
298. Pavia, M., et al., *Organic Functionalization of Carbon Nanofibers for Composite Applications* Polymer Composites, 2010. **31**(3).
299. Vidick, D., et al., *Comparison of functionalized carbon nanofibers and multi-walled carbon nanotubes as supports for Fe-Co nanoparticles*. Journal of Materials Chemistry A, 2013. **1**: p. 2050 - 2063.
300. Said, Z., et al., *Acid-functionalized carbon nanofibers for high stability, thermoelectrical and electrochemical properties of nanofluids* Journal of Colloid and Interface Science, 2018. **520**: p. 50 - 57.